The Second Skin Approach: Skin Strain Field Analysis and Mechanical Counter Pressure Prototyping for Advanced Spacesuit Design

by

Kristen Bethke

B.S.E., Mechanical and Aerospace Engineering, Princeton University (2003)

SUBMITTED TO THE DEPARTMENT OF AERONAUTICS AND ASTRONAUTICS
IN PARTIAL FULFILLMENT OF THE REQUIREMENTS FOR THE DEGREE OF

MASTER OF SCIENCE IN AERONAUTICS AND ASTRONAUTICS
AT THE
MASSACHUSETTS INSTITUTE OF TECHNOLOGY

JUNE 2005

Signature of Author.....
Department of Aeronautics and Astronautics
May 20, 2005

Certified by.....
Dava J. Newman
Professor of Aeronautics and Astronautics and Engineering Systems
MacVicar Faculty Fellow
Thesis Supervisor

Accepted by.....
Jaime Peraire
Professor of Aeronautics and Astronautics
Chair, Committee on Graduate Students

The Second Skin Approach: Skin Strain Field Analysis and Mechanical Counter Pressure Prototyping for Advanced Spacesuit Design

by

Kristen Bethke

Submitted to the Department of Aeronautics and Astronautics
on May 20, 2005 in Partial Fulfillment of the
Requirements for the Degree of Master of Science
in Aeronautics and Astronautics

Abstract

The primary aim of this thesis is to advance the theory of advanced locomotion mechanical counter pressure (MCP) spacesuits by studying the changes in the human body shape during joint motion. Two experiments take advantage of three-dimensional laser scan technology to measure the shape changes of the human body. The first experiment is an analysis of the surface area and volume of the thigh, knee, calf, and entire leg during knee flexion. The second experiment is an analysis of the full-field strain on the skin surface of the leg during knee flexion. A repeatable and quantitative technique for mapping the leg skin strain field is developed. The results of the algorithm indicate the magnitude of strain over the entire surface of the leg, as well as the direction of minimum leg skin stretching during knee flexion. For 88% of the leg surface, knee flexion causes skin strain between -0.3 and 0.3 (less than 30% contraction or extension). However, just below the patella, longitudinal strain is as high as 0.7, and at the knee hollow, it is as low as -0.6. Circumferential strain values are as high as 1.0 and 0.5 just below the patella and over the calf muscle, respectively, and along the anterior surface of the lower leg, they are as low as -0.7. The leg area, volume, and skin strain results lead to quantitative design requirements for highly mobile second skin spacesuits, and they inspire two prototype MCP leg sleeves: a hybrid urethane-foam bladder garment and a skintight nylon fiber lines of non-extension garment. These two prototypes are constructed and tested for mobility and skin surface pressure. Pressurization of the hybrid foam prototype inhibits leg mobility. However, the nylon lines of non-extension prototype shows promise as an advanced locomotion spacesuit design concept. During pressurization to leg surface pressure of 7.5 kPa (56 mmHg, 1.1 psi), the prototype preserves easy mobility to 90 degrees of knee joint flexion. Recommendations are made for improving its pressure production performance to the desired 30 kPa (222 mmHg, 4.3 psi) level.

Thesis Supervisor: Dr. Dava J. Newman
Title: Professor of Aeronautics and Aeronautics and Engineering Systems Division; MacVicar Faculty Fellow

Acknowledgements

This work is supported by the NASA Institute for Advanced Concepts (NIAC contract 070605-003-006) and the National Science Foundation Graduate Research Fellowship.

In addition to financial resources, the work of this thesis has been made possible by the intellectual contributions and emotional support of many people, and I am thankful for all of them.

First, I am grateful to Professor Dava Newman for providing me with so many opportunities during the past two years – the opportunity to study at MIT, to perform interesting and challenging research on the Bio-Suit project, to travel to interesting places, to meet many interesting people in the world of human spaceflight, and to pursue my development not just as a researcher but also as a person.

I am grateful to Brain Corner, Peng Li, and Steven Paquette of the Anthropometry division at Natick Soldier Systems Center for their invaluable support in collecting data with the whole-body laser scanner. For assistance with data processing back at MIT, I thank Professor Raul Radovitzky for his patient guidance on strain field analysis. Thanks to Dave Robertson and Chris Krebs for their help with 3D leg printing. For their construction of the foam hybrid prototypes and their advice about the lines of non-extension prototype, I am very grateful to Gui Trotti and Cam Brensinger. I thank other members of the Bio-Suit team for their ideas and support, especially Professor Jeff Hoffman and Alec Jessiman.

Without the friendship and guidance of my fellow MVL students, I cannot imagine completing this work. You are truly a remarkable crew. Thanks especially to Brad Pitts for providing a thorough introduction to the world of MCP spacesuits and for initiating the laser scanning and body analysis work. Thanks to Chris Carr for so much intellectual assistance, general wisdom, and essential encouragement, to Phil Ferguson for a sense of humor, computer help, and a listening ear, to Erika Wagner and Jessica Marquez for much support and encouragement, to Jessica Edmonds and Liang Sim for reminding me to have fun, and to Kevin, Sophie, Nicole, Julie, Jeremie, Paul, Dan, and Aaron for being great lab mates in general. Two undergraduate students were particularly helpful to my research: thanks to Jeremy Conrad and Cameron Dube.

Other faculty members and administrators were also very helpful: thank you to Chuck Oman and Larry Young for their guidance of MVL students, thanks to Liz Zotos for keeping us all organized, always with a smile, thank you to Sally Chapman for keeping me well stocked with so many prototyping materials, and especially thank you to Phyllis for keeping us straight in the MVL and for always being so encouraging.

Finally, I thank all of my friends and family who have been so supportive, from close by or far away, during the past two years. I am grateful to Amy and Johanna and all the students of LEM for their care and fellowship and enrichment of my MIT experience. Thank you to all my lovely roommates - Lisa, Kate, Jen, Beth, Anna Rose - for keeping me well fed and full of laughter. Thanks to Laura G., Laura D., Rosa, and all my fellow 03'ers for their constant support.

Most of all, I thank Chris and my amazing family. Thank you to Chris for your love, laughter, providing plenty to talk about besides spacesuits, making it through two engineering theses, and sharing your life with me. And thank you to my family for their love, support, and consistent and genuine interest in my academic life, and for their promises to hang in there with me on whatever path it takes me. I am incredibly blessed, and I am incredibly grateful for all of you.

Table of Contents

List of Figures

List of Tables

CHAPTER 1: INTRODUCTION

Future space missions will require astronauts to be highly mobile as they explore planetary surfaces on foot. Explorer-astronauts will need spacesuits with revolutionary capabilities compared to the current Extravehicular Mobility Unit (EMU) spacesuits. These future spacesuits must enable mobility and at the same time provide all aspects of life support.

The purpose of this thesis is to advance the theory and practice of mechanical counter pressure (MCP) spacesuit design as an alternative to gas pressure spacesuits. MCP techniques use the mechanical tension of a skintight garment rather than the compression of a gas to produce pressure on the body surface. The MCP pressurization method is intended to maximize astronaut mobility while still meeting the physiological need for a balance of breathing pressure and body surface pressure.

The life support demands of spacesuits are many: the suit system must supply oxygen for breathing, remove carbon dioxide, control humidity, protect from environmental hazards including radiation and dust, regulate temperature, supply water and nourishment, and allow for communication with other explorers. Different researchers have pursued advancements in several of these areas; for example, Hodgson [2003] has studied advanced thermoregulation and atmospheric control, and Remington et al. [1992] and Chodack and Spampinato [1991] have focused on micrometeroid and debris protection. This thesis, however, focuses on meeting the life support demand of body pressurization.

In the five chapters of this thesis, I will show that an operational MCP suit can be realized if the design effort is predicated by a thorough investigation of the shape changes of the locomotive[1] human body. Included in this investigation is an analysis of leg surface area and volume changes, as well as the creation of a technique for leg skin strain field mapping. The analytical results inspire the design of two prototype MCP leg sleeves.

The following sections provide a concise problem statement, the motivation for this research, and a guide for reading the subsequent chapters.

1.1 PROBLEM STATEMENT

The primary goal of this thesis is to provide quantitative design requirements for a highly mobile spacesuit by measuring the shape changes of the human body during locomotion. To achieve this goal, the research has been guided by the three following research objectives.

[1] The term "locomotive" is used to distinguish exploration-class astronauts who will walk on a planetary surface from Shuttle and International Space Station astronauts who rely on upper body mobility and use their arms to move about in their weightless environment. In this study, flexion (bending) of the knee joint approximates one of the major aspects of human locomotion.

1.1.1 RESEARCH OBJECTIVE 1

Develop a systematic, repeatable, and quantitative technique for determining and displaying the strain field on the skin surface of the human body in motion, using laser scanning for data collection, low computational demands, and an intuitively understandable visual display of the analysis's results.

1.1.2 RESEARCH OBJECTIVE 2

Mathematically determine two types of strain (stretch/contraction) information for a representative sample of leg surface points: 1) the normal and shear strain in the leg's local "longitudinal" and "circumferential" directions, and 2) the direction and magnitude of minimum stretch along the leg surface. This information will identify in which direction and with what magnitudes a "second skin" pressure suit must stretch or contract at each location on the body surface.

1.1.3 RESEARCH OBJECTIVE 3

Construct prototype mechanical counter pressure leg garments based on mathematical representations of leg shape changes, and test the garments' ability to produce constant and even pressure on a human subject.

1.2 MOTIVATION

A fundamental paradox of spacesuit design is that freedom of movement must be maintained while constant and even pressure is simultaneously applied to the body surface. This challenge represents a conflict between a *life support* requirement and a *productivity* requirement: applying sufficient body surface pressure at the same time as allowing for free locomotion.

The motivation for mechanical counter pressure suits (and hence for the study of skin strain) becomes apparent if we take a closer look at the trade between body surface pressure and mobility. Physiologically, the pressure pushing inward on the body surface must equal the breathing pressure in the lungs, which must be a minimum of 21 kPa (158 mmHg, 3.05 psi) of oxygen [Barratt & Newman, 1997]. Historically, for all extravehicular activity, this pressure requirement has been met by enclosing the astronaut in a gas pressure suit. In the U.S. spacesuit, the astronaut is immersed in the same 29.6 kPa (222 mmHg, 4.29 psi) of oxygen that he or she is breathing. This conventional technique for applying a pressure, p, on the body surface mandates that there is a volume of gas, V, between the wearer and the suit. Consequently, any motion by the wearer that compresses some part of that volume will require extra work output, as energy is required to compress a constant amount of pressurized gas into a smaller space. This energy, called pressure-volume work, is analogous to the effort that is required to bend a long inflated cylindrical balloon. Because there is an upper limit to the amount of torque that a human's joints can exert, there is an upper limit to the amount of pressure-volume work a spacesuit-wearer can achieve. Thus, there is an upper limit to the mobility that he or she has in a gas pressure suit. For Shuttle and International Space Station activities, limited and primarily upper-body mobility has been adequate. For future surface exploration, however, lower body mobility will be required, and the limited mobility of the current EMU is not sufficient. New designs for efficiently producing body surface pressure are needed.

The technique called mechanical counter pressure (MCP) is an alternative way to satisfy the life support requirement of body surface pressure. MCP techniques use the mechanical tension of a

skintight garment rather than the compression of a gas to produce pressure over the entire body surface.

The only functioning full-body MCP suit prototype that is known to have been built and tested was the Space Activity Suit (SAS) developed by Webb and Annis in the 1960s [Annis & Webb, 1971]. It enabled much greater mobility than the Apollo pressure suit and caused a decreased metabolic rate compared to the Apollo suit. However, the knee flexion range in the SAS was still less than the unsuited range (81 degrees suited average vs. 141 degrees unsuited average), and its energy cost of locomotion was 1.64 times greater than the unsuited cost [Annis & Webb, 1971]. The sources of this increased energy cost and decreased mobility in the SAS remain unknown. Descriptions of the SAS do not discuss what design improvements, if any, would avoid an increase in metabolic rate and a decrease in mobility from an unsuited baseline.

Since MCP suits are skintight, with direct application of pressure to the skin, more information about the changing shape of the human body in motion is needed to specify design requirements for an optimal MCP suit. Although it may seem unlikely that bioastronautics researchers have not already studied the changing human body shape, current human factors research is indeed insufficient for MCP design. The shortcoming of previous human factors research for the design of spacesuits and space vehicles is that it has looked only at changes in the position of *bones* and *joints* (traditional landmark anthropometry). Furthermore, when researchers study the shape changes that occur during joint bending, they model the bending joint as a gas-filled uniform cylindrical tube surrounded by a membrane [Main, Peterson, & Strauss, 1994, 1995; Schmidt, 2001]. These models do not encapsulate the intricacies of the surface deformation of a true human joint. In summary, with the exception of Iberall, whose research will be introduced in Chapter 2, the bioastronautics community has not examined the deformation of *skin*.

In this thesis, the purpose of mapping the skin surface strain field is to provide advanced spacesuit researchers with a quantitative description of the human body shape changes that a spacesuit must accommodate. Specifically, for development of a skintight mechanical counter pressure spacesuit as an alternative to the gas pressure spacesuit, designers must understand not only the overall motion of the joints but also the local stretching and rotating of the skin during joint movements.

This analysis is essential to the spacesuit research community, but it also has potential engineering applications outside of the spacesuit community. Information about the deformation of the skin over the entire body surface may be useful to the fields of high performance athletic apparel, prosthetics and orthotics, surgery, and body tissue engineering.

1.3 HYPOTHESES

The work of this thesis can be separated into two main efforts: first, the investigation of human body shape changes during locomotion and a resulting mathematical representation of the changes, and second, the construction and testing of custom-fit MCP leg garment prototypes. Two separate hypotheses direct the specific research activities within these two areas.

1.3.1 HYPOTHESIS 1

I hypothesize that the human leg's "lines of non-extension" [2] *and "lines of minimum stretch"* [3] *will be revealed by the strain field created on the leg*

[2] The term "lines of non-extension" was coined by Iberall [1970] to describe the curves on the surface of the body along which the skin does not stretch with body movement.

surface during knee flexion. On the surface of the patella and the popliteal fossa (the shallow depression on the posterior surface of the knee), lines of only minimum stretch, rather than lines of non-extension, will be found. In other words, I predict that in all locations on the leg surface except the patella and the back of the knee, the strain field caused by knee flexion will reveal directions in which zero deformation occurs. At the patella and the back of the knee, deformation will occur in all directions.

1.3.2 HYPOTHESIS 2

I hypothesize that an operational MCP suit can be realized if the design effort is predicated by a thorough investigation of the surface strain field of the locomotive human body.

1.4 CONTRIBUTIONS OF THESIS

This thesis makes contributions to several different fields of research, including advanced spacesuit design, digital mechanics analysis, three-dimensional (3D) laser scanning, skin biomechanics, and apparel design. These contributions build on the key literature on mobile pressure suits and the mechanical properties of human skin.

In solid mechanics, it is a difficult problem to measure full-field two-dimensional (2D) surface strain on a 3D irregular body. This thesis offers a first-order solution to this problem. It presents a simple algorithm for estimating 2D surface strain that uses laser scans, rather than optical images, as the data set for digital strain field mapping. This algorithm is appropriate and useful for experiments when laser scanners are more readily available than stereographic camera set-ups, when 3D computer data already exists, when accuracy requirements are relaxed, or when high computational power is not available. The laser scan strain mapping method described in Chapter 3 is the first published account, to our knowledge, of analyzing full-field surface deformation with a laser scanner as the primary tool.

To the field of advanced spacesuit design, this thesis contributes the first quantitative analysis of the required strain distribution for a mechanical counter pressure suit. The results described herein include a full-field description of the magnitude and direction of strain (stretch/contraction) on the skin surface of the human leg. This strain field map tells spacesuit designers the amount of stretching and contracting that a second skin spacesuit needs to accommodate over the entire leg surface. This pattern of skin stretching also has applications for the fields of athletic apparel design, biomechanical engineering, and prosthetics.

Finally, with two prototyping efforts, this thesis further proves the feasibility of generating desired levels of mechanical counter pressure (~30 kPa) on the leg surface. Two designs are presented: 1) a hybrid urethane-foam prototype and 2) a skintight, lines of non-extension garment that directly applies mechanical counter pressure. These prototypes demonstrate that MCP can be achieved. Most importantly, the prototype design process demonstrates how mathematical representations of human skin deformation can be applied to quantitative apparel design.

---

[3] I use the term "lines of minimum stretch" to indicate that at some regions of the body, the skin deforms in all directions during joint motion, so lines of non-extension do not exist in these regions, and I look instead for the curves along which the skin minimally stretches.

1.5 ROADMAP TO THESIS

This thesis offers the reader helpful background information, explains the methods and results for the two major experimental efforts of human body shape analysis and pressure suit prototyping, and finally discusses the implications and limitations of these results.

Chapter 2, "Background and Literature Review," begins with an introduction to the current U.S. spacesuit and a further explanation of the alternative mechanical counter pressure spacesuit. The physics of locomotion in a spacesuit are discussed, and previous research on mechanical counter pressure suits is reviewed. The second half of Chapter 2 reviews three topics relevant to the measurement of human body shape changes: the biomechanics of locomotion, the mechanical properties of skin, and the techniques of digital image correlation and laser scanning for optical skin strain analysis.

Chapter 3, "The Changing Shape of the Human Leg: Three-Dimensional Dynamic Anthropometry," covers the investigation of the human leg shape changes during knee flexion. First, the methods and results for characterizing leg surface area and volume changes are presented. Then, a technique for mathematically representing skin stretch and mapping the leg skin strain field is explained. Ideally, the results of Chapter 3 should suggest an MCP suit pattern that provides optimal mobility for locomotion.

In Chapter 4, "Designing and Prototyping Mechanical Counter Pressure Suits for the Changing Leg Shape," the reader can discover how data on the shape changes of the flexing human leg are transformed into specifications for an MCP suit that generates and maintains the necessary body surface pressure. The designs and testing results for two MCP leg prototypes are presented. First, the shape-responsive hybrid MCP leg garment is described. Second, the lines of non-extension leg sleeve is discussed.

Chapter 5, "Discussion," contains reflections on the leg shape analysis as well as the prototyping efforts. The most important skin strain field results are highlighted, and then the implications and limitations of the skin strain field experiment are discussed. After considering this experiment, Chapter 5 reviews the lessons learned from both the shape-responsive hybrid prototype and the lines of non-extension prototype. Next, the limitations of this thesis are acknowledged, and recommendations are made for further body analysis and MCP design. Finally, the thesis ends with a restatement of key contributions and an expression of the broader vision for this work.

Chapter 1 References

1. Annis, J.F., and Webb, P. "Development of a space activity suit," NASA Contractor Report CR-1892,Webb Associates, Yellow Springs, Ohio, 1971.
2. Chodack, J., Spampinato, P. "Spacesuit glove thermal micrometeroid garment protection versus human factors design parameters." *Proceedings of the 21st International Conference on Environmental Systems,* Society of Automotive Engineers, San Francisco, CA, July 1991.
3. Hodgson, E. "The chameleon suit – a liberated future for space explorers." *Gravitational and Space Biology Bulletin.* Vol. 16, No. 2, June 2003, p. 107-119.
4. Iberall, A.S. "The experimental design of a mobile pressure suit." *Journal of Basic Engineering,* June 1970 p. 251- 264.
5. Main, J. A., Peterson, S. W., Strauss, A. M. "Design and structural analysis of highly mobile space suits and gloves." *Journal of Spacecraft and Rockets,* Vol. 31, No. 6, 1994, p. 1115-1122.
6. Main, J. A., Peterson, S. W., Strauss, A. M. "Beam-type bending of space-based inflatable structures." *Journal of Aerospace Engineering,* Vol. 8, No. 2, April 1995, p. 120-125.
7. Remington, B., Cadogan, D. "Enhanced softgoods structures for spacesuit micrometeroid/debris protective systems." *Proceedings of the 22nd International Conference on Environmental Systems,* Society of Automotive Engineers, Seattle, WA, July 1992.
8. Schmidt, P. *An Investigation of Space Suit Mobility with Applications to EVA Operations.* Ph.D. Thesis, Massachusetts Institute of Technology, 2001.

CHAPTER 2: BACKGROUND AND LITERATURE REVIEW

Before discussing the human body analysis and pressure suit prototyping that were the main emphasis of this thesis effort, an overview of background information, previous research, and relevant physical concepts is necessary. This chapter begins with a discussion of the current NASA spacesuit and the basic physics of locomotion in that spacesuit. Next, the physics of the alternative mechanical counter pressure suit are introduced, followed by a review of previous literature on mechanical counter pressure prototyping and experimentation. The work of Iberall is mentioned here. His study of skin and mobility leads to a discussion of the shape changes of the human body in motion. The biomechanical mechanisms of locomotion are described, and the literature on the biomechanical structure of human skin is reviewed. The chapter concludes on the topic of measuring human body shape changes, with introductions to the techniques of Digital Image Correlation for optical strain analysis and laser scanning for three-dimensional anthropometry.

2.1 LOCOMOTION IN THE EXTRAVEHICULAR MOBILITY UNIT

Any time that an astronaut moves outside of a pressurized space vehicle or habitat, he or she is engaging in extravehicular activity (EVA). The first EVA took place in March of 1965, when Alexei Leonov, attached to a 5-meter umbilical cord, spent over ten minutes outside the Russian Voskhod spaceraft [Barratt & Newman, 1997]. Since then, EVAs have occurred outside Gemini spacecraft, Apollo lunar landers, Soyuz spacecraft, Skylab, the Space Shuttle, Mir Space Station, and the International Space Station. During EVA, a spacesuit protects the astronaut from the vacuum of space or the extremely sparse atmosphere of another planet. The spacesuit must provide thermal regulation, a breathable atmosphere, shielding from radiation, protection from environmental contaminants such as dust and orbital debris, and body surface pressure.

On all EVA missions from the U.S. Space Shuttle and most from the International Space Station, these requirements have been satisfied by NASA's Extravehicular Mobility Unit (EMU), consisting of a pressurized spacesuit assembly and a portable life support system. As described in Table 2.1, the spacesuit is made out of multiple fabric layers attached to an aluminum and fiberglass hard upper torso unit, and it is pressurized with 100% oxygen at 29.6 kPa (222 mmHg, 4.29 psi). The pressurized oxygen provides a breathable atmosphere within the EMU in addition to generating body surface pressure. This pressurization method, and the EMU in general, have enabled useful work to be accomplished in the microgravity environment of Earth orbit.

The EMU has established many advancements in spacesuit design and performance and has been an impressive tool for Shuttle and Station missions. However, the mobility enabled by the EMU is not sufficient for locomotion on planetary surfaces.

Table 2.1 Layers of the EMU spacesuit. Layer 1 is the innermost layer [Adapted from Frazer, 2003, p. 17, and Kozloski, 1994].

Layer	Textile	Function
1	Nylon/spandex lined with tricot, with ethylene-vinyl-acetate plastic tubing	Liquid cooling and ventilation garment
2	Polyurethane-coated nylon	Bladder for pressurization
3	Dacron woven with primary and secondary axial lines	Restraint and control of longitudinal extension
4	Neoprene-coated nylon ripstop	Liner
5-9	Aluminized mylar backed with unwoven Dacron	Thermal insulation
10	Gore-tex and Nomex fibers woven and backed with Kevlar network	Abrasion and flame resistance and micrometeroid protection

Because of its pressurized gas and restrictive mechanical joints, the EMU is simply not very accommodating to body limb manipulations. Upper body motion requires significant effort, and lower body motion is severely limited. These mobility restraints are partly intentional and partly undesired. Most EVA work in Earth orbit is carried out in foot restraints and relies on the stiffness of the suit's lower body to transmit forces from the upper body. Consequently, the EMU was intentionally designed for mainly upper body motion. The suit's hip joint is a single-axis joint that allows only twisting motion only about the torso's long axis. Below the hip, only forward and backward leg motion is allowed; no abduction or adduction is possible [Schmidt, 2001]. In addition to these intentional mobility limits, the suit's joint angles ranges are limited by the pressurization of the EMU limbs. Bending at the joints requires pressure-volume work, which places high torque demands on the hip, knee, and ankle joints and consequently narrows the joint angle ranges. A 1-g study of suited subjects found the hip flexion range to be 20 to 40 degrees (for a specification of 0 to 70 degrees), the knee flexion range to be 10 to 90 degrees (for a specification of 0 to 120 degrees), and the ankle flexion range to be −35 to 30 degrees (for a specification of −40 to 40 degrees) [Schmidt, 2001, p. 76].

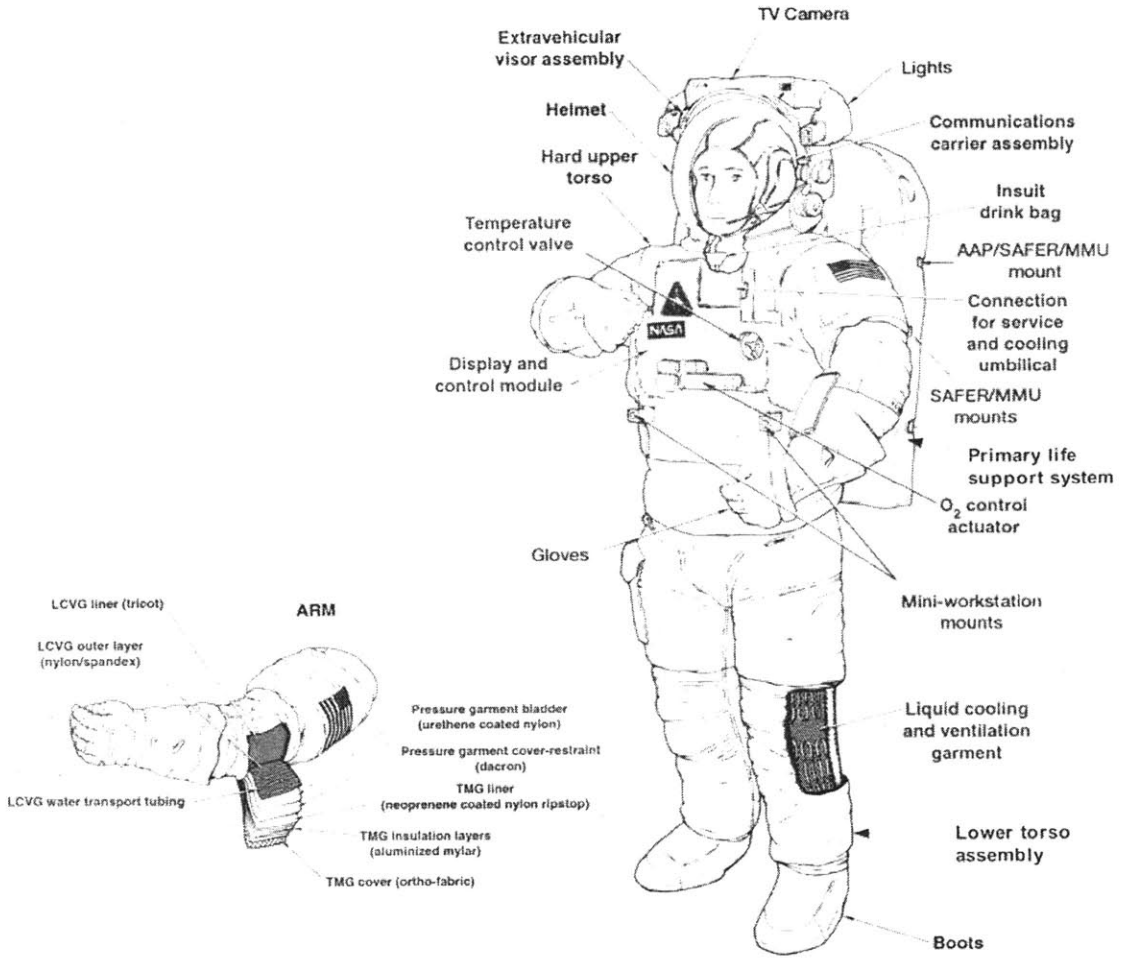

Figure 2.1 Main components and layers of the Extravehicular Mobility Unit [Courtesy Hamilton Sundstrand].

These limited joint angle ranges can be understood by briefly considering the thermodynamics of deforming a pressurized fabric suit. The work, W, to bend a spacesuit joint is given by Equation 2.1.

$$W = W_p + W_e \tag{2.1}$$

where W_p is the work done against pressure and W_e is the work done against the elastic forces of the fabric [Iberall, 1970]. When an astronaut attempts to bend an EMU joint, the fabric cylinder folds on the inside of the bend while the outside essentially retains its initial length. Consequently, the volume of the joint decreases, and the astronaut must provide the work for this volume decrease, W_p, as well as the work to bend the spacesuit fabric, W_e. Because the EMU is maintained at a constant pressure, the work required to change the volume of gas enclosed in the joint is given by Equation 2.2.

$$W_p = \int_{V_1}^{V_2} -p\,dV = -p(V_2 - V_1) = p(V_1 - V_2) \tag{2.2}$$

where p is the suit pressure (a constant) and V is the joint volume [Barratt & Newman, 1997]. The work output required by the astronaut is stipulated by the magnitude of volume change, $(V_1 - V_2)$. The higher this volume change, the higher the work output, and the lower the joint angle range (or mobility). From Equation 2.2, it is evident that one key to enabling mobility in spacesuits is to drive the joint flexion volume change towards zero.

2.2 AN ALTERNATIVE TO THE EMU: MECHANICAL COUNTER PRESSURE SUITS

It actually is possible to generate body surface pressure without any gas shell volume at all. To satisfy the EVA pressure requirement, an alternative to pressurizing gas around the body is tensing a skintight garment around the body. Oxygen is still provided through a closed helmet, but to balance the breathing pressure over the rest of the body, mechanical pressure is applied over the arms, leg, and torso. In 1968, Paul Webb conceived of this mechanical counter pressure (MCP) technique and unveiled it in the form of an experimental Space Activity Suit (SAS).

In an MCP suit, the pressure felt on the body surface is equal to the tension, T (per unit length down the long axis of the body part), in the skintight fabric divided by the body's local radius of curvature, κ, as shown in Equation 2.3 (full derivation in Appendix A) [Annis & Webb, 1971; Pitts 2003; Bethke, Carr, Pitts, & Newman, 2004].

$$p_{MCP} = \frac{T}{\kappa} \tag{2.3}$$

Hence, for a certain mechanical counter pressure p_{MCP}, the required tension per unit length, T, is found by Equation 2.4.

$$T_{req} = p_{MCP}\,\kappa. \tag{2.4}$$

Because the cross-sectional radius of the body limb, κ, depends on longitudinal position along the limb, on joint flexion angle, and on muscle flexion state, the required MCP tension is also a function of these three quantities. Consequently, an MCP suit that produces *uniform* body surface pressure actually is under *variable* levels of tension, depending on body segment and joint position.

Webb's suit succeeded in supplying the tension that would apply the necessary breathing pressure to the wearer's skin. However, it did not succeed in ease of use; it was extremely difficult to put on and take off (don and doff). Consisting of seven layers of elastic material, it required several hours and several people to be stretched onto the wearer's body and to be pried off of the wearer's body. An additional problem was that although the SAS greatly improved mobility over the Apollo gas pressure suits, its knee flexion range was still less than the unsuited range (81 degrees suited average vs. 141 degrees unsuited average), and the energy cost of locomotion was 1.64 times greater than the unsuited cost [Annis & Webb, 1971]. NASA did not pursue development of a mechanical counter pressure spacesuit after the SAS was demonstrated as a novel concept.

Figure 2.2. Bending backwards in Annis and Webb's Space Activity Suit, which was the first operational full-body prototype of the mechanical counter pressure spacesuit concept [Annis & Webb, 1971].

However, several researchers have sustained the idea of mechanical counter pressure suits. The first publication after Webb's work was by Clapp, who designed and tested an MCP glove and compared its performance to the A7L-B Skylab era gas pressure glove [Clapp, 1983]. Subjects tested the elastic "skinsuit" glove in a partial vacuum of 24 kPa (180 mmHg, 3.5 psi) for 30 continuous minutes. While wearing the skinsuit glove, subjects retained 90% of bare-skin finger mobility, compared to 30% mobility in the A7L-B gas pressure glove. Slight edema occurred over the palm of the hand, but Clapp dismissed this swelling as negligible, and he reported that no other health problems were observed. Later, Clapp developed a hybrid inflatable glove concept, which used the elastic glove as a restraint layer over a gas-tight pressure bladder. This design is similar to the traditional EMU glove but uses elastic over the pressure bladder rather than fabric convolutes. In 2002, Korona built upon Clapp's work by comparing performance in a hybrid gas-elastic glove with performance in a 4000-series EMU glove. Though Korona's glove was not a true mechanical counter pressure garment, it did incorporate elastic pressure, and in a test of 15 subjects, he found that the hybrid elastic glove outperformed the EMU glove in both mobility and perceived exertion levels [Korona, 2002].

Webb and colleagues revived MCP research with studies of the physiological effects of elastic MCP gloves and arm sleeves. Their elastic glove produced 27 kPa (200 mmHg, 3.9 psi) of skin compression on all regions of the hand except the palm, where the compression levels were reduced to about 9.3 kPa (70 mmHg, 1.4 psi) [Waldie et al., 2002]. The glove functioned under partial vacuum conditions and prevented the blood flow increase, tissue edema, and finger swelling that occurred on the naked hand in a partial vacuum of −6.7 kPa (-50 mmHg, 0.97 psi) [Tourbier et al., 2001]. The researchers concluded that MCP gloves sufficiently inhibit blood shift and tissue expansion, as desired, when the hand is exposed to underpressure. Next they developed an elastic MCP sleeve for the full arm [Tanaka et al., 2003]. The pressure produced by the sleeve varied from 21 kPa (160 mmHg, 3.1 psi) at the forearm and upper arm to 31 kPa (230 mmHg, 4.5 psi) at the finger, dorsum of hand, and wrist. Despite the variations in pressure,

during partial vacuum tests, the sleeve prevented harmful changes in skin blood flow and skin temperature and enabled subjects to tolerate underpressures of up to −20 kPa (-150 mmHg, 2.9 kPa) for 5 minutes. Inflatable or gel inserts for the wrist and hand dorsum were suggested as solutions to the uneven pressure distribution. Inserted between the skin and the elastic suit, these thin pockets of air or compressible gel would add curvature to the body limb and allow the suit to function more like a cylindrical pressure shell.

A different approach to mechanical counter pressure was taken by German manufacturers of a novel anti-gravity (anti-G) suit called the Libelle® suit [Eiken et al., 2002]. This suit is composed of a stretch-resistant textile instead of elastic fabric. The traditional anit-G suit uses pneumatic *gas* bladders to produce positive pressure on the lower body of aircraft pilots during high G maneuvers. The Libelle suit, in contrast, is a hydrostatic suit that produces pressure through the changing shape of *liquid*-filled columns that run along the body, from the heart level to the ankles and from the shoulders to the wrist. Under high G loads, the cross-sectional shape of these columns becomes circular. As a result of the fabric's inextensibility, the now circular columns reduce the diameter of the garment, pull the suit closer to the pilot's body, and create mechanical counter pressure. This suit is commercially available for aircraft pilots but has not been considered for space EVA use, except as the inspiration for the hybrid one-channel lower leg MCP prototype designed at MIT by Pitts in 2003.

Pitts developed a lower leg MCP garment that uses a thin inflatable channel of air to tense a high-modulus (stretch-resistant) fabric sleeve around the leg [Pitts, 2003; Bethke et al., 2004]. An eight-segment inextensible sailcloth garment is patterned to fit as close to the skin as possible without providing any pressure. A longitudinal channel of 10-cm wide lay-flat polyethylene tubing lies between the skin and the garment. When the channel expands with gas, it creates tension in the sailcloth, producing mechanical counter pressure over the lower leg surface. Pitts tested his prototype under partial vacuum conditions, and it maintained the subject's comfort for 30-minute tests. However, the measured surface pressure varied from 20 kPa (150 mmHg, 2.9 psi) to 67 kPa (500 mmHg, 9.7 psi), and it is unknown if these variations would have been tolerable for longer than 30 minutes [Pitts, 2003].

A final researcher who provided unique insights into the problem of mobility in gas pressure suits is Iberall, a contemporary of Annis and Webb. Although Iberall worked with gas pressure rather than mechanical counter pressure suits, the ideas he implemented may have direct applicability to modern MCP design. Iberall insisted that gas pressure suits could be restrained in such a way that the wearer's mobility would be almost completely maintained [Iberall, 1951, 1958, 1964, 1970]. Since he focused on the design of the "restraint layer," his suggestions easily transfer to mechanical counter pressure suits, which are essentially restraint layers for the skin.

Iberall convinced himself that pressure suit mobility was within research by applying a unique perspective to the physics of spacesuit deformation. He separated the work that the wearer has to do against the spacesuit into three components: pressure-volume work, bending work, and stretching work. He conceived of the problem of moving in the spacesuit "shell" as exerting three types of work: pressure-volume work to compress a volume of gas, stretching work to stretch the elements of the shell, and bending work to bend the shell's membrane at the joints. If each quantity of work could become negligible, then full mobility in the spacesuit could be achieved. Iberall dismissed pressure-volume work as being easy to reduce, by maintaining a close-fitting spacesuit with a very small volume of pressurized gas. He focused instead on reducing the stretching and bending work, and he recast the mobile spacesuit problem as a "topological" study. He wondered if the body surface could be covered by an optimal grid or net whose angles distort but whose edges do not stretch. Iberall suggested that this optimal grid-like surface covering is made up of "lines of non-extension," which he found by observing circles deform into ellipses on the surface of the body. In special cases, there are two diameters that belong to both circle and ellipse; thus, the length of these diameters does not change. As the circle stretches, these two lines rotate with respect to their intersection point, but they do not stretch or contract. The lines

trace the body surface curves along which the skin does not stretch during body movement. The process of mapping these lines is really the process of finding the "swiveling grid," or net, that covers the body's surface.

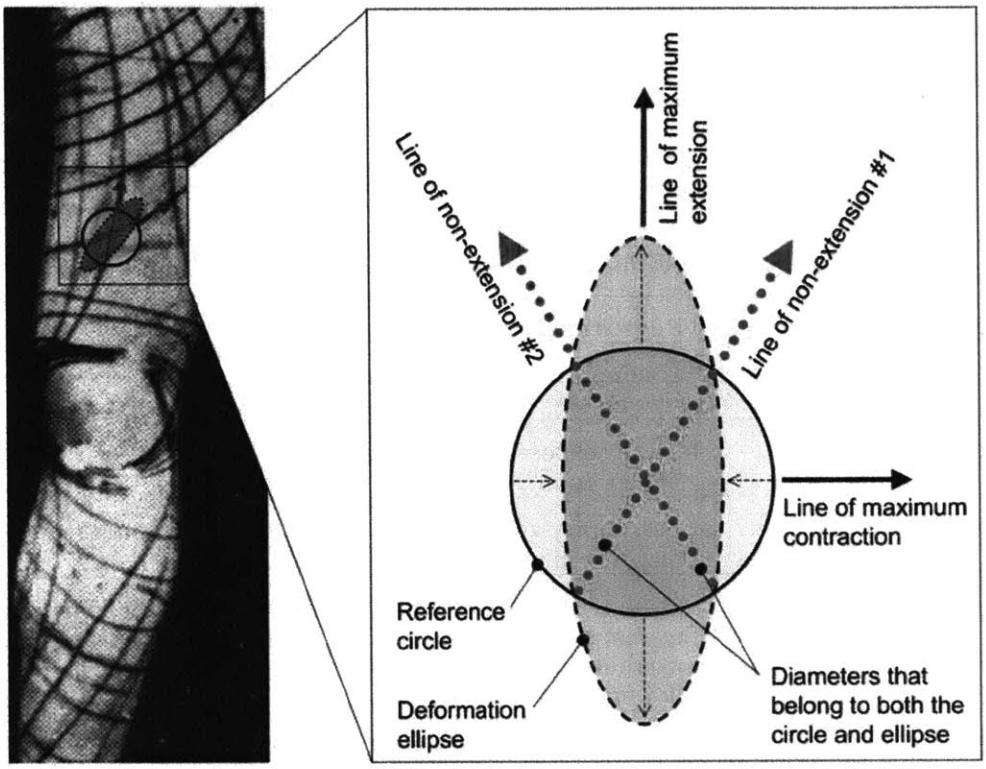

Figure 2.3 (Left) Depiction of Iberall's "lines of non-extension," which suggest an optimal net or grid covering for a mobile pressure suit. The angles of the optimal grid distort, but the grid edges do not stretch. (Right) Iberall found this grid by observing circles deform into ellipses on the surface of the body. In special cases, there are two diameters, shown as dotted lines, that belong to both the circle and ellipse; these are lines of non-extension. As the circle deforms, these two lines rotate with respect to their intersection point, but they do not stretch or contract [Adapted from Iberall, 1970, p. 254].

Until this thesis, no one had furthered Iberall's work (in published form), and today the question remains of whether this lines of non-extension body surface pattern is a useful construct. Iberall's mapping of the lines was a lengthy and complicated process, and it did not provide information that was easily quantifiable or transferable. This thesis relies on digital technology to facilitate the process of finding the lines of non-extension, so that questions about their utility can be addressed.

It seems that perhaps Webb's and Iberall's ideas were simply revelations ahead of their time. Webb lacked material that could be tensioned at a specific point in time (after donning), and Iberall lacked the computational power to quantify and record his ideas about ideal restraint layers. Since then, advances in materials science, human modeling, and noninvasive measurements should have allowed both of their ideas to progress. Instead, only incremental advancements in mechanical counter pressure suit theory have been achieved. Perhaps what is needed is the combination of Webb's and Iberall's theories – a combination of Webb's

physiological conviction that mechanical pressure can adequately counter breathing pressure and Iberall's conviction that a mobile pressure suit is achievable.

This mixture of Webb's and Iberall's ideas leads to the concept of a mechanical counter pressure suit that mimics the shape changes of the human body. The purpose of this thesis is to advance the theory of such a suit, by performing human body analysis and designing a second skin suit that provides both easy mobility and uniform body pressure.

Table 2.2 lists the requirements that should serve as the guiding principles in the design of an advanced locomotion MCP suit [Bethke et al., 2004]. For quantitative completeness, Table 2.3 shows the tension per unit length that must be generated and maintained by an MCP suit at various locations on the leg of one female subject, if 23 kPa (170 mmHg, 3.3 psi) is the desired body surface pressure (p_{MCP} = 23 kPa; see Equation 2.4).

Table 2.2 Requirements for an advanced locomotion mechanical counter pressure suit.

Suit Function	Requirement
Pressure Production	Continuosly maintain fabric tension to apply at least 23 kPa (170 mmHg, 3.3 psi) of pressure at body surface.
Pressure Production	Locally expose no more than 1 mm² surface area of the skin [Webb, 1968].
Pressure Distribution	Distribute pressure evenly, with no more than 20 mmHg spatial variation in pressure [Carr, 2005].
Mobility	Require no more than 2 N-m of extra work (joint torque) against the suit to flex the knee to 90 degrees. (Current EMU requires 3.74 N-m to bend the knee to 72 degrees [Schmidt, Newman, & Hodgson, 2001]).
Mobility	Allow full unsuited range of lower body joint rotations.
Operational Feasibility	Don and doff times of less than 10 minutes
Operational Feasibility	Don and doff by an individual wearer.

Table 2.3 Required circumferential fabric tension per unit longitudinal length to create 23 kPa of body surface pressure on female subject, as a function of position on leg. Subject's body mass and height are 59 kg (130 lb) and 168 cm (66 in), respectively.

Cross Section Location	Knee Angle (deg)	Estimated Cross-sectional Radius (cm)	Required Tension per Unit Length for 23 kPa Pressure
Top of thigh	0	8.6	20 N/cm (4.5 lb/cm)
Bottom of thigh	0	6.1	14 N/cm (3.1 lb/cm)
Top of calf	0	5.5	13 N/cm (2.9 lb/cm)
Bottom of calf	0	3.8	8.6 N/cm (1.9 lb/cm)

2.3 SHAPE CHANGES OF THE HUMAN BODY IN MOTION

2.3.1 BIOMECHANICS OF LOCOMOTION

The requirements for advanced locomotion spacesuits are all derived from the exploration missions that astronauts will be fulfilling as they wear these suits: traversing the surface of another planetary body. In order to accomplish this exploration, astronauts will need to carry out the activity of free locomotion. In the 1-g (Earth gravity) environment, humans primarily use two methods, or "gaits," for locomotion: walking and running. Walking requires one foot to be always in contact with the ground; the leg connected to this foot is called the "stance" leg, and the other leg is the "swing" leg [McMahon, 1984]. In running, there is never ground contact by both feet at the same time [Barratt & Newman, 1997]. In partial gravity environments, humans may adapt the additional gait of loping, which is an extension of running characterized by a step length increase and an increase in aerial time during the stride cycle [Newman & Alexander, 1993]. Besides walking, loping, and running, the locomotive activities of climbing, squatting, and kneeling may also be necessary for the exploration of mountainous planetary surfaces. The design of an advanced locomotion spacesuit must take into consideration the characteristics of all these activities.

Scholars of the mechanics of locomotion vary in their description of the motion of the limbs during walking. One useful description proposed by Saunders, Inman, and Eberhart in 1953 and adopted by McMahon in 1984, distinguishes six determinants of gait; these determinants should be taken into account in spacesuit design. Each determinant adds one level of complexity to the mechanical model of walking. The six determinants, adapted from McMahon's 1984 description, are:

1. Compass gait: The body's trunk moves in an arc about the planted foot for each step, as the stance leg remains stiff always. Only hip extension/flexion occurs.
2. Pelvic rotation: Rotary motion of the pelvis about a vertical axis is added, allowing for a greater effective length of the leg, a longer step, and a greater and hence flatter radius for the hip arc.
3. Pelvic tilt: The radius of the hip arc is made even flatter by allowing the pelvis to tilt about a horizontal axis so that the stance side hip rises higher than the swing side hip. This tilt requires knee flexion of the swing leg to be added to the hip flexion.
4. Stance leg knee flexion: Knee flexion of the stance leg is added, again flattening out the arc traced by the pelvis center.
5. Plantar flexion of the stance ankle: The sole (plantar surface) of the foot moves down ("plantar flexes") just before toe-off of the stance leg. This ankle flexion smoothes the transition from stance support phase to the swing phase. Now ankle, knee, and hip flexion are all occurring.
6. Lateral displacement of the pelvis: The body rocks from side to side during walking, with a sinusoidal motion at half the frequency of the vertical motions.

To achieve mobility in a spacesuit, ideally all six of these limb motions should be enabled. However, this thesis focuses on knee flexion – its effect on leg shape, skin strain, and mechanical counter pressure suit design. This choice was made because knee flexion is a major determinant of the ability to climb, squat, and kneel, in addition to being important for walking, running, and loping. From this point forward in this thesis, the complex issues of locomotion will be modeled by simpler one-degree-of-freedom knee flexion. Figure 2.4 shows the main leg positions of one cycle of a walking gait and highlights the importance of knee flexion to locomotion.

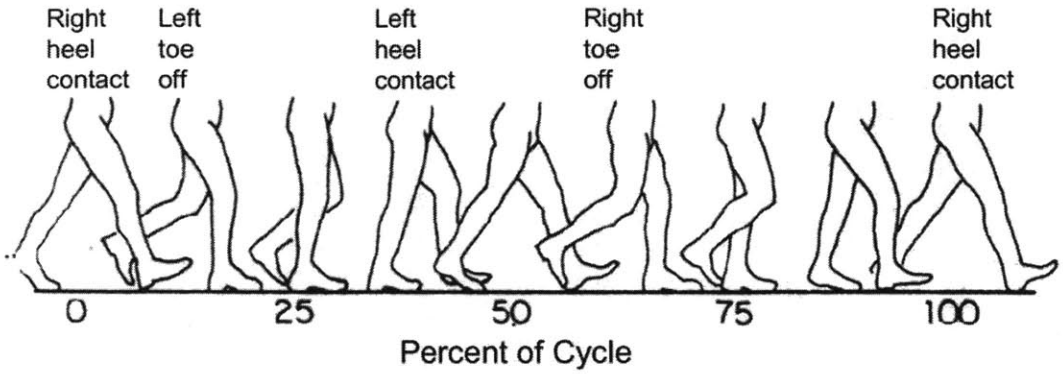

Figure 2.4 Heel contacts, toe offs, and knee flexion angles that occur during one walking gait cycle [Adapted from McMahon, 1984].

One other piece of introductory material for any discussion of locomotion is a description of the anatomical terms for different portions of the body surface. Figure 2.5 explains the terms that are used in thesis to refer to different sides of the body: the anterior, medial, posterior, and lateral surfaces.

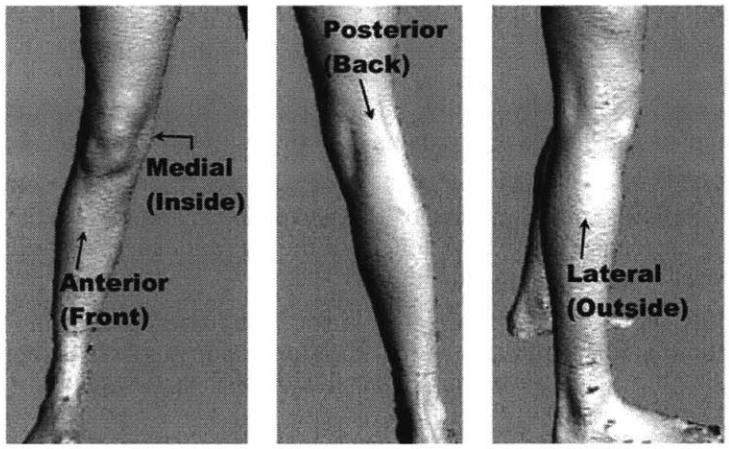

Figure 2.5 The portions of the leg that are referred to as the anterior (front), medial (inside), posterior (back), and lateral (outside) surfaces.

2.3.2 THE STRUCTURE AND BIOMECHANICAL PROPERTIES OF HUMAN SKIN

The previous section contained a mechanical description of *motions*, and this section moves on to a mechanical description of *structure*: the structure of human skin. For the design of a *gas* pressure suit, human locomotion is the main biomechanical system that must be understood. But for a *second skin* mechanical counter pressure suit, the biomechanics of human skin must also be studied.

STRUCTURE OF SKIN - Like all biological tissues, skin has complicated mechanical properties; it has a nonlinear stress-strain relationship, it is heterogeneous (i.e., its properties depend on anatomical location), it is anisotropic (i.e., its stiffness varies with direction), and it is viscoelastic (i.e., its stress level is a function of both strain and time). The anisotropy of skin was first characterized by Langer in 1861, when he identified the directions of maximum *in vivo* skin tension that are now referred to as "Langer's lines." The complex cellular and macromolecular

make-up of skin is responsible for these lines and for the other unique mechanical properties of skin. Silver provides a thorough review of the mechanobiology of skin, and his remarks are summarized here [Silver, Siperko, & Seehra, 2003].

Skin is a connective tissue, composed of an upper cellular layer called the epidermis and a lower layer of fibers and cells called the dermis. The epidermis, which is 0.06 mm to 1 mm thick, contains a basement membrane of macromolecules and anchoring fibrils, topped with three to four layers of viable keritanocyte cells, then two to three flattened granular cell layers, then finally the surface layer of flattened, cornified, non-viable squamous epithelium. In the viable cells, cytoskleton filaments determine shape and structural integrity [Silver et al., 2003].

The much thicker dermis, between 1 mm and 4 mm thick, is mainly an extracellular matrix of mostly collagen and elastin fibers, interspersed with fibroblast cells and some helper macromolecules. It can be separated into two layers: the upper papillary dermis is a loose network of thin collagen fibers and immature elastic fibers, and the lower reticular dermis is a denser interwoven network of large collagen fibers and mature elastic fibers. When the *in vivo* skin tension is low, these fibers are in a wavy state. Collagen makes up about 75% of skin by weight, with collagen type I as the major type [Reihsner & Menzel, 1996]. Fibroblast cells lie along the surface of collagen fibrils and are concentrated in the papillary dermis. An amorphous gel surrounds the collagen, elastin, and fibroblasts of the dermis [Reihsner & Menzel, 1996]. Figure 2.6 depicts the elements and structure of skin that are most important for skin stress and strain.

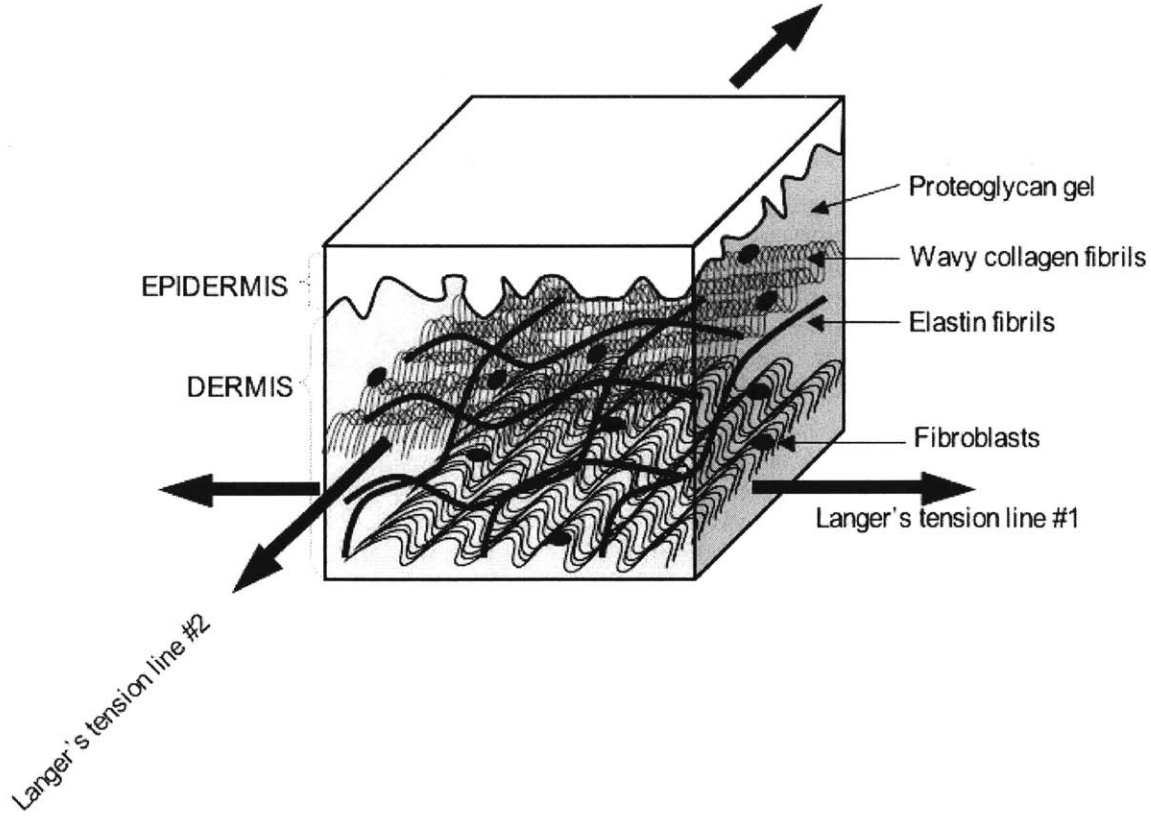

Figure 2.6 Structure of skin [Adapted from Silver et al., 2003, p. 4].

The basement membrane of the epidermis marks the boundary between dermis and epidermis. At this boundary, which is depicted in Figure 2.7, the two layers are mechanically bridged by keratin filaments that connect the keratinocytes' cytoskletons with the extracellular matrix of the dermis [Silver et al., 2003]. Internal stresses in the dermis are transferred to the epidermis through these anchoring fibrils [Silver et al., 2003].

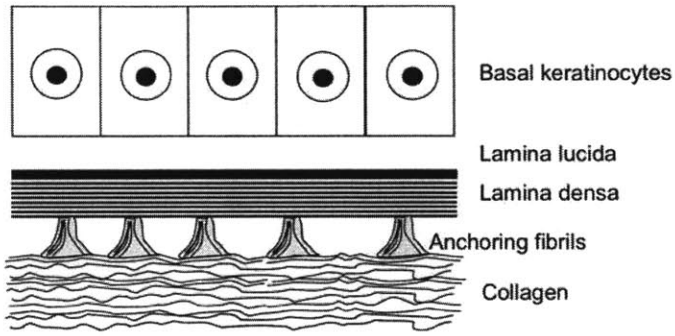

Figure 2.7 Sketch of skin epidermal-dermal junction [Adapted from Reihsner & Menzel, 1996, p. 155]. Basement membrane consists of lamina lucida, lamina densa, and anchoring fibrils. Basal keratinocytes are the bottom of the epidermis; collagen is in the papillary dermis.

FORCE TRANSMISSION IN SKIN - Internal forces on the skin arise from two sources: passive tension in the collagen fibrils of the dermis, and active cellular tension generated by the fibroblasts attached to the collagen fibrils. These forces cause the keratinocyte cells to pull on each other [Silver et al., 2003].

External forces on the skin similarly cause tension between keratinocytes in the epidermis, which then causes stretching of the epidermal-dermal junction. The result is stretching of elastic and collagen fibrils and stretching of collagen-fibroblast and fibroblast-fibroblast interfaces [Silver et al., 2003]. The response of the elastic and collagen fibers to this stretching is a primary determinant of the mechanical properties of skin. The process is iterative: external forces cause cellular activity and – over time – a certain extracellular matrix structure; this structure then determines how skin reacts to external forces.

The response of skin to external forces is described by a force-displacement (or stress-strain) curve that is initially concave up, then linear, then concave down, as shown in Figure 2.8. In the initial low modulus region, the elastic fibers deform and dominate in bearing the tensile load, while the collagen fibers remain wavy. At a certain strain level, the collagen fibers begin to offer resistance to deformation. In the subsequent linear high-modulus region, the collagen fibers dominate in bearing load [Silver et al., 2003].

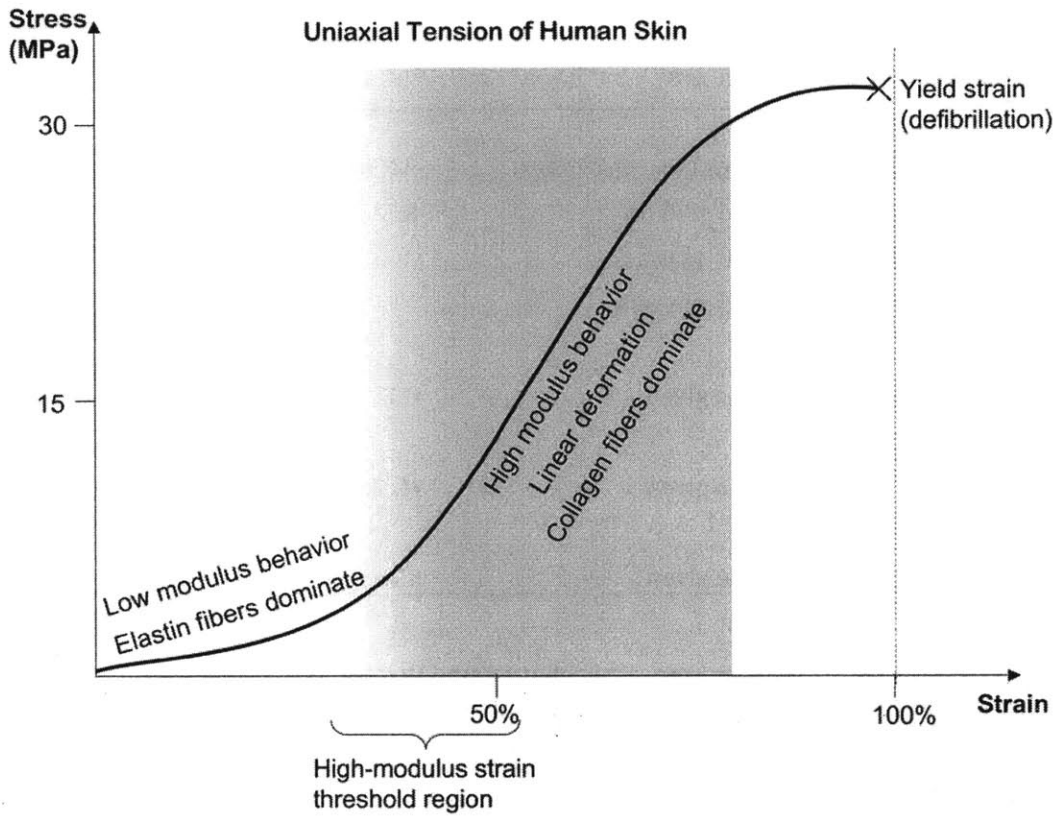

Figure 2.8 Approximate stress-strain curve for human skin. The region where skin begins to behave like a high-modulus (stretch-resistant) material is indicated by the gradation in shading.

Markenscoff and Yannas offer a mathematical explanation for this behavior of abruptly entering a high-modulus region after passing through a certain threshold strain level [Markenscoff & Yannas, 1979]. They first provide a review of published data on the high-modulus strain thresholds of skin for various subject ages and directions of load. It is reproduced here in Table 2.4. Threshold strain values vary from 15% to 80%, depending mostly on age. By modeling skin as mainly collagen fibers with random orientation in plane, Markenscoff and Yannas predict that the stiffness of skin will abruptly increase at 57% strain. The abrupt stiffness increase corresponds to the uncrimping of all of the fibers in the load direction. If fibers have not a random but a preferential direction prior to being loaded, then these authors predict earlier threshold strain values, at closer to 30% to 50% strain. These predictions for strain level at skin's entry into the high-modulus region are corroborated by experimental results and Langer's observations.

Table 2.4 Strain levels at human skin's entry into high modulus region [Adapted from Markenscoff & Yannas, 1979, p. 128].

Strain threshold	Subject description	Authors
0.5-0.65	Aged 18 days	R.M. Kenedi et al, 1965
0.3-0.5	Aged 43 years	
0.15-0.2	Aged 74 years	
0.4-0.65	None given	C.H. Daly, in Millington et al, 1971
0.65-1.00	None given	H. Yamada, 1970
0.3	None given	Silver, 2003

ORIENTATION OF SKIN FIBERS - Researchers have found that the skin rarely operates in the low-modulus region. Instead, the pre-stress in skin is about 10 MPa, which corresponds to about 40% uniaxial strain [Silver et al., 2003]. Consequently, even in the absence of external loading, the skin operates in the linear region of its stress-strain curve, where the collagen fibers dictate behavior. The exact level of pre-stress varies according to anatomical region; it is highest on the arms, sternum, thigh, patella, and tibia and lowest on the back. This internal pre-stress is generated by the tension incorporated into the collagen network during its construction and by fibroblast contraction of the collagen fibers [Silver et al., 2003]. Since the collagen bears the tensile load for skin, the maximum stress in skin is oriented in the direction of the collagen fibers. The lines that correspond to the maximum pretension in the skin were discovered by Langer in 1861. Thus, the collagen fibers lie more or less in the direction of Langer's lines [Reihsner & Menzel, 1996].

How are the collagen fibers laid down with a specific orientation, a phenomenon which has been dubbed *tensegrity* [Ingber, 1997; reported in Silver et al., 2003]? Special macromolecule units on the dermis cell surface bind the cell to the matrix of collagen fibers. Evidence suggests that these binding units are mechanosensors that translate local forces into directional assembly of fibers, as illustrated in Figure 2.9. Directional assembly is necessary to minimize the amount of stretching required of the collagen fibers. Because collagen fibers are the stiffest component of skin, the long axis of the collagen fibers will stipulate the stiffest or least extensible direction of the skin. Hence, the collagen fiber is laid down in the direction of lowest skin strain sensed by the cells' mechanosensors at each location on the body surface. In other words, the direction of maximum *in vivo* skin tension (collagen fiber axis) should agree with the direction of minimum skin strain. This is the rationale for this thesis's hypothesis that Langer's lines and Iberall's lines should agree.

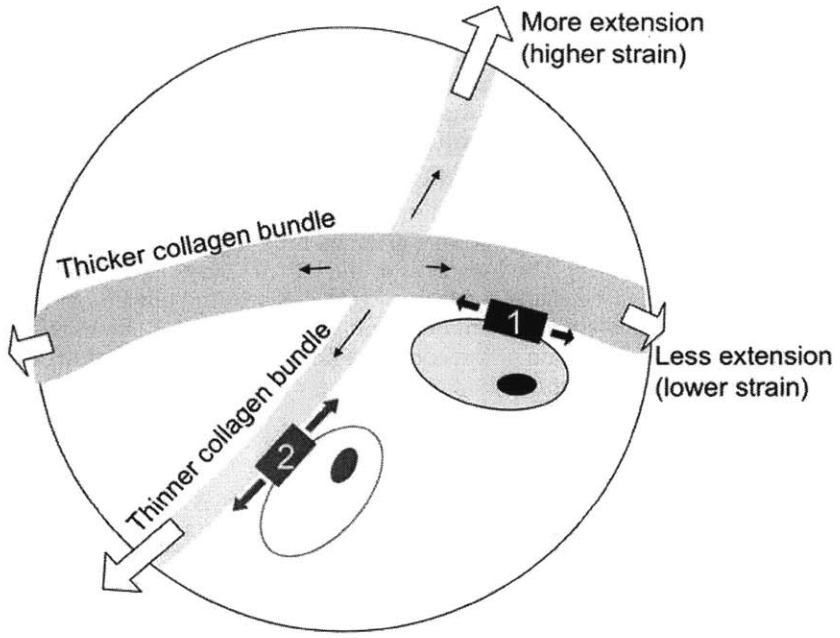

Figure 2.9 The tensegrity of skin: cellular instructions for the orientation of load-bearing collagen fibers. The two dermis cells pictured here are both equipped with binding units, labeled #1 and #2, that sense skin strain. If, over time, cell #1 senses lower strain than cell #2, more collagen fibers will be laid down parallel to the fibers attached to cell #1. Consequently, Langer's lines of maximum skin tension (i.e., collagen fiber direction) should align with Iberall's lines of minimum skin strain [Adpated from Silver et al., 2003, p. 4].

2.3.3 A REVIEW OF EXPERIMENTS ON THE TENSION STATE OF HUMAN SKIN

Silver and Markenscoff and Yannas explain the cellular and macromolecular structure of skin, and their descriptions could be applied to skin at any location on the body. In other words, they describe *global* properties of skin. Other researchers characterize macroscopic properties that occur at specific locations on the skin as a result of its cellular and macromolecular structure. In other words, they have looked for *local* stress and strain information.

LINES OF MAXIMUM SKIN TENSION (LANGER'S LINES) - The first researcher to publish his findings on the variable stress and strain of skin was Langer, in 1861. Langer, an anatomy professor, observed that in the skin of cadavers, a round hole punched into the skin produced not a round wound but a "linear cleft" [Langer, 1861]. He assumed that if clefts were placed close enough together, they could be grouped into lines that would be an expression of the fiber pattern of the skin:

> "..the clefts...would show a definite relationship to each other in the various parts of the body and it would be possible to group the clefts into lines and areas arranged topographically in a similar way to the already known patterns of hairs. These lines, ... an expression of the fibre pattern of the skin, would... provide a technique of orienting the dermal tissue and differentiating the lengthwise incision from the transverse" [Langer, 1861].

Using a 2-mm diameter spike, Langer punctured the skin of cadavers at many locations and noted the long axis of the elliptical-shaped resulting wounds. He then connected these long axes together to find the lines of maximum *in vivo* tension. Reproductions of his originally published drawings are shown in Figure 2.10. These lines are today called "Langer's lines." Langer found

the lines to be largely parallel, although they did cross at more or less right angles at some places. According to Langer, the lines were the same for all individuals at the joints, face, back, and chest, but they varied among individuals at the central forearm, lower leg, and anterior abdominal wall. These variations seemed to be due to the constitution of the cadaver.

Langer also studied the underlying structure of the skin; he stretched an excised ellipse along its major axis and examined the stretched skin under microscope. He found the fibers tightly grouped and interwoven into bundles, which were oriented into "a lattice work with very extended rhomboidal meshes" [Langer, 1861]. The long axes of the lattice always had the same orientation as macroscopic ellipses. When he made a cut at a right angle to the ellipse orientation, in the microscope he found all the fiber bundles obliquely cut. He concluded, "The microscope studies leave no doubt that the cleft orientation of the corium is dependent on the fiber arrangement; the stab clefts are manifestly nothing more that a widening of the meshes of the corium fibres" [Langer, 1861].

Figure 2.10 Reproduction of Langer's original drawings of the "cleavage lines" on the adult arm and leg. The short dashes indicate the directions of maximum *in vivo* skin tension, which are the directions of the linear "clefts" that formed when Langer punctured the skin with a round tool [Adapted from Langer, 1861]. The longer continuous lines have been added here to illustrate how Langer connected the cleft dashes to determine continuous lines of maximum skin tension.

MODERN USAGE OF LANGER'S LINES - Today, Langer's lines are often used as guidelines for surgical incisions. One surgery textbook states that scars will be narrower and less conspicuous if the wound is parallel to or within Langer's lines, which are purported to lie generally perpendicular to the long axis of underlying muscles [Schwartz & Seymour, 1999]. Interestingly, this textbook chapter incorrectly states that Langer's lines are equivalent to lines of minimal tension. Actually, they are lines of *maximal* tension; surgeons are advised to cut along them because if they were to cut perpendicular to them, the high tension would pull the wound farther open.

The surgery textbook's error in describing Langer's lines is just one example of a number of misunderstandings and misuses of the lines by physicians. One physician claims that Langer's lines are simply ritual and that they vary too much between individuals to be clinically useful [Edlich, 1998]. He also points out that Langer's clefts or ellipses indicated the *direction* of predominant local skin tension, with no information about the *magnitude* of the tension. Most importantly, he asserts that the charts of Langer's lines in modern textbooks are usually erroneous because they neglect the effects of body movement on scar healing. Langer identified only static skin tension; he did not consider the dynamic influence of the musculoskeletal system. Edlich writes, "Static tensions are the natural tensions existing in normal skin. In contrast, dynamic tensions are caused by a combination of forces that are associated with joint movement, mimetic and other voluntary muscle activity, and gravity" [Edlich, 1998, p. 759]. Edlich points out the need for a more precise characterization of "kinetic influences" on specific regions of the skin.

Wilhemi and his plastic surgery colleagues continue the debate on the utility of Langer's lines [Wilhemi, Bradon, Blackwell, & Phillips, 1999]. They point out that even Langer himself noted that the directions of his lines would change with body position; he developed them on cadavers with extremities in extension and thus his lines are longitudinal over joints. Because the lines depended on position, and because Langer was an anatomy professor and not a surgeon, he did not intend his lines to be surgery guides. Wilhemi suggests Borges' relaxed skin tension lines as alternative guidelines for facial incisions and Kraissl's wrinkle lines as alternatives for body incisions. Both Borges and Kraissl were surgeons.

MODERN VERIFICATION OF LINES OF MAXIMUM STRESS - Although the merits of using Langer's lines as surgical guidelines are debatable, biomechanists continue to be interested in them as the directions of maximum skin tension. Consequently, several researchers have attempted to verify these lines with modern experimental and modeling methods.

One research group tried to replicate Langer's lines on dog skin [van Ratingen, et al., 1993]. They placed 121 markers on small (10 cm by 10 cm *in situ* dimensions) excised samples of skin, stretched the skin back to its *in situ* dimensions, allowed it to relax for 15 minutes, and finally used video recordings and digital image analysis to determine displacement field. Their results are the stiffness parameters along two orthogonal axes; these stiffness parameters predict Langer's lines. Their study only measures skin in its natural state of pretension; it provides no information about the tension due to the dog's body motions.

A similar attempt to recreate Langer's lines via mechanical testing of *in vitro* skin samples was carried out by Reihsner, whose group studies human skin and considers Langer's lines to be the directions of minimum *in vivo* extension [Reihsner, Balogh, & Menzel, 1995]. By re-stretching *in vitro* samples to *in vivo* dimensions and measuring the magnitude and direction of tension required to do so, they examined skin's two-dimensional stress-strain relationship. They tested 80 samples, representing 16 different body areas, to determine stress-strain as a function of anatomical site. Their multi-axis tensile loading apparatus allowed them to find the direction of maximum *in vivo* stress. They found agreement between directions of minimum *in vivo* extension (their definition of Langer's lines) and directions of maximum *in vivo* stress to within ± 10 degrees. Their most interesting results include the finding that the maximum *in vivo* skin strain for joints at 0-degree angles ranges from 15% for an 80-year-old to 30% for a 25-year-old. Their results also indicate that the degree of anisotropy is most pronounced on patella, abdomen, and

shoulder, mainly areas where there is low *in vivo* tension. In a follow-up publication, they report that the greatest disagreements between minimum extension and maximum stress directions occur at the upper back, inside thigh, hollow of knee, and sternum [Reihsner & Menzel, 1996]. For each anatomical site tested, they provide six orthotropic elastic constants, as a function of age and incremental strain level. Although their data is thorough, and they tested samples from several different regions of the body, the sites are spread too far apart to yield sufficient data for a continuous full-body garment pattern.

Bischoff studied the mechanical behavior of skin with purely finite element modeling, unaccompanied by experimentation [Bischoff, Arruda, & Grosh, 2000]. The parameters of Bischoff's constitutive model were collagen fiber-free length and network collagen chain density. Bischoff used his finite element model to simulate other researchers' experiments on rat skin. His output satisfactorily matched the experimental results, and he attributed the success to starting his model with the initial conditions of an anisotropic pre-stress state. This work emphasizes the importance of understanding the stress state of a nonlinear material in any modeling work. In other words, to model the behavior of skin accurately, the *in vivo* stress-strain field must be known.

The most recent efforts to characterize human skin stress-strain relationships have utilized the noninvasive strain measurement of digital image correlation (DIC). These efforts are the most relevant and most inspirational for the research of this thesis. Douven carried out *in vivo* uniaxial force-displacement measurements of a 1 cm by 2 cm patch of skin from the forearm, with displacement history determined by optical analysis [Douven, Meijer, & Oomens, 2000]. Vescovo and Varchon and their group published the first detailed description of digital image correlation software for skin [Marcellier, Vescovo, Varchon, Vacher, & Humbert, 2001]. They subjected small excised samples of skin to uniaxial tension and recorded images of its deformation. With DIC software, they calculated the strain field from the displacement field. In a second study, Vescovo's group used a new uniaxial *in vivo* extension apparatus to develop a viscoelastic model for forearm skin, including the main directions of anisotropy [Khatyr, Imberdis, Vescovo, Varchon, & Lagarde, 2004]. The apparatus can apply load as extension or compression, and creep or relaxation. They carried out tests in four different directions on the forearm of each of 63 subjects. The average main direction of anisotropy was 5.3 ± 5.8 degrees about the longitudinal axis of the arm. The average elastic modulus along the arm axis was $6.6 \pm 2.2 \times 10^5$ Pa, and the average elastic modulus perpendicular to the arm axis was $1.3 \pm 0.6 \times 10^5$ Pa.

Vescovo and Varchon's research is promising, and it is the inspiration for the non-invasive measurement of skin strain for spacesuit design. However, their work has several shortcomings that mandate a different experiment to answer the research questions of this thesis. First, the tensioning apparatus used in their experiments is invasive to the subject. Second, they measure strain for externally-applied uniaxial tension only, and the uncertainty in strain measurement is at least 8%. The current software is useful only for plane surfaces that undergo plane deformations; Vescovo and his colleagues are awaiting 3D software for curved surfaces. A final shortcoming of their work is that the sample size accommodated by their equipment measures only 4 cm by 4 cm, so global conclusions about the entire human body surface would require many repetitions of the experiment.

The biomechanicists and plastic surgeons cited here have contributed much to the body of knowledge about the cellular structure of skin, its mechanical properties, and its variability with age and anatomical region. However, they have never conducted studies that simultaneously consider whole-body, *in vivo*, and quantitative characteristics. No researcher has carried out a quantitative full-field study of the strain response of skin to the natural loading caused by locomotion. Langer and the modern researchers who recreated Langer's lines did find information over the whole body surface, but they were studying the body in a static, non-extended, non-externally loaded state. Researches who did apply external loads or look at dynamic responses studied only small patches of skin. Because anisotropy and other properties

vary with respect to anatomical region, their results cannot be extended globally for the entire skin surface, an extension which is necessary for clothing or spacesuit design.

Table 2.5 Summary table of experimental studies of skin stress and strain, and their shortcomings with respect to second skin spacesuit design specifications.

Authors	Year	Study	Main Shortcomings
Langer	1861	Find directions of maximum *in vivo* skin tension by examining round punctures deform into ellipses.	Not quantitative; considers pre-tension state of skin only; neglects the effect of joint motion on skin.
Iberall	1970	Find directions of minimum skin extension during joint motion by observing marked circles of skin deform into ellipses.	Not quantitative or easily repeatable. Time consuming. Not readily transferable to computer data or to manufacturing devices.
Faga	1981	Determine directions of maximum *in vivo* skin tension by observing stream lines of hair.	Not quantitative or readily transferable to computer data. Small sample size (n = 8). Methodology not verified.
van Ratingen	1983	Find lines of maximum tension in dog skin by stretching and carrying out digital image analysis on small excised skin samples.	Invasive (requires excised skin samples). Method only applied to dog skin.
Reihsner, et al.	1995, 1996	Measure anisotropy of human skin as function of anatomical region, using small cadaver skin samples.	Only 16 anatomical sites studied. Invasive measurement apparatus (requires excised samples).
Bischoff, et al.	2000	Finite element modeling of stress-strain response of skin based on collagen fiber network, using isotropic constitutive model.	Model requires pre-stress state of skin as input. Predicts stress-strain behavior for rat skin rather than human skin.
Douven	2000	Optically measure displacement of markers on small sample of skin, during forcible stretching with attached pads.	Considers externally-applied loading; neglects the effect of joint motion on skin. Small (1 cm by 2 cm) samples rather than entire body surface.
Vescovo & Varchon, et al	2001,2004	Map strain fields for excised sections of human skin subject to applied deformation, through photo analysis of initial and deformed samples.	Requires excised samples. Considers externally-applied loading; neglects the effect of joint motion on skin. Digital strain field mapping algorithm does not yet apply to curved surfaces.

In noting the limitations of the studies discussed above, it becomes clear that a more global, quantitative, and easily reproducible picture of the skin strain behavior must be created for advanced locomotion spacesuit design. A mechanical counter pressure suit must allow for the skin's deformation, translation, and rotation without demanding the exertion of extra work by the wearer. Consequently, a preliminary step in the design of an operational MCP suit is to map the local deformations of the skin that occur as body joints are bent and muscles are contracted. The following section offers a review of methods for non-invasively measuring full-field 3D strain and for studying complex three-dimensional anthropomorphic shapes.

2.3.4 NEW METHODS FOR MEASURING HUMAN BODY SHAPE CHANGES: OPTICAL STRAIN ANALYSIS AND THREE-DIMENSIONAL ANTHROPOMETRY

The concepts of mechanical counter pressure and lines of non-extension have been introduced, along with an overview of the mechanics of locomotion and the biomechanical properties of skin. Since this thesis is concerned with measuring the leg skin's response to locomotion in order to verify the lines of non-extension for an MCP suit, the final concept in need of introduction is the *measurement* of skin's response to locomotion. This measurement will consist of a skin strain field map. Thus, what follows is an overview of methods for carrying out noninvasive measurement of surface strain.

The field of "photomechanics" is devoted to studying mechanical properties and responses through optical analysis only. Within photomechanics, the technique of Digital Image Correlation, referred to as DIC, has become the standard method for measuring the full-field strain of a surface undergoing deformation. In DIC, a pair of optical camera images of an object are recorded before and after a deformation increment and are then compared by a mathematical function. This image processing function, or algorithm, computes strain by identifying and tracking the position of slight variations in color on the object's surface. If an object is not adequately variegated in appearance, it is covered with speckle paint before undergoing deformation. DIC was first proposed as an automated approach for solid mechanics problems by Peters and Ranson in 1982. They measured the surface strain of a flat plate undergoing uniform tension. In 1996, Helm, McNeil, and Sutton proposed a technique for DIC of curved surfaces; they optically measured the surface strain of a cylinder [Helm, McNeil, & Sutton, 1996]. Two cameras, positioned at different angles to the object's surface, are required for this technique. In 1999, Bay expanded on DIC to develop a method for measuring 3D strains of trabecular bone tissue with data from microCT scans (X-ray tomography), and he called this Digital Volume Correlation, or DVC [Bay, Smith, Fyhrie, & Saad, 1999]. Wang and Cuitiño's study of the full-field strain of open-cell polyurethane foam contains a detailed explanation of the mathematical implementation of DVC [Wang & Cuitiño, 2002].

The strain measurement technique of this thesis does not employ true Digital Image Correlation because the data in this thesis is gathered with a laser scanner rather than an optical camera system. However, the method of marking the skin and the mathematical algorithm for converting position measurements to surface strain were inspired by the technique of Digital Image Correlation. Further study of the full-field strain of the human skin might more easily be carried out with optical camera systems and commercially available DIC software (Correlated Solutions, Inc., West Columbia, SC). For this study, however, the data collection tools were 3D laser scanners.

There is a history of using laser scanners for 3D anthropometry data and surface detail information. Laser scanning has been particularly useful for computer scientists trying to push the envelope of realistic computer animations. In computer graphics, it is difficult to produce realistic human body deformations because the shifting of bones, muscles, and soft tissues is not fully understood by animators. Real-time finite-element models of the body's variegated soft tissue would enable mathematically-driven and true-to-life animations, but anatomical finite

element models for the whole body are extremely computationally expensive and have not yet been realized. For example, one researcher devoted several years to building a soft tissue finite element model of only the leg [Hirota, 2002]. Instead of building mathematical models from first principles, computer animators are performing "reverse engineering": they use optical scanners to capture the static shape of humans and then derive posable models from the 3D snapshots. In the past, dynamic deformations derived from these static shapes have not appeared fully realistic. Allen and his colleagues in computer animation propose a new process to derive realistic human body deformation graphics, by interpolating between laser scans of body parts in a series of key poses [Allen, Curless, & Popovic, 2002]. Researchers marked the body with reflective markers, automatically found markers by using a color filter, and labeled the markers. Their algorithm then derived a kinematic skeletal model from the positions of the markers (using a k-nearest neighbors scheme) and refitted the surfaces in between the markers to look as realistic as possible during deformation. Their result was "an example-based, posable model that captures high definition shape changes over large ranges of motion" [Allen et al., 2002, p. 618]

The design of advanced locomotion spacesuits requires interdisciplinary research; it draws from the fields of space human factors and life support, biomechanics, physiology (of respiration and of skin), solid mechanics, and computer science. Accordingly, this Background and Literature Review chapter has touched on a broad variety of topics, in an effort to introduce the reader to all of the fields relevant to this research. The chapter began with a discussion of the current U.S. spacesuit and its limits of mobility. Next, the concept of mechanical counter pressure (MCP) spacesuits was explained. A review of MCP prototypes revealed necessary design improvements and demonstrated the need for a quantitative study of the shape changes of the human body in motion. An outline of the biomechanics of locomotion and a discussion of human skin structure provided the background information for this human body analysis. Then, previous experiments to measure and describe the mechanical properties and response behavior of skin were reviewed. The shortcomings of these experiments were highlighted, and as an alternative, optical strain analysis through Digital Image Correlation was introduced. Finally, the chapter concluded by explaining the application of 3D laser scanners to realistic computer animations of the human body.

This chapter's introduction to 3D laser scanning, optical strain measurement, and skin physiology has prepared the reader for the next chapter's description of human body shape analysis. To create a mechanical counter pressure suit that provides adequate body pressure and fits like a second skin to allow for free locomotion, the spacesuit designer requires new quantitative information about the shape changes of the human body during locomotion. Chapter 3 describes the methods and results for two studies of the shape changes of the human leg during knee flexion: an experiment to determine surface area and volume changes of the leg, and a technique for creating a full-field strain map of the skin surface of the leg.

Chapter 2 References

1. Allen, B., Curless, B., Popovic, Z. "Articulated body deformation from range scan data." *ACM Transactions on Graphics*, Vol. 21, No. 3, 2002, p. 612-619.
2. Bay, B.K., Smith, T.S., Fyhrie, D.P., Saad, M. "Digital volume correlation: three-dimensional strain mapping using x-ray tomography." *Experimental Mechanics*, Vol. 39, No. 3, September 1999, p. 217-226.
3. Bethke, K., Carr, C.E., Pitts, B.M., Newman, D.J. "Bio-Suit development: viable options for mechanical counter pressure?" *Proceedings of the 34th International Conference on Environmental Systems*, Society of Automotive Engineers, Colorado Springs, CO, 2004.
4. Bischoff, J.E., Arruda, E.M., Grosh, K. Finite element modeling of human skin using an isotropic, nonlinear elastic constitutive model. *Journal of Biomechanics*, Vol. 33, No. 6, June 2000, p. 645-652.
5. Carr, C.E. Personal communication. April 2005.
6. Clapp, W., *Design and Testing of an Advanced Spacesuit Glove*, Massachusetts Institute of Technology, 1983.
7. Douven, L., Meijer, R, Oomens, C., "Characterisation of mechanical behaviour of human skin in vivo." In *Laser-Tissue Interaction XI: Photochemical, Photothermal, and Photomechanical,* D. Duncan, J.O. Hollinger, S.L. Jacques, Editors, Proceedings of SPIE Vol. 3914, 2000.
8. Edlich, R. "Predicting scar formation: from ritual practice (Langer's lines) to scientific discipline (static and dynamic skin tensions)." *The Journal of Emergency Medicine*, Vol. 16, No. 5, 1998, p. 759-760.
9. Eiken, O., Kolegoard, R., Lindborg, B., Aldman, M., Karlmar, K-E., Linder, J. "A New Hydrostatic Anti-G Suit vs. a Pneumatic Anti-G System: Preliminary Comparison." *Aviation, Space, and Environmental Medicine*, Vol. 73, No. 7, July 2002.
10. Faga, A. "A new method to visualize Langer's lines." *The Journal of Dermatologic Surgery and Oncology*. Vol. 7, No. 1, 1981, p. 53-55.
11. Frazer, A. *Modeling Human-Spacesuit Interactions*, S.M. Thesis, Massachusetts Institute of Technology, 2003.
12. Helm, J.D., McNeill, S.R., Sutton, M.A. "Improved three-dimensional image correlation for surface displacement measurement." *Optical Engineering*, Vol. 35, No. 7, July 1996, p. 1911-1920.
13. Hirota, G. *An improved finite element contact model for anatomical simulations*. Ph.D. Thesis, University of North Carolina at Chapel Hill, 2002.
14. Iberall, A. S. "Fundamental Considerations of the Design of Mobile Pressure Suits." National Bureau of Standards report 6.2/3508, Bureau of Aeronautics, Department of the Navy, April 1951.
15. Iberall, A.S. "The Experimental Design of a Mobile Pressure Suit," *Journal of Basic Engineering*, June 1970, p. 251- 264.
16. Iberall, A.S., "Development of a Full-Pressure Altitude Suit," WADC Technical Report 58-236, ASTIA Document No. AD 303813, Wright Air Development Center, Wright-Patterson AFB, Ohio, June 1958.
17. Iberall, A.S., "The Use of Lines of Nonextension to Improve Mobility in Full-Pressure Suits," AMRL-TR-64-118, Rand Development Corporation report to Behavioral Sciences Laboratory, Wright-Patterson AFB, Ohio, November 1964.
18. Khatyr, F., Imberdis, C., Vescovo, P., Varchon, D., Lagarde, J.M. "Model of the viscoelastic behavior of skin in vivo and study of anisotropy." *Skin Research and Technology* Vol. 10, 2004, p. 96-103.
19. Korona, F., *Development and Testing of a Hybrid Elastic Space Suit Glove*, Masters Thesis, University of Maryland, 2002.

20. Kozloski, L. D., *U.S. Space Gear: Outfitting the Astronaut.* Smithsonian Institution Press, Washington, D.C., 1994.

21. Langer, K. "On the anatomy and physiology of the skin: I. The cleavability of the cutis," Reprinted in *British Journal of Plastic Surgery,* Vol. 31, 1978, p. 3-8. Translated from the original in Sitzungsbericht der Mathematisch-naturwissenschaftlichen Classe der Kaiserlichen Academie der Wissenschaften, 44, 19.

22. Marcellier, H., Vescovo, P., Varchon, D., Vacher, P., Humbert, P. "Optical analysis of displacement and strain fields on human skin." *Skin Research and Technology,* Vol. 7, 2001, p. 246-253.

23. Markenscoff, X., Yannas, I. V. "On the stress-strain relation for skin." *Journal of Biomechanics.* Vol. 12, 127-129, 1979.

24. McMahon, T. A. *Muscles, Reflexes, and Locomotion.* Princeton University Press, Princeton, NJ, 1984.

25. Newman, D., Alexander, H. "Human locomotion and workload for simulated lunar and Martian environments." *Acta Astronautica.* Vol. 29, No. 8, 1993, p. 613-620.

26. Newman, D., Barratt, M. "Life Support and Performance Issues for Extravehicular Activity," in S. Churchill (Ed): *Fundamentals of Space Life Sciences,* Krieger Publishing, Malabar, Florida, 1997.

27. Peters, W.H., Ranson, W.F. "Digital imaging techniques in experimental stress analysis." *Optical Engineering.* Vol. 21, No. 3, May-June 1982, p. 427-431.

28. Pitts, B.M, *Spacesuit: Space Craft.* S.M. Thesis. Massachusetts Institute of Technology, 2003

29. Reihsner, R., Balogh, B., Menzel, E.J. "Two-dimensional elastic properties of human skin in terms of an incremental model at the in vivo configuration." *Medical Engineering and Physics,* Vol. 17, 1995, p. 304-313.

30. Reihsner, R., Menzel, E.J. "On the orthogonal anisotropy of human skin as a function of anatomical region." *Connective Tissue Research,* Vol. 34, No. 2, 1996, p. 145-160.

31. Schmidt, P. *An Investigation of Space Suit Mobility with Applications to EVA Operations.* Ph.D. Thesis, Massachusetts Institute of Technology, 2001.

32. Schmidt, P., Newman, D., Hodgson, E. "Modeling Space Suit Mobility: Applications to Design and Operations," *Proceedings of the 31st International Conference on Environmental Systems,* Society of Automotive Engineers, Orlando, FL, July, 2001.

33. Schwartz, B., Seymour, I., Eds. *Principles of Surgery.* New York, McGraw-Hill, 1999.

34. Silver, F., Siperko, L., Seehra. G. "Mechanobiology of force transduction in dermal tissue." *Skin Research and Technology,* Vol. 9, 2003, p. 3-23.

35. Sutton, M., McNeill, S., Helm, J., Chao, Y. "Advances in two-dimensional and three-dimensional computer vision," in P.K. Rastogi (Ed.): *Photomechanics, Topics Appl. Phys.,* Vol. 77, 2000, p. 323-372.

36. Tanaka, K., Limberg, R., Webb, P., Reddig, M., Jarvis, C., Hargens, A. "Mechanical Counterpressure on the Arm Counteracts Adverse Effects of Hypobaric Exposures." *Aviation, Space, and Environmental Medicine,* Vol. 74, No. 8, 2003, p. 827-832.

37. Tourbier, D., Knudsen, J., Hargens, A., Tanaka, K., Waldie, J., Webb, P., Jarvis, C. "Physiological Effects of a Mechanical Counter Pressure Glove," *Proceedings of the 21st International Conference on Environmental Systems,* Society of Automotive Engineers, San Francisco, CA, July 1991.

38. van Ratingen, M.R, Petterson, R., Drost, M.R., Oomens, C.W.J., Janssen, J.D., "A mixed numerical/experimental method to find Langer's lines of skin." *Advances in Bioengineering,* ASME Winter Annual Meeting, Vol. 26, 1993, p. 63-65.

39. Waldie, J., Bus, B., Tanaka, K., Tourbier, D., Webb, P., Jarvis, W. Hargens, A. "Compression under a Mechanical Counterpressure Space Suit Glove." *Journal of Gravitational Physiology,* Vol. 9, No. 2, 2002, p. 93-97.

40. Wang, Y., Cuitiño, A.M. "Full-field measurements of heterogeneous deformation patterns on polymeric foams using digital image correlation." *International Journal of Solids and Structures,* Vol. 39, 2002, p. 3777-3796.

41. Webb, P. "The Space Activity Suit: An Elastic Leotard for Extravehicular Activity." *Aerospace Medicine,* Vol. 39, 1968, p. 376-383.

42. Wilhemi, D., Bradon J., Blackwell, S.J., Phillips, L.G. "Langer's lines: to use or not to use." *Plastic and Reconstructive Surgery,* Vol. 104, No. 1, 1999, p. 208-214.

CHAPTER 3: THE CHANGING SHAPE OF THE HUMAN LEG: THREE-DIMENSIONAL DYNAMIC ANTHROPOMETRY

Moving forward from Chapter 2's introduction to laser scanning, optical strain analysis, and skin physiology, Chapter 3 presents the methods and results of two human body shape analyses for spacesuit design. These analyses help to determine individualized specifications for mechanical counter pressure (MCP) spacesuits. For maximum mobility, the fabric of a skintight pressure suit must stretch and rotate with the wearer's skin and body movements. Thus, an improved understanding of the deformation of the body's soft tissue during locomotion will help to stipulate quantitative design requirements for MCP suits. To gain this improved understanding, the investigations described in Chapter 3 consider the human body as a pressure vessel with a volume that locally deforms and a surface that stretches, rotates, and translates as muscles contract and relax to bend the joints.

Novel anthropometric measurements of the body in different positions led to two pilot studies of this body deformation, amounting to an implementation of *dynamic three-dimensional anthropometry*. Both studies observed only the right leg, used knee flexion as a representation of locomotion, and used three-dimensional (3D) laser scanning technology and digital analysis for data collection and processing. The first experiment was an attempt to measure *global* changes in the shape of the leg by tracking the surface area and volume of the thigh, knee, and calf during knee bends. The second experiment, a skin strain analysis, zeroed in on *local* changes in leg shape by tracking the knee-bend induced deformation of the skin at many points distributed over the entire leg. The skin strain analysis implemented the techniques of strain gage rosettes and the strain ellipse concept from large deformation theory. This research contributes a *skin strain field map* that depicts the stretching and rotating of the leg surface during knee flexion.

This chapter describes the methods and results for both attempts at characterizing the change in shape of the leg during knee flexion. The first section describes the surface area and volume measurements, and the second section outlines the skin strain field experiment and analysis.

3.1 SURFACE AREA AND VOLUME CHANGES OF THE LEG DURING LOCOMOTION

3.1.1 THE RELATIONSHIPS BETWEEN SURFACE AREA, VOLUME, AND SPACESUIT JOINT TORQUES

Ideally, anthropometric data would directly stipulate MCP suit design by specifying the proper fiber orientation and tension as a function of body position and muscle tension. Before achieving this level of sophistication, however, 3D anthropometry enables the exploration of a simpler question: what is the minimum work required from the wearer to carry out locomotion in a spacesuit? Novel anthropometric measurements of leg surface area and volume help to answer this question: surface area change requires work output in the form of strain energy, and volume change requires work output in the form of pressure-volume energy. These sources of work output can be seen in Equation 3.1, where the energy of locomotion is parsed into two parts.

$$W = W_p + W_e \tag{3.1}$$

W is the total work required to bend a spacesuit joint angle by a given amount, W_p is the portion of this work that changes the interior volume of a pressurized spacesuit, and W_e is the portion of the work that bends and stretches the "elastic" membrane or shell of the spacesuit. The total work, W, can also be called the joint torque.

Recall that the pressure work depends on the operating pressure, p_o, of the spacesuit and the incremental changes, dV, in the volume enclosed between the spacesuit shell and the body surface, as shown in Equation 3.2.

$$W_p = \int_{V_1}^{V_2} p\,dV = p_o \int_{V_1}^{V_2} dV = p_o(V_2 - V_1) \tag{3.2}$$

In a gas pressure suit, V_1 and V_2 are determined by the volume of the body segments within the spacesuit shell. Consequently, for a gas pressure spacesuit, information about a body segment's initial and final volume during a joint motion helps to determine how much pressure work is required from the wearer. If the body segment volume remains constant during a joint motion, then as long as the volume between suit and body remains constant, zero pressure work is required from the wearer. In an MCP suit, however, the pressure work W_p is always necessarily zero, as there is no pressurized volume of gas between the spacesuit shell and the body surface (V_1 and V_2 are both zero). This is shown in Equation 3.3.

$$W_{p,MCP} = 0 \tag{3.3}$$

Therefore, any measurements of the volume changes of body segments during locomotion are more applicable to the design of gas pressure spacesuits than to the design of MCP spacesuits. However, understanding the volume changes of the human leg during locomotion also leads to improved theory for MCP suit design. The claim that MCP can, in theory, passively produce constant pressure without requiring net work output from the wearer requires verification that the *overall* volume of the leg does not change during locomotion. Information about the volume changes of *localized* leg segments can also facilitate MCP suit patterning.

The elastic work, W_e , is the most important quantity for MCP suit design. Equation 3.4 shows that in MCP suits, the elastic work is dominated by the work done to stretch the elements of the spacesuit shell.

$$W_{e,MCP} = W_s \tag{3.4}$$

This stretch work, W_s, is dependent on changes in the surface area of the body enclosed by the MCP suit. In the following explanation, the MCP suit is treated as a thin membrane or shell. From solid mechanics theory, for a given volume of a membrane, the stretch work is proportional to the strain energy [Crandall, Lardner, & Dahl, 1978], as shown in Equation 3.5.

$$W_s \propto u \tag{3.5}$$

For the simplest case of uniaxial deformation, the strain energy per unit volume, u, is equal to the product of half the maximum stress, σ, and strain, ε, as shown in Equation 3.6. This product can be written in terms of strain and elastic modulus only.

$$u = \tfrac{1}{2}\sigma\varepsilon = \tfrac{1}{2}E\varepsilon^2 \tag{3.6}$$

Now for this simple uniaxial case, the strain of the membrane given by Equation 3.7. It is equal to the change in length over the initial length.

$$\varepsilon = \frac{\Delta l}{l_o} \tag{3.7}$$

The change in the membrane's surface area is equal to product of the initial surface area and the uniaxial strain, as shown in Equation 3.8.

$$\Delta A = A\varepsilon \Rightarrow \varepsilon = \frac{\Delta A}{A} \tag{3.8}$$

Equations 3.9 and 3.10 show that since the stretch work is proportional to the square of the strain, it is also proportional to the square of the percentage change in surface area ($\frac{\Delta A}{A}$).

$$u = \tfrac{1}{2}E\varepsilon^2 = \tfrac{1}{2}E\left(\frac{\Delta A}{A}\right)^2 \tag{3.9}$$

$$W_s \propto u \Rightarrow W_s \propto \varepsilon^2 \Rightarrow W_s \propto \left(\frac{\Delta A}{A}\right)^2 \tag{3.10}$$

In conclusion, if the percentage change in surface area is known, then the relative magnitude of the stretch work is also known. The stretch work required to execute a joint motion is revealed by a body segment's initial and final surface area. If the change in surface area is zero, then the stretch work is zero. In this way, changes in body surface area suggest minimum work requirements for an MCP spacesuit. In other words, the total MCP joint torque, W_{MCP}, is directly proportional to the strain energy of the body surface, which is proportional to the square of the strain or to the square of the percentage change in surface area. Equation 3.11 indicates these relationships.

$$W_{MCP} \propto \left(\frac{\Delta A}{A}\right)^2; \quad W_{MCP} \propto \varepsilon^2 . \tag{3.11}$$

This section has described how volume, surface area, and strain measurements aid in the study of the work demands of locomotion in a spacesuit.

3.1.2 METHODS FOR CHARACTERIZING SURFACE AREA AND VOLUME CHANGE OF THE LEG

Although human body surface area and volume measurements are useful for studying the physics of spacesuits, such measurements are not easy to make by hand. The following section describes an experiment in which laser scanning technology enabled efficient and repeatable studies of these 3D body measurements. The experiment tracked the surface area and volume of the thigh, knee, calf, and entire leg during 90-degree knee bends.

Traditionally, human body measurements, or "anthropometry" data, have been limited to one-dimensional length and girth data [NASA-STD-3000, 1995]. These data are based on the distances between anthropometric landmarks and the perimeter around the body. In this thesis, the primary interest is not in the distances between or perimeters around body landmarks; this data has already been well catalogued by previous anthropometric studies. Instead, the important "landmarks" for this thesis are adhesive markers fixed to the surface of the skin, which allow the body to be divided into different 3D segments. The surface area and volume of the segments can be measured for different body positions, amounting to an experiment in "three-dimensional anthropometry."

DATA COLLECTION – Surface area and volume measurements were made possible by laser scanning technology, which was used to collect digital data of the human shape at various states of motion. The data consisted of 3D "snapshots" of the human body; these snapshots contain the 3D position of thousands of points on the surface of the human body. The data collection equipment consisted of a Cyberware ™ (Monterey, CA) whole body 3D laser scanner, shown in Figure 3.1, and associated PC and CyScan software (Cyberware ™, Monterey, CA). In the pilot study, four subjects were scanned three times at each of four different knee flexion angles, resulting in twelve 3D polygonal mesh models for each of the four subjects. The tested knee flexion angles were 0, 30, 60, and 90 degrees, seen in Figure 3.2. This angle is defined by the exterior angle of the femur and tibia axes, with the knee at the vertex. An angle of 0 degrees describes the leg in full extension, and 90 degrees describes the knee flexed so that the thigh and calf are perpendicular. Before laser scanning, the subject's leg surface was outfitted with reference marks, and these marks remained fixed to the same locations on the skin surface for all knee flexion angles.

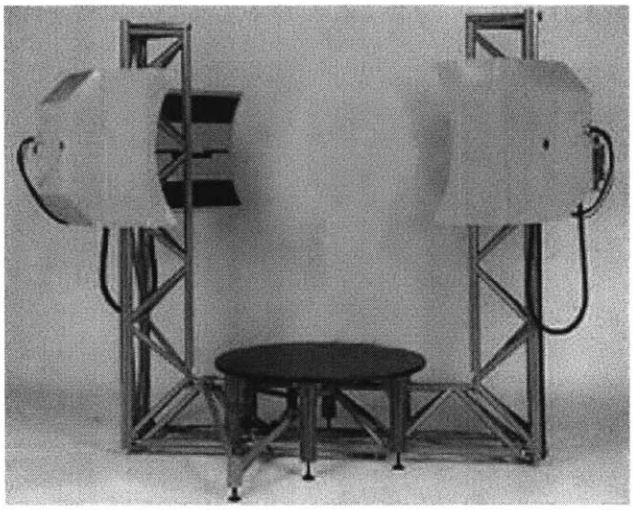

Figure 3.1 Cyberware™ (Monterey, CA) whole body laser scanner. To be scanned, the subject stands on the platform in the center of the scanner.

DATA PROCESSING – The first step in data processing was to isolate the right leg from each laser scan model. This solid model editing was accomplished in the virtual workspace of the CyScan (Cyberware™, Monterey, CA) laser scanning software application. Figure 3.2 shows the laser scan models of the subject's right leg at four different angles. The data for only one of the four subjects was completely analyzed. This subject is a female with a mass of 59 kg and a height of 66 inches, placing her in the 75th height percentile and 25th weight percentile of American females over 20 years of age [National Center for Health Statistics, 2003]. It is important to recognize that the data presented here are for a pilot study with a single subject and a small number of measurements. Further experimentation will be necessary to determine whether or not these leg shape changes are consistent across a wide sample of body sizes and shapes.

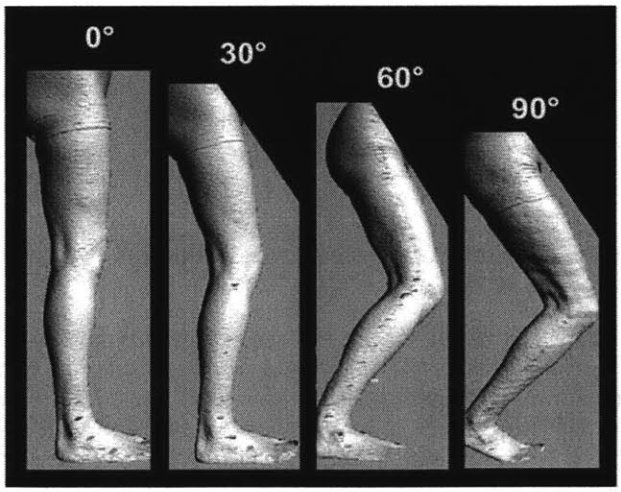

Figure 3.2 Screenshots of 3D laser scan models of the leg at four different knee flexion angles.

The next step in data processing was to divide the leg into the three segments of "thigh," "knee," and "calf," using reference marks on the skin to create four cutting planes perpendicular to the

leg's long bones (Figure 3.3). The foot and hip were not considered as part of the leg. The most superior and inferior of the cutting planes specified where the foot and hip were removed, and the two inner cutting planes separated the thigh from the knee and the knee from the calf.

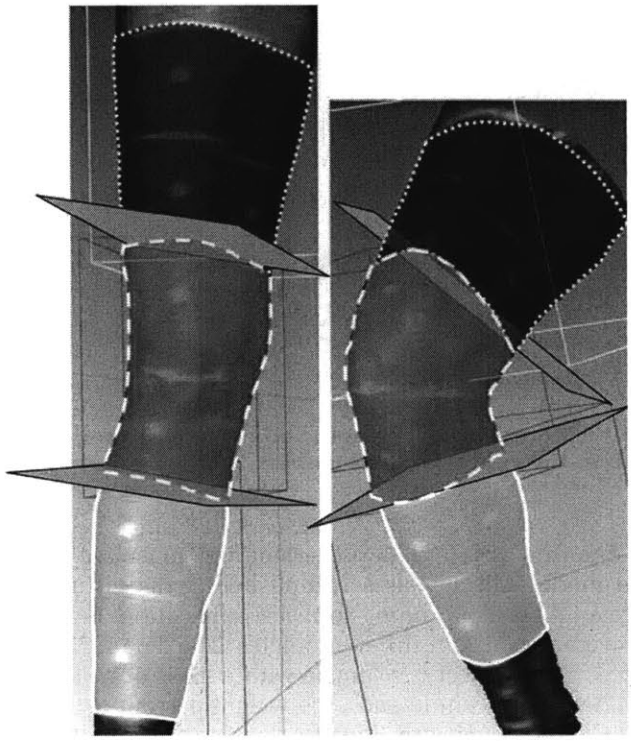

Figure 3.3 Division of leg into thigh, knee, and calf segments, demarcated by adhesive points and bands fixed to specific locations on the skin. Only the two interior cutting planes are shown in these laser scan snapshots.

SURFACE AREA AND VOLUME MEASUREMENTS – RapidForm (INUS Technology, San Jose, CA) 3D scanning and solid modeling software was used to compute the surface area of the thigh, knee, calf, and full leg for each of the three scans at each knee angle. The same software was used to digitally compute the volume of the same segments. These measurements are provided in Appendix B.

3.1.3 RESULTS: SURFACE AREA AND VOLUME CHANGE OF THE LEG DURING KNEE FLEXION

SURFACE AREA CHANGES - The results of the surface area computations indicate that there is no change in the total leg surface area as the knee flexion angle increases from 0 to 90 degrees. An analysis of variance shows that the uncertainty within trials for one flexion angle does not differ significantly from the uncertainty between the means for different flexion angles (Analysis of Variance p-value = 0.58; n = 3 measurements per angle). Analyzed data are for one subject, with three measurements at each knee angle. Figure 3.4 illustrates that knee flexion angle had no significant effect on overall leg surface area. Again, this effect was observed for a single subject, and further study of a greater range of human body size and type is needed.

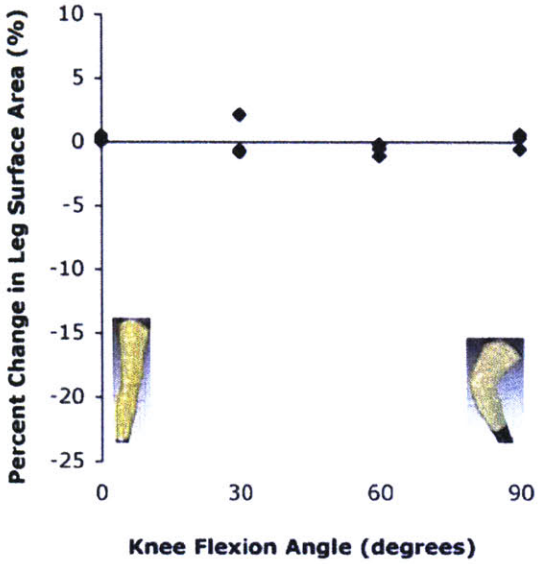

Figure 3.4 Effect of knee flexion angle on total leg surface area. Percent change calculated as knee flexion angle changes from 0 degrees (extended leg) to 30, 60, and 90 degrees (flexed leg). The baseline surface area (0% change) is the average surface area at the 0-degree knee angle. Data are all from a female subject. Each data point represents a different laser scan measurement trial. No significant difference in total leg surface area was measured.

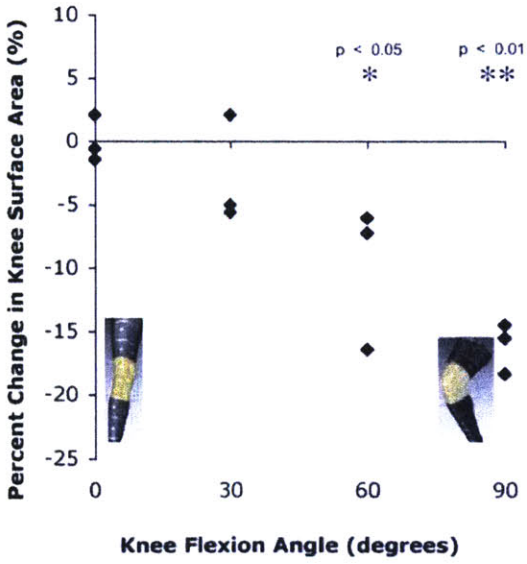

Figure 3.5 Effect of knee flexion angle on local knee surface area. Percent change is calculated as knee flexion angle changes from 0 degrees (extended leg) to 30, 60, and 90 degrees (flexed leg). The baseline surface area (0% change) is the average knee surface area at the 0-degree knee angle. Data are all from a female subject. Each data point represents a different laser scan measurement. Between 0-degree and 90-degree flexion angles, a statistically significant ($p < 0.01$) 16% decrease in mean knee surface area was measured. Between 0-degree and 60-degree flexion angles, a statistically significant ($p < 0.05$) 10% decrease in mean knee surface area was measured.

A statistically significant change in surface area did occur for the skin covering just the knee segment of the leg as the knee flexion angle increases from 0 to 60 degrees (ANOVA p-value < 0.05) and from 0 to 90 degrees (ANOVA p-value < 0.01). The mean percent change in knee surface area between 0-degree knee flexion and 90-degree knee flexion was –16%. When this subject changed her knee joint angle from 0-degree extension to 90-degree flexion, the surface area of the knee section experienced a 16% two-dimensional net contraction. The relative deformation magnitudes are shown in Figure 3.5.

VOLUME CHANGES - No significant change in overall leg volume was found as the knee flexion angle increased from 0 to 90 degrees. An analysis of variance shows that the uncertainty within measurements for one flexion angle did not differ significantly from the uncertainty between the means of the measurements for different flexion angles, for three measurements at each angle for the single subject (ANOVA p-value = 0.64). This result was expected; it has been shown that muscle tissue is isovolumetric when it contracts [McMahon, 1984].

While the overall leg volume did not change with knee flexion angle (Figure 3.6), a statistically significant volume change did occur for the isolated knee segment during knee flexion from 0 to 60 degrees (ANOVA p-value < 0.05) and from 0 to 90 degrees (ANOVA p-value < 0.01). The mean percent change in knee segment volume between 0-degree knee flexion and 90-degree knee flexion was –18%, as shown in Figure 3.7.

There is concern that such a large change in volume might be an artifact of the laser scanner measuring method, which might tend to overestimate the volume of a bent object with concavities, such as the 90-degree knee. However, the data show a decrease in knee volume with flexion, and such a laser scanner artifact cannot explain this decrease.

When this subject's leg was bent from 0 degrees to 90 degrees of knee flexion, the knee segment volume decreased by 18%. Further study will examine the consistency of this effect for a greater range of body sizes.

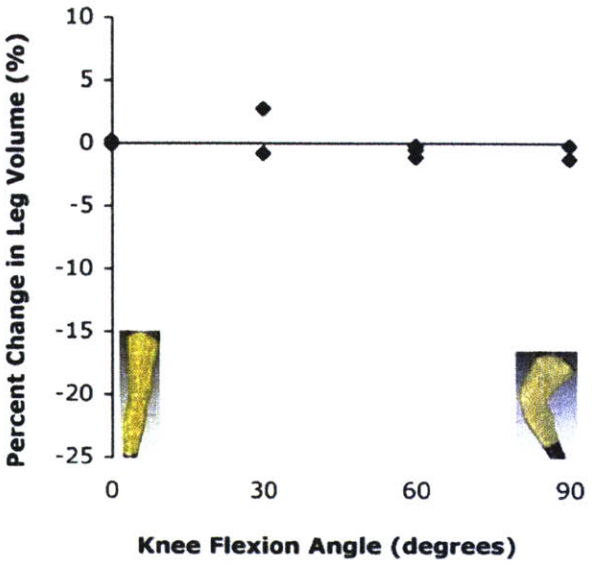

Figure 3.6 Effect of knee flexion angle on total leg volume. The knee flexion angle changes from 0 degrees (extended leg) to 30, 60, and 90 degrees (flexed leg). The baseline volume (0% change) is the average volume at the 0-degree knee angle. Data are all from a female subject. Each data point represents a different laser scan measurement. No significant difference in total leg volume was measured.

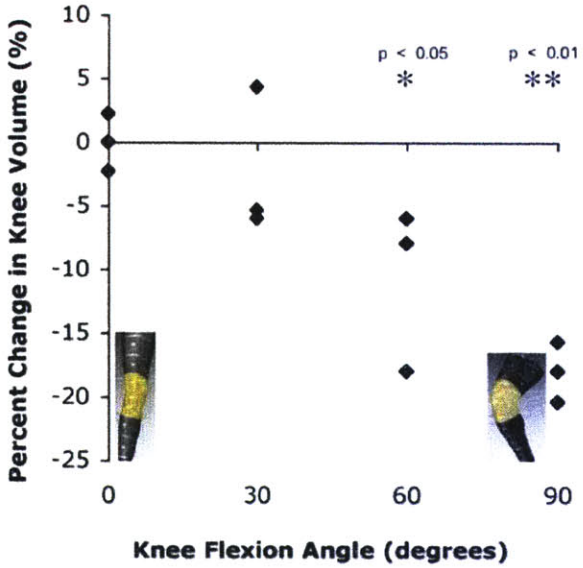

Figure 3.7 Effect of knee flexion angle on local knee volume. Percent change is calculated as knee flexion angle changes from 0 degrees (extended leg) to 30, 60, and 90 degrees (flexed leg). The baseline volume (0% change) is the average knee volume at the 0-degree knee angle. Data are all from a female subject. Each data point represents a different laser scan measurement. Between 0-degree and 90-degree flexion angles, a statistically significant 18% decrease in mean knee volume was measured. Between 0-degree and 60-degree flexion angles, a statistically significant ($p < 0.05$) 11% decrease in mean knee volume was measured.

3.2 QUANTIFYING THE STRAIN FIELD ON THE SKIN SURFACE OF THE LEG DURING LOCOMOTION

The primary goal of the following section is to explain a repeatable and quantitative technique for determining and displaying the strain field on the skin surface of the human body in motion. Results for leg surface area and volume, described in the previous section, lead to general recommendations for the behavior of an MCP suit tailored to one subject: during knee flexion to 90 degrees, the surface area and volume of its knee region must decrease by 16% and 18%, respectively. However, the leg's overall surface area and volume remain constant, and in theory, a suit that does not require strain work output or pressure-volume work output from its wearer could be designed (Equations 3.1 through 3.11).

While theoretically important, these *global* conclusions about leg changes do not assist in the detailed design of an MCP suit. To make specific design recommendations for the materials and patterning of a skintight suit, smaller scale changes of the body's skin during locomotion must be investigated. *Local* skin deformation is studied by measuring skin strain – the stretch, contraction, and angular distortion of skin during knee flexion.

This investigation is facilitated by a repeatable and quantitative technique for mapping the strain field on the skin surface of the human body. This technique includes the use of laser scanning for data collection, a low-computational-resource algorithm for data analysis, and an intuitively understandable visual display of the analysis's results. The strain field representation provides two types of strain information for a representative sample of body surface points: 1) the normal and shear strain in the body limb's local longitudinal and circumferential directions (Figure 3.8), and 2) the directions and magnitudes of minimum normal strain, or "minimum stretch."

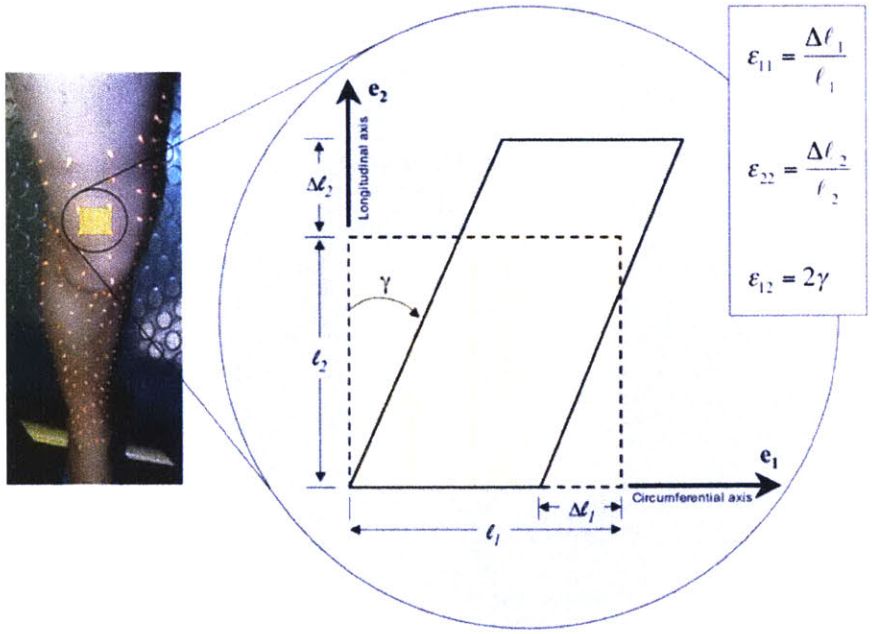

Figure 3.8 Normal and shear strain along local longitudinal and circumferential directions. Longitudinal strain is represented by ε_{22}, circumferential strain is represented by ε_{11}, and shear strain is represented by ε_{12}.

This information specifies in which directions and with what magnitudes a second skin pressure suit must stretch or contract at each location on the body surface. In another sense, the surface strain field can be interpreted as a map that indicates the desired modulus of elasticity of a second skin suit at each location on the body surface. The garment modulus should vary with the strain so as to generate everywhere the same amount of mechanical stress and thus skin surface pressure. Alternatively, the directions of minimum stretch suggest minimum strain energy "pathways" on the skin and hence a minimum strain energy "pattern" for the fibers or tension lines of a second skin spacesuit.

The aim of this work is to show that an operational MCP suit can be realized if the design effort is predicated by a thorough investigation of the surface strain field of the locomotive human body.

3.2.1 METHODS FOR CHARACTERIZING LEG SKIN STRAIN

SYNOPSIS OF STRAIN FIELD ALGORITHM - To measure the strain of the human skin *in vivo* during locomotion, the non-invasive strain measurement technique of Digital Image Correlation (or, in this case, Volume Correlation) was applied to data sets gathered by a 3D laser scanner rather than by optical cameras [Helm, McNeill, & Sutton, 1996]. The technique measured the 3D deformation of the body surface and then constrained this deformation to 2D plane strain. In this pilot study, the representative movement for human locomotion was one subject's knee flexion from 0 to 90 degrees. Here, the stretching, rotating, and translating of the leg skin during knee bends were assumed to be representative of the most substantial straining of the human skin that a pressure suit has to accommodate.

The major steps of the analysis are outlined in the flowchart in Figure 3.9. To collect information about the 3D deformation of the leg surface, the leg surface was marked with 156 position trackers that could be identified in 3D virtual reconstructions of the leg surface. Each tracked point was separated by approximately 3 cm from adjacent points, and each triad of points defined a local surface reference frame with a longitudinal and a circumferential direction. Normal strains emanating out from each tracked point were estimated by comparing the initial separation of each pair of adjacent points to the deformed separation of each pair. Strain gage rosette equations were used to transform these strains from extension/contraction along arbitrary axes to the normal and shear components of the orthogonal strain tensor, with respect to the longitudinal and circumferential axes. Eigenvalue analysis of this strain tensor revealed the directions and magnitudes of principal strain. Finally, application of the strain ellipse concept from large deformation theory enabled the computation of the directions of minimum normal strain, or in other words, "directions of minimum stretch." These directions of minimum stretch suggest a template for the weave orientation for the fibers of an MCP suit.

The following section acknowledges the assumptions inherent in the skin strain field algorithm and then describes the steps of the skin strain field algorithm in greater detail. A self-authored MATLAB™ (Natick, MA) script implemented the algorithm. This code is included in Appendix C. Before being applied to experimental data, the MATLAB™ code was verified by being applied to simulated data files. These data sets described cylinders undergoing prescribed strain, translation, and rotation. The algorithm correctly detected the simulated cylinder deformations.

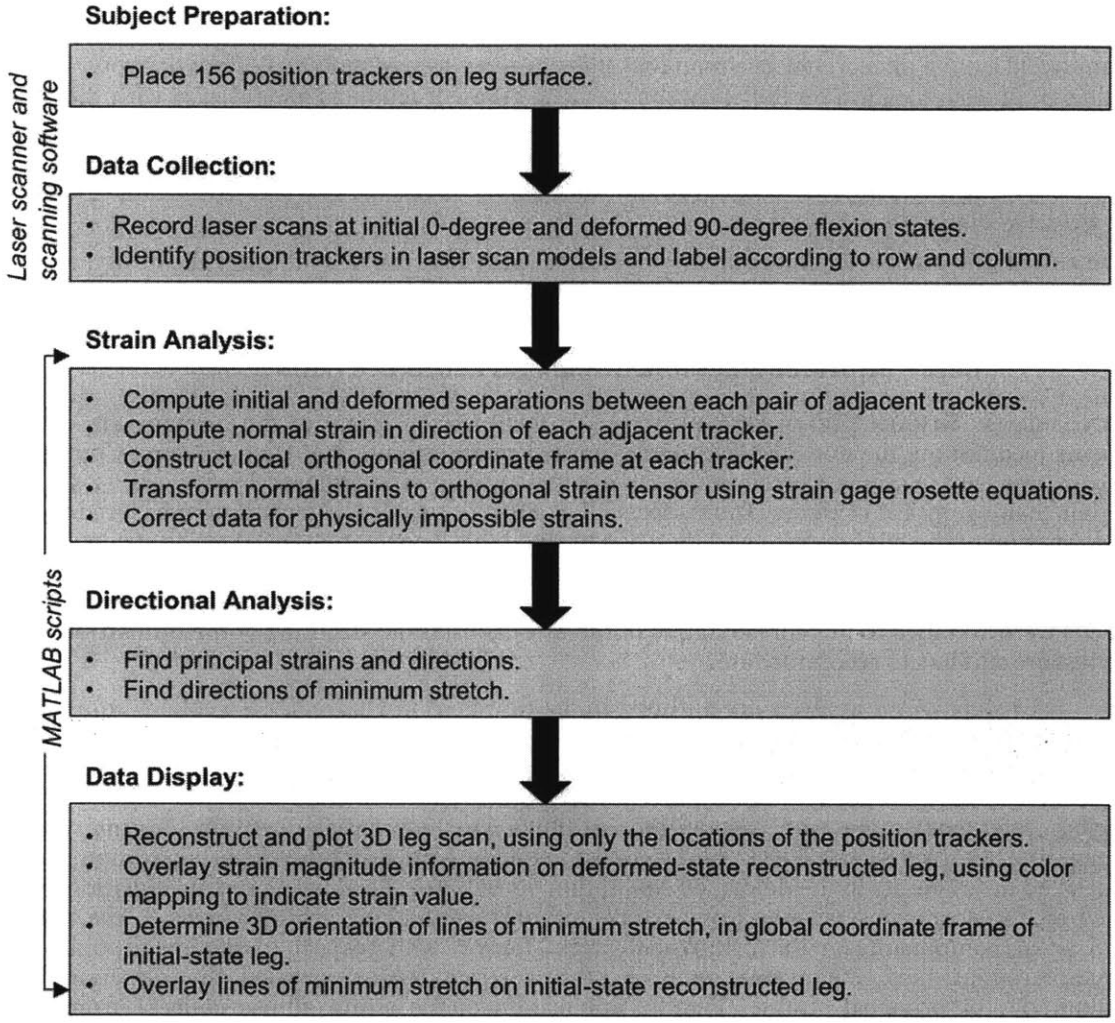

Figure 3.9 Flowchart for creating leg skin strain field maps and determining lines of minimum stretch.

ASSUMPTIONS OF THE METHOD – The following statements express the assumptions of the skin strain field algorithm.

1. Human locomotion is sufficiently modeled with simple knee flexion from a knee joint angle of 0 degrees to a knee joint angle of 90 degrees.
2. The body "in motion" is sufficiently approximated with data from only the initial and final states of the movement.
3. One subject is representative enough to develop a repeatable quantitative technique, demonstrate the general magnitude and range of possible strain results, and suggest preliminary spacesuit design recommendations.
4. The error inherent in laser scanning is tolerable during this phase of developing a technique, whose protocol can be improved in future trials.

5. A sensor density of one sensor per 9 cm^2 is adequate to attain a first-order understanding of the distribution of leg surface strain.
6. One subject is representative enough to make recommendations for a technique to be applied to much larger sample of subjects.

STEP 0: DATA COLLECTION – Before laser scans are taken, 156 stiff paint dots (Tulip® Dimensional Paint, Micheals Stores, Inc., Everett, MA) are affixed to the surface of the leg, separated from each other by approximately 3 cm, to form 12 columns of 13 points running down the length of the leg. The right leg is laser-scanned three times at 0-degree knee flexion and three times at 90-degree flexion. The angle is measured with a goniometer. In both positions, the subject keeps her right and left feet flush with the ground. For each of the three scans at each position, the subject rotates her body by 120 degrees, so that any shadows cast in one scan fall on a different part of the leg during the other two scans.

STEP 1: ROW AND COLUMN NOMENCLATURE - The results of the skin marking and laser scanning are the positions of a finite set of material points on the skin surface in the initial (0-degree) and deformed (90-degree) configurations of the leg. Each marked material point is identified by its "row" and "column" location, specified by indices i and j. Thirteen rows and 12 columns of locations comprise a leg surface grid of 156 markers. The rows i = 1, 2, 3,..., 13 of the labeled material points are ordered such that the rows increase from i = 1 for a cross-section through the top of the thigh, to i = 13 for a cross-section around the middle of the calf. The columns j = 1, 2, 3,..., 12 are ordered such that the columns increase from the anterior surface towards the medial surface (i.e., j = 1 for the longitudinal line through the patella; j = 4 for the longitudinal line down the medial surface of the leg; j = 6 for the longitudinal line that passes through the back of the knee; j = 12 for the longitudinal line that goes through the point just to the outside of the patella). Figure 3.10 shows the rows and columns of markers on the anterior surface of the leg.

Let $\vec{X}_{i,j}$ be the initial (reference) configuration position of a material point in the i^{th} row and j^{th} column of the grid marked on the surface of the leg. Let $\vec{x}_{i,j}$ be the deformed configuration position of this material point in the i^{th} row, j^{th} column. Accordingly, $\vec{X}_{i+1,j+1}$ refers to the initial position of the material point one row towards the ankle and one column to the right of the material point referred to by $\vec{X}_{i,j}$. The reference frame for the initial configuration and the deformed configuration need not be identical. Figure 3.11 depicts a triad of points as it deforms from its initial 0-degree configuration to its deformed 90-degree configuration.

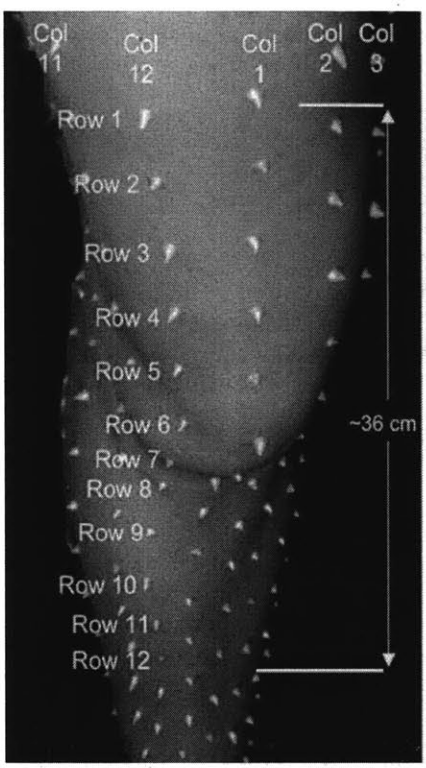

Figure 3.10 Raised grid dots (156 total) that serve as position trackers for the leg surface. The position trackers are labeled such that rows increase from thigh to calf; columns increase from the anterior surface towards the medial surface.

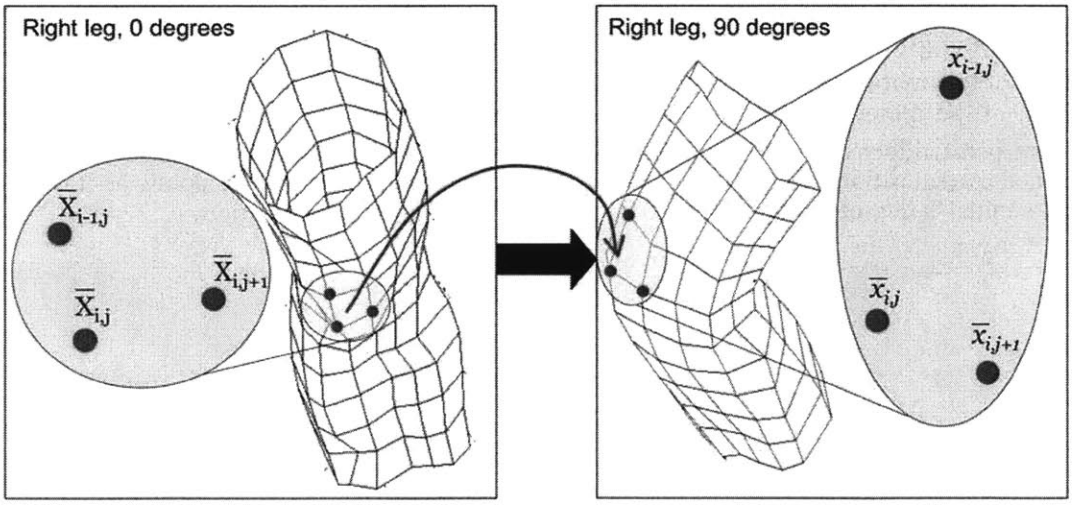

Figure 3.11 Reconstructions of the right leg in the initial 0-degree knee flexion configuration (left) and the deformed 90-degree configuration (right). Reconstructions are defined only by the positions of the tracked points. The technique of "digital volume correlation" is applied to these two leg volumes, which in their digital form are comprised of 13 circumferential "rows" and 12 "columns" of tracked points. The curved dotted arrow indicates the displacement of three adjacent points on the patella surface.

STEP 2: SEPARATION BETWEEN ADJACENT GRID POINTS - Let $\vec{D}_{i+1,j+1}$ be the full three-dimensional vector between a material point at location (i,j) and its neighboring material point at location $(i+1,j+1)$, in the *initial* configuration of the leg. The magnitude of the distance between the two points is given by $D_{i+1,j+1} = \left|\vec{D}_{i+1,j+1}\right|$. The position of each grid point with respect to all of its adjacent grid points, in the initial configuration of the leg, is fully described by eight such separation vectors, which are illustrated in Figure 3.12:

$\vec{D}_{i,j+1}$ is the vector pointing to the neighbor directly to the right of location (i,j).
$\vec{D}_{i-1,j+1}$ is the vector pointing to the neighbor to the upper right of location (i,j).
$\vec{D}_{i-1,j}$ is the vector pointing to the neighbor directly above location (i,j).
$\vec{D}_{i-1,j-1}$ is the vector pointing to the neighbor to the upper left of location (i,j).
$\vec{D}_{i,j-1}$ is the vector pointing to the neighbor directly to the left of location (i,j).
$\vec{D}_{i+1,j-1}$ is the vector pointing to the neighbor to the lower left of location (i,j).
$\vec{D}_{i+1,j}$ is the vector pointing to the neighbor directly below location (i,j).
$\vec{D}_{i+1,j+1}$ is the vector pointing to the neighbor to the lower right of location (i,j).

Similarly, let $\vec{d}_{i+1,j+1}$ be the full three-dimensional separation vector between a material point at location (i,j) and its neighboring material point at location $(i+1,j+1)$, in the *deformed* configuration of the leg. The magnitude of the distance between the two deformed configuration points is given by $d_{i+1,j+1} = \left|\vec{d}_{i+1,j+1}\right|$. There are eight such $\vec{d}_{i+m,j+n}$ parameters to characterize the position of each grid point with respect to all of its adjacent grid points in the deformed configuration (for all combinations of m = -1,0,1; n = -1,0,1).

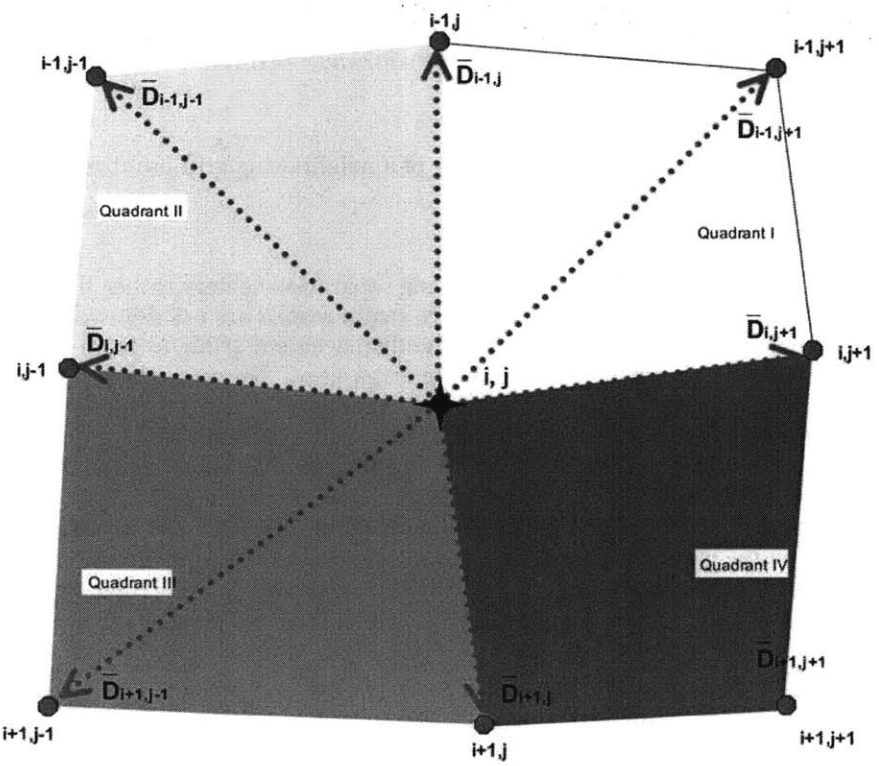

Figure 3.12 "Virtual strain gage rosette," illustrating the eight nearest-neighbor separation vectors for a material point in its initial configuration.

STEP 3: A "VIRTUAL" STRAIN GAGE ROSETTE - This purpose of this step is to estimate normal strain in the direction of adjacent grid points. This technique is called a "virtual strain gage rosette" because strain gages measure only normal strain, and a combination of strain gages in a rosette allows for orthogonal normal and shear strain to be computed [Crandall, Dahl, & Lardner, 1978; Hannah & Reed, 1992]. Now let $\varepsilon_{i+1,j+1}$ be the normal strain component for a grid point in the initial direction of the $(i+1, j+1)$ neighbor. Under the assumption of small strains, the value of $\varepsilon_{i+1,j+1}$ is given by Equation 3.12, and $\varepsilon_{i-1,j-1}$ is similarly given by Equation 3.13. The equations are similar for all eight directions emanating from each grid point.

$$\varepsilon_{i+1,j+1} = \lim_{D_{i+1,j+1} \to 0} \frac{d_{i+1,j+1} - D_{i+1,j+1}}{D_{i+1,j+1}} \qquad \textbf{(3.12)}$$

$$\varepsilon_{i-1,j-1} = \lim_{D_{i-1,j-1} \to 0} \frac{d_{i-1,j-1} - D_{i-1,j-1}}{D_{i-1,j-1}} \qquad \textbf{(3.13)}$$

In a set of discrete position data, the initial grid spacings $d_{i+m\,j+n}$ have finite value rather than approaching zero. Therefore the *approximate* normal strain components $\varepsilon_{i+m\,j+n}$ (for m = -1,0,1; n = -1,0,1) in eight directions at each grid point are given by Equation 3.14 [Crandall, Dahl, & Lardner, 1978].

$$\varepsilon_{i+m,j+n} = \frac{d_{i+m,j+n} - D_{i+m,j+n}}{D_{i+m,j+n}}, \text{ for } (m = -1,0,1;\ n = -1,0,1) \qquad \textbf{(3.14)}$$

In other words, the normal strain in the direction of a neighboring grid point is equal to the ratio of $\frac{\textit{the change in separation between neighbors}}{\textit{the initial separation between neighbors}}$.

The rationale for determining normal strain by using separation vectors rather than by computing displacement gradients is to ensure that the surface strain results are not dependent on rigid body rotations. In the absence of rigid body rotation, the displacement gradient from one grid point to another is equivalent to the percent change in separation between those two grid points. However, for a body in which different portions experience different amounts of rigid body rotation, surface strains found by computing displacement gradients will be distorted by these rigid body rotations. Another justification for finding surface strains by comparing separations is that the initial and deformed configuration positions need not be measured with respect to the same inertial frame. The displacement gradient method requires the initial and deformed material points to be measured in the same inertial frame. In this experiment, the laser scanner collected position data in different frames for different laser scans, so the displacement gradient method would have required the extra step of transforming the position vectors to the same coordinate frame.

The eight normal strain components are now utilized as a virtual "strain gage rosettes": one three-axis rosette in each of the four quadrants around each grid point [Hannah & Reed, 1992].

STEP 4: CONSTRUCTION OF LOCAL SURFACE REFERENCE FRAME - For each grid point, a two-dimensional orthogonal coordinate system, approximately tangent to the surface of the leg, is constructed in each of the four quadrants of adjacent grid points. The normal strain components are transformed to the orthogonal coordinate system in each quadrant. Let $\vec{e}_1$ and $\vec{e}_2$ be the unit vectors that define the axes of the orthogonal coordinate system at a given grid point. We will construct these vectors so that $\vec{e}_1$ points in the circumferential, or "hoop", direction, and $\vec{e}_2$ points in the longitudinal direction at each grid point. These orthonormal basis vectors are constructed as follows.

Let $\vec{n}$ be the unit normal vector to the leg surface patch consisting of one quadrant of adjacent points to a given grid point, in the initial configuration of the leg. The first quadrant of adjacent points consists of the points directly above, to the upper right, and to the right of a given grid point. Compute $\vec{n}^I$ in this first quadrant with the triad of points that consists of the given grid point, its $(i\text{-}1, j)$ neighbor directly above, and its $(i\text{-}1, j\text{+}1)$ neighbor to the upper right, as shown in Equation 3.15.

$$\vec{n}^I = \frac{\vec{D}_{i-1,j+1} \times \vec{D}_{i-1,j}}{\left|\vec{D}_{i-1,j+1} \times \vec{D}_{i-1,j}\right|} \tag{3.15}$$

Now let $\vec{e}_2{}^I$ be the unit vector that has direction of the first quadrant's y-axis, which is defined in Equation 3.16 by the vector pointing from a given grid point to the neighboring grid point one row above.

$$\vec{e}_2{}^I = \frac{\vec{D}_{i-1,j}}{\left|\vec{D}_{i-1,j}\right|} \tag{3.16}$$

The y-axis for the first quadrant is the longitudinal axis that points up the leg towards the hip. Now the x-axis, in the direction of the unit basis vector $\vec{e}_1{}^I$, is simply defined by the direction that is perpendicular to both the unit normal vector $\vec{n}^I$ and the longitudinal vector $\vec{e}_2{}^I$, as shown in Equation 3.17.

$$\vec{e}_1{}^I = \vec{e}_2^I \times \vec{n}^I \tag{3.17}$$

The x-axis for the first quadrant is the circumferential axis, pointing in the hoop direction in the direction of increasing columns.

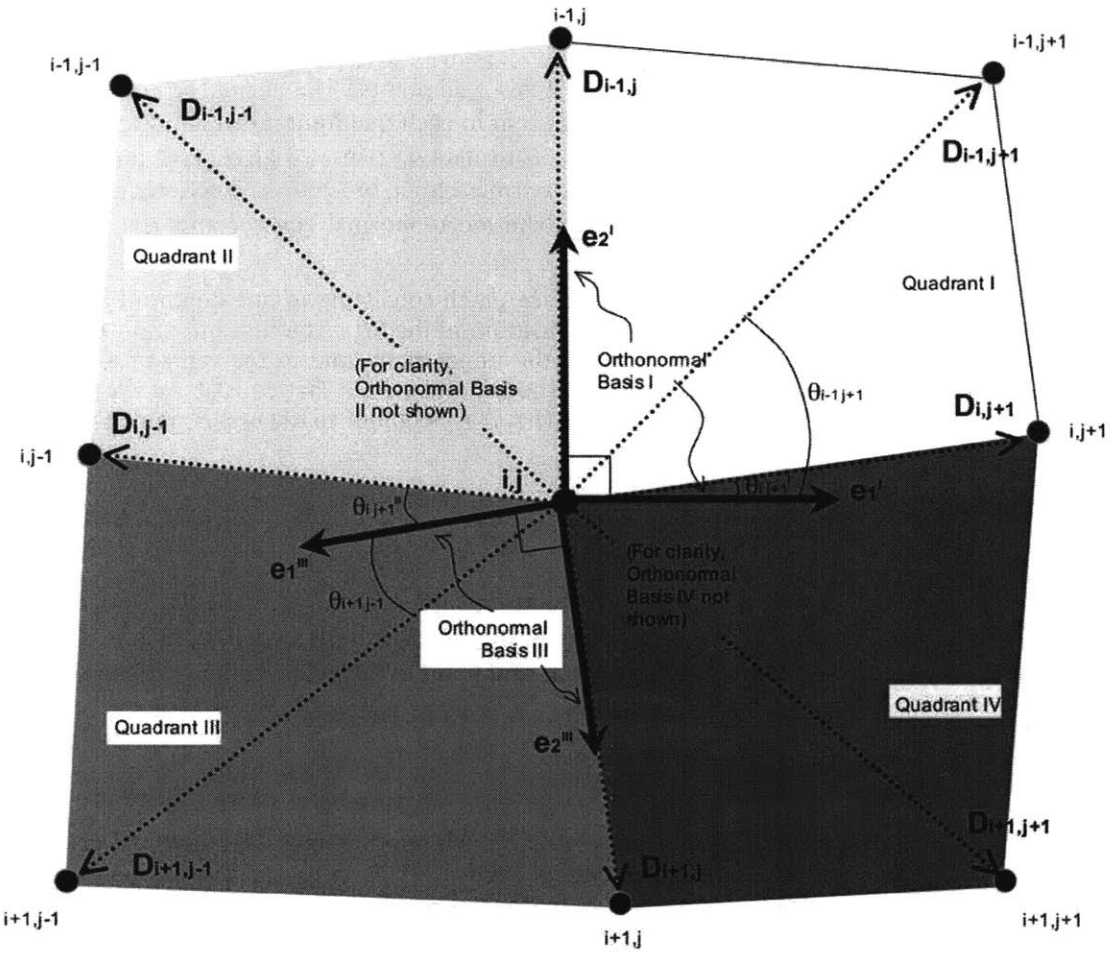

Figure 3.13 Surface coordinate system with orthogonal reference frames.

STEP 5: TRANSFORMATION OF ROSETTE STRAINS TO ORTHOGONAL FRAME – At this point, the algorithm has computed the magnitude of strain in the arbitrary directions of the adjacent grid points. To display the strain data in a consistent manner for all tracked points, the skin strain should be expressed in the orthogonal directions along the skin surface, $\vec{e}_1$ and $\vec{e}_2$. Therefore, the measured normal strains must be transformed onto the orthogonal surface coordinate system. This transformation is accomplished with the basic equations for a three-gage strain gage rosette, with strain gages rotated by any three arbitrary angles θ_p, θ_q, and θ_r from the x-axis (the $\vec{e}_1$ direction). The relation between the normal strains ε_p, ε_q, and ε_r and the normal and shear strains ε_{11}, ε_{22}, and ε_{12} with respect to the orthogonal x- and y-axes are given by Equations 3.18 through 3.20 [Crandall, Lardner, & Dahl, 1978, p. 249].

$$\varepsilon_p = \varepsilon_{11} \cos^2 \theta_p + \varepsilon_{22} \sin^2 \theta_p + 2\varepsilon_{12} \cos \theta_p \sin \theta_p ; \qquad \textbf{(3.18)}$$

$$\varepsilon_q = \varepsilon_{11} \cos^2 \theta_q + \varepsilon_{22} \sin^2 \theta_q + 2\varepsilon_{12} \cos \theta_q \sin \theta_q ; \tag{3.19}$$

$$\varepsilon_r = \varepsilon_{11} \cos^2 \theta_r + \varepsilon_{22} \sin^2 \theta_r + 2\varepsilon_{12} \cos \theta_r \sin \theta_r ; \tag{3.20}$$

Consequently, the adjacent-grid-point normal strains in the first quadrant are related to the normal and shear strains in the first quadrant's orthogonal measurement basis (Equations 3.21 through 3.23).

$$\varepsilon_{i,j+1} = \varepsilon_{11}^I \cos^2 \theta_{i,j+1}^I + \varepsilon_{22}^I \sin^2 \theta_{i,j+1}^I + 2\varepsilon_{12}^I \cos\theta_{i,j+1}^I \sin\theta_{i,j+1}^I \tag{3.21}$$

$$\varepsilon_{i-1,j+1} = \varepsilon_{11}^I \cos^2 \theta_{i-1,j+1}^I + \varepsilon_{22}^I \sin^2 \theta_{i-1,j+1}^I + 2\varepsilon_{12}^I \cos\theta_{i-1,j+1}^I \sin\theta_{i-1,j+1}^I \tag{3.22}$$

$$\varepsilon_{i-1} = \varepsilon_{22}^I \tag{3.23}$$

The angles $\theta_{i,j+1}^I$ and $\theta_{i-1,j+1}^I$ are computed by Equations 3.24 and 3.25.

$$\theta_{i,j+1}^I = \arccos\left(\frac{\bar{D}_{i,j+1} \bullet \bar{e}_1}{\left|\bar{D}_{i,j+1}\right| \left|\bar{e}_1\right|}\right) \tag{3.24}$$

$$\theta_{i-1,j+1}^I = \arccos\left(\frac{\bar{D}_{i-1,j+1} \bullet \bar{e}_1}{\left|\bar{D}_{i-1,j+1}\right| \left|\bar{e}_1\right|}\right) \tag{3.25}$$

Equations 3.21 through 3.23 are solved simultaneously for $\varepsilon_{11}{}^I$, $\varepsilon_{22}{}^I$, and $\varepsilon_{12}{}^I$.

STEP 6: REPETITION OF PROCEDURE FOR ALL ADJACENT-POINT QUADRANTS – For a given grid point, this procedure of orthonormal basis construction and strain transformation is carried out four times – once in each of the four quadrants surrounding the grid point. The second quadrant normal, $\vec{n}^{II}$, is defined by the $(i\text{-}1,j)$ and $(i\text{-}1,j\text{-}1)$ neighbors. The third quadrant normal, $\vec{n}^{III}$, is defined by the $(i+1,j\text{-}1)$ and $(i+1,j)$ neighbors. The fourth quadrant normal, $\vec{n}^{IV}$, is defined by the $(i+1,j)$ and $(i+1,j+1)$ neighbors. These vectors are described in Equations 3.26 through 3.28. All normal vectors are unit vectors and are normal to the *initial* configuration leg surface.

$$\vec{n}^{II} = \frac{\vec{D}_{i-1,j} \times \vec{D}_{i-1,j-1}}{\left|\vec{D}_{i-1,j} \times \vec{D}_{i-1,j-1}\right|} \tag{3.26}$$

$$\vec{n}^{III} = \frac{\vec{D}_{i+1,j-1} \times \vec{D}_{i+1,j}}{\left|\vec{D}_{i+1,j-1} \times \vec{D}_{i+1,j}\right|} \tag{3.27}$$

$$\vec{n}^{IV} = \frac{\vec{D}_{i+1,j} \times \vec{D}_{i+1,j+1}}{\left|\vec{D}_{i+1,j} \times \vec{D}_{i+1,j+1}\right|} \tag{3.28}$$

In the first and second quadrants, the longitudinal axes, defined by the unit basis vectors $\vec{e}_2{}^{I}$ and $\vec{e}_2{}^{IV}$, point *up* the leg in the direction of decreasing rows, towards the hip. In the third and fourth quadrants, the longitudinal axes defined by the unit basis vectors $\vec{e}_2{}^{II}$ and $\vec{e}_2{}^{III}$ point *down* the leg in the direction of increasing rows, towards the ankle.

For completeness, Equations 3.29 to 3.31 define each quadrant's longitudinal y-axis.

$$\vec{e}_2^{\,II} = \frac{\vec{D}_{i-1,j}}{\left|\vec{D}_{i-1,j}\right|} \tag{3.29}$$

$$\vec{e}_2^{\,III} = \frac{\vec{D}_{i+1,j}}{\left|\vec{D}_{i+1,j}\right|} \tag{3.30}$$

$$\vec{e}_2^{\,IV} = \frac{\vec{D}_{i+1,j}}{\left|\vec{D}_{i+1,j}\right|} \tag{3.31}$$

Finally, each quadrant's circumferential x-axis is the cross product of the quadrant's y-axis unit vector and unit normal vector, as shown in Equations 3.32 through 3.34.

$$\vec{e}_1^{\,II} = \vec{e}_2^{\,II} \times \vec{n}^{II} \tag{3.32}$$

$$\vec{e}_1^{\,III} = \vec{e}_2^{\,III} \times \vec{n}^{III} \tag{3.33}$$

$$\vec{e}_1^{\,IV} = \vec{e}_2^{\,IV} \times \vec{n}^{IV} \tag{3.34}$$

As a result, the circumferential basis vectors $\vec{e}_1{}^{I}$ and $\vec{e}_1{}^{IV}$ in the first and fourth (upper right and lower right) quadrants point around the leg in the direction of increasing columns. The circumferential basis vectors $\vec{e}_1{}^{II}$ and $\vec{e}_1{}^{III}$ in the second and third (upper left and lower left) quadrants point around the leg in the direction of decreasing columns (Figure 3.14).

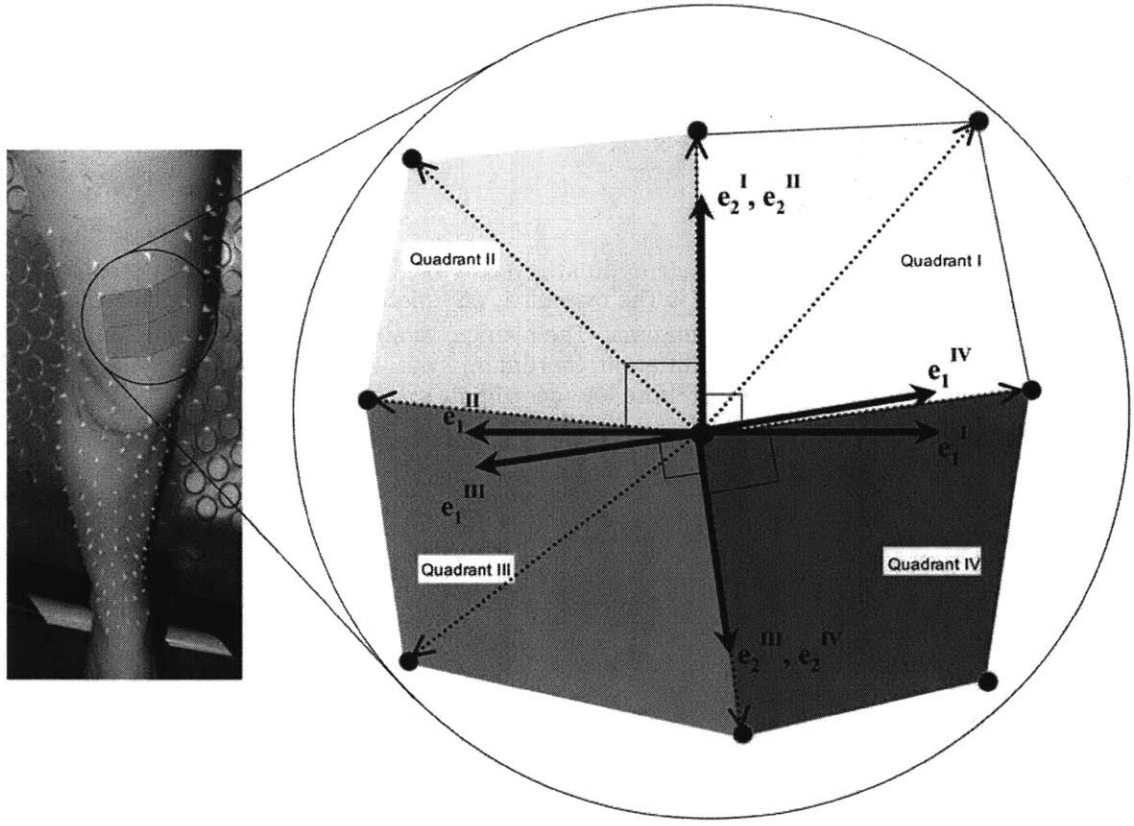

Figure 3.14 Circumferential vectors pointing in direction of increasing columns or decreasing columns. In Quadrants I and IV, positive circumferential direction is toward increasing columns (anterior to medial direction). In Quadrants II and III, positive circumferential direction is toward decreasing columns (anterior to lateral direction).

In each quadrant, the virtual strain gage rosette technique is used to transform the normal adjacent-grid-point strains into orthogonal normal and shear strain values. Appendix D contains the equations that repeat the transformation process in the remaining three quadrants.

The results of this procedure are circumferential strain measured in four different quadrants (ε_{11}^{I}, ε_{11}^{II}, ε_{11}^{III}, ε_{11}^{IV}), longitudinal normal strain measured in four different quadrants (ε_{22}^{I}, ε_{22}^{II}, ε_{22}^{III}, ε_{22}^{IV}), and shear strain measured in four different quadrants (ε_{12}^{I}, ε_{12}^{II}, ε_{12}^{III}, ε_{12}^{IV}).

STEP 7: LONGITUDINAL-CIRCUMFERENTIAL STRAIN TENSOR – A useful strain tensor for each grid point on the leg surface is foundy by applying Equations 3.35 through 3.37, which compute the average of each set of four strain values.

$$\varepsilon_{11} = \frac{\left(\varepsilon_{11}^{I} + \varepsilon_{11}^{II} + \varepsilon_{11}^{III} + \varepsilon_{11}^{IV}\right)}{4} \tag{3.35}$$

$$\varepsilon_{22} = \frac{\left(\varepsilon_{22}^{I} + \varepsilon_{22}^{II} + \varepsilon_{22}^{III} + \varepsilon_{22}^{IV}\right)}{4} \tag{3.36}$$

$$\varepsilon_{12} = \frac{\left(\varepsilon_{12}^{I} + \varepsilon_{12}^{II} + \varepsilon_{12}^{III} + \varepsilon_{12}^{IV}\right)}{4} \tag{3.37}$$

Then the first quadrant is chosen as the coordinate system for these average strain values. Thus, the overall $\vec{e}_1$ direction is the vector $\vec{e}_1^{\,I}$. The overall $\vec{e}_2$ direction is the vector $\vec{e}_2^{\,I}$. This choice of coordinate system is a broad approximation. The average strain values come from four values that were computed with respect to different coordinate systems, but in this step the average strain values are ascribed to just one of those four coordinate systems.

Now, for each grid point on the leg surface, we have a strain tensor with respect to orthonormal basis vectors that are approximately tangent to the surface and that point longitudinally up the leg and circumferentially around the leg.

$$[\varepsilon] = \begin{bmatrix} \varepsilon_{11} & \varepsilon_{12} \\ \varepsilon_{12} & \varepsilon_{22} \end{bmatrix} \tag{3.38}$$

STEP 8: DATA CORRECTION - Before moving forward with data processing, the strain tensor results are reviewed, and strain component values of greater than 100% are corrected. The value is corrected by converting it to the average of the adjacent points' values for that strain component. The justification for this correction step is that 100% is beyond the failure strain of most human skin. The rationale behind the method of correction is that because the skin is a continuous membrane, it is assumed that there are no discontinuous changes in strain values, and the average of adjacent strains is a reasonable estimate for a location whose strain is unknown. Future work is needed to explain exactly why some impossible results occur and to build robustness into the computational algorithm to avoid them.

STEP 9: PRINCIPAL STRAINS AND DIRECTIONS – Now eigenvalue analysis is carried out on the corrected strain tensors. The eigenvalues and eigenvectors of the orthogonal strain tensor give the principal strains, ε_I and ε_{II}, and the principal directions, $\vec{v}_I$ and $\vec{v}_{II}$, at the given material point on the leg surface.

The directions $\vec{v}_I$ and $\vec{v}_{II}$ indicate in which directions, with respect to $\vec{e}_1$ and $\vec{e}_2$, the skin strain is pure extension or contraction (i.e., purely normal strain), without any angular distortion (i.e., without shear strain). The values of ε_I and ε_{II} indicate the magnitude of that extension or contraction, where ε_I and ε_{II} are always labeled so that ε_I is less than ε_{II}. If ε_I and ε_{II} are both positive values, then there is pure extension along both principal directions, and extension actually occurs in all directions. If ε_I and ε_{II} are both negative values, then there is pure contraction along both principal directions; in fact, contraction occurs in all directions. If ε_I is negative but ε_{II} is positive, then the skin contracts in the direction of $\vec{v}_I$, and the skin stretches in the direction of $\vec{v}_{II}$. For each leg surface grid point, the principal strains are computed.

Table 3.1 Three cases of deformation and the resulting behavior along the principal strain directions.

Case	ε_I	ε_{II}	Behavior along Principal Direction $\vec{v}_I$	Behavior along Principal Direction $\vec{v}_{II}$
1	-	+	Contraction	Extension
2	+	+	Extension	Extension
3	-	-	Contraction	Contraction

STEP 10: DIRECTIONS OF MINIMUM STRETCH – The magnitude and directions of the principal strain provide enough information to determine directions of *minimum* normal strain, or "minimum stretch." A conceptual tool used by mechanists to visualize principal strains and their orientation is the strain ellipse, also called the deformation ellipse [Ramsay & Lisle, 2000]. The deformation ellipse shows a material section in its deformed state. By studying the ellipse shape, the initial size of the material section can be determined. The long axis of the ellipse corresponds to the maximum principal direction of the center material point, and the short axis corresponds to the minimum principal direction. By overlaying the initial circle on the deformation ellipse, the direction of minimum stretching can be found. Table 3.2 and Figure 3.15 illustrate the three unique cases of a deformation ellipse and explain what they indicate about the behavior of the included material.

If ε_I is negative and ε_{II} is positive, then in between the two principal directions $\vec{v}_I$ and $\vec{v}_{II}$, there is some direction in which *no* normal strain occurs. This non-stretching direction and its reflection about $\vec{v}_{II}$ are "directions of zero stretch," alternatively called directions of zero normal strain or directions of pure shear, and labeled as $\vec{w}_I$ and $\vec{w}_{II}$. In the case of two positive principal strains or of two negative principal strains, the directions of *zero* stretch do not exist. Instead, the "direction of minimum stretch" is determined and labeled as $\vec{w}_I$. This direction is the one in which the normal strain has the lowest absolute value, and it is equivalent to the principal direction with strain magnitude closest to zero. In the case of two positive strains, the direction of minimum stretch is principal direction I, and in the case of two negative strains, the direction of minimum stretch is principal direction II. Table 3.2 outlines these three cases and the resulting directions of minimum stretch.

Table 3.2 Three cases of deformation and their resulting directions of minimum stretch.

Case	ε_I	ε_{II}	Deformation Ellipse Shape	Directions of *Zero* Stretch	Directions of *Minimum* Stretch
1	-	+	Thinner and taller	ϕ degrees from maximum principal direction	Same as directions of zero stretch
2	+	+	Wider and taller	Do not exist	In direction $\vec{v}_I$ of principal strain with smallest absolute magnitude
3	-	-	Thinner and shorter	Do not exist	In direction $\vec{v}_{II}$ of principal strain with smallest absolute magnitude

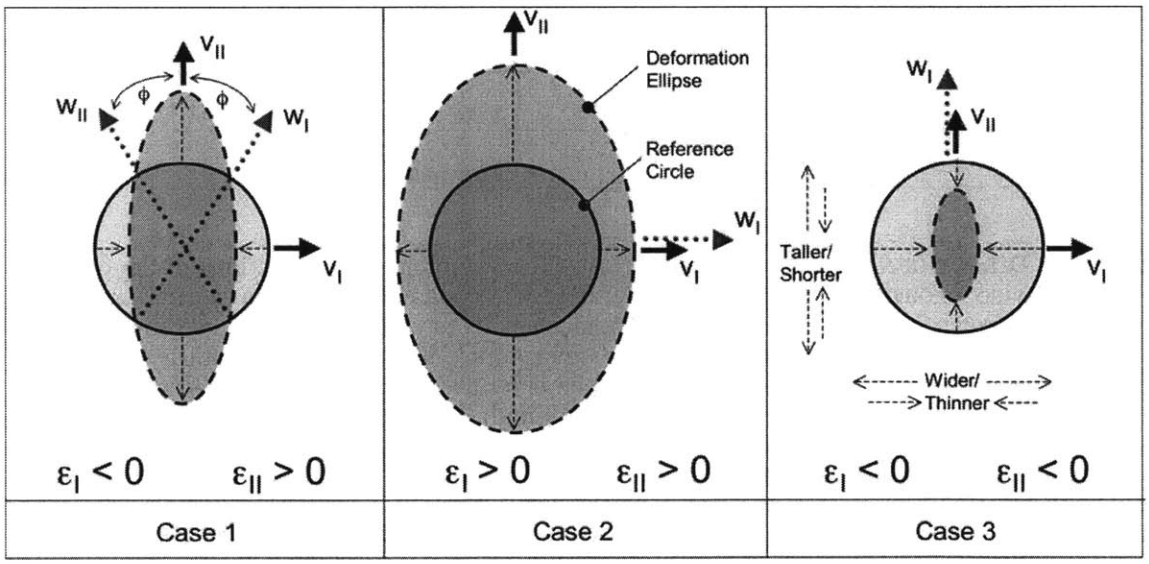

Figure 3.15 Three cases of the deformation ellipse. Darker gray deformation ellipse is overlaid on the lighter gray original circle. In Case 1, with both a negative and a positive principal strain (one ellipse axis is longer than the circle diameter; the other ellipse axis is shorter than the circle diameter), the directions of minimum stretch are equivalent to the directions of zero stretch, shown with dotted arrows. In Case 2, with both principal strains positive (both ellipse axes longer than the circle diameter), there is only one direction of minimum stretch, oriented in the direction of the smaller principal strain. In Case 3, with both principal strains negative (both ellipse axes shorter than the circle diameter), there is also only one direction of minimum stretch, oriented in the direction of the principal strain with smaller absolute value.

If the principal strain values ε_I and ε_{II} do span zero, then Equation 3.39 gives the zero-stretch directions, rotated by an angle of $\pm\phi$ from the direction $\vec{v}_{II}$ of maximum principal strain [Ramsay, 1983, p. 294]. In Equation 3.39, $+\phi$ is the angle between $\vec{v}_{II}$ and $\vec{w}_I$, and $-\phi$ is the angle between $\vec{v}_{II}$ and $\vec{w}_{II}$. For this case, the directions of minimum stretch, $\vec{w}_I$ and $\vec{w}_{II}$, are equivalent to the directions of zero stretch.

$$\tan^2 \phi = \frac{\varepsilon_{II}}{\varepsilon_I}, \text{ where } \varepsilon_I < 0 \text{ and } \varepsilon_{II} > 0 \qquad \textbf{(3.39)}$$

For the uniformly stretching or uniformly contracting cases, only the direction of *minimum* normal strain can be found. In these cases, there is only one direction of minimum stretch, $\vec{w}_I$, and it is equivalent to one of the principal directions, as reiterated in Equations 3.40 and 3.41.

$$\text{If } \varepsilon_I > 0 \text{ and } \varepsilon_{II} > 0\text{: } \vec{w}_I = \vec{v}_I \qquad \textbf{(3.40)}$$

$$\text{If } \varepsilon_I < 0 \text{ and } \varepsilon_{II} < 0\text{: } \vec{w}_I = \vec{v}_{II} \qquad \textbf{(3.41)}$$

The minimum-stretch directions provide information with respect to the local 2D coordinate frame at each grid point. To display these directions in three dimensions, they must be transformed back into the original 3D coordinate frame for the initial leg configuration.

3.2.2 RESULTS: SKIN STRAIN FIELD OF THE LEG DURING KNEE FLEXION

The first section of this chapter explained how data from 3D laser scans of a human leg determined the global surface area and volume changes that must be accommodated by mechanical counter pressure. In the second experiment described, the object of analysis was a *membrane* rather than a *volume*; this experiment studied the local deformation of the membrane that envelops the leg volume. By tracking the knee-flexion-induced displacement of specific points on the surface of the leg, the three components of the orthogonal strain tensor and the directions of minimum stretch were computed for a representative sample of leg skin points. In other words, the experiment measured the stretch, contraction, and distortion of the leg skin during knee bends. By implementing the algorithm described in the preceding Methods section, leg skin strain was characterized in an efficient and repeatable manner.

In brief, the results of the skin strain analysis indicate that most of the leg skin undergoes less than 30% contraction or extension during knee flexion from 0 to 90 degrees. The experimental results indicate that the skin at 88% of the trackers experiences between −0.3 and 0.3 strain, and the skin at 94% of the tracked locations on the leg experiences between −0.4 and 0.4 skin strain. As expected, the highest longitudinal strains were found at the anterior and posterior surface of the knee. The largest circumferential and shear strains, which are less intuitively predictable, were found mainly at the anterior surface of the knee and over the gastrocnemius (calf) muscle of the lower leg. Lines of *zero* normal strain, or zero stretch, were found at 63% of the tracked points, but were noticeably absent at the patella, the hollow of the knee, and the gastrocnemius

muscle. Lines of *minimum* stretch were found at all points, and they suggest a minimum-strain-energy weave orientation for the fibers of a skintight garment.

The following sections display the data for each of the three strain tensor components, highlight the most important results, and display the resulting lines of minimum stretch. The *corrected* strain data are shown here; the uncorrected results are included in Appendix E. Grayscale versions of Figures 3.16, 3.17, and 3.18 are provided in Appendix F.

LONGITUDINAL STRETCHING – Figure 3.16 shows the magnitude of the longitudinal normal strain during knee flexion at all of the tracked locations on the surface of the leg. The results of the strain field computations indicate that the largest stretch of the leg skin in the longitudinal direction occurs in the region under and just above the patella. The highest decile of longitudinal strains is found in this region, with values ranging from 0.30 strain 6 cm above and inside of the patella to a high of 0.70 strain 9 cm below the knee cap. The lowest decile of longitudinal strains (the greatest contractions) occur over the back of the knee, in the range from -0.25 to 0.59.

CIRCUMFERENTIAL STRETCHING – Figure 3.17 illustrates the magnitude of the circumferential, or "hoop," strain at each tracked point on the leg skin surface. These results are more difficult to predict intuitively and also more subject to error from the uncertainties of the data collection process. Of the circumferential strain results, 6% required correction. Of the top decile of the corrected circumferential strain values, all but one are on the medial surface of the leg and below the patella. Values in this decile range from 0.31 to 0.99 strain. The circumferential strain values in the lowest decile (the most contraction around the leg circumference) occur mostly at the lower posterior surface, over the lower portion of the flexor digitorum longus (medial shin) muscle. The values in this decile range from –0.15 to 0.69 strain. Circumferential strain is close to zero for most of the posterior and medial surface of the leg, with the exception of the region over the gastrocnemius (calf) muscle, where substantial stretching occurs.

ANGULAR DISTORTION - Finally, Figure 3.18 shows the magnitude of the engineering shear strain overlaid at the tracked points. Note that these magnitudes represent the value of engineering shear strain; true angular distortion strain is half of this value. The top decile of shear strain values are distributed over the entire leg. The values in this decile range from 0.13 to 0.54 engineering shear strain, which is equivalent to 0.065 to 0.27 true angle distortion. The values in the lowest decile of shear strain range from –0.13 to –0.75 engineering shear strain, which is equivalent to –0.065 to –0.38 true angle distortion.

Table 3.3 lists the mean, median, and standard deviation of the distribution of measurements for each strain component. The distribution of longitudinal strain measurements has the largest variance and the lowest percentage (46%) of measurements within 0.1 strain units of zero. Of the circumferential strain measurements, 62% are between -0.1 and 0.1 strain. The shear strain measurements have a much narrower distribution, with 76% within 0.1 strain units of zero. A more comprehensive picture of the strain distributions is provided in Figure 3.19.

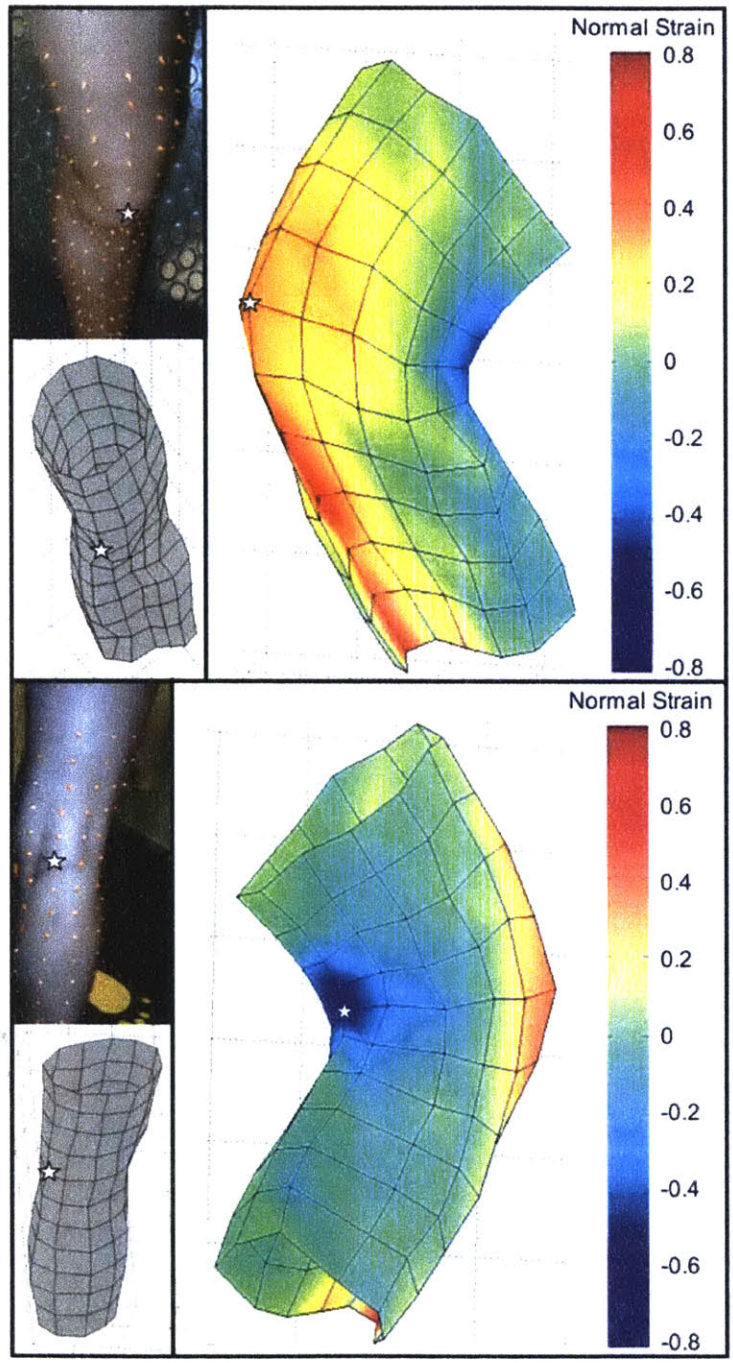

Figure 3.16 Longitudinal strain of the leg skin during knee flexion. Strain data are displayed on a snapshot of a 3D reconstruction of the deformed position of each tracked point, with the magnitude of the longitudinal strain represented by the color of the surface surrounding each point. On the sides are photos and 3D reconstructions of the leg in its 0-degree state. Light green represents zero strain, while yellow represents 20% stretch, and cyan represents 20% contraction. The stars indicate the location of the patella and knee hollow, respectively.

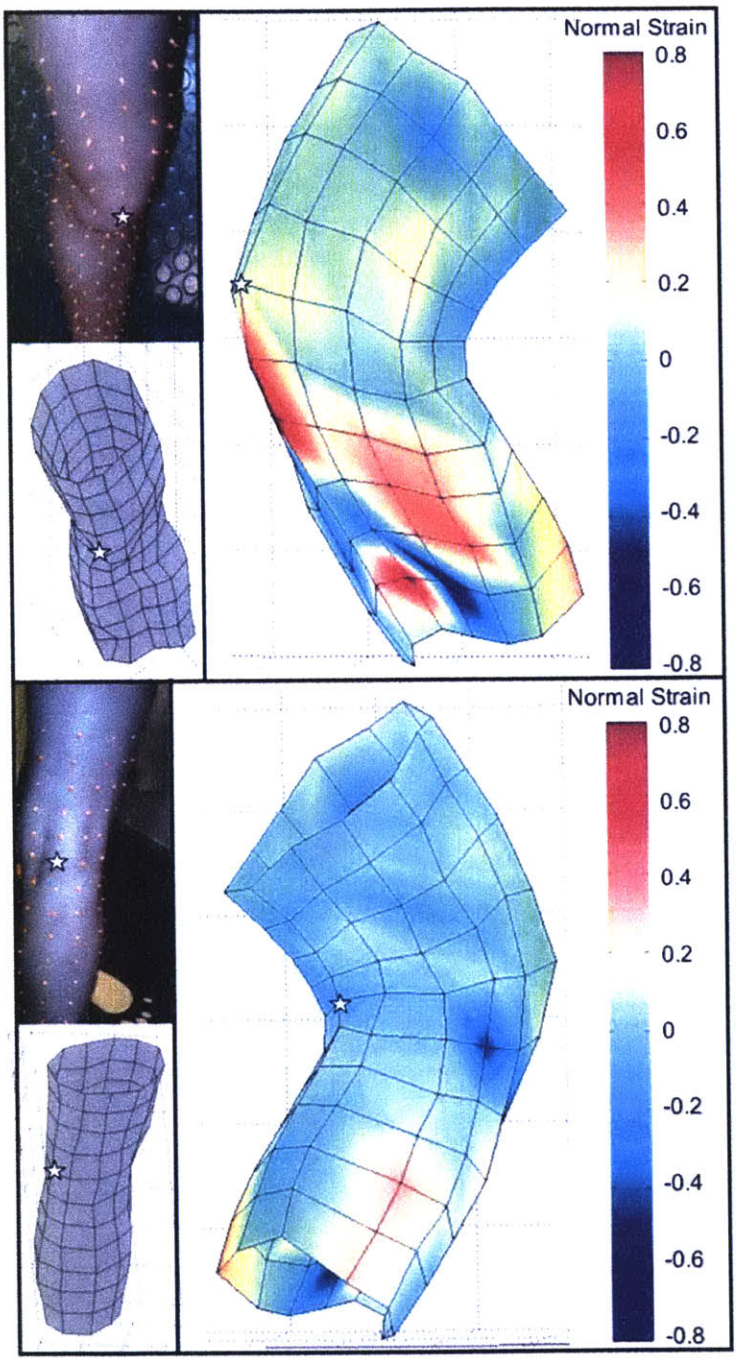

Figure 3.17 Circumferential strain of the leg skin during knee flexion. Strain data are displayed on a snapshot of a 3D reconstruction of the deformed position of each tracked point, with the magnitude of the circumferential strain represented by the color of the surface surrounding each point. On the sides are photos and 3D reconstructions of the leg in its initial 0-degree state. Light green represents zero strain, while yellow represents about 20% stretch, and cyan represents 20% contraction. The stars indicate the location of the patella or knee hollow, respectively.

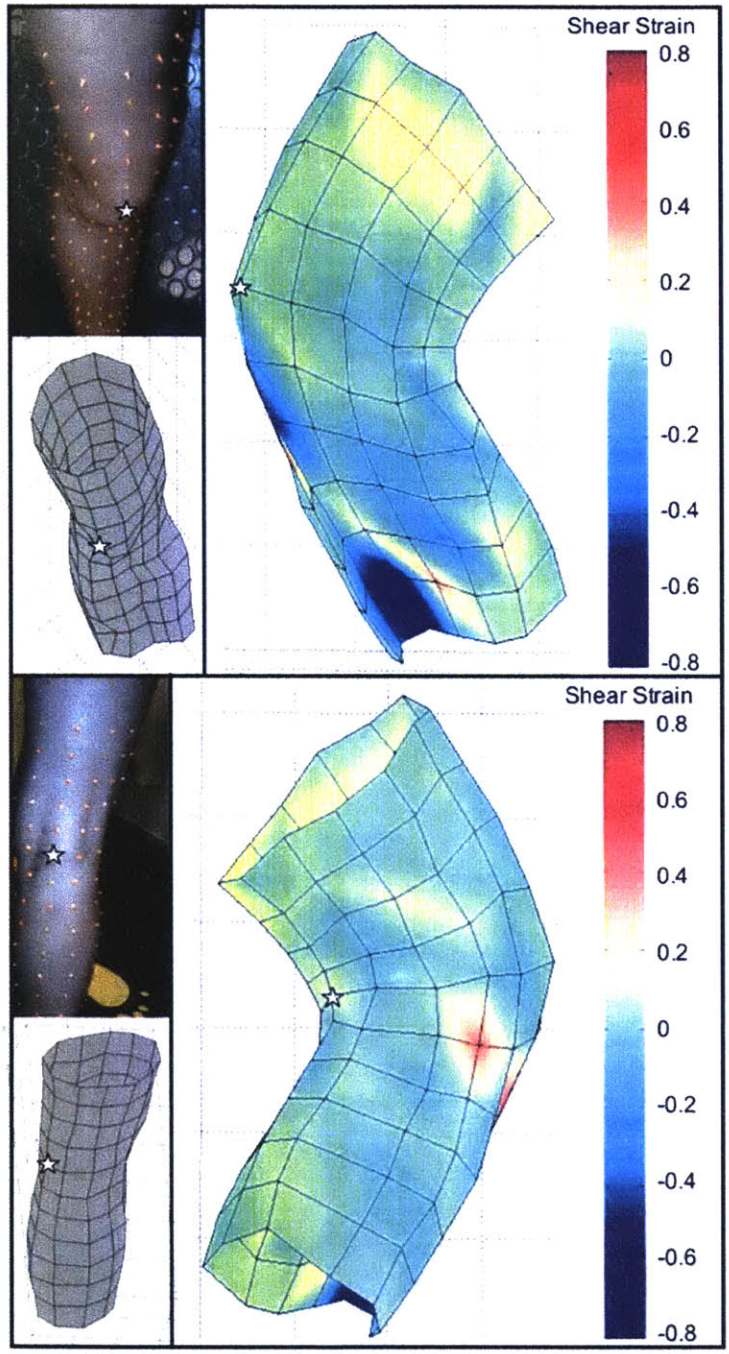

Figure 3.18 Engineering shear strain of the leg skin during knee flexion. Strain data are displayed on a snapshot of a 3D reconstruction of the deformed position of each tracked point, with the magnitude of the longitudinal strain represented by the color of the surface surrounding each point. On the sides are photos and 3D reconstructions of the leg in its initial 0-degree state. Light green represents zero strain, while yellow represents about 20% stretch, and cyan represents about 20% contraction. The stars indicate the location of the patella and knee hollow, respectively.

Table 3.3 Summary statistics and percentage of strain measurements with absolute value less than 0.1, 0.3, and 0.4.

Strain Type	Median Strain Magnitude	Standard Deviation	% of Measurements Between -0.4 and 0.4	% of Measurements Between -0.3 and 0.3	% of Measurements Between -0.1 and 0.1
Longitudinal	-0.001	0.213	93%	84%	46%
Circumferential	0.023	0.206	93%	86%	62%
Shear	0.007	0.158	95%	93%	76%
All Components	0.012	0.194	94%	88%	61%

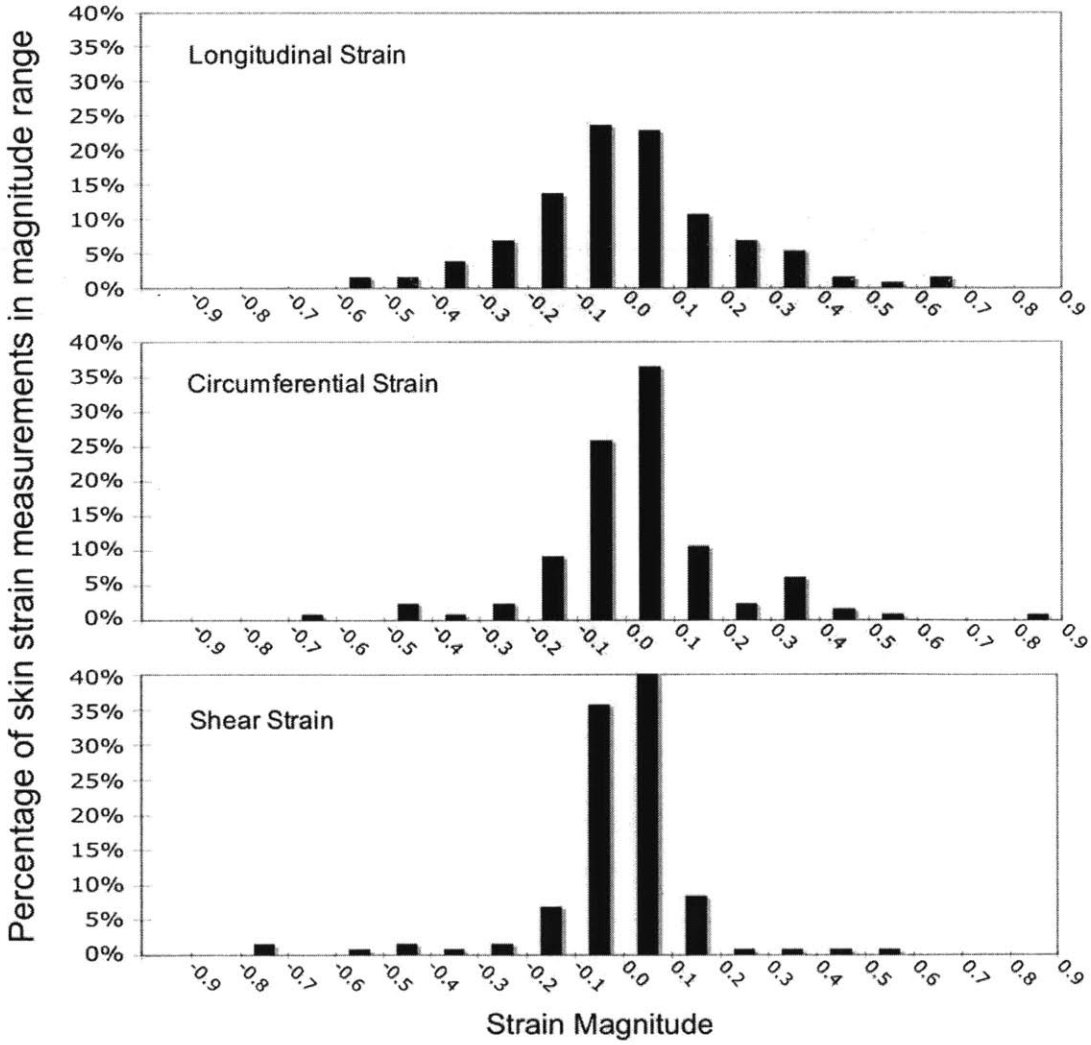

Figure 3.19 Distributions of strain magnitudes for each component of orthogonal strain tensor.

For the data analyzed in this study, the largest stretch of the leg skin in the longitudinal direction occurs 3 cm to 9 cm below the patella; longitudinal normal strain magnitudes in this region range from 0.30 to 0.70. The largest stretching in the circumferential direction occurs on the anterior surface 3 cm below the patella and on the medial surface of the mid-calf, with normal strain values of 0.99 and 0.80, respectively. Shear strain, or angular distortion of the skin, is near zero for most of the anterior and posterior surfaces of the leg. Appendix F lists all the strain data, as well as the magnitude and location of the highest and lowest deciles of strain, for each of the three strain tensor components.

Eigenvalue analysis and strain ellipse equations transform the orthogonal strain components into principal and minimum stretch directions. Illustrated in Figures 3.20 and 3.21, the set of minimum stretch directions suggests the "pattern" or "weave" direction of the tensile fibers of the spacesuit. Proper fiber patterning will allow for maximum mobility and ease of locomotion, which are essential requirements for advanced spacesuit designs for future missions to the moon or Mars.

This chapter has described how laser scanning technology can be used to measure the effect of knee flexion on leg surface area, volume, skin strain, and stretching direction. The experiment described in the first section of the chapter revealed that while the overall leg surface area and volume remain constant during knee flexion, a substantial decrease occurs in the surface area and volume of the knee segment alone. For the subject in this pilot study, the knee surface area decreased by 16% during 90-degree knee flexion, and the knee volume decreased by 18%. The analysis described in the second section of this chapter demonstrated that laser scans can also be used as a tool for digital strain analysis, and that the leg skin strain induced by knee flexion is highest over the patella, knee hollow, and calf muscles. The second section of this chapter also demonstrated the use of skin strain analysis to determine directions of minimum normal strain. These lines of minimum stretch were found wherever strain was measured. In the next chapter, these lines of minimum stretch and other human body shape analyses are translated into designs for mobile mechanical counter pressure spacesuits.

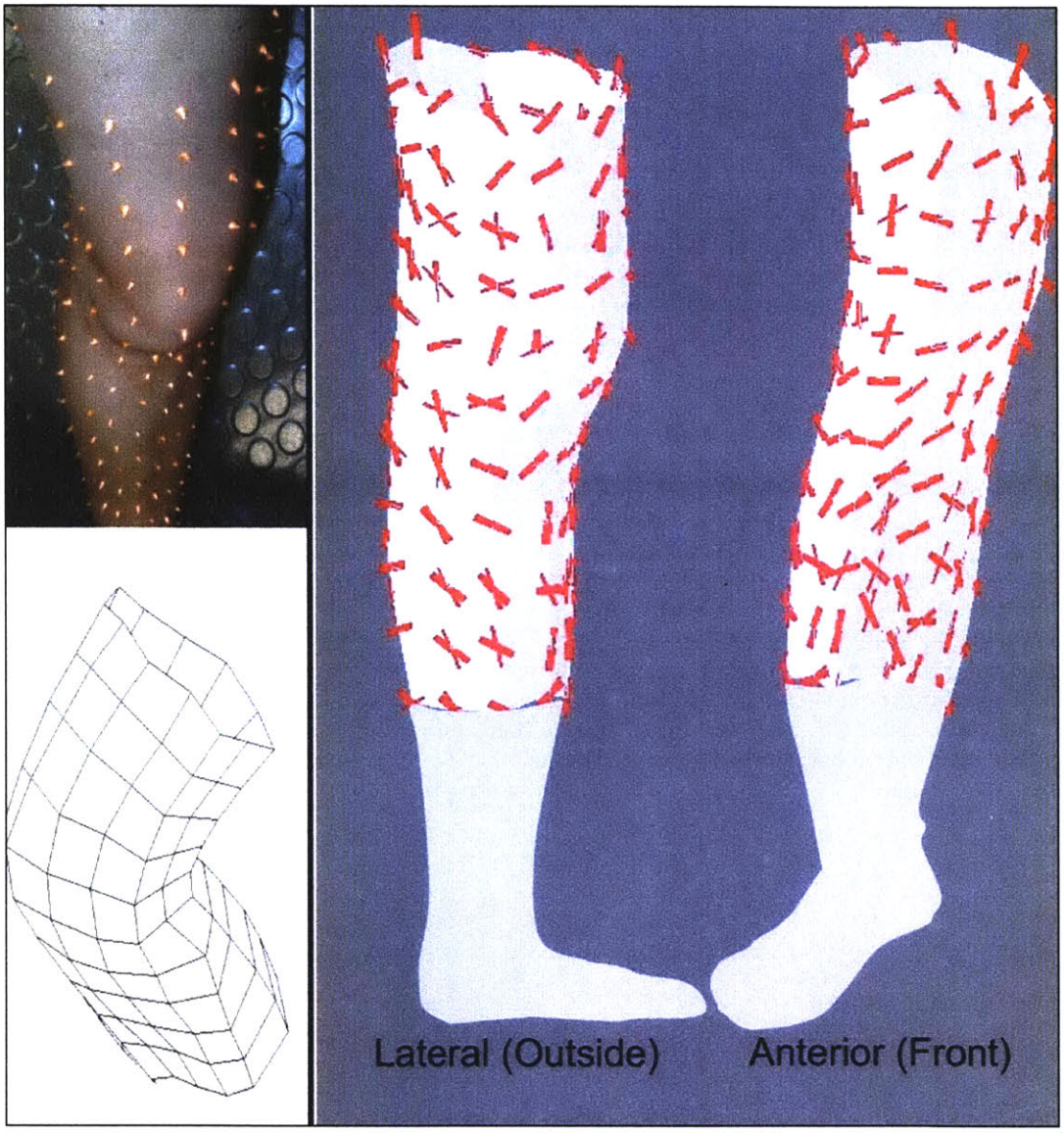

Figure 3.20 Orientation of the lines of minimum stretch on the lateral and anterior leg surfaces. Indicated by the short thick lines at each row and column intersection on the leg surface, the lines point in the direction in which the skin stretches and contracts the least during knee flexion. Where two intersecting thick lines appear together, directions of zero stretch were found. Where one thick line appears alone, only a direction of minimum stretch was found. For reference, the photos on the sides of the figure show the actual appearance of the leg at 0-degree knee flexion, and the reconstructions show the appearance of the leg at 90-degree knee flexion.

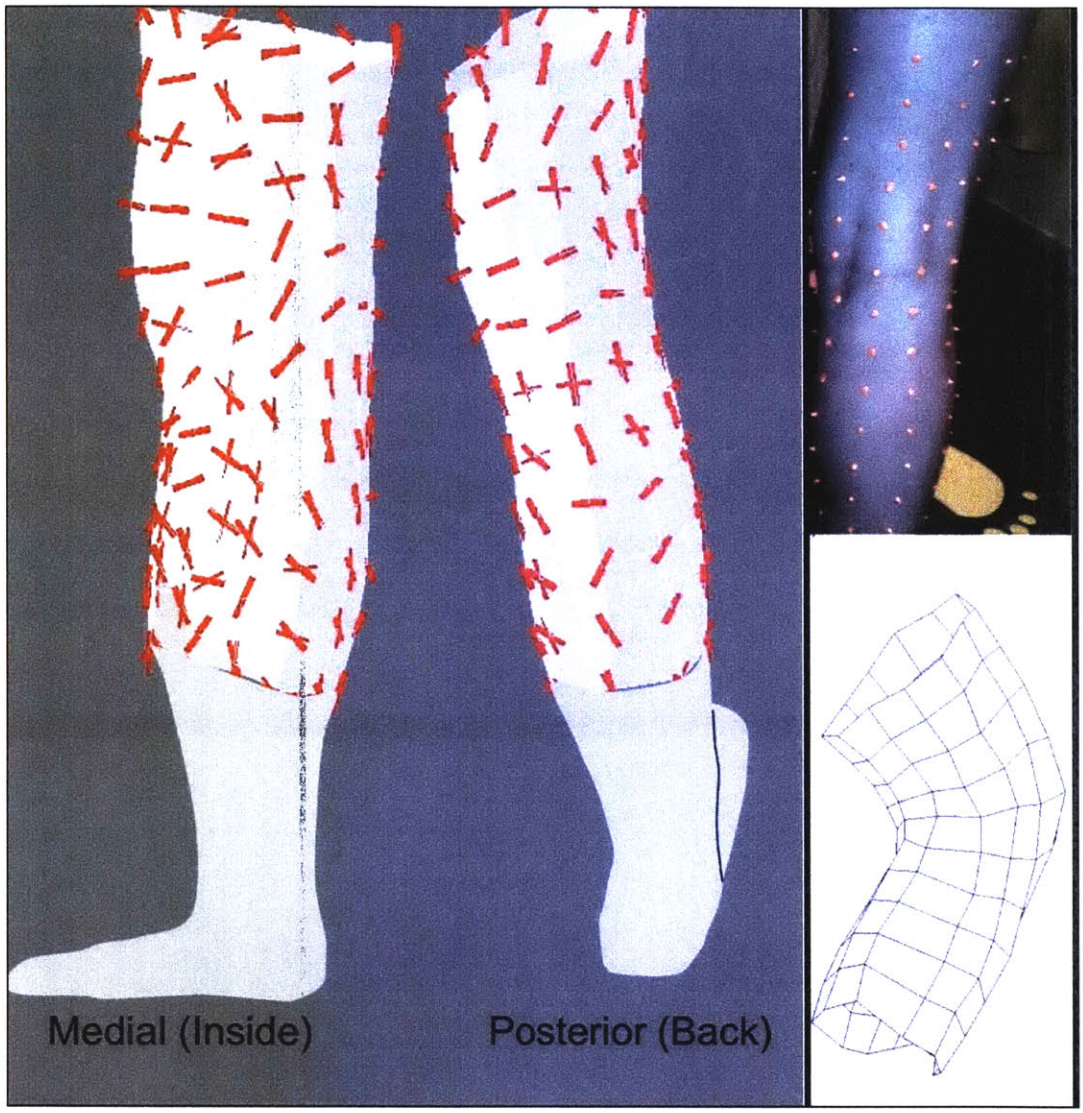

Figure 3.21 Orientation of the lines of minimum stretch on the medial and posterior leg surfaces. Indicated by the short thick lines at each row and column intersection on the leg surface, the lines point in the direction in which the skin stretches and contracts the least during knee flexion. Where two intersecting thick lines appear together, directions of *zero* stretch were found. Where one thick line appears alone, only a direction of *minimum* stretch was found. For reference, the photos on the sides of the figure show the actual appearance of the leg at 0-degree knee flexion, and the reconstructions show the appearance of the leg at 90-degree knee flexion.

Chapter 3 References

1. Crandall, S.H., Lardner, T.J., Dahl, N.C. *An Introduction to the Mechanics of Solids*. McGraw-Hill, 1978.
2. Helm, J.D., McNeill, S.R., Sutton, M.A. "Improved three-dimensional image correlation for surface displacement measurement." *Optical Engineering*. Vol. 35, No. 7, July 1996, p. 1911-1920.
3. Hannah, R.L., Reed, S.E., Eds. *Strain Gage Users' Handbook*. New York, Elsevier Applied Science, 1992.
4. McMahon, T.A. *Muscles, Reflexes, and Locomotion*. Princeton University Press, Princeton, NJ, 1984.
5. National Aeronautics and Space Administration. *Manned System Integrations Standards* [NASA-STD-3000], Revision B, Volume I. NASA, 1995.
6. National Center for Health Statistics. Anthropometric Reference Data, United States, 1988 – 1994. *NHANES III Data*, 2003. http://www.cdc.gov/nchs/about/major/nhanes/Anthropometric%20Measures.htm. Last accessed 1 May 2005.
7. Ramsay, J., Huber, M. *Modern Structural Geology, Volume 1: Strain Analysis*. Academic Press, New York, 1983.
8. Ramsay, J., Lisle, R. *Modern Structural Geology, Volume 3: Applications of continuum mechanics in structural geology*. Academic Press, New York, 2000.

CHAPTER 4: DESIGNING AND PROTOTYPING MECHANICAL COUNTER PRESSURE SUITS BASED ON THE CHANGING LEG SHAPE

Leg shape and skin strain information, analyzed via the methods of Chapter 3, can be translated into specifications for custom-fit mobile mechanical counter pressure (MCP) leg garments. This chapter describes the design, construction, and testing of two different MCP leg prototypes that utilize dynamic body shape change information. The first is a shape-responsive hybrid leg garment that provides pressure to the leg through a low-profile urethane foam bladder and a conformal stretch-resistant restraint layer. The second prototype is a true MCP skintight garment made out of high-strength nylon fibers oriented in the directions of minimum skin stretch. It should be noted that schedule constraints necessitated that prototype construction begin before finalization of the 3D anthropometry results; consequently, these two prototypes were inspired by, but not directly derived from, the results described in Chapter 3. The hybrid prototype relied instead on estimated changes in leg cross-sectional diameter during knee flexion. The nylon fiber prototype relied on Iberall's description of the lines of non-extension rather than on the directions of minimum stretch depicted in Chapter 3. Accordingly, the research presented in Chapter 3 is best described as the development of a *technique* or process for specifying MCP suit designs. The prototyping methods and results of Chapter 4 are examples of efforts that will be made much more efficient and robust in the future by the technique developed in Chapter 3. The technique was not defined in time for this thesis's cycle of prototyping.

4.1 SHAPE-RESPONSIVE HYBRID MCP LEG GARMENT

Previous research showed that counter pressure can be exerted on the lower leg through a hybrid design that combines gas pressure and mechanical tension [Pitts, 2003; Newman, Bethke, Carr, Hoffman, & Trotti, 2004]. Particular success was achieved with a lower-leg implementation of a paint-on urethane layered foam concept [Newman et al., 2004]. In addition to producing sufficient mechanical counter pressure (~ 30 kPa), this prototype illustrated the merits of "paint-on" construction, which is the application of the spacesuit material directly to an exact replica of the wearer's body. To construct the garment, laminated strips of open-cell foam were sandwiched between painted-on urethane layers, resulting in a highly flexible garment that conforms to a mannequin's lower leg (Figure 4.1). The layered foam design applied mechanical counter pressure to the leg with the desired 1:1 input-to-output pressure ratio (Figure 4.2). These results were much improved from earlier attempts to pressurize the lower leg with a single column of air rather than a continuous foam bladder (Figure 4.3).

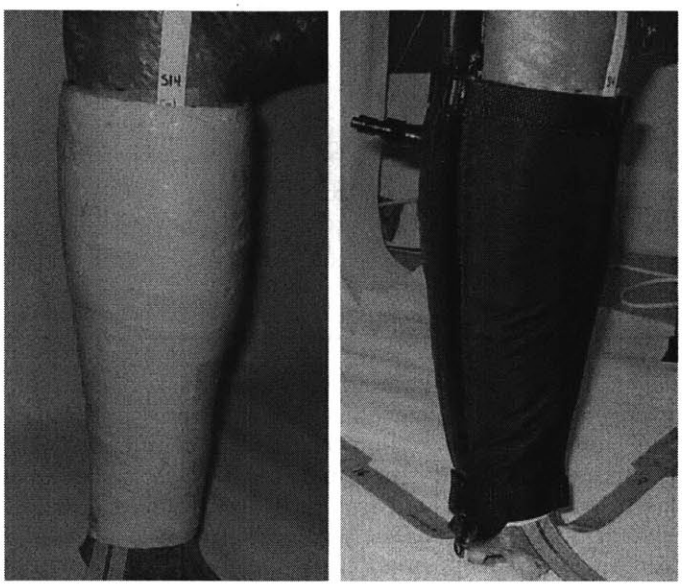

Figure 4.1 The urethane foam MCP prototype for the lower leg consists of two layers. (Left) To create the pressurizing layer, urethane open cell foam is sealed between two layers of paint-on urethane. (Right) A custom-fit inextensible restraint layer prevents the foam bladder from expanding outward.

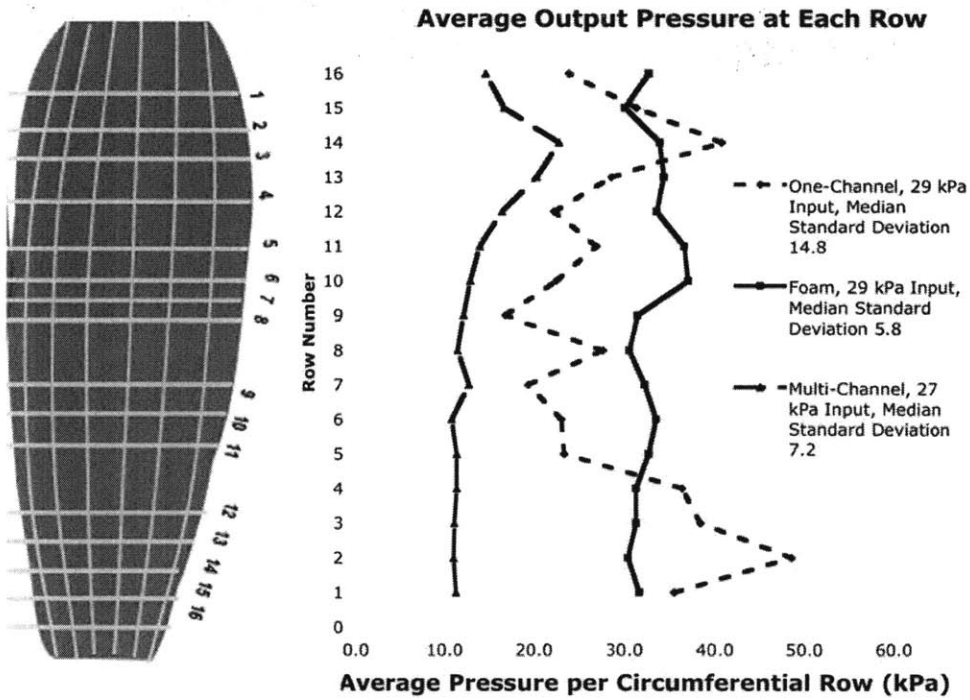

Figure 4.2 Row-average MCP results for tests of the lower leg urethane-foam prototype, as well as two previous lower leg hybrid prototypes, on a full-scale leg replica. Average leg surface pressure for each circumferential row is shown in kPa. Results are shown for bladder input pressures of 27 kPa (205 mmHg, 4.0 psi) and 29 kPa (220 mmHg, 4.3 psi). The urethane-foam prototype achieved the desired 1:1 input-to-output pressure ratio and produced the most even pressure distribution of all three lower leg prototypes.

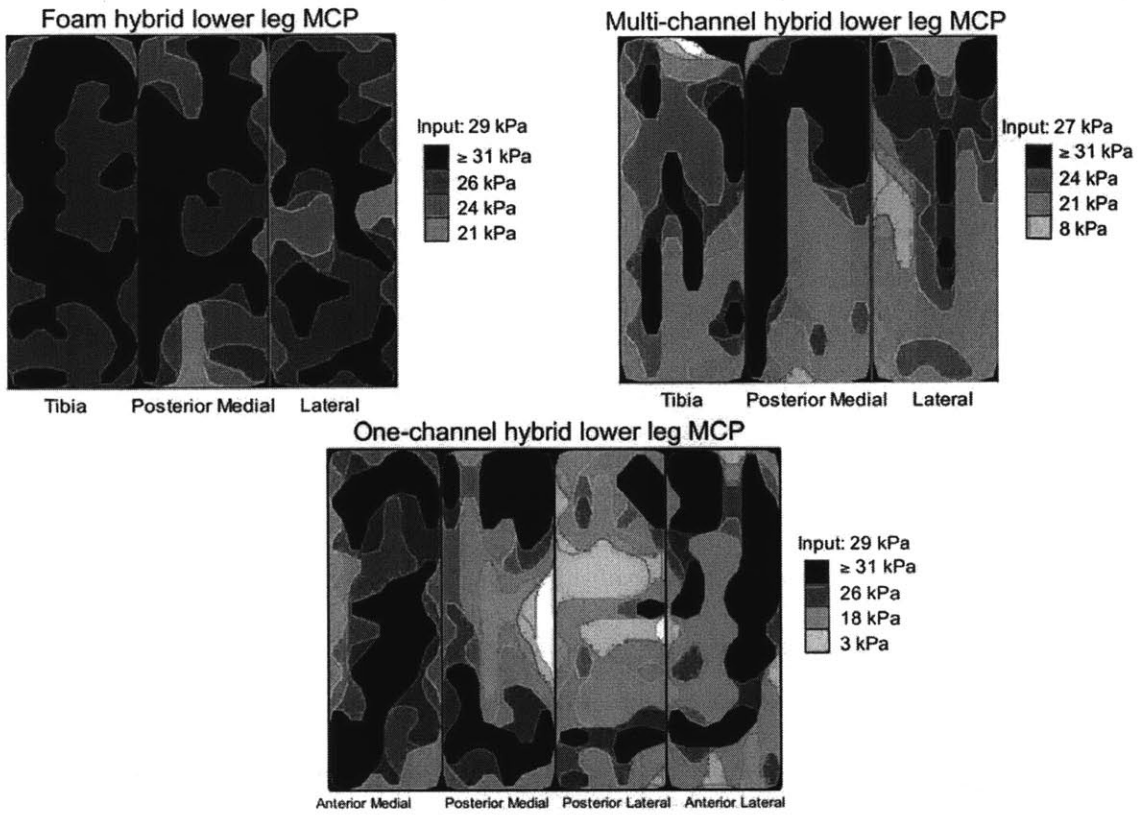

Figure 4.3 Pressure production on the surface of 3D leg replica for three different hybrid MCP lower leg prototypes. The urethane-foam prototype generated surface pressure with greater magnitude and less spatial variation than the channel prototypes.

The purpose of the shape-responsive hybrid MCP prototyping effort is to determine if the hybrid technique can apply counter pressure to the entire leg, including the knee, while still allowing for mobility. The following sections describe the design, construction, and testing of a shape-responsive hybrid concept for full-leg MCP. A hybrid combination of gas pressure and inextensible fabric generates mechanical counter pressure on the surface of the leg. The prototype covers the entire length of the leg and consists of a open-cell foam air bladder surrounded by an stretch-resistant restraint layer that is designed to respond to changes in leg shape. When the body-hugging foam bladder is inflated with air, the surrounding restraint layer prevents the bladder's expansion. The inner layer of the bladder then pushes back against the wearer's skin, and mechanical counter pressure is achieved.

4.1.1 DESIGNING THE FULL-LEG URETHANE FOAM BLADDER

The concept for hybrid MCP relies on the inflation of a pressure bladder underneath a restraint layer, which then transfers pressure back onto the wearer's skin. This method could conceivably be implemented for the entire body, but in this current effort only the leg was studied. The following paragraph proposes a design for the pressure bladder portion of a full-leg shape-responsive MCP garment.

> *The desired result is a form-fitting pressure bladder that envelops the entire leg and maintains a constant thickness from the leg during locomotion. The air or gas in the bladder does not come into contact with the wearer's skin, as the bladder is sealed on both the surface near the skin and the surface towards the outside environment. To ensure that the bladder conforms to the wearer's leg, the bladder is molded to a full-scale three-dimensional replica of the wearer's leg. The inclusion of a compressible internal support structure within the bladder mandates the smallest possible separation between the leg surface and the bladder's outer surface. Brushable, paint-on urethane provides the material for the bladder's surfaces, and open-cell urethane foam provides structural support within the bladder.*

4.1.2 DESIGNING THE SHAPE-RESPONSIVE RESTRAINT LAYER

The following paragraph describes the design of the restraint layer portion of the full-leg shape-responsive MCP suit.

> *The intended purpose of the shape-responsive restraint layer is to constrain the foam pressure bladder from all outward expansion except at specific locations where the leg surface is known to deform during locomotion. At these shape-changing sites, extra separation is added in between the unpressurized bladder and the restraint layer, such that before pressurization, gaps exist between the outer layer of the bladder and the inside of the restraint layer at certain locations. The rationale for these expansion gaps is that they provide the leg with space in which to deform during knee flexion, so that the overall volume encased between the leg skin surface and the restraint layer remains constant. If a constant pressure suit can be constructed so that it remains at constant volume, the wearer can move freely without exerting extra work against the pressurized gas.*

4.1.3 CONSTRUCTING THE SHAPE-RESPONSIVE HYBRID MCP PROTOTYPE

The designs explained above were implemented to create an actual full-leg prototype of the shape-responsive hybrid MCP concept. A urethane foam pressure bladder and a custom-patterned restraint layer comprise the full-leg prototype. In the following sections, the procedures for constructing the pressure bladder and the restraint layer are outlined.

The pressure bladder consists of two paper-thin layers of brush-on urethane, sandwiching a constant-thickness layer of open cell urethane foam. The inner layer of urethane is 0.5 mm thick, the foam is 7 mm thick, and the outer layer of urethane is 2 mm thick. Figure 4.4 shows a cross-section of the ankle portion of the bladder.

Figure 4.4 Cross-section of ankle portion of foam air bladder, showing two layers of urethane sandwiching the open-cell foam layer.

The bladder was formed on a full-scale replica of the wearer's leg, positioned at a 30-degree knee flexion angle (Figure 4.5). This replica was built using a Z Corp three-dimensional printer (Z Corporation, Burlington, MA), which physically reconstructed virtual solid models of the leg that had been captured by a whole-body laser scanner. Appendix G describes in more detail the process for building full-scale leg replicas.

Figure 4.5 Full-scale 3D leg replicas, created with Z Corp 3D Printer. (Left) 30-degree knee flexion replica. (Right) 90-degree knee flexion replica.

The inner urethane layer was formed by painting brush-on urethane directly onto the leg replica. Before this urethane cured, strips of the 7-mm foam were affixed on top of the urethane layer. Finally, the outer layer of urethane was painted onto the foam, creating an airtight seal over the entire surface of the leg. The bladder extends from the mid-thigh, 12 cm above the patella, to the top of the ankle, 18 cm below the patella. Figure 4.6 shows the three stages of bladder construction, beginning with the application of the inner urethane layer to the leg replica surface.

Figure 4.6 Urethane-foam pressure bladder construction. From left to right: First coating of urethane on full-scale leg replica; open-cell foam to maintain bladder thickness; second coating of urethane to seal foam bladder.

To create the restraint layer, the bladder was first modified by temporarily adding 2.5 cm by 2.5 cm foam tiles of varying thickness at certain locations. A pattern for the restraint layer was then constructed to conform exactly to the shape of this modified bladder, and textile pieces were cut to match the pattern.

These additional "placeholder" foam tiles were placed according to the magnitude and location of the shape changes of the leg during knee flexion from 30 degrees to 90 degrees. To determine these leg shape changes, the 30-degree knee flexion leg replica was compared to a replica of the leg at a 90-degree knee flexion angle. Both leg replicas were marked off at 3-cm intervals down the long axis of the leg, forming ten 3-cm bands, and the circumference of each band was measured. For each band, the increase in diameter indicated the required separation between the outer bladder surface and the inner restraint layer surface at the location of that band. Temporary foam tiles, of thickness equal to the diameter increase, were placed on top of the outer bladder surface to hold the place of this shape-change separation. The thickness of these foam tiles corresponded to the increase in diameter at the given segment of the leg. The tiles were placed at the location on that segment that seemed most anatomically appropriate. For example, for the segment at mid-calf height, the placeholder foam tiles were placed on the posterior surface of the leg, were the gastrocnemius muscle bulges outward during knee flexion. Similarly, for the segment around the knee, the placeholder foam tiles were placed on the posterior surface of the knee where the hamstring tendons push outward during knee flexion. The shaded segments in the diagrams of Figure 4.7 indicate where extra separation was placed between the bladder and the restraint layer.

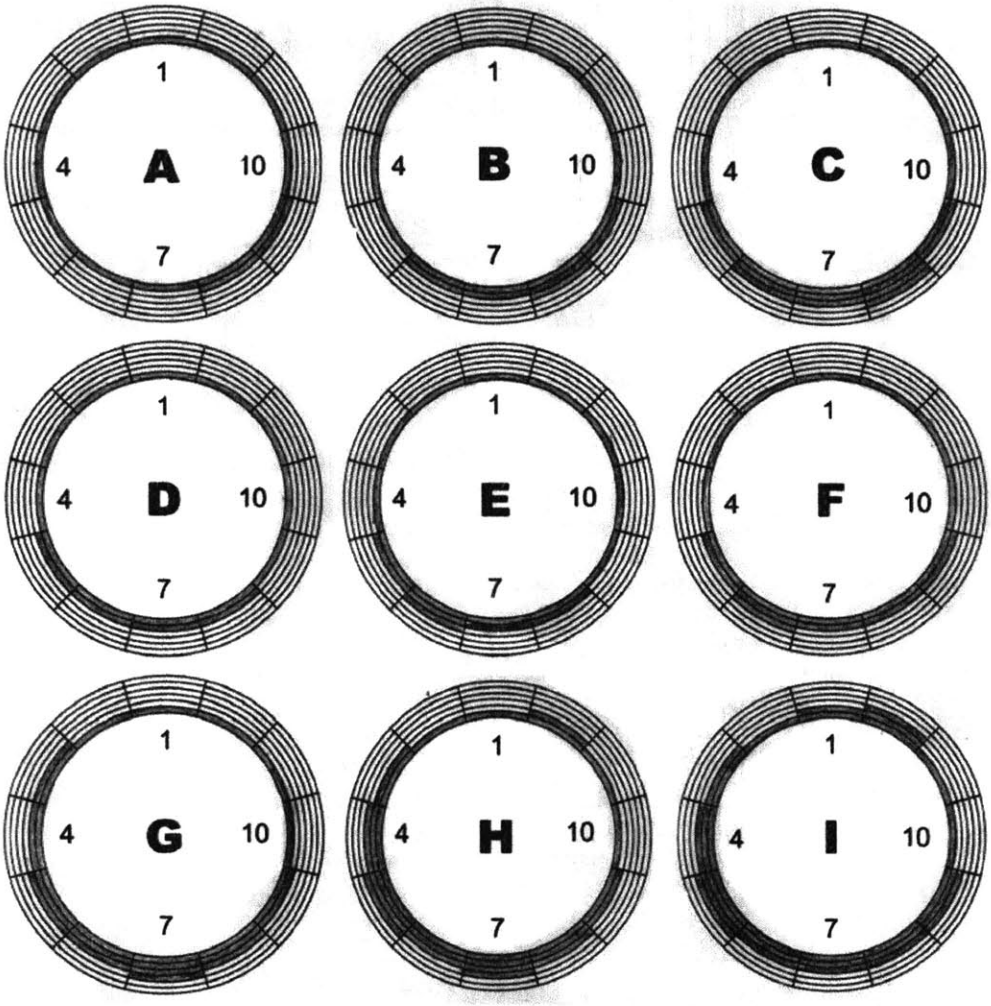

Figure 4.7. Leg cross sections with shaded blocks that show the location of additional tiles needed between the pressure bladder and restraint layer. The innermost circle represents the bladder outer surface. Letters A through I indicate the height of the leg cross-section which each diagram represents; "A" falls at the upper thigh with each subsequent cross-section 3 cm closer to the ankle.

After placing these placeholder foam tiles on top of the bladder, which was covering the 30-degree leg replica, a restraint layer was fashioned to fit exactly to the bladder plus extra tiles (Figure 4.8). The restraint layer consists of anisotropic sailcloth textiles (Dimension-Polyant, Inc., Putnam, CT) oriented so that the garment is extremely stretch resistant in the circumferential direction but just flexible enough in the longitudinal direction to allow for the full range of knee flexion.

Figure 4.9 shows the lateral and posterior surface of the non-inflated pressure bladder, surrounded by the unzipped restraint layer, as well as the restraint layer zipped over the inflated pressure bladder.

Figure 4.8 Development of the restraint layer pattern. (Left and center) Placeholder foam tiles temporarily pasted to the pressure bladder. (Right) Pattern created directly from the leg replica plus bladder and extra tiles.

Figure 4.9 (Left) Lateral-posterior view of foam air bladder, resting on unzipped restraint layer. The slight bend in the bladder reveals that it was formed on a leg replica positioned at a 30-degree knee angle. (Right) Completed restraint layer, zipped on a 3D replica of the subject's leg.

4.1.4 TESTING THE SHAPE-RESPONSIVE HYBRID MCP PROTOTYPE

DONNING AND DOFFING – Several techniques for donning and doffing the bladder and restraint layer were attempted, and the most successful method is described here and shown in Figure 4.10. To ease the donning process, the subject first donned a smooth low-power nylon stocking that had been coated with talcum powder. After turning the urethane bladder inside out, the subject inserted her foot directly into the ankle opening of the bladder, instead of first passing through the upper leg portions. Since the urethane foam is resistant to stretching, and the heel diameter is much larger than the ankle diameter, this was the most difficult step. The subject required one assistant to stretch the ankle opening as wide as possible and a second assistant to provide stability and balance. After the foot and heel passed through the ankle opening, the bladder was turned right side out, slowly making its way up to meet the rest of the leg surface. In total, five to ten minutes are required to apply the urethane bladder.

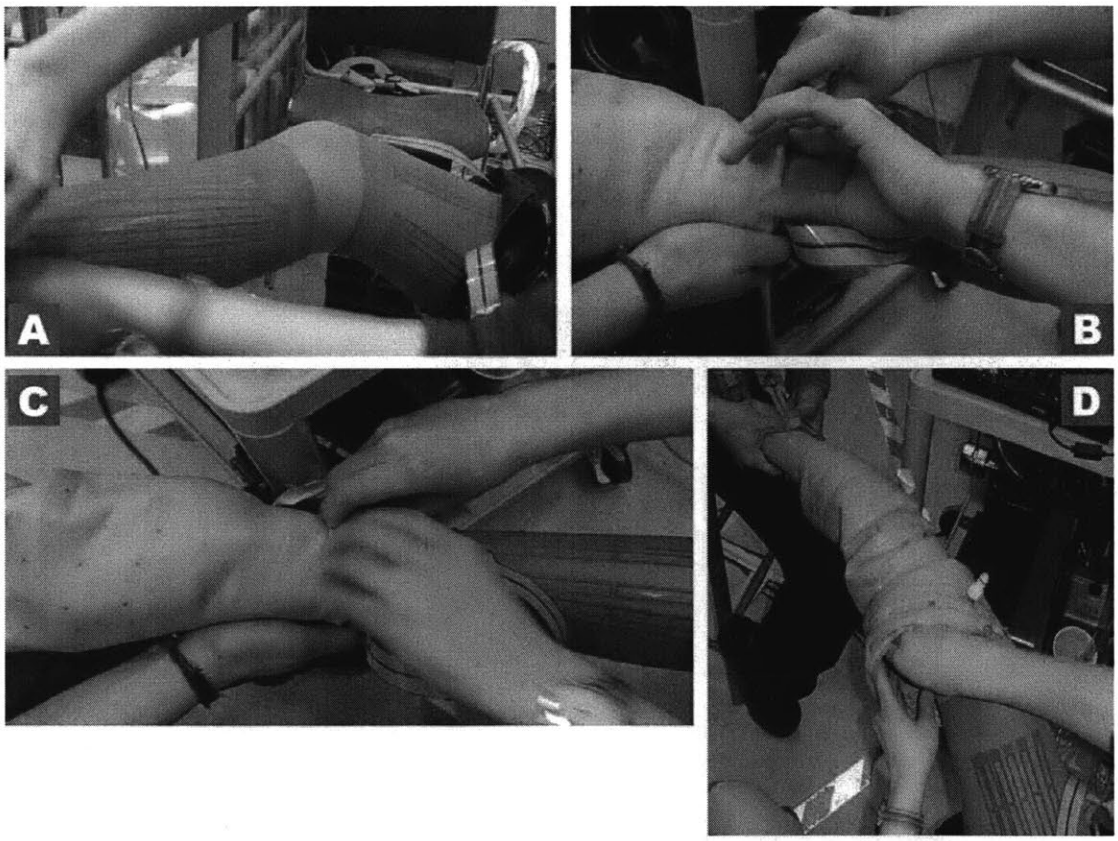

Figure 4.10 Doning the full-leg foam bladder over pressure sensor and comfort layers. (A) Tekscan pressure sensors strips located on the thigh and calf to measure MCP generated on the skin. The sensors consist of six columns; each column consists of 16 individual pressure-sensing elements, or sensels. (B, C) The bladder must be turned inside out so that the ankle opening is pulled over the heel first. (D) After the ankle opening passes over the heel, the bladder is turned right side out over the rest of the leg.

To apply the restraint layer, the subject also required two assistants. One assistant compressed the foam and held the restraint layer closed, while the other assistant pulled the zipper closed. Due to poor fit around the lower leg, it was impossible to zip the restraint layer all the way down to the ankle. To protect the bottom 3 cm of the bladder, it was wrapped tightly with stretch-

resistant Velcro straps. It took an additional three to five minutes to don the restraint layer, resulting in an eight-to-fifteen minute donning time for the entire hybrid prototype.

Unzipping and removing the restraint layer was easy, and the subject completed this step without assistance. However, removal of the urethane bladder was as difficult as pulling it on. First, the thigh, knee, and calf portions were pulled downwards, to turn the bladder inside out again. When the reversed bladder was suspended from the ankle, then one assistant stretched open the ankle opening while the other assistant helped the subject remove her foot and heel. The subject felt slight pain during this process due to pinching of the skin and contortion of the foot and ankle.

DURABILITY – The hybrid prototype was donned a total of five times, and each trial created new holes and cracks in the inner and outer urethane layers. The urethane was extremely stressed by the pulling and twisting that are a necessary part of fitting the ankle opening over the wearer's heel. The third doffing process caused a 10-cm tear approximately 2.5 cm from the ankle opening of the bladder (Figure 4.11). To address this problem, the bottom 2.5 cm of the bladder were removed, and the bottom surface was resealed. Tears of less than 1 cm were sealed with Aqua Seal or Seam Grip, both commercially available urethane sealers (McNett Corporation, Bellingham, WA). After sealing all of the visible tears, the bladder still leaked with a pressure-loss rate of approximately 10 mmHg (1.3 kPa, 0.19 psi) per second.

Pressurization also stressed the urethane bladder. At the locations where the restraint layer did not fit snugly to the bladder, the bladder expanded, stretching the urethane. Both attempts to pressurize the bladder beyond 20 kPa (150 mmHg, 2.9 psi) caused sudden rips in the inner urethane layer at the front of the thigh.

Figure 4.11 Tear that developed near the urethane bladder ankle opening during the third doffing trial.

SKIN SURFACE PRESSURE - To measure the pressure produced by the prototype on the leg surface, the leg skin was outfitted with six 20-cm by 8-cm (8-inch by 3-inch) paper-thin pressure sensors (Model 9801, Tekscan Inc., South Boston, MA). The locations of the sensors are shown in Figure 4.12. Sensors were placed on the thigh and calf and held in place between a smooth nylon stocking and a nylon sleeve. Acting as a barrier between skin and sensor, and between urethane and sensor, the nylon removed any shear load that might have confounded measurement of the normal pressure load. Pressure measurements were made at ambient conditions with the prototype inflated to a target pressure of 13 kPa (100 mmHg, 1.9 psi). Appendix H includes more details about the pressure sensors.

The average pressure felt under the area of each sensor is indicated in Table 4.1. These results indicate that at the locations of the sensors, the 13 kPa (100 mmHg, 1.9 psi) bladder pressure did not transfer efficiently to surface pressure on the skin. Since the skin pressure was not uniform, the pressure was also not uniform within the bladder. Non-uniform bladder pressure can be explained by the presence of numerous leaks, which caused constant motion of the air and thus variable dynamic pressure. Pressure was high at some locations and very low at other locations, depending on the preferred path of air movement into the valve and out through the leaks.

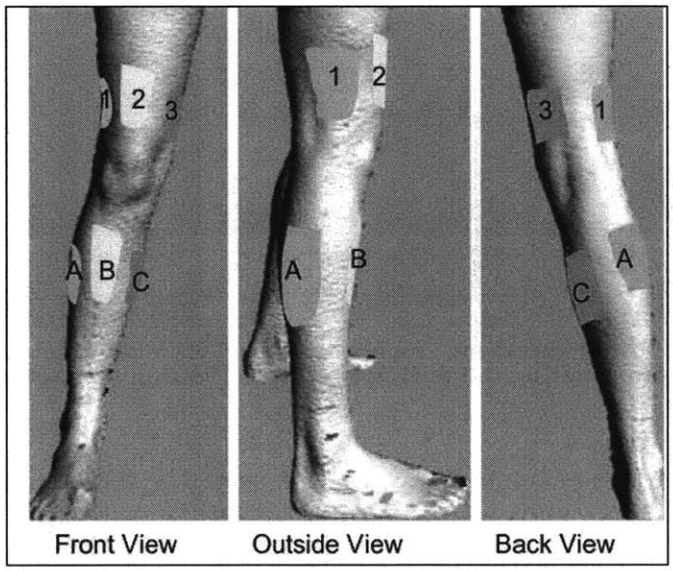

Figure 4.12 Location of six Tekscan pressure sensors. Sensors 1-3 were placed on the thigh; sensors A-C were placed around the calf.

Table 4.1 Average pressure on leg surface for bladder pressure of 13.3 kPa (100 mmHg).

Location	Description	Average Pressure
1	Outside Thigh	3.3 kPa (25 mmHg)
2	Front Thigh	3.1 kPa (23 mmHg)
3	Inside Thigh	0.7 kPa (5 mmHg)
A	Outside Calf	2.8 kPa (21 mmHg)
B	Shin	4.5 kPa (34 mmHg)
C	Inside/Back Calf	3.9 kPa (29 mmHg)

As shown in Figure 4.13, an attempt was made to inflate the prototype to 29 kPa (220 mmHg, 4.3 psi) in the low-pressure leg chamber (Appendix I). However, the high leak rate prevented 29 kPa of pressure from being maintained in bladder. The chamber pressure was then reduced to 13 kPa (100 mmHg, 1.9 psi). With the bladder connected to atmospheric pressure, it was able to maintain only 1.3 to 2.7 kPa (10 to 20 mmHg, 0.19 to 0.39 psi) of pressure. Consequently, the leg skin was feeling an underpressure of 11 kPa (80 mmHg, 1.6 psi). Because several minutes of exposure to this underpressure caused slight pain, tests in the low-pressure chamber were discontinued.

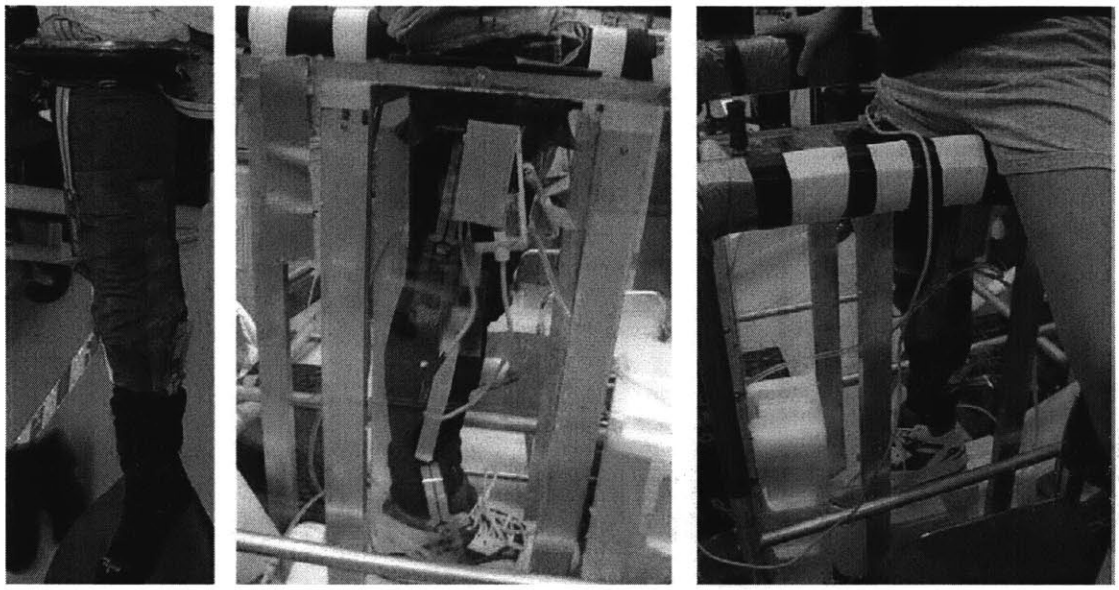

Figure 4.13 Attempt to test the shape responsive hybrid MCP prototype in the low pressure chamber. (Left) Subject wearing full prototype; (Right) Testing the prototype in the custom-built chamber.

MOBILITY AND COMFORT – To study mobility, the subject performed leg exercises with the bladder inflated to 13 kPa (100 mmHg, 1.9 psi). These tests occurred under atmospheric conditions. As the subject performed standing leg lifts (flexing the knee to lift the foot) and squats, her subjective comfort was noted, and her knee angle was measured with a goniometer.

At a bladder pressure of 13 kPa (100 mmHg, 1.9 psi), the subject's knee and calf felt very constricted and uncomfortable. However, the subject felt almost no discomfort around her thigh, where the bladder had wrinkled and migrated towards her knee in the longitudinal direction. The larger diameter of the knee then prevented further downward sliding. This longitudinal compression loosened the garment around the thigh such that the subject could slip her hand between her thigh surface and the inner bladder surface.

Standing leg lift exercises were discontinued at a knee flexion angle of 90 degrees. At 90 degrees, the subject complained of pain at the hamstring tendons, and the bladder pressure had increased from 13 kPa (100 mmHg, 1.9 psi) to 19 kPa (140 mmHg, 2.7 psi). This pressure increase indicates that the leg bladder was not isovolumetric during knee flexion.

Squat exercises to a knee flexion angle of 100 degrees required extra work output from the subject and increased the bladder pressure from 13 kPa (100 mmHg, 1.9 psi) to 20 kPa (150 mmHg, 2.9 psi). At a knee angle of 110 degrees, the bladder pressure increased to 21 kPa (160 mmHg, 3.1 psi), and then the bladder suddenly ruptured. The rupture occurred at the front thigh surface in the

inner urethane layer and was not repairable. In summary, squats beyond the 100-degree knee angle initiated bladder rupture.

The state of the pressure sensors and leg skin after prototype testing is shown in Figure 4.14 and Figure 4.15. No residual or delayed onset pain was felt after removal of the hybrid prototype. However, temporary indentations were left in the skin around the upper thigh, lower calf, and ankle.

Figure 4.14. Doffing process and posttest state of Tekscan pressure sensors.

Figure 4.15. Markings and indentations on leg surface after 60 minutes of wearing prototype.

4.2 LINES OF NON-EXTENSION MCP LEG GARMENT

The second MCP prototype inspired by the human body shape analyses is a skintight "lines of non-extension" prototype, which consists of high-strength nylon fibers in a precise mesh pattern suggested by skin strain analysis. This section of Chapter 4 describes the first iteration and preliminary tests of the lines of non-extension prototype. Originally, the fiber pattern was to be specified by the directions of minimum stretch that were revealed by the digital strain field analysis of Chapter 3. However, prototype construction began before the results of the digital analysis were well understood. Therefore, the prototype pattern was specified by Iberall's lines of non-extension rather than by the directions of minimum stretch.

4.2.1 DESIGNING THE LINES OF NON-EXTENSION MCP GARMENT

Analysis of the leg skin strain during knee flexion reveals lines of non-extension and lines of minimum skin stretch, and these lines suggest the optimal directions for the tension-bearing fibers of an MCP leg garment. For maximum mobility, the tension-bearing fibers of a pressure garment should lie along the directions of non-extension or of minimum skin stretch. The following paragraph describes the design for a lines of non-extension prototype.

> *Ideally, the lines of non-extension spacesuit is a mechanical counter pressure garment that truly functions like a second skin. Its high-strength biocompatible fibers are laid out in a grid with a density that is high enough to protect the skin membrane but low enough to expose small segments (~ 1 mm²) of the skin to the external environment. The fibers are precisely oriented to trace the directions in which the skin stretches the least during the activities of locomotion – the directions called the "lines of non-extension." While the fibers carry the tension loads that apply pressure to the underlying skin surface, they also preserve free locomotion, even after pressurization. Easy mobility is maintained because fiber tension does not change the ability of the lines of non-extension to rotate with respect to each other; it merely shortens the edge length of the circumferential fibers that run parallel to the tightening straps.*

4.2.2 CONSTRUCTING THE LINES OF NON-EXTENSION MCP PROTOTYPE

Before plans were made for the actual lines of non-extension prototype, an empirical test of Iberall's lines of non-extension was conducted. The goal of this test was to determine if a leg garment patterned by Iberall's lines would actually preserve knee flexion mobility. Iberall's lines were drawn on a 3D full-scale replica of the subject's leg, using Iberall's 2D drawings (Figure 4.16) as a guide for the 3D recreation (Figure 4.17). Extremely high-strength, non-stretch Kevlar fibers (Kevlar 49 Aramid Fiber, Du Pont, Inc.) were laid out on top of the lines, using double-sided tape to temporarily hold them onto a base of nylon stocking. To lock the fibers into place, a joint was formed at each fiber intersection by adhering the two crossing fibers together with urethane epoxy resin (DOUBLE/BUBBLE® Urethane, Elementis Specialities, Inc., Belleville, NJ). Kevlar fibers were chosen because they are virtually inextensible; if knee flexion demanded stretching of the fibers, the subject would not be able to provide the force required to stretch them, and it would be evident that the line was not actually a line of "non-extension."

To test the "non-extension" property of Iberall's lines, the Kevlar garment and its nylon backing were removed from the leg replica and put on the subject's leg. The subject easily achieved full knee flexion, without extra work output or discomfort (Figure 4.18).

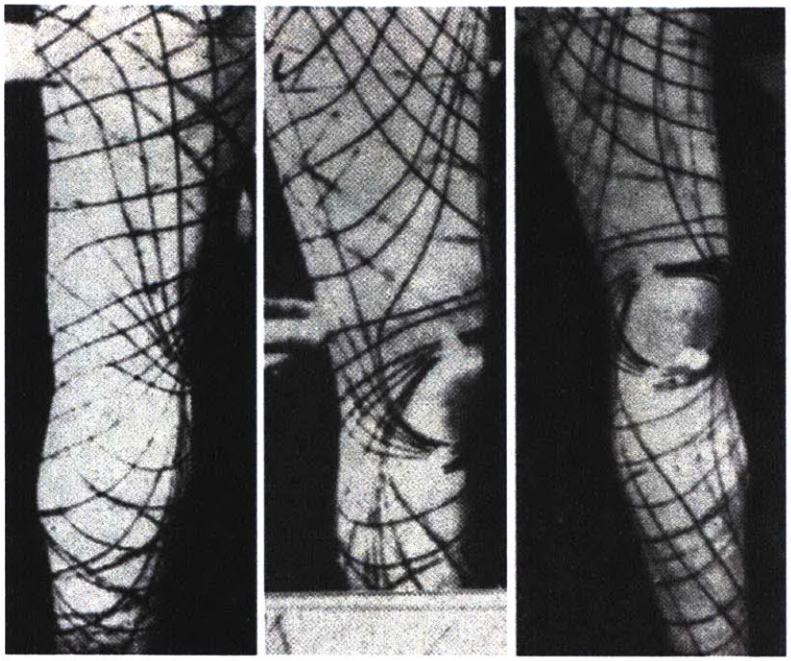

Figure 4.16 Iberall's depiction of the lines of non-extension, drawn on a mannequin [Iberall, 1970, p. 254].

Figure 4.17 Recreation of Iberall's lines on a full-scale replica of a current subject, with Kevlar and epoxy garment overlaid on top. Yellow fibrous strands are Kevlar; black and white dots are epoxy sealant used to fuse the Kevlar joints. The Kevlar garment was used to test the usefulness of the lines of non-extension.

Figure 4.18 Kevlar test garment worn by the subject. As the Kevlar mesh fibers rotate (but do not stretch), knee flexion to 90 degrees and beyond was easily achieved.

The Kevlar test garment verified that knee mobility is not hindered by the lines of non-extension pattern. Accordingly, construction of the actual lines of non-extension prototype proceeded.

To begin prototype construction, the lines of non-extension were again drawn on the 3D leg replica. Then the density of the line pattern was increased by a factor of two; a new line was added in between each parallel pair of original lines. The average edge length of Iberall's mesh was 2 cm, and the average edge length of this new increased density mesh was 1 cm.

After the increased density pattern was drawn, the leg replica was covered with a low power nylon stocking and a layer of stretchable double-sided tape. The pattern was then overlaid with high-strength flat multi-filament nylon (1680 Denier Nylon, Providence Yarn Company Inc., Providence, RI). As the filament was applied, it was placed under just enough tension to fit skintight but no tighter, so that the garment could be worn without applying pressure.

The third step of prototype construction was the fusion of each intersection of nylon fibers. The lines of non-extension may rotate with respect to each other, but to preserve the edge lengths, they cannot slip past each other. To meet this non-slip requirement, a 1-mm to 2-mm dot of transparent epoxy (2 Ton/ Clear Weld Epoxy System, ITW Performance Polymers, Riviera Beach, FL) was applied to each fiber intersection. Figure 4.19 shows the prototype as it appeared after the epoxy had sealed the nylon fibers in place relative to each other.

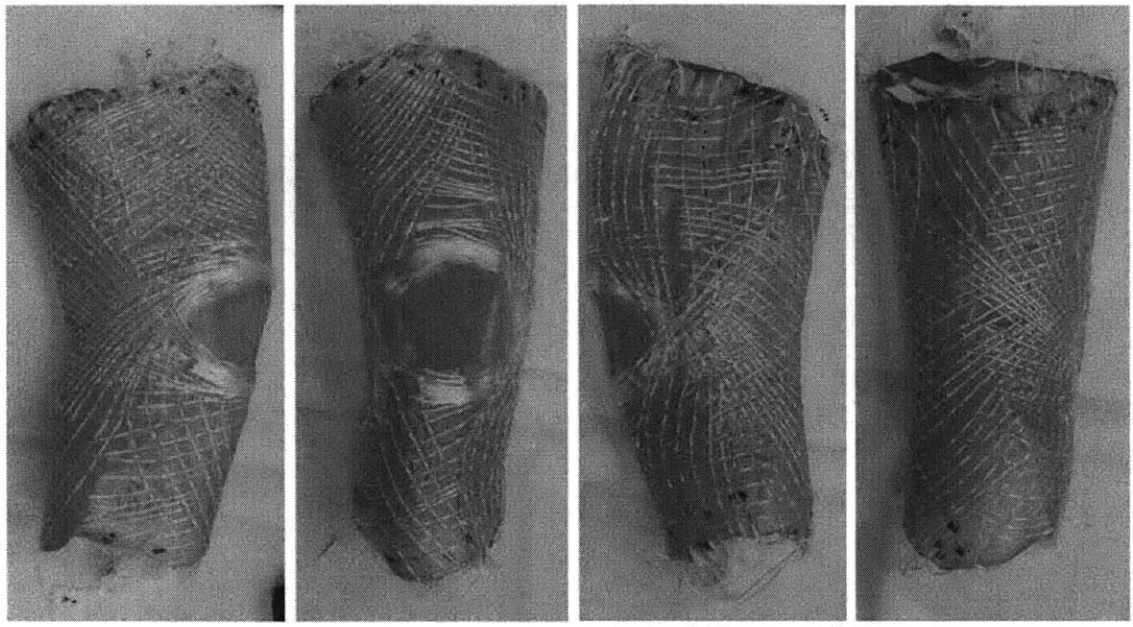

Figure 4.19 Lines of non-extension prototype, made out of a low-power nylon sleeve, high strength multifilament nylon fiber, and transparent epoxy resin. In these images, the prototype has been removed from the 3D leg replica, but the tightening device has not yet been added. Because the nylon fibers are not elastic and are adhered to the nylon sleeve backing, the garment generally retains its leg shape even without the structural support of the 3D leg replica.

The final aspect of prototype construction was the creation of a pressurization mechanism – a device for tightening the garment around the leg once it has been donned. Two columns of 25 0.5-cm diameter brass rings, called grommets, were punched into two strips of high-strength non-stretch sailcloth (110 denier polyester ripstop sailcloth, Doyle Sailmakers/Dimension-Polyant, Putnam, CT) (Figure 4.20). The sailcloth strips were then knotted to the prototype down the length of the medial surface. Each of the two grommet columns traces the path of a line of non-extension that runs longitudinally down the leg. The columns are separated by a third parallel longitudinal line of non-extension (Figure 4.21). At each grommet, the sailcloth strip is knotted to a nylon fiber that passes circumferentially underneath the grommet. Essentially, each grommet marks an intersection of a longitudinal line of non-extension with a circumferential line of non-extension.

To complete the tightening mechanism, a multifilament nylon fiber was knotted to one of each pair of grommets and looped through the other grommet in the pair. These fibers serve as tightening "laces." Each set of three adjacent laces was affixed to a 7.5-cm long piece of 2.5-cm nylon webbing covered with Velcro (Figure 4.22). These straps correspond to matching Velcro pieces attached to the anterior surface of the prototype. Each Velcro strap offers over 130 N (30 lb) of shear strength, which is well above the MCP requirement (Appendix K) of 60 N of tension for every 3 cm of leg length (3 cm is the approximate longitudinal separation between each tightening strap). Figure 4.23 displays the 3D leg replica being pressurized by the completed prototype in its "tightened" state.

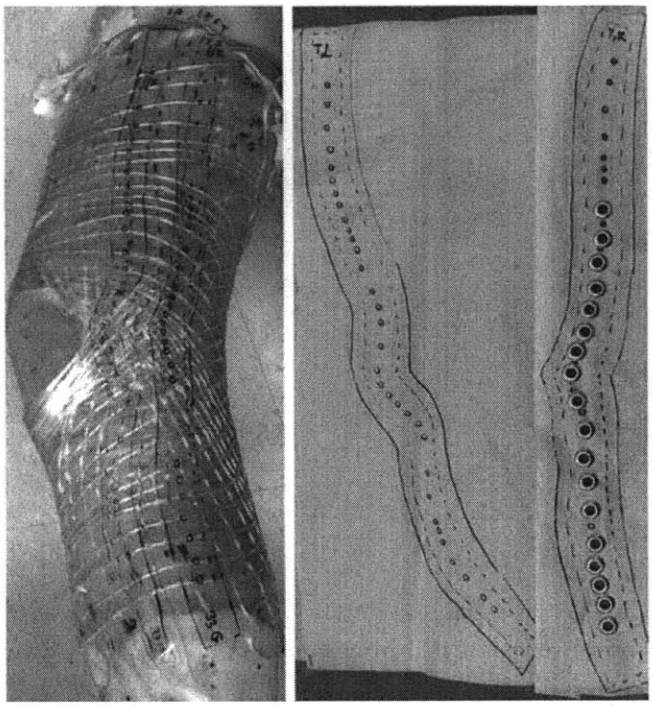

Figure 4.20 Creation of tightening device for lines of non-extension prototype. (Left) Pattern was drawn on transparent material over the lines of non-extension. (Right) Brass lacing grommets were punched into high-strength stretch-resistant sailcloth, which was cut into strips to follow the lines of non-extension running longitudinally down the medial leg surface.

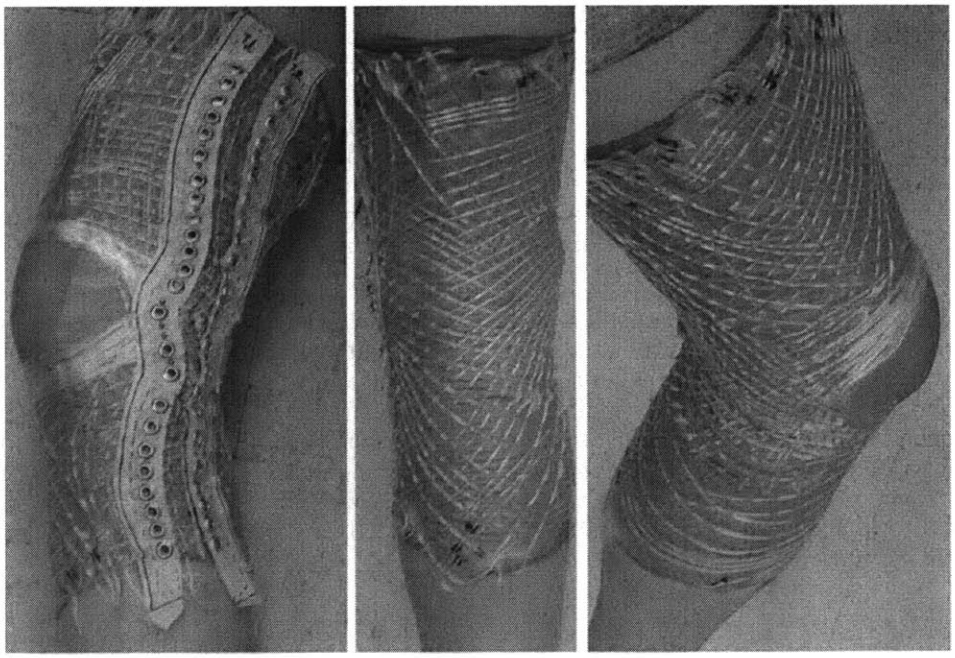

Figure 4.21 Lines of non-extension prototype worn by subject, before laces were added to the tightening device (white strips with brass grommets running down medial leg surface).

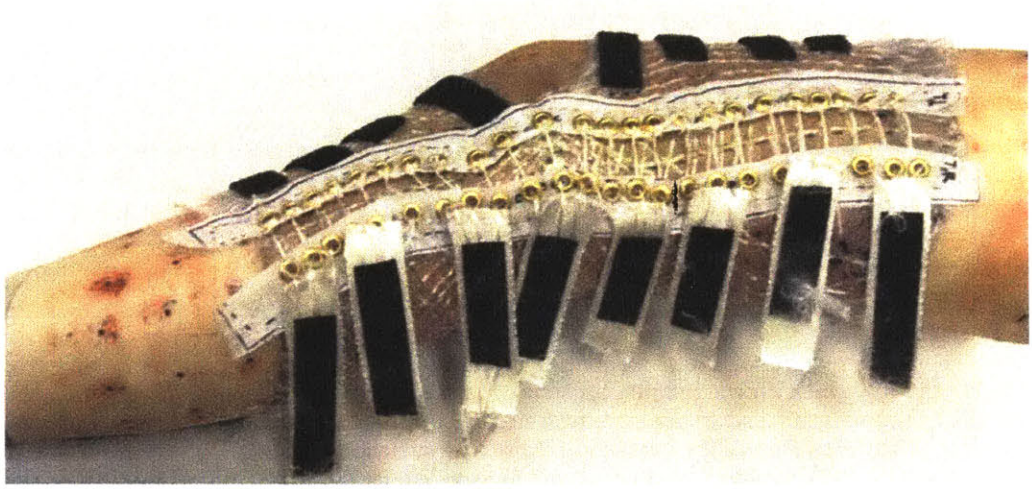

Figure 4.22 Completed tightening device for the lines of non-extension prototype, shown on the 3D leg replica. Each pair of grommets is threaded with a nylon multifilament tightening "lace," and every set of three adjacent laces is connected to a tightening strap made out of nylon webbing and Velcro. Each Velcro strap runs parallel to the underlying circumferential lines of non-extension. There are 24 tightening laces, connected to eight tightening straps. This allows for eight different tension levels along the length of the leg; variable tension levels compensate for the variable leg radius and allow uniform pressure to be produced.

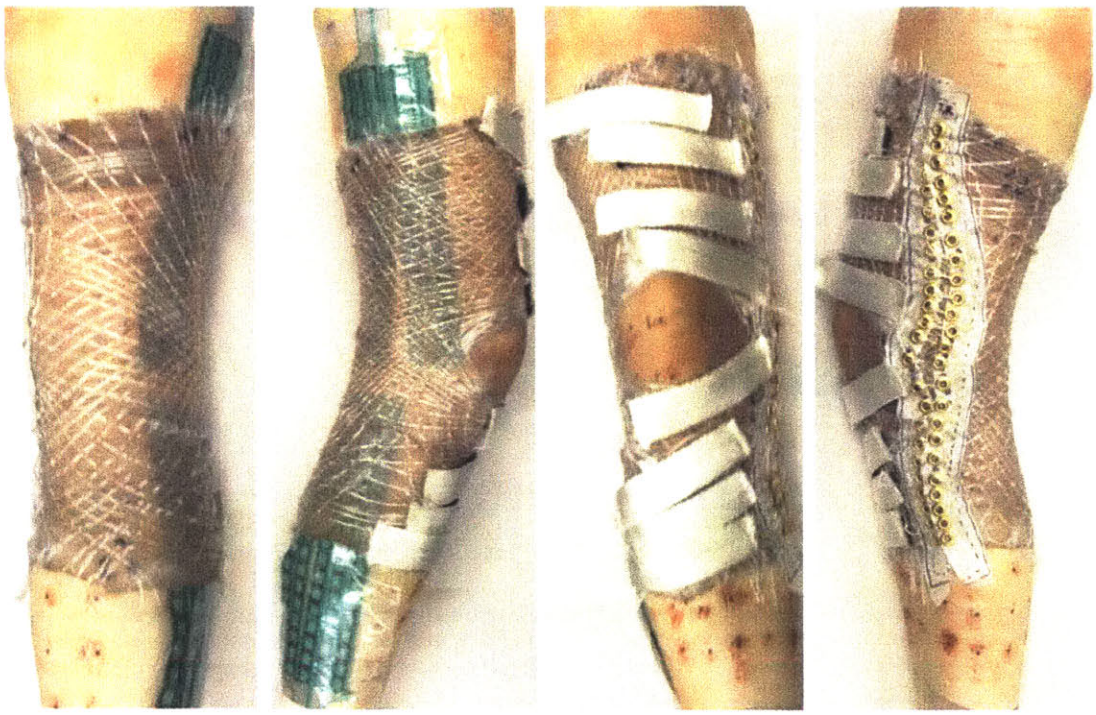

Figure 4.23 Completed lines of non-extension prototype with the tightening device closed. The prototype has been placed on the 3D leg replica and tightened to produce approximately 12 kPa of pressure on the leg surface.

4.2.3 TESTING THE LINES OF NON-EXTENSION MCP PROTOTYPE

DONNING AND DOFFING – The lines of non-extension prototype is easily pulled onto and off of the leg, as long as the anterior surface of the prototype is lined up to meet the anterior surface of the leg. In all trials, the subject required approximately 30 seconds to don and doff the garment without an assistant.

DURABILITY – After three trials on a human subject and several instances of being removed from and replaced onto the 3D leg replica, the nylon fiber and epoxy structure has remained intact. However, the connection between the thin tightening laces and the Velcro/nylon tightening straps has loosened. Also, when the Velcro catches on the nylon multifilament, either in the lacing or on the body of the prototype, it causes some fraying of the multifilament.

SKIN SURFACE PRESSURE – Two preliminary tests of the prototype's pressure production ability have been carried out. The prototype was tested around the human subject's leg and the 3D leg replica. The subject manually "activated" the prototype by closing the tightening device around her leg or the replica. With the manual tensioning applied in these preliminary tests, an average of 7.5 kPa (56 mmHg, 1.1 psi) of pressure was achieved on the human subject's leg surface, while an average of 12 kPa of pressure was produced on the surface of the 3D leg replica (Table 4.2). Certain locations on the subject's actual leg felt average circumferential pressures of up to 15 kPa (110 mmHg, 2.2 psi) while several average circumferential pressures on the leg replica exceeded 15 kPa (Figure 4.24).

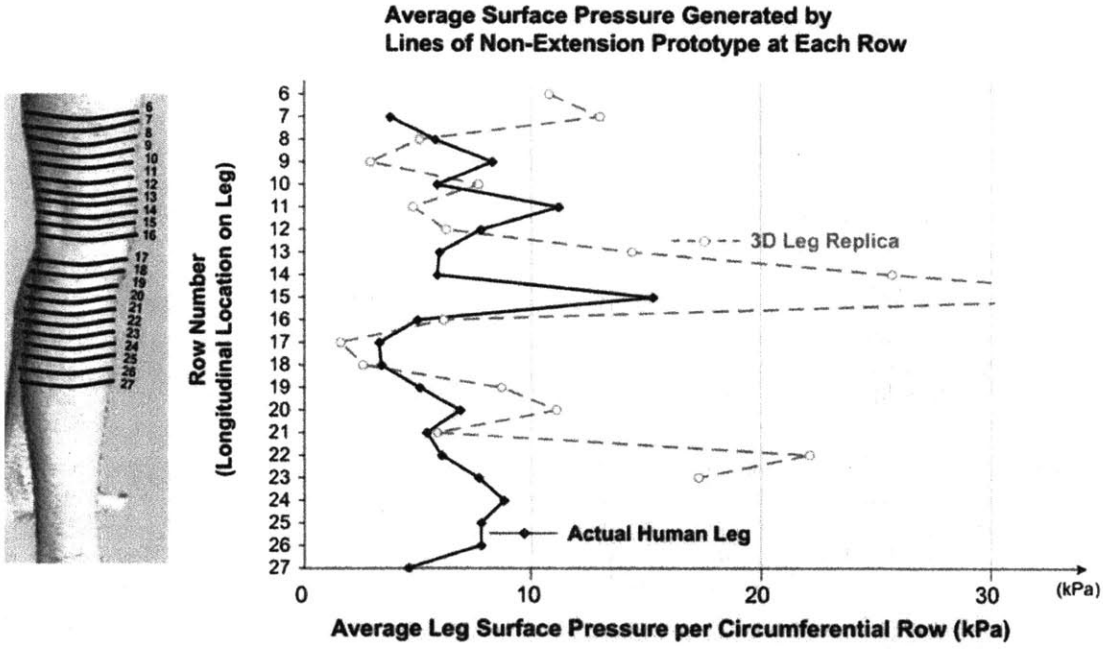

Figure 4.24 Average surface pressure produced around various leg circumferences by the lines of non-extension prototype, on the 3D leg replica and the subject's actual leg. Both the replica and the actual leg were positioned at a 30-degree knee flexion angle during pressure measurement.

For these preliminary tests, only the subject herself operated the tensioning device. In the future, more rigorous testing will utilize assistants and tensile force measuring devices to place the tightening laces under greater and more precise tension, which enables the leg surface to be placed under greater and more uniform pressure.

Table 4.2 Overall average surface pressures generated by lines of non-extension prototype for each sensor region.

Subject	Sensor Location	Average Leg Surface Pressure
Actual Leg	Lateral Thigh Surface	8.3 kPa (62 mmHg, 1.2 psi)
Actual Leg	Lateral Calf Surface	6.6 kPa (50 mmHg, 0.96 psi)
3D Leg Replica	Lateral Thigh Surface	13 kPa (98 mmHg, 1.9 psi)
3D Leg Replica	Lateral Calf Surface	11 kPa (83 mmHg, 1.6 psi)

MOBILITY AND COMFORT – The subject was able to carry out knee flexion to 90 degrees while wearing the lines of non-extension prototype in its tightened state (Figure 4.25). No pain was felt during donning, pressurization, or doffing of the prototype. While knee flexion to 90 degrees was completely comfortable, attempting to bend the knee past 100 degrees of flexion did cause slight discomfort at the hamstring tendons.

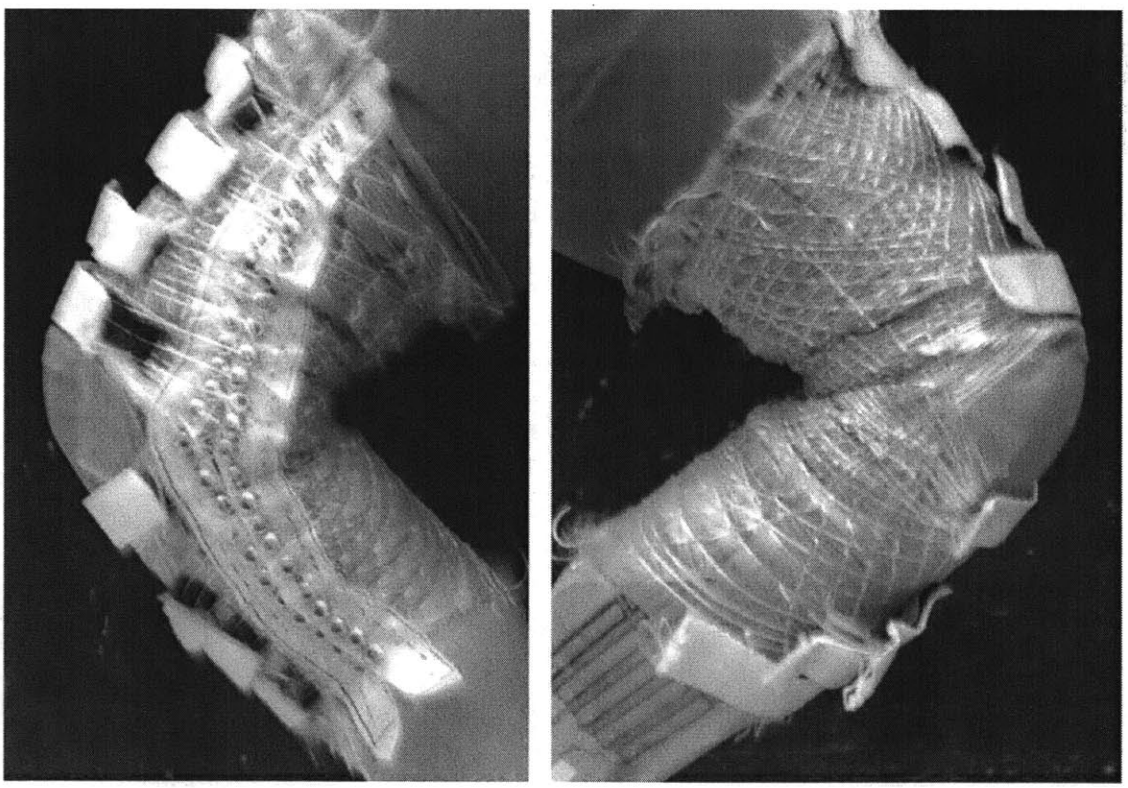

Figure 4.25 Knee flexion to 90 degrees while wearing the lines of non-extension prototype, which has been tightened to a surface pressure level of approximately 7.5 kPa.

Preliminary tests of the nylon-fiber lines of non-extension prototype suggest that it fulfills two major design intents: it allows for comfortable knee flexion mobility even in its pressurized state, and it can be worn without being pressurized. With manual tightening by one person, however, it produced an average leg surface pressure of only 7.5 kPa, which falls short of the desired 30 kPa pressure level. It remains to be seen if a more forceful and more precise tensioning technique will improve its pressure production performance.

This section has described the construction and preliminary testing of a skintight MCP prototype patterned after the lines of non-extension. The lines of non-extension prototype represents an alternative approach to the problem of custom MCP suit design; as summarized in Table 4.3, it differs significantly from the hybrid foam prototype presented in the first section of this chapter. The next chapter, the Discussion, will explore the main lessons learned from the prototypes and suggest reasons for the shortcomings and successes of each of them. It will also return to the human body analyses of Chapter 3 and discuss the major implications of their results for spacesuit design.

Table 4.3 Summary of construction methods and testing results of the two prototypes designed for the changing shape of the human leg.

Prototype	Materials	Use of Body Shape Analysis	Pressurization Method	Mobility	Average Leg Surface Pressure
Shape-responsive foam hybrid	Paint-on urethane Urethane open-cell foam Sailcloth restraint layer	Measure changes in leg diameter during knee flexion Localize extra spacing between foam bladder and restraint layer according to these changes	Inflate foam bladder with air	Hindered by pressurization Bladder ruptures at 110 degrees knee flexion.	3.1 kPa (23 mmHg)
Lines of non-extension	Flat multifilament nylon fiber Epoxy resin Low-power nylon backing	Determine the directions in which skin stretches the least during knee flexion Orient fibers of suit along these "lines of non-extension"	Close straps to squeeze the garment tighter around the leg	Knee flexion to 90 degrees not hindered by pressurization Slight discomfort at 100 degrees knee flexion	7.5 kPa (55 mmHg)

Chapter 4 References

1. Newman, D.J., Bethke, K., Carr, C.E, Hoffman, J., Trotti, G. "Astronaut Bio-Suit System to Enable Planetary Exploration," *Proceedings of the International Astronautical Congress*, Vancouver, British Columbia, Canada, 2004.
2. Pitts, B.M. *Spacesuit: Space Craft.* S.M. Thesis. Massachusetts Institute of Technology, 2003.

CHAPTER 5: DISCUSSION

The two preceding chapters suggest that the design of mobile, second skin pressure suits is facilitated through the analysis of human body shape and skin surface strain during joint motions. This thesis has focused on the development of two procedures for the advancement of spacesuit design: first, a quantitative procedure for measuring human body shape change and skin strain during joint motions, and second, a design procedure for creating a highly mobile spacesuit based on such human body measurements. Three main objectives guided the research activities. The first objective was to develop a 3D laser scanning protocol and a simple computational algorithm to map the strain field on the skin surface of the human leg in motion. The second objective was to expand on the skin surface strain field to compute the directions of minimum normal strain as well as the normal and shear strain tensor components. The third research objective was to construct and test mechanical counter pressure leg garments based on leg shape and skin strain measurements. By performing research to achieve these objectives, a two-fold hypothesis could be tested. This hypothesis suggests that "lines of minimum stretch" would be revealed through a strain field analysis of the leg skin surface and that an operational mechanical counter pressure (MCP) suit would be enabled by the results of the skin strain field analysis.

This chapter begins with a discussion of the uncertainty in the skin surface strain field results and their application to spacesuit design despite this uncertainty. Next, the lessons learned from the shape-responsive hybrid prototype and the lines of non-extension prototype are presented. The key challenges of this work are identified and possible improvements to its methods are suggested. Remaining questions and future research activities are outlined, and finally the thesis concludes with an overview of its key conclusions and major contributions.

5.1 DISCUSSION OF SKIN STRAIN FIELD RESULTS

Before explaining the utility of the skin strain field maps and the lines of minimum stretch, this section will acknowledge the sources of error in the data collection and processing steps and will estimate the uncertainty that results from the propagation of this error.

SOURCES OF ERROR - Position data was collected by manually locating the 156 position trackers (raised dots) on 3D solid models on the computer screen. In most cases, these dots were easily identifiable, as they were small (4-mm diameter at the base) pointed protrusions from the smooth leg surface. However, this method for sensing position has inherent errors. First, the sharpness of some of the dots may have degraded during leg bending, so that they were more smudged in the deformed position than in the reference position. Second, because the dots were identified manually, there was inconsistency in the precise location on the dot that was chosen. The procedure called for selecting the sharp tip of the protrusion, but a point closer to the base of the protrusion could have been chosen in error. Third, the accuracy of the results depends on labeling the dots equivalently in the reference and deformed states of the leg. If one dot was mislabeled or overlooked in the reference configuration but not in the deformed configuration, then all the strain results in that vicinity would be erroneously increased. Finally, errors can result from the solid modeling program's virtual reconstruction of the leg and dots. Bit errors can cause the dislocation of a dot or of an entire region of the leg surface. For example, if the laser

scanner cannot "see" a region of the leg because it is somehow shaded by another object, the solid modeling algorithm may approximate the missing surface as a flat plate instead of a curved surface. Alternatively, the solid modeling algorithm may simply remove the shaded region and join the known edges together. In this case the shape of the 3D reconstruction is even more altered from the object's true shape.

After the position data was gathered from the 3D virtual workspace, it was processed to determine the skin strain field. Sources of error are also present in the data processing algorithm. When the leg surface surrounding a dot is unsymmetrical or highly curved, two approximations in the algorithm become less appropriate and can introduce error into the results. The first of these approximations is that the surface defined by a triad of dots is equivalent to its tangent plane. The second approximation is that the leg surface surrounding a position tracker is symmetrical about both the longitudinal and circumferential axes so that the strains from the four quadrants surrounding the position tracker can be averaged.

As a result of these sources of error in data collection and data processing, each strain magnitude result has an uncertainty of ± 0.2 strain, and each result for the direction of a line of minimum stretch is accurate to within ± 30 degrees. The full derivations of these uncertainties are provided in Appendix J. In future trials, improved protocol and additional position tracker measurements will allow these uncertainty values to be substantially reduced.

CONTRIBUTIONS OF STRAIN FIELD TECHNIQUE - In spite of the uncertainty of 0.2 strain units in the magnitude of the strain tensor components, the 3D anthropometry data can still be translated into credible requirements for a skintight spacesuit. At the very least, before any data processing occurs, the raw position vector data of the tracked points, or "virtual sensors," allows a designer to measure the circumference of transverse sections of the legs at many different locations and with many different cutting plane orientations. These measurements can all be taken without any inconvenience to the wearer, and if a new measurement is needed, the designer simply returns to the digital model and makes the measurement rather than scheduling a new fitting session with the wearer. Immediately, the designer knows the size of the leg to which the spacesuit must be fitted. In addition to measuring overall circumference at various locations, the designer can compute the radius of curvature at any location on the surface (radius of curvature varies even around one continuous circumference, because most leg cross-sections are irregular or elliptical instead of circular). Values of radius of curvature directly stipulate the tension in the suit textile needed to generate a certain mechanical counter pressure. It is true that circumference and radius of curvature could be measured without laser scanning and solid modeling technology. However, the value added by laser scanning is that it allows all these measurements to be made by efficient computer algorithms; all the required measurements can be calculated in a matter of minutes.

Besides static measurements of circumference and curvature, the 3D anthropometry described herein provides designers with the optimal direction for the spacesuit textile to be tensed. In this case, "optimal direction" is defined as the fiber orientation that requires the least amount of energy from the wearer to deform the suit into the shapes required by locomotion. These optimal directions are the directions of minimum stretch, which when taken as a whole, comprise a map of the minimum strain energy pathway on the surface of the leg. The major design recommendation of this thesis is that the tensed fibers (in another sense, the load-carrying struts) of the spacesuit are patterned to lie in the direction of minimal normal strain. This fiber orientation mimics the behavior of skin, which aligns its least extensible direction along the path of minimum normal strain.

Alternatively, at a certain point and in a certain direction that a spacesuit designer is anticipating placing a restraint fiber, the strain tensor components can be transformed into normal and shear strain in the direction of that possible fiber. For example, if a designer chooses to orient a skintight spacesuit's elastic fibers longitudinally and circumferentially, the fibers must allow for longitudinal stretching in the range of 40 to 70% on the front of the patella, for longitudinal

contraction of 40 to 70% in the concavity of the knee, and for circumferential stretching of 30 to 70% over the shin and calf skin (Figure 5.1).

Figure 5.1 Specifications for the stretching capability of a second skin suit whose fibers are oriented in the traditional longitudinal and circumferential directions. Tensioning fibers are shown in gray, and key stretch and contraction requirements are shown in red (with outward arrows) and blue (with inward arrows), respectively. During knee flexion, the fibers over the patella, knee hollow, shin, and calf must be capable of maintaining body pressure while stretching or contracting the given amount.

Efficiency is the primary advantage of determining the skin strain field via laser scanner and digital volume correlation rather than by measuring skin stretch by hand. With efficient computational algorithms, all the needed data, from laser scan to spacesuit specifications, can be generated in a matter of minutes. The input for these algorithms is the position of the tracked points; the output is the pattern for a second skin spacesuit.

COMPARISON WITH PREVIOUS WORK - One could argue that Langer [1861] and Iberall [1970] had already defined patterns for spacesuits – that is, minimum strain energy pathways – in their studies of skin stretching. Langer defined lines of maximum skin tension [Langer, 1861], and Iberall asserted that he had found the lines of zero extension [Iberall, 1970]. Nonetheless, neither researcher demonstrated a method for easily and quickly mapping the lines onto an actual human subject. Furthermore, the sensitivity of the orientation of the lines to an individual's age, level of fitness, body type, and muscular tone is unclear from Langer's and Iberall's work. The contribution of this new skin strain field technique is that it can be tailored to each human subject and can quickly determine a 3D model of the line pattern.

It is still interesting, however, to compare Langer's and Iberall's lines to this study's lines of minimum stretch. If Langer and Iberall had possessed digital technology, would their spacesuit pattern have matched this study's field of minimum stretch lines? In Figure 5.2, Langer's lines, Iberall's lines, and the lines of minimum stretch are displayed side-by-side. It appears that

Langer and Iberall are in general agreement, with the exception of the patella surface. Here their disagreement makes sense, for Langer could specify *minimum* extensibility (in his words, maximum tension), while Iberall was looking for *zero* extension. It is interesting that their results match so closely because their approaches were different. Langer found the natural state of stress in skin, while Iberall looked for responses to the loading of locomotion. However, further thought reveals that their results should be the same: skin cells remodel, or lay down collagen and elastin fibers, in response to the natural loading of locomotion. To minimize energy expenditure, the cells seek to orient the skin's stiffest direction (the direction of least extensibility) along the pathway of lowest normal strain, or least stretching. Iberall looked directly for these pathways of least stretching, and Langer looked for the directions of maximum stiffness of the skin fibers. Therefore, one might expect their lines to follow the same pattern.

Now we can examine how the results of this thesis compare to Iberall's lines, and if they are different, we can discuss why they are different. At some locations on the leg surface, the orientation of this thesis's lines of minimum stretch (short red dashes, center right of Figure 5.2) seems to agree quite well with Iberall's lines of non-extension (long black lines, center left of Figure 5.2). This agreement is particularly evident at the lateral-anterior surface of the thigh, and at the medial surface of the lower leg. At these locations, the two sets of lines point in same direction.

A key result to be drawn from the depiction of the lines of minimum stretch (center right, Figure 5.2) is that over certain regions of the leg, only lines of *minimum* stretch (single dashes) were found, instead of lines of *zero* stretch (intersecting dashes). In these regions with only directions of minimum stretch, the skin stretches by some amount in every direction, or alternatively, contracts by some amount in every direction. This thesis's hypothesis was that these regions of omni-directional stretching would be found over the surface of the patella and at the hollow of the knee. In the center right of Figure 5.2, the patella and hollow of the knee do in fact show clusters of minimum stretch dashes rather than intersecting lines of zero stretch. Interestingly, however, there are also clusters of minimum-stretch dashes (rather than zero-stretch intersecting lines) over the posterior surface of the calf.

The absence of lines of zero stretch at the patella agrees with Iberall's findings; Iberall shows no lines of non-extension over the anterior knee surface. However, the absence of lines of zero stretch at the hollow of the knee and posterior calf surface deviates from Iberall's findings. The cause of this difference could be the uncertainty in strain magnitude measurements, which could cause a small negative strain to be recorded incorrectly as a small positive strain, and this error could propagate into an error in classifying the lines of minimum stretch. For example, imagine the situation where skin extension (positive strain) occurs in the longitudinal direction, and skin contraction (negative strain) occurs in the circumferential direction. If the contraction in the circumferential direction were erroneously measured as an extension, then only a line of *minimum* stretch would result, when in reality two lines of *zero* stretch exist. It is also possible, however, that true lines of non-extension do not actually exist over the knee hollow and posterior calf surfaces. With the 0.2 strain uncertainty and the 30-degree uncertainty in orientation of the lines, it is not possible to refute Iberall's findings definitively.

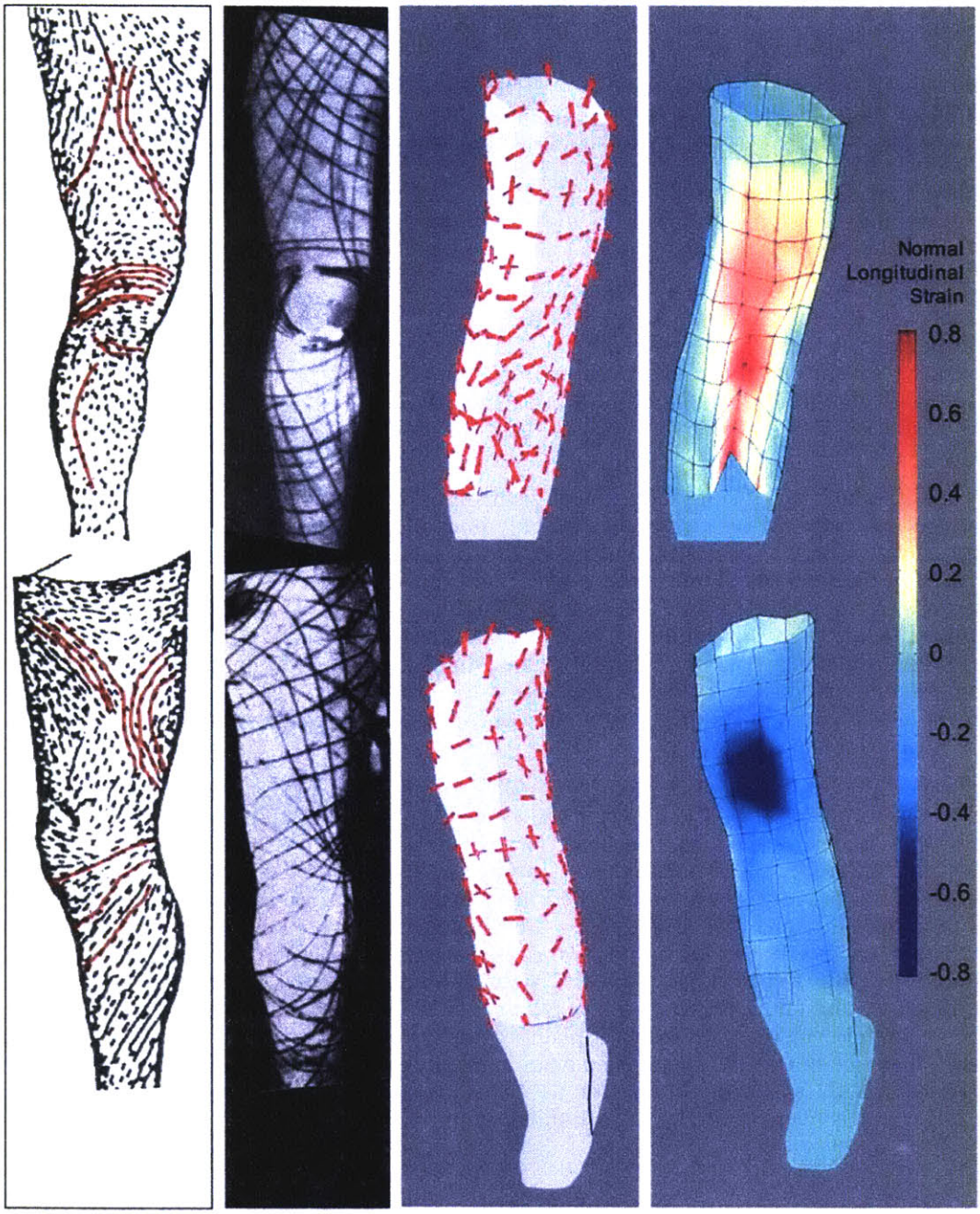

Figure 5.2 Comparison of Langer's lines, Iberall's lines, and this study's lines of minimum stretch. (Left) Langer's lines are the directions of maximum *in vivo* skin tension [Langer, 1861]. (Center Left) Iberall's lines of non-extension are the directions of zero skin extension during joint motions [Iberall, 1970]. (Center Right) The short red dashes are the lines of minimum skin stretch during knee flexion, found in this thesis. Two intersecting red dashes indicate a location where *zero* stretch occurs in two directions. One lone red dash indicates a location where there is only a direction of *minimum* stretch. (Right) Magnitude of longitudinal skin stretch during knee flexion, reported in Chapter 3 of this thesis.

Regardless of how this thesis's lines of minimum stretch compare to Iberall's lines, we must consider how well they translate into a spacesuit pattern; after all, the purpose of newly mapping the lines was to specify the pattern of a second skin mechanical counter pressure spacesuit. The successful lines of non-extension prototype fulfilled this purpose; it proved that the lines of minimum stretch are indeed a useful construct for spacesuit patterning. The lines comprise a pressure suit fiber pattern that allows for knee flexion mobility even during direct pressure application, when the fibers are loaded with 5 to 30 N of tension. However, Iberall's lines already suggested this mobile spacesuit pattern, so we must ask: if the lines of minimum stretch, once corrected for uncertainty, do turn out to be identical to Iberall's lines, what have we gained with this new method for finding them? There are several advantages of this thesis's method for digitally mapping the skin strain field and the directions of minimum skin stretch. First, the digital analysis method is easily repeatable. The same computer algorithm can be used to find the strain field and lines of minimum stretch for many new subjects; each new subject simply needs to be marked with position trackers and scanned with a laser scanner. Because the data are stored numerically (strain *tensors* and minimum stretch *vectors*), the results from different subjects can easily be compared. Second, the data that results from the digital analysis method are quantitative and consequently are easily shared among different designers and different aspects of the design process. The pressure suit designer can choose from a number of options for display of the data. Color strain field maps and drawings of the lines of minimum stretch are generated automatically, and they can be transformed into and printed as static 2D projections, or they can be maintained as 3D virtual solid models and viewed on computers with 3D solid modeling software. The use of solid modeling software for 3D viewing suggests another advantage of the digital human body analysis: computer-aided design (CAD) and computer-aided manufacturing (CAM) of soft spacesuits is now possible. The lines of minimum stretch constitute a set of instructions for the orientation of spacesuit fibers. If this fiber pattern is transferred to solid modeling/CAD software, then computer-controlled "3D-knitting" manufacturing devices can precisely lay down fibers in the specified orientation. Computer-controlled polymer deposition devices are a relatively young technology, but they show promise as tools for future spacesuit construction. Digital human body analysis to map the lines of minimum stretch is an important preliminary step for the use of such promising spacesuit manufacturing tools

5.2 DISCUSSION OF PROTOTYPE RESULTS

The shape-responsive hybrid prototype and the lines of non-extension prototype were both inspired by the human body shape analysis, and they represent an attempt to translate body-shape-change data into spacesuit design requirements. In some sense, these prototypes represent the first foray into *automated* spacesuit patterning. This section of the Discussion reviews the lessons learned from the two prototype design processes.

SHAPE-RESPONSIVE HYBRID PROTOTYPE - The hybrid prototype's restraint layer was designed to maintain a constant volume in the foam bladder by responding to changes in leg shape during knee bends. Previously, the feasibility of the foam hybrid MCP concept was proven with a lower leg garment [Newman, Bethke, Carr, Hoffman, & Trotti, 2004]. This urethane-foam lower leg prototype generated relatively uniform counter pressure, and it also demonstrated the value of "paint-on" construction. The mechanical counter pressure attained by the urethane-foam lower leg garment was delivered with an efficient 1:1 input-to-output pressure ratio. This foam prototype was a substantial improvement over earlier hybrid prototypes, which were pressurized by thin columns of air rather than a continuous foam bladder.

In contrast to the successful lower leg foam hybrid garment, the full-leg hybrid prototype does not function as we had hoped. The fault lies in the compressibility of the foam. The design relies on the fact that the total surface area of the leg remains constant during knee flexion, as shown in Figure 3.4 of this thesis. Since the surface area of the leg is constant, if the average separation between leg and restraint layer also remains constant, the volume occupied by the pressurized gas

will remain constant. The design was intended to mandate a constant average separation, but the actual prototype fails to do so. When the knee is bent, surface area is lost in the hollow of the knee; the prototype collapses there and bladder thickness goes to zero. The design assumed that pressurized air from behind the knee would flow to the extra space created at the front of the knee, and the total volume occupied by the pressurized air would remain constant. This maintenance of constant volume would only occur if the thickness of the bladder on top of the patella increased to compensate for the compression of the foam behind the knee. However, the foam has a negative Poisson's ratio so that when it is *stretched* in the lateral direction across the patella, it *contracts* in the axial (through-thickness) direction. Consequently, the foam is compressed both behind the knee and in front of the knee, and the total volume available for the pressurized air is reduced. Even though the restraint layer was fashioned to respond to shape changes, it cannot control the behavior of the foam in the direction moving towards the leg, away from the restraint layer. The performance of this prototype prompted us to focus on deriving spacesuit patterns from two-dimensional skin surface strain rather than from three-dimensional leg cross-section changes.

LINES OF NON-EXTENSION PROTOTYPE - To create the lines of non-extension prototype, the 3D anthropometry laser scan data was interpreted with a different approach. Instead of sizing the suit with measurements from the *raw* data of leg diameter and circumference, the suit pattern was inspired by the *processed* data of the skin's lines of minimum stretch. Because the digital strain field analysis was not fully completed by the start of the prototyping cycle, Iberall's lines non-extension served as a stand-in for the digitally-determined lines of minimum stretch. The tension-bearing fibers of the lines of non-extension prototype were oriented along the directions in which, according to Iberall, the skin does not stretch during joint flexion.

In preliminary testing of its pressure production and mobility, the lines of non-extension prototype shows promise as a viable concept for an MCP spacesuit. It succeeds in allowing for comfortable knee flexion mobility even in its pressurized state. It also meets the requirement of being able to be worn without being pressurized. The primary shortcoming revealed in preliminary testing is that with manual operation of its tightening straps, the prototype applies an average leg surface pressure of only 7.5 kPa. This pressure level falls short of the 30 kPa goal. The low pressure level is not a result of a flaw in the skintight nylon fiber design, but rather it is the fault of an imprecise method for operating the garment's tightening device. The next step for this prototype is to develop a more forceful and more precise tensioning technique; this development will likely improve its pressure production performance.

Several lessons were learned from the first iteration of construction and the preliminary round of testing of the lines of non-extension garment. First, the subject's ability to perform knee bends while wearing the garment suggests that the unique orientation of its fibers compensate for their inherently non-stretch characteristic. The multifilament nylon fibers have a high modulus; if they had been oriented along longitudinal and circumferential directions, the subject would not have been able to provide the large force required to stretch them as much as the leg skin stretches in those directions during knee flexion. Because the fibers instead traced the directions of zero skin stretching, the subject was able to perform knee flexion without working against the strength of the fibers. The garment's preservation of mobility suggests that Iberall's lines of non-extension, as well as the digitally-determined lines of minimum stretch, are indeed a useful construct for second skin spacesuit design.

The second conclusion to be drawn from the prototype is that tensioning (and shortening) of optimally-oriented fibers does not hinder mobility. When tightening laces cause the grommet columns to overlap, a portion of the lines of non-extension pattern is essentially deleted. However, the section between the grommet columns was chosen with care; it is a longitudinal section on the medial surface of the leg, and its long edges are marked by two roughly parallel lines of non-extension. Tightening of the laces simply brings these two parallel lines toward each other. Thus, pressurization of the suit does not alter the precise angles between the suit fibers, and consequently, the mobility of the suit does not significantly decrease.

The third important lesson from this prototyping effort is that manually operated tightening laces are not an adequate mechanism to produce 30 kPa of pressure uniformly on the leg surface. Two options for improvement exist: the creation of a new tightening device or the development of an improved method for applying specific levels of tension to the tightening laces. This pressure production problem does not seem untenable, and the next section of this chapter includes suggestions for overcoming the problem.

5.3 MOVING FORWARD

5.3.1 KEY CHALLENGES

In working to advance the design of MCP suits, the main challenges include developing mechanisms for suit pressurization, selecting or fabricating the most appropriate suit materials, and creating the hardware and procedures for evaluating prototypes.

DECOUPLING OF SUIT DONNING AND SUIT PRESSURIZATION - It is simple to state that ideally, an MCP suit will be capable of being worn, and donned and doffed, without being pressurized to 30 kPa. It is difficult, however, to conceive of a mechanism that actually decouples pressurization from donning/doffing and still preserves mobility. The lower-leg and full-leg foam hybrid prototypes were an attempt at this decoupling; they are donned first and then later pressurized by being filled with air. Unfortunately, inflation with air substantially limits the mobility of the full-leg hybrid prototype. In contrast to the hybrid foam bladder, the lines of non-extension prototype is powered by a simple lacing mechanism that can produce pressure at any desired time after donning. Since this prototype's weave is oriented along the skin's directions of non-stretching, activation of the lacing mechanism does not hinder mobility. However, the challenge with this prototype is that the lacing mechanism maintains just one level of tension in the garment. When locomotion causes the leg shape to change, the garment's shape tries to change. Unfortunately, because the lacing mechanism has a fixed tension level, the body surface pressure changes at the locations where the leg shape changes. The design of a more adaptive pressurization mechanism still remains as a key challenge in MCP construction.

MATERIALS DEFINITION - A second main challenge is defining the material requirements for a mobile MCP suit and finding, implementing, or fabricating usable materials that meet those requirements. The top-level requirement of producing 30 kPa of surface pressure on leg diameters from 10 to 20 cm stipulates that the suit textile must have an ultimate tensile strength of at least 60 N per cm of width (see derivation in Appendix K). Comfort and feasibility mandate that the textile have a thickness of less than 1 mm and a strain value of between 0.05 and 0.7 when loaded with 50 N/cm width. Now the task is to find an available textile that meets these requirements, and this task is difficult because textile vendors do not often specify the mechanical properties of their products. Nylon monofilament and Spandura™ elastane fiber (synthetic yarn made by alternating hard polyurethane segments with soft polyester or polyether segments) have been identified as potential materials [Kikuta, 2003]. More ideal materials may exist, but searching for them in a systematic manner is a challenge. Figure 5.3 suggests the characteristics of the ideal material for a mobile MCP suit, and it also displays the characteristics of the real Spandura™ material.

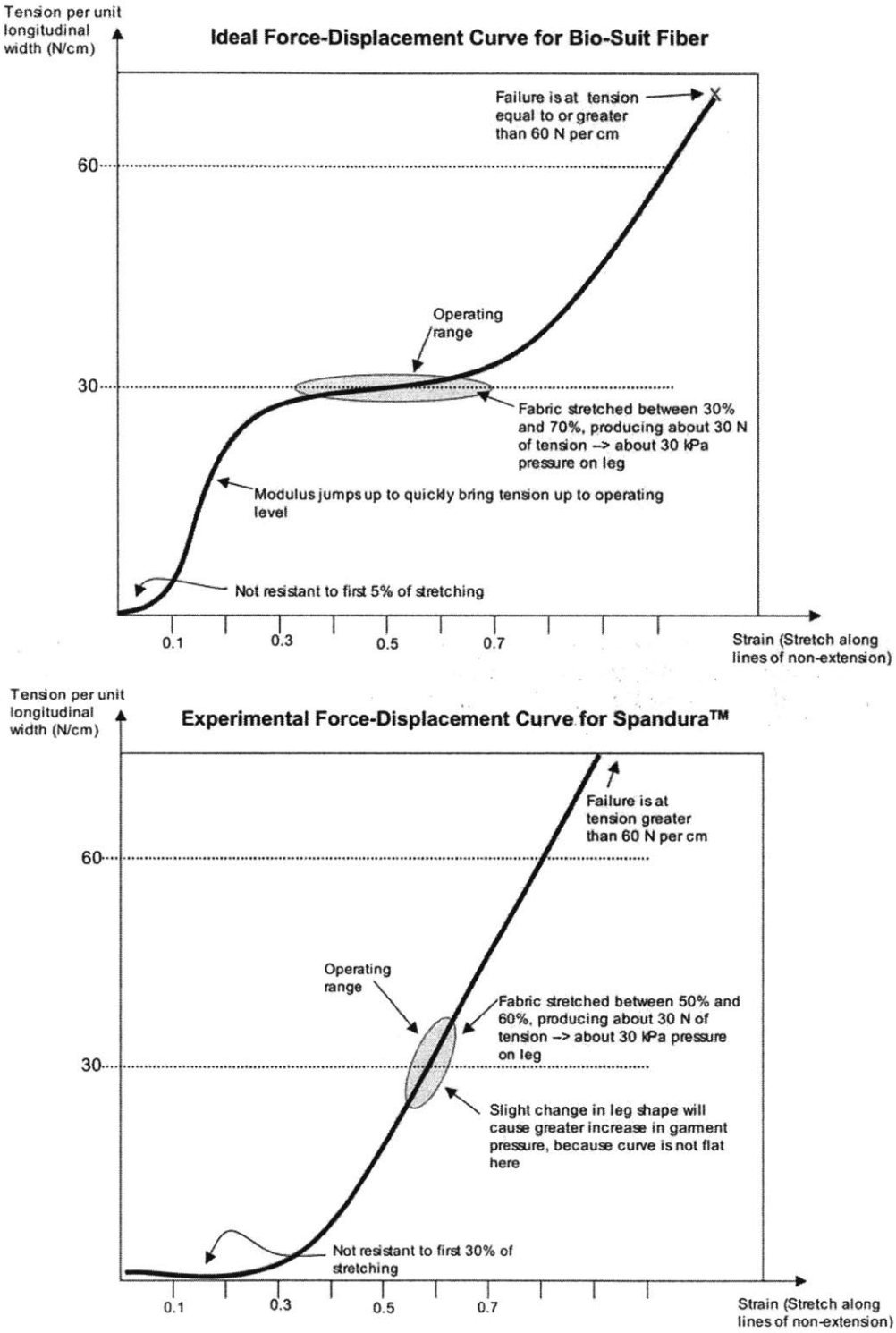

Figure 5.3 (Top) Ideal stress-strain curve for a pressure-producing MCP fiber, whose operating range is defined by a tension level of about 30 N/cm and strains from 30% to 70%. (Bottom) Actual stress-strain curve for a sample of high-strength yet stretchable Spandura™ nylon-lycra fabric [Adpated from Kikuta, 2003].

PROTOTYPE EVALUATION - Once a prototype has been created, the most difficult remaining task is to evaluate its performance in a reliable manner. Testing at hypobaric pressures (in a low pressure chamber) and accurately measuring body surface pressure both present major practical challenges. The capability to test at hypobaric pressures is important because the body cannot tolerate 30 kPa of positive pressure over a large portion of its surface for long periods of time [Annis & Webb, 1971]. EVA excursions may last up to eight hours, and we need a way to test MCP garments for similar time periods without producing positive pressure. Our solution has been to create a low-pressure leg chamber (Appendix I). This chamber allows the environmental pressure around the leg to be reduced, so that a subject wearing a prototype on one leg can continue to breathe atmospheric pressure and have lung pressure balanced by atmospheric pressure over the entire body surface. While in theory this low-pressure chamber solution is adequate, many obstacles were encountered in making the chamber operational. To save costs, the chamber was designed to be rectangular, rather than cylindrical, so that readily available sheets of transparent polycarbonate could form its walls. Though simple to design and construct, this non-ideal pressure chamber shape requires structural support ribs along its walls and is susceptible to leaks along all 12 of its edges. These problems have been solved, but the chamber's remaining disadvantage is that the thigh seal that separates the chamber from the surroundings produces positive pressure on the leg, creating somewhat of a tourniquet effect. The seal is not so tight that it causes pain, but it is tight enough to affect skin temperature and hemodynamics in the lower leg. Before extended duration hypobaric testing occurs, this seal must be improved so that the upper thigh does not feel the adverse effects of positive pressure.

The other barrier to reliable testing of MCP prototypes is the uncertainty of the system for measurements of contact pressure under an irregularly-shaped skintight garment. The thin-film Tekscan™ pressure sensors used in this thesis are subject to error from several sources: they are sensitive to changes in temperature, changes in humidity, shear loads, bending, and wrinkling. Any of these disturbances can create sensor noise, which varies according to the degree of compounding interaction between all the disturbances. Underneath a skintight MCP prototype, wrinkling, bending, and temperature changes are common. Results from testing of these conditions in a calibration device suggest that the resultant error in sensor output may be as much as 20% for each pressure sensing cell (Appendix H includes additional information about this uncertainty and about Tekscan sensors in general). Such a large error makes it very difficult to draw conclusions about the spatial variation of pressure produced by a prototype. The inability to correct for sources of error is a serious drawback to the use of Tekscan pressure sensors in MCP testing.

5.3.2 RECOMMENDATIONS FOR IMPROVEMENT

In this section, several suggestions are offered for improving the human body shape data analysis and suit design techniques.

OPTICAL CAMERA SYSTEM - The first recommendation is to implement a true *digital volume correlation* (DVC) system as an alternative to the modified laser scanner volume correlation method. This suggestion represents the greatest departure from the methods of this thesis. The true DVC method collects information about the shape of the leg with a stereographic optical camera system rather than a laser scanner. A DVC camera system determines an object's 3D position by imaging the object with two different optical cameras whose lines of sight are separated by a known angle. If the object has a natural speckle pattern or can be coated with a speckle pattern that contrasts its natural color, the 3D positions of specific locations on the object's surface can also be determined. Well-developed algorithms exist for using speckle patterns to identify specific locations on the surface of an object. DVC algorithms then compare the speckle pattern of the object in a reference state to the pattern in a deformed state and consequently determine the strain distribution due to that deformation. One difference between DVC and the laser scan method is that the speckle patterns detected by DVC have a much denser

and more randomized distribution of markings, allowing a much finer determination of the strain distribution than the 3-cm grid described in Chapter 3. Another difference is that DVC has a much higher accuracy in determining 3D positions than the laser scanner method described herein. DVC determines 3D position by compounding two 2D position vectors in two different reference frames. Because 2D image analysis is a well-developed technology, these two 2D positions are known with a high degree of accuracy. As a result, the error in strain measurements by DVC is less than 5% (5% relative error, not 5% absolute strain) [Wang & Cuitiño, 2002]. In the laser scanner method of this thesis, even if the previously discussed sources of error in protocol are mitigated, the laser scanner results are still inherently less accurate because they rely on positions computed directly from a 3D reconstruction of an object. These laser scan reconstructions are susceptible to errors in 3D computer vision, a much newer technology than 2D image analysis. A final advantage of DVC is that both hardware and software for DVC are now commercially available (Vic-3D, Correlated Solutions, Inc., West Columbia, SC).

LASER SCAN PROCEDURES - In the case that the laser scanner (rather than optical cameras) continues to be the preferred data collection instrument for skin strain field analysis, the accuracy of its position data might be improved through several key adjustments to the laser scanning procedure. First, the leg should be marked with position tracker dots that are not only raised above the leg surface but that also contain highly reflective pigment. Second, these position trackers should be more finely spaced in the regions of the leg with the highest curvature. A grid spacing of 3 cm is adequate for the upper thigh, but the patella and hollow of the knee may require a position tracker every 0.5 cm or less. Third, the method for identifying the position trackers in the laser scanner's solid model reconstructions of the leg should be automated. The current method is too susceptible to human error in picking on the precise location on the solid model. Instead, a computer algorithm should determine the average level of the leg surface, and then recognize any points that extrude out from this average surface by more than a threshold distance. In this way, all of the position trackers would be identified. Similarly, if the trackers were highly reflective, the searching algorithm could compute the average reflectivity of the leg surface, recognize all the areas that exceed that average reflectivity by a certain amount, and record the location of the midpoint of all those reflective regions.

TRUE FINITE ELEMENT METHODS - Whether the position vector fields are determined by laser scanner or by stereographic optical cameras, implementing *finite element methods* for the data processing algorithm will improve the fidelity of the conversion from position data to strain field. Currently, the position data is fed into the algorithm as a pre-determined mesh. The points are ordered and labeled as belonging to a certain row and column. This method mandates a very particular form for the input position vector data. The advantage of this method is that it does not require the computational resources necessary to automatically order the points into a surface mesh. The disadvantage is that it excludes from its potential input data any set of randomly distributed, unordered position vectors, such as the data that would be provided by a DVC speckle pattern. A more robust, finite-element-method algorithm would allow any two sets (reference and deformed configurations) of position vectors as input, as long as the two sets have an identical number of data points. A basic finite element algorithm determines its best guess for the surfaces defined by these sets of points (by computing nearest neighbors) and then order each set of points into a surface mesh. Then it labels the points equivalently in both data sets, so that each point's reference configuration location, $\overline{X}$, can be compared to its deformed configuration location, $\overline{x}$. With the data now ordered into two arrays of position vectors, the displacement vector array, $\overline{u}$, is created by subtracting the reference positions from the deformed positions [Radovitzky, 2004; Boyce, 2004].

$$\overline{u}(\overline{X},t) = \overline{x}(\overline{X},t) - \overline{X}(\overline{X},t) \tag{5.1}$$

From $\overline{u}$ the strain can easily be computed by applying the finite element method equations for large deformation theory. First, the displacement gradient tensor is computed by differentiating the displacement with respect to the initial configuration locations:

$$\text{Displacement gradient} = \frac{\partial \overline{u}}{\partial \overline{X}}. \tag{5.2}$$

The deformation gradient tensor, $\underline{\underline{F}}$, is then found by adding the identity matrix to the displacement gradient tensor:

$$\underline{\underline{F}} = \underline{\underline{1}} + \frac{\partial \overline{u}}{\partial \overline{X}} = \frac{\partial \overline{x}}{\partial \overline{X}} \tag{5.3}$$

The deformation gradient $\underline{\underline{F}}$ can be separated into its polar decomposition of rigid body rotation, $\underline{\underline{R}}$, and stretch, $\underline{\underline{U}}$, where

$$\underline{\underline{F}} = \underline{\underline{R}}\,\underline{\underline{U}} \tag{5.4}$$

and $\underline{\underline{U}}$ is found by the relation

$$\underline{\underline{U}}^2 = \underline{\underline{F}}^T \underline{\underline{F}} \tag{5.5}$$

Finally, the finite Green-Lagrange strain tensor, $\underline{\underline{E}}$, is computed with by Equation 5.6.

$$\underline{\underline{E}} = \tfrac{1}{2}\left(\underline{\underline{F}}^T \underline{\underline{F}} - \underline{\underline{1}}\right) \tag{5.6}$$

The eigenvalues and eigenvectors of $\underline{\underline{E}}$ are the principal strains and principal directions, and these can be translated into the directions of minimum stretch (Equation 3.39), which are the ultimate goal of human skin strain analysis for spacesuit design.

There are two key difficulties in executing this finite element method. The first is devising the mapping (interpolation) that transforms the three-dimensional positions onto a two-dimensional surface mesh. This compression into two-dimensional coordinates must occur in order to compute *surface* strain rather than *volumetric* strain. The second difficulty is computing the displacement gradient, which contains a partial differentiation that requires the initial and deformed configuration position vectors to be in the same reference frame. This requirement is difficult to satisfy when different portions of the body are undergoing different rigid body rotations relative to each other (i.e., during knee flexion, the lower leg rotates with respect to the upper leg, and the entire leg is rotated at the hip joint). Appendix L contains the MATLAB™ script for a first attempt at overcoming these difficulties and implementing the above finite element method for the leg surface position data. This script remains a work in progress; it does not execute correctly, but its flaws have not yet been identified.

LINES OF NON-EXTENSION PROTOTYPE - These final suggestions aim to improve the performance of the lines of non-extension MCP garment. The prototype succeeds at preserving knee flexion capability and at decoupling donning from pressurization. However, to increase the prototype's average pressure production from 7.5 kPa to 30 kPa, its tightening device should be improved. Implementation of the following recommendations may improve the prototype's pressurization performance:

1. Separate the two grommet columns by an additional 1 cm to 2 cm. One cause of the pressure production problem is that the columns are too close together, and pulling them towards each other does not place the garment's

nylon fibers under adequate tension. The nylon fibers require a greater change in length (strain) to exert the tension required to produce 30 kPa of pressure on the leg surface.

2. Allow each of the 24 grommet pairs to be tightened separately, instead of in groups of three.
3. Avoid tightening the grommet pairs by wrapping a high-strength lace back around the leg. If such a tightening lace does not precisely trace a line of non-extension as it wraps around the leg, it will constrict joint movement.
4. Instead of joining the grommet pairs by wrapping laces around the leg, cinch each grommet pair with a device that is located only above the grommets themselves, such as a fabric loop with a cinching buckle (Slide Bar Buckle, McMaster-Carr, Inc.), or a twisting wire (thread a stiff wire through both grommets, join the wire's two ends, point them radially outwards from the leg, and then twist the wire ends together to decrease the separation distance between the grommets). Once the grommets are at the correct distances from each other, lock them into place with an added zipper, longitudinal clamp, or other sealing mechanism.
5. With a tension spring scale (Linear Dual-Scale Hanging Scale, McMaster-Carr, Inc.), measure the tension applied to the garment's nylon fibers at each grommet pair. Using the tension scale to pull on the fibers, decrease the separation between each grommet pair until the corresponding garment fibers are at the correct tension level for the current leg diameter (see Table 2.3). Mark the position of the grommets, fibers, and cinching device so that for future donning, the tension scale will not be necessary.

The final major recommendation for the next iteration of this prototype is to transform the pattern creation process from a manual procedure into an automatic procedure. The manual method consists of drawing the line pattern by hand on the 3D leg replica, but a more efficient and precise automatic method would virtually construct the lines in a solid modeling software application (see "Streamlined Design Process" below). In the future, digital maps of the lines of minimum stretch will facilitate the patterning process by creating a pattern tailored to each individual wearer.

5.3.3 DIRECTIONS FOR FUTURE RESEARCH

The adventures in human modeling and pressure suit design described in this thesis represent just the tip of the iceberg – just the very beginning of a new computational approach to the problem of mobile spacesuits. My hope is that the techniques and lessons found in the previous pages will encourage others in the spacesuit community to undertake a more comprehensive study of human skin strain, and to work towards a mobile spacesuit that truly mimics the function of that skin as it provides the essential 30 kPa of surface pressure. To tackle these problems, many questions remain to be answered, and much work remains to be done. Here I will briefly present my thoughts on key questions for future research.

MULTIPLE SUBJECTS - The experiments described in this thesis are only pilot studies, with one subject and limited data. Although these experiments succeeded in identifying good practices and developing repeatable quantitative techniques, they do not provide evidence to draw conclusions about human body shape changes for the overall population. Future experiments should study how the parameters of human body volume, surface area, and skin strain field are affected by variability in the subject's body type, age, muscle tone, posture, gait, weight, and height. If the skin strain field can indeed be interpreted as a pattern for the weave of a spacesuit, then we need to know if the skin strain field is common to all humans or if it varies across the population. If it

is variable, is the variability great enough to affect spacesuit construction, and are there certain body characteristics that predict its orientation? To answer these questions, controlled experiments that perform digital volume correlation on multiple subjects should be conducted.

FULL-BODY STRAIN FIELD - Also, to translate the skin strain field into a pattern for an entire spacesuit, then the strain field for the surface of the entire body is needed. A study of the full body, rather than just the right leg, must be undertaken. Accordingly, suit prototypes must be designed for the entire body, with consideration paid to the interfaces between body segments.

STREAMLINED DESIGN AND CONSTRUCTION PROCESS - Once a design for the entire body has been developed and multiple subjects have been studied, then remains the work of streamlining the design process. How can the design and construction proceed from laser scanner or optical camera scan to completed spacesuit, in the least costly and most efficient manner? My vision for a streamlined spacesuit construction process includes the following steps:

1. Laser or optical camera scan of subject's full body, with position trackers.
2. Automatic digital volume correlation to compute skin strain field.
3. Automatic display of lines of minimum stretch, on a virtual 3D reconstruction of full body.
4. Automatic transformation from lines of minimum stretch to spacesuit solid model, with textile width, textile thickness, and suit interior volume specified.
5. Spacesuit solid model displayed on computer aided design (CAD) software.
6. Full body solid model displayed on CAD software; translation into format that is readable by 3D printer.
7. Creation of 3D "print," or replica, of full body (3D printer, Z Corporation, Boston, MA).
8. Spacesuit solid model translated into format that is readable by a computer-controlled 3D electrospinlacing device or other 3D fiber depositing device.
9. Automatic computer-controlled spinlacing of appropriate polymer fiber onto 3D replica of full body.
10. Manual addition of tightening mechanism (for pressurization) and zipper (for doffing).

PHYSIOLOGICAL STUDY – The feasibility of mechanical counter pressure design concepts has been proven, but still it is unknown if mechanical counter pressure will adequately protect the body's tissues from the low-pressure environment of space for long periods of time. Future research must include extended physiological testing of the body's tolerance to hypobaric pressure while wearing MCP garments.

INCORPORATION OF ACTIVE MATERIALS – Active materials may provide the ideal solution for regulating constant and uniform body surface pressure and for activating pressurization at a specific point in time. The most promising materials are shape memory alloys and shape memory polymers, which contract upon heating, as well as dielectric elastomers (or EAPs, for electroactive polymers), which expand laterally upon a through-thickness electric potential. It should be possible to construct cylindrical constricting sleeves out of these three types of materials. If cylindrical pressure sleeves can be constructed, then further work should investigate the ability of these materials to pressurize the more complicated irregular 3D shape of a human limb.

5.4 FINAL CONCLUSIONS

KEY FINDINGS – In this thesis, several questions were investigated through analysis of 3D laser scans of the extended and flexed leg. During knee flexion, where does the volume of the leg change the most, and by how much? Where on the leg is surface area lost or gained? Most importantly, in what direction and with what magnitude does the leg skin stretch, and how can this stretching be represented mathematically? The quantitative answers to these questions were in turn translated into designs for a second skin spacesuit – a suit that, ideally, mimics the shape changes of the body and consequently always conforms to the body's outer envelope, the skin. The most important conclusions from the study of these questions are listed below.

1. The surface area and volume of the entire leg are conserved during knee flexion from 0 to 90 degrees; but the surface area and volume of the knee decrease by 18% and 16%, respectively, for the one subject studied herein.
2. Over most (88%) of the leg surface, knee flexion causes a skin strain of between -0.3 and 0.3 (less than 30% contraction or extension). However, longitudinal strain reaches up to 0.7 at the anterior surface just below the patella, and circumferential strain reaches up to 1.0 at the patella and up to 0.5 at the medial lower leg surface, over the gastrocnemius muscle. Longitudinal contraction up to -0.6 strain occurs at the posterior surface at knee level, and circumferential contraction up to -0.7 strain occurs along the anterior surface of the lower leg.
3. An estimated 60% of the leg skin has some direction of "non-extension," a direction in which zero stretching or contracting of the skin occurs during knee flexion. Over the remaining 40% of leg skin surface, directions of minimum skin extension, or "lines of minimum stretch," can be found. Typically, these directions have similar orientation to Iberall's "lines of non-extension" [Iberall, 1970] but deviate from "Langer's lines" of maximum *in vivo* skin tension [Langer, 1861].
4. Although mechanical counter pressure is successfully generated on the lower leg with a continuous foam bladder encased in a stretch-resistant restraint layer, a full-leg, knee-inclusive version of the inflated foam bladder does not allow for sufficient mobility or pressure distribution, even if the bladder is constructed with a paint-on approach and conforms well to the leg surface.
5. However, a "lines of non-extension" prototype leg garment does preserve knee flexion mobility. This prototype, a second skin garment whose high-strength fibers lie along the directions of minimum stretch, preserves mobility even when the fibers are tensed so that the garment is providing 7.5 kPa (56 mmHg, 1.1 psi) of counter pressure to the skin surface.

MAJOR CONTRIBUTIONS – This thesis makes contributions to several different fields of research, including advanced spacesuit design, digital mechanical analysis, 3D laser scanning, skin biomechanics, and apparel design. As illustrated in Figure 5.4, these contributions build on the key literature on advanced locomotion MCP suits, the mechanical properties of human skin, and digital strain field mapping.

In the field of digital strain mapping, Peters and Ranson [1982] were responsible for the first major development: the basic Digital Image Correlation technique for computing the surface strain field by comparing optical images of an initial and deformed 2D surface. Later, Bay proposed an expansion of the method to study the 3D strain of 3D objects [1999]. Most recently, Wang and Cuitiño used this Digital Volume Correlation method to determine the strain field of a

heterogenous open cell foam [2002]. All of these researchers rely on multiple-camera systems and optical images to gather their displacement field data. This thesis advances their work by demonstrating that laser scans, rather than optical images, can be used as an alternative data set for digital strain field mapping. (However, if high-grade optical cameras and high computational power are available, they will provide more reliable reconstructions of 3D surfaces than laser scanners, at least at this stage of laser scanner technology development.)

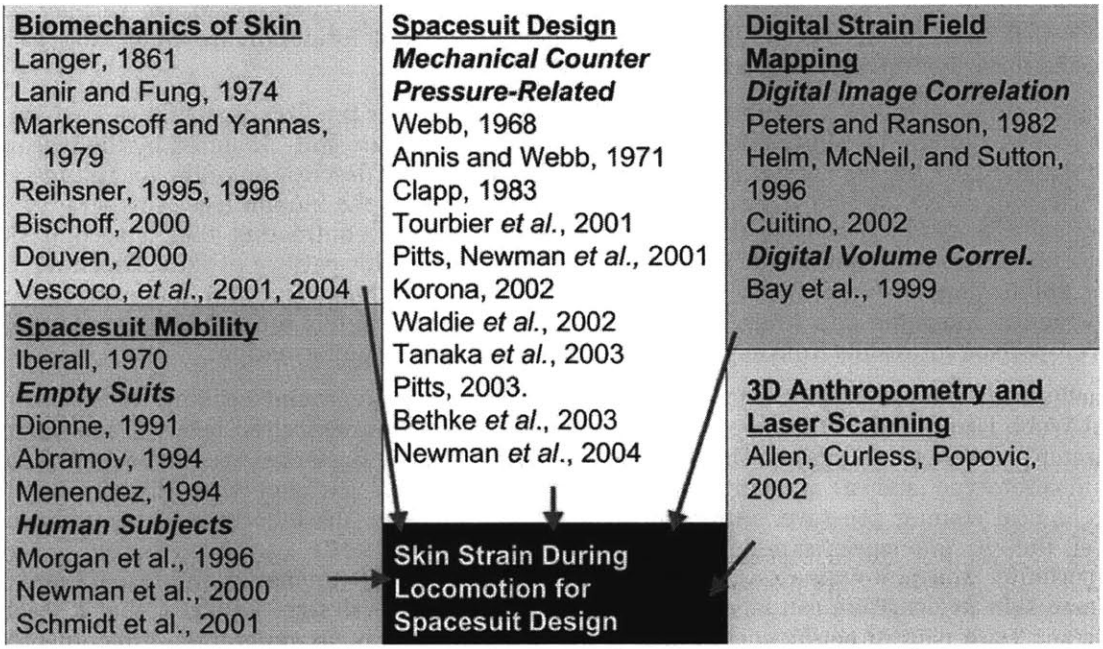

Figure 5.4 Where a study of human body shape change and skin strain fits into previous research.

In solid mechanics, it is a difficult problem to measure full-field 2D surface strain on a 3D irregular body; any solution must constrain strain to a 2D surface while measuring deformation that is irregular in three dimensions. This thesis offers a first-order solution to this problem by suggesting a simple algorithm for estimating 2D surface strain on a 3D irregular body. This algorithm is appropriate and useful for experiments when laser scanners are more readily available than stereographic camera set-ups, when 3D computer data already exists, when accuracy requirements are relaxed, or when high computational power is not available. The laser scan-strain mapping method described in Chapter 3 is the first published account of analyzing full-field surface deformation with a laser scanner as the primary tool. A more minor contribution of this account is a survey, included in Appendix M, of the software used to process laser scan data. CyScan (Cyberware, Inc., Monterey, CA) is the appropriate choice for laser scan manipulation, and RapidForm (INUS Technology, Inc., Seoul, Korea) is recommended as the best software to use for body shape analysis, volume correlation analysis, and reverse engineering.

In the field of skin biomechanics, Langer was responsible for one of the first characterizations of the tension state of skin over the surface of the entire body [1861]. Many modern biomechanicists attempted to verify Langer's results with mechanical testing and mathematical modeling of the skin [Markenscoff & Yannas, 1979; Reihsner, Balogh, & Menzel, 1995; Douven, Meijer, & Oomens, 2000; Bishoff, Arruda, & Grosh, 2000; Marcellier, Vescovo, Varchon, Vacher, & Humbert, 2001]. However, their studies do not simultaneously provide information about the full-body skin surface and the *in vivo* response of skin to the natural loading of knee flexion. The fields of human factors and bioastronautics are other possible sources of information about human skin

deformation, but among researchers of mobile spacesuits, Iberall is the only one to have applied knowledge of skin stress and strain to the design of a pressure suit [Iberall, 1970]. Unfortunately, his analysis and prototyping methods are tedious and qualitative; they are not easily subjected to structural analysis, nor or they easily transferrable to manufacturing equipment. This thesis builds upon Iberall's work by developing a repeatable technique for digitally mapping strain fields on the surface of the human skin. This strain field mapping technique and the resulting mathematical representation of skin strain allows Iberall's predictions to be verified and quantified. As a result, Iberall's understanding of human skin deformation are much more easily applied to garment patterning and design.

To the field of advanced spacesuit design, this thesis contributes the first quantitative analysis of the required strain distribution for a mechanical counter pressure suit. Inspired by the research of Iberall [1970], the results described herein include a full-field description of the magnitude and direction of strain (stretch/contraction) on the skin surface of the human leg. This strain field map tells spacesuit designers the amount of stretching and contracting that a second skin spacesuit needs to accommodate over the entire leg surface. This pattern of skin stretching also has applications for the fields of athletic apparel design, biomechanical engineering, and prosthetics. Also, the skin strain field measurements provided in this thesis can serve as a point of comparison for results from any finite element modeling of leg deformation.

Finally, with two prototyping efforts, this thesis builds upon the groundbreaking work of Annis and Webb [1971] and further supports the potential for generating desired levels of mechanical counter pressure (~ 30 kPa) on the leg surface. Two designs are presented: 1) a hybrid urethane-foam prototype and 2) a skintight, lines of non-extension garment that directly applies mechanical counter pressure. Although in preliminary testing, these early prototypes did not meet the 30 kPa specification, they still demonstrate that MCP can be achieved. Most importantly, the prototype design process demonstrates how mathematical representations of human skin deformation can be applied to quantitative apparel design. I suggest that a second skin spacesuit pattern not be constrained to the longitudinal and circumferential directions that normally serve as a framework for clothing. Rather, the optimal second skin suit pattern mimics the orientation of the lines of minimum stretch. If the fibers are oriented according to these lines, the wearer need only provide the energy for *rotation* of the fibers rather than for additional *stretching* of the fibers. Pressure suit fibers should be oriented along lines of minimum skin stretch rather than along the longitudinal and circumferential directions.

This thesis has been an exercise in applying the concepts of solid mechanics and the tools of digital technology to mechanical analyses of the human body shape and skin surface. The results of these human body analyses inspired the design of two second skin spacesuit prototypes. Although the full-leg foam bladder prototype did not meet design requirements for mobility and pressure production, it demonstrates the potential application of human body shape analysis – in the form of surface area and volume measurements – to the creation of mechanical counter pressure spacesuits. The lines of non-extension prototype was better able to fulfill mobility and body pressure requirements, and consequently, it proves the value of human body analysis in the form of skin strain field mapping. It also inspires further work to expedite the process of mapping the strain field and minimum stretch lines and of transferring them to actual spacesuit prototypes.

It is my hope that this work encourages others to apply rigorous mathematical analysis of the human body surface to the design of next generation spacesuits. For astronauts to be as productive and comfortable as possible while they explore another planetary surface, they must feel that their spacesuits fit like second skins. A suit that fits like a second skin imitates the stretching and twisting of the human skin as its wearer moves about, without demanding the exertion of extra work by the wearer. This thesis demonstrates that such a suit can indeed be achieved, if we can follow Iberall's lead in deepening our understanding of the dynamic human body shape, while we simultaneously follow Webb's lead in considering creative methods for providing body surface pressure and other life support needs of future planetary explorers.

Chapter 5 References

1. Annis, J.F., Webb, P. "Development of a Space Activity Suit," NASA Contractor Report CR-1892, Webb Associates, Yellow Springs, Ohio, 1971.
2. Bathe, K.M. *Finite Element Procedures.* Prentice Hall, 1996.
3. Bischoff, J.E., Arruda, E.M., Grosh, K. Finite element modeling of human skin using an isotropic, nonlinear elastic constitutive model. *Journal of Biomechanics*, Vol. 33, No. 6, June 2000, p. 645-652.
4. Boyce, Mary C. "Lecture 15 Notes: Finite Deformation" from MIT course 2.071: Mechanics of Solid Materials. December, 2004.
5. Douven, L., Meijer, R, Oomens, C., "Characterisation of mechanical behaviour of human skin in vivo." In *Laser-Tissue Interaction XI: Photochemical, Photothermal, and Photomechanical,* D. Duncan, J.O. Hollinger, S.L. Jacques, Editors, Proceedings of SPIE Vol. 3914, 2000.
6. Iberall, A.S. "The Experimental Design of a Mobile Pressure Suit," *Journal of Basic Engineering*, June 1970, p. 251- 264.
7. Kikuta, M. *Mechanical Properties of Candidate Materials for Morphing Wings.* M.S. Thesis, Virginia Polytechnic Institute and State University, 2003.
8. Langer, K. "On the anatomy and physiology of the skin: I. The cleavability of the cutis," Reprinted in *British Journal of Plastic Surgery*, Vol. 31, 1978, p. 3-8. Translated from the original in Sitzungsbericht der Mathematisch-naturwissenschaftlichen Classe der Kaiserlichen Academie der Wissenschaften, 44, 19.
9. Marcellier, H., Vescovo, P., Varchon, D., Vacher, P., Humbert, P. "Optical analysis of displacement and strain fields on human skin." *Skin Research and Technology*, Vol. 7, 2001, p. 246-253.
10. Markenscoff, X., Yannas, I. V. "On the stress-strain relation for skin." *Journal of Biomechanics.* Vol. 12, 1979, p. 127-129.
11. Newman, D.J., Bethke, K., Carr, C.E, Hoffman, J., Trotti, G. "Astronaut Bio-Suit System to Enable Planetary Exploration," *Proceedings of the International Astronautical Congress*, Vancouver, British Columbia, Canada, 2004..
12. Radovitzky, Raul. "Lecture Notes" from MIT Course 16.225: Computational Mechanics of Materials. Fall, 2003.
13. Reihsner, R., Balogh, B., Menzel, E.J. "Two-dimensional elastic properties of human skin in terms of an incremental model at the in vivo configuration." *Medical Engineering and Physics*, Vol. 17, 1995, p. 304-313.

List of Appendices

APPENDIX A: DERIVATION OF MECHANICAL COUNTER PRESSURE EQUATION, P = T/K

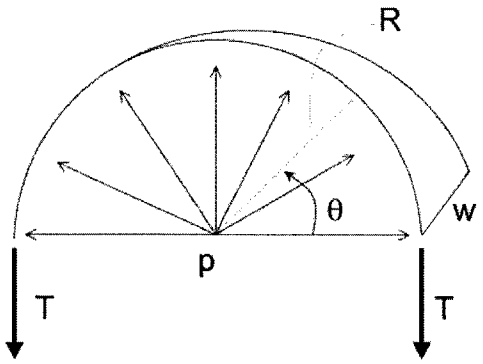

T = circumferential tension per unit membrane width, w

p = pressure exerted by surface on membrane; - p = pressure exerted by membrane on surface

R = radius of cylindrical surface

Equilibrium Equation:

$$\sum F_y = 0$$

$$-2T + \int_{\theta=0}^{\theta=\pi} pR\sin\theta\, d\theta = 0$$

$$-2T + pR\int_0^{\pi} \sin\theta\, d\theta = 0$$

$$-2T - pR\cos\theta\Big]_0^{\pi} = 0$$

$$-2T - pR(\cos\pi - \cos 0) = 0$$

$$-2T + 2pR = 0$$

$$2pR = 2T$$

$$p = \frac{T}{R} \quad \Rightarrow \quad p_{MCP} = \frac{T}{\kappa}$$

APPENDIX B: LEG SURFACE AREA AND VOLUME MEASUREMENTS

Surface Area Measurements During Knee Flexion

Trial #	Angle	Total Leg SA (cm^2)	% Change from SA at 0 deg, trial #1	Thigh SA (cm^2)	% Change from mean SA at 0 deg	Knee SA (cm^2)	% Change from mean SA at 0 deg	Calf SA (cm^2)	% Change from mean SA at 0 deg
1	0	2397	0.0	968	0.1	665	-1.5	764	0.5
2	0	2408	0.5	968	0.1	689	2.1	751	-1.2
3	0	2401	0.2	965	-0.2	671	-0.6	765	0.7
AVG	*0*	*2402*		*967*		*675*		*760*	
1*	30	2448	1.9	972	0.5	689	2.1	787	3.6
2	30	2377	-1.0	960	-0.7	637	-5.6	780	2.6
3	30	2380	-0.9	962	-0.5	641	-5.0	776	2.1
1	60	2383	-0.8	969	0.2	626	-7.3	798	5.0
2	60	2391	-0.5	965	-0.2	634	-6.1	793	4.3
3	60	2369	-1.4	961	-0.6	564	-16.4	844	11.1
1	90	2383	-0.8	986	2.0	551	-18.4	846	11.3
2	90	2404	0.1	1006	4.0	577	-14.5	821	8.0
3	90	2410	0.3	1004	3.8	570	-15.6	837	10.1

*Data thrown out: poor data set, many holes and discontinuities in surface

Volume Measurements During Knee Flexion

Trial #	Angle	Total Leg Vol (cm^2)	% Change from mean vol at 0 deg	Thigh Vol (cm^2)	% Change from mean vol at 0 deg	Knee Vol (cm^2)	% Change from mean vol at 0 deg	Calf Vol (cm^2)	% Change from mean vol at 0 deg
1	0	6880	-0.1	3510	0.3	1730	-2.3	1590	0.0
2	0	6900	0.1	3500	0.0	1810	2.2	1570	-1.3
3	0	6890	0.0	3490	-0.3	1770	0.0	1610	1.2
AVG	*0*	*6890*		*3500*		*1770*		*1590*	
1*	30	7080	2.7	3490	-0.3	1850	4.3	1700	6.5
2	30	6830	-0.9	3520	0.6	1670	-6.0	1650	3.6
3	30	6830	-0.9	3480	-0.6	1680	-5.4	1650	3.6
1	60	6870	-0.3	3450	-1.4	1640	-7.9	1770	10.2
2	60	6850	-0.6	3420	-2.3	1670	-6.0	1750	9.1
3	60	6810	-1.2	3460	-1.2	1500	-18.0	1830	13.1
1	90	6800	-1.3	3460	-1.2	1470	-20.4	1840	13.6
2	90	6870	-0.3	3540	1.1	1530	-15.7	1790	11.2
3	90	6870	-0.3	3490	-0.3	1500	-18.0	1840	13.6

*Data thrown out: poor data set, many holes and discontinuities in surface

Statistical Analysis of Surface Area Measurements of Full Leg and Knee Alone

Total Surface Area (cm^2)

	Mean	Std. Dev.	Freq.	t-statistic	p = 2*Pr(t9<t)	Sig. pair diff.?
0 deg	2402	5.57	3	0	1	No
30 deg	2402	40.2	3	0	1	No
60 deg	2381	11.1	3	1.160	0.276	No
90 deg	2399	14.2	3	0.166	0.872	No
Total	2396	21	12			

Analysis of Variance

Source	SS	df	MS		
Between groups	906	3	302		
Within groups	3937	8	492		
Total	4843	11	440		
				F = MSB/MSW	0.6138
				p = Pr(F2,9>F)	0.56
				Sig diff somewhere?	No

Knee Surface Area (cm^2)

	Mean	Std. Dev.	Freq.	t-statistic	p = 2*Pr(t9<t)	Sig. pair diff.?
0 deg	675	12.5	3	0	1	No
30 deg	656	28.9	3	0.922	0.381	No
60 deg	608	38.3	3	3.194	0.011	Yes, alpha 0.05
90 deg	566	13.5	3	5.196	0.001	Yes, alpha 0.01
Total	626	49.5	12			

Analysis of Variance

Source	SS	df	MS		
Between groups	21615	3	7205		
Within groups	5285	8	660		
Total	26900	11	2445		
				F = MSB/MSW	10.92
				p = Pr(F2,9>F)	0.0039
				Sig diff somewhere?	Yes, alpha 0.01

Statistical Analysis of Volume Measurements of Full Leg and Knee Alone

Total Volume (cm^3)

	Mean	Std. Dev.	Freq.	t-statistic	p = 2*Pr(t9<t)	Sig. pair diff.?
0 deg	6890	10	3	0	1	No
30 deg	6913	144	3	0.368	0.722	No
60 deg	6843	30.6	3	0.751	0.472	No
90 deg	6847	40.4	3	0.687	0.509	No
Total	6873	72.3	12			

Analysis of Variance

Source	SS	df	MS		
Between groups	104667	3	3489		
Within groups	47000	8	5875		
Total	57467	11	5224		
				F = MSB/MSW	0.6679
				p = Pr(F2,9>F)	0.54
				Sig diff somewhere?	N0

Knee Volume (cm^3)

	Mean	Std. Dev.	Freq.	t-statistic	p = 2*Pr(t9<t)	Sig. pair diff.?
0 deg	1770	40	3	0	1	No
30 deg	1733	101	3	0.6259	0.5469	No
60 deg	1603	90.7	3	2.8250	0.0199	Yes, alpha 0.05
90 deg	1500	30	3	4.5673	0.0014	Yes, alpha 0.01
Total	1651	128	12			

Analysis of Variance

Source	SS	df	MS		
Between groups	138033	3	46011		
Within groups	41933	8	5242		
Total	179967	11	16361		
				F = MSB/MSW	8.777
				p = Pr(F2,9>F)	0.0077

APPENDIX C: MATLAB™ CODE FOR SKIN STRAIN FIELD ALGORITHM

```
% Filename: surface_mapped13.m
% Date of last change: March 2005
% Author: Kristen Bethke
% Description: Implementation of Skin Strain Field Analysis Algorithm
% This routine operates on specially formatted data (data file = tecplot_data_new3.txt)
that % % % contains the initial and deformed positions of 156 points on the surface of
the leg, which are % label with their row and column number (i.e., point in 4th row, 6th
column is labeled 0406).


load tecplot_data_new3.txt; %new extracted data using Tecplot, which can import .ply
files
data = tecplot_data_new3; %no coordinate transformations applied; data is raw
%consequently we have to multiply by 100 to bring from meters to
%centimeters
%previously, transform_to_leg.m had done this scaling



%data = input;  %use this when inputting cylinder simulation data
[num_mark, num_coord] = size(data);

NUM_ROWS = floor(max(data(:,1))/100);
%NUM_COL = mod(max(data(:,1)),100);
NUM_COL = 12;

marker = struct('label',0,'initial',[0 0 0],'deformed',[0 0 0],'disp',[0 0 0],...
    'e1',[0 0 0],'e2',[0 0 0],'prin_2d',[0 0;0 0],'prin_3d',[0 0;0 0;0 0],...
    'epsLL',[0 0 0 0], 'epsTT',[0 0 0 0],'epsLT',[0 0 0 0]);

for i = 1:num_mark,
    marker(i).label = data(i,1);
    marker(i).initial = 100*data(i,2:4);
    marker(i).deformed = 100*data(i,5:7);
    marker(i).disp = marker(i).deformed - marker(i).initial;
end


for j = 13:144,  %just do rows 2 through 12

    rc = marker(j).label;
    col = mod(rc,100);
    row = floor(rc/100);

%vectors pointing from the center marker to each of the 8 neighboring
%markers
%(location of neighbor indicated by
%approximate angle of vector from center marker to neighbor marker,
%where angle 0 indicates a vector pointing transversely across leg towards
%the marker with a higher column number (going ccw if looking down leg),
%and angles advance ccw

if col <= 11 && col >= 2,
e0 = marker(j+1).initial - marker(j).initial;
e45 = marker(j-11).initial - marker(j).initial;
e90 = marker(j-12).initial - marker(j).initial;
e135 = marker(j-13).initial - marker(j).initial;
e180 = marker(j-1).initial - marker(j).initial;
e225 = marker(j+11).initial - marker(j).initial;
e270 = marker(j+12).initial - marker(j).initial;
e315 = marker(j+13).initial - marker(j).initial;

e0p = marker(j+1).deformed - marker(j).deformed;
e45p = marker(j-11).deformed - marker(j).deformed;
e90p = marker(j-12).deformed - marker(j).deformed;
e135p = marker(j-13).deformed - marker(j).deformed;
```

```
e180p = marker(j-1).deformed - marker(j).deformed;
e225p = marker(j+11).deformed - marker(j).deformed;
e270p = marker(j+12).deformed - marker(j).deformed;
e315p = marker(j+13).deformed - marker(j).deformed;
end

if col == 1,
e0 = marker(j+1).initial - marker(j).initial;
e45 = marker(j-11).initial - marker(j).initial;
e90 = marker(j-12).initial - marker(j).initial;
e135 = marker(j-1).initial - marker(j).initial;
e180 = marker(j+11).initial - marker(j).initial;
e225 = marker(j+23).initial - marker(j).initial;
e270 = marker(j+12).initial - marker(j).initial;
e315 = marker(j+13).initial - marker(j).initial;

e0p = marker(j+1).deformed - marker(j).deformed;
e45p = marker(j-11).deformed - marker(j).deformed;
e90p = marker(j-12).deformed - marker(j).deformed;
e135p = marker(j-1).deformed - marker(j).deformed;
e180p = marker(j+11).deformed - marker(j).deformed;
e225p = marker(j+23).deformed - marker(j).deformed;
e270p = marker(j+12).deformed - marker(j).deformed;
e315p = marker(j+13).deformed - marker(j).deformed;
end

if col == 12,
e0 = marker(j-11).initial - marker(j).initial;
e45 = marker(j-23).initial - marker(j).initial;
e90 = marker(j-12).initial - marker(j).initial;
e135 = marker(j-13).initial - marker(j).initial;
e180 = marker(j-1).initial - marker(j).initial;
e225 = marker(j+11).initial - marker(j).initial;
e270 = marker(j+12).initial - marker(j).initial;
e315 = marker(j+1).initial - marker(j).initial;

e0p = marker(j-11).deformed - marker(j).deformed;
e45p = marker(j-23).deformed - marker(j).deformed;
e90p = marker(j-12).deformed - marker(j).deformed;
e135p = marker(j-13).deformed - marker(j).deformed;
e180p = marker(j-1).deformed - marker(j).deformed;
e225p = marker(j+11).deformed - marker(j).deformed;
e270p = marker(j+12).deformed - marker(j).deformed;
e315p = marker(j+1).deformed - marker(j).deformed;
end



%in the orthogonal basis tangent to the leg surface,
%the first vector is defined by the vector pointing from
%the central marker to the marker
%longitudinally above or below the central marker
e2_i = e90;
e2_ii = e90;
e2_iii = e270;
e2_iv = e270;
marker(j).e2 = e2_i/norm(e2_i);
marker(j).e2p = e90p/norm(e90p);

%surface normals for each quadrant of markers
n_i = cross(e0,e90)/norm(cross(e0,e90));
n_ii = cross(e90,e180)/norm(cross(e90,e180));
n_iii = cross(e180,e270)/norm(cross(e180,e270));
n_iv = cross(e270,e0)/norm(cross(e270,e0));
np = cross(e0p,e90p)/norm(cross(e0p,e90p));
marker(j).n_i = n_i;

%this second vector completes the orthogonal basis tangent to the leg surface
e1_i = cross(e2_i,n_i)/norm(cross(e2_i,n_i));  %order of vectors being crossed is
important! (don't flip e2_i and n_i arbitrarily)
```

```
e1_ii = cross(n_ii,e2_ii)/norm(cross(n_ii,e2_ii));
e1_iii = cross(e2_iii,n_iii)/norm(cross(e2_iii,n_iii));
e1_iv = cross(n_iv,e2_iv)/norm(cross(n_iv,e2_iv));
marker(j).e1 = e1_i;
marker(j).e1p = cross(marker(j).e2p,np)/norm(cross(marker(j).e2p,np));
marker(j).e90 = e90;
marker(j).e90p = e90p;
marker(j).e180 = e180;
marker(j).e180p = e180p;
marker(j).e0p = e0p;
marker(j).e0 = e0;
marker(j).e45 = e45;
marker(j).e45p = e45p;

%find the strain along each marker-defined ("neighboring marker") direction
eps0 = (norm(e0p) - norm(e0))/norm(e0);
eps45 = (norm(e45p) - norm(e45))/norm(e45);
eps90 = (norm(e90p) - norm(e90))/norm(e90);
eps135 = (norm(e135p) - norm(e135))/norm(e135);
eps180 =(norm(e180p) - norm(e180))/norm(e180);
eps225 = (norm(e225p) - norm(e225))/norm(e225);
eps270 = (norm(e270p) - norm(e270))/norm(e270);
eps315 = (norm(e315p) - norm(e315))/norm(e315);

eps22_i = eps90;
eps22_ii = eps90;
eps22_iii = eps270;
eps22_iv = eps270;

%a and b are the angles between the 1 axis and each non-orthogonal axis
%defined by a neighboring marker location
a_i = acos(dot(e1_i,e0)/(norm(e1_i)*norm(e0)));
b_i = acos(dot(e1_i,e45)/(norm(e1_i)*norm(e45)));
a_ii = acos(dot(e1_ii,e180)/(norm(e1_ii)*norm(e180)));
b_ii = acos(dot(e1_ii,e135)/(norm(e1_ii)*norm(e135)));
a_iii = acos(dot(e1_iii,e180)/(norm(e1_iii)*norm(e180)));
b_iii = acos(dot(e1_iii,e225)/(norm(e1_iii)*norm(e225)));
a_iv = acos(dot(e1_iv,e0)/(norm(e1_iv)*norm(e0)));
b_iv = acos(dot(e1_iv,e315)/(norm(e1_iv)*norm(e315)));
%%%%
%%%%
%%%%
%save all the angles:
marker(j).angles = [a_i b_i;a_ii b_ii;a_iii b_iii; a_iv b_iv];

%Build the LHS matrix that holds all the known values (the "constants")
left_i = [eps0 - sin(a_i)*sin(a_i)*eps22_i; eps45 - sin(b_i)*sin(b_i)*eps22_i];
left_ii = [eps180 - sin(a_ii)*sin(a_ii)*eps22_ii; eps135 - sin(b_ii)*sin(b_ii)*eps22_ii];
left_iii = [eps180 - sin(a_iii)*sin(a_iii)*eps22_iii; eps225 -
sin(b_iii)*sin(b_iii)*eps22_iii];
left_iv = [eps0 - sin(a_iv)*sin(a_iv)*eps22_iv; eps315 - sin(b_iv)*sin(b_iv)*eps22_iv];

%Build the RHS matrix that holds the coefficients of the unknown values
right_i = [cos(a_i)*cos(a_i)  2*sin(a_i)*cos(a_i); cos(b_i)*cos(b_i)
2*sin(b_i)*cos(b_i)];
right_ii = [cos(a_ii)*cos(a_ii)  2*sin(a_ii)*cos(a_ii); cos(b_ii)*cos(b_ii)
2*sin(b_ii)*cos(b_ii)];
right_iii = [cos(a_iii)*cos(a_iii)  2*sin(a_iii)*cos(a_iii); cos(b_iii)*cos(b_iii)
2*sin(b_iii)*cos(b_iii)];
right_iv = [cos(a_iv)*cos(a_iv)  2*sin(a_iv)*cos(a_iv); cos(b_iv)*cos(b_iv)
2*sin(b_iv)*cos(b_iv)];

%unknowns = [e11; e12]
%left = right * unknowns
%inv(right)*left = unknowns

%Multiply the LHS by the inverse RHS matrices to solve for the unknowns strain_11 and
strain_12
eps_orthog_i = inv(right_i)*left_i;
eps_orthog_ii = inv(right_ii)*left_ii;
```

```
eps_orthog_iii = inv(right_iii)*left_iii;
eps_orthog_iv = inv(right_iv)*left_iv;

%Extract the strain_11 and strain_12 values out of the product matrix
eps11_i = eps_orthog_i(1);
eps11_ii = eps_orthog_ii(1);
eps11_iii = eps_orthog_iii(1);
eps11_iv = eps_orthog_iv(1);

eps12_i = eps_orthog_i(2);
eps12_ii = eps_orthog_ii(2);
eps12_iii = eps_orthog_iii(2);
eps12_iv = eps_orthog_iv(2);

%Compute the average longitudinal, transverse, and shear strains, averaging
%from all four quadrants of neighbors
marker(j).epsTT = [eps11_i eps11_ii eps11_iii eps11_iv];
marker(j).epsLL = [eps22_i eps22_ii eps22_iii eps22_iv];
marker(j).epsLT = [eps12_i eps12_ii eps12_iii eps12_iv];
marker(j).epsall = [eps0 eps45 eps90 eps135 eps180 eps225 eps270 eps315];
if j == 124,
    marker(j).epsTT = [-0.2 eps11_ii eps11_iii eps11_iv];
    marker(j).epsLT = [0 eps12_ii eps12_iii eps12_iv];
end


%%%%%%
%Compute the principal strains:
eps_tens = [mean(marker(j).epsTT) mean(marker(j).epsLT); mean(marker(j).epsLT)
mean(marker(j).epsLL)];
[V,D] = eig(eps_tens);
marker(j).prin_s1 = D(1,1);
marker(j).prin_s2 = D(2,2);
marker(j).prin_2d = V;
dotpr(j) = dot(V(:,1),V(:,2));

%in 3d space:
prin3d1 = marker(j).prin_2d(:,1)'*[marker(j).e1; marker(j).e2];
prin3d1 = prin3d1/norm(prin3d1);
prin3d2 = marker(j).prin_2d(:,2)'*[marker(j).e1; marker(j).e2];
prin3d2 = prin3d2/norm(prin3d2);

%with the following command, the lengths of the 2 vectors in this prin_3d matrix
%are equal to the magnitude of the 2 principal strains
%marker(m).prin_3d = [abs(marker(m).prin_s(1,1))*prin3d1'
abs(marker(m).prin_s(2,2))*prin3d2'];

%with this following command instead, the 2 vectors are unit vectors
marker(j).prin_3d = [prin3d1' prin3d2'];

%Compute the directions of zero longitudinal strain (these are theta
%degrees from the
%principal directions, which are directions of pure normal strain)
%Reference: Ramsay, Modern Structural Geology, 1983. p.294
%(tan phi)^2 = (prin_stretch_1 - 1)/(1 - prin_stretch_2),
%where phi = angle between principal direction #1 and the no-strain
%direction in the initial configuration,
% and prin_stretch = 1 + strain in the principal direction
%(principal stretch is also called "quadratic extension")
% --> phi = arctan(sqrt( (prin_stretch_1 - 1)/(1 - prin_stretch_2) ))
if marker(j).prin_s1 < 0 && marker(j).prin_s2 > 0,
    %direction of zero longitudinal strain only
    %exists if there is extension along one principal
    %direction and contraction along the other principal direction)
    prin_stretch_1 = 1 + marker(j).prin_s1;
    prin_stretch_2 = 1 + marker(j).prin_s2;
    phi(j) = atan(sqrt( (prin_stretch_2 - 1)/(1 - prin_stretch_1) ));
    %Ramsay equation has larger prin stretch in numerator, smaller in
    %denominator
```

```
    %construct rotation matrix to take vector from principal direction to
    %no-stretch direction:
    Cphi_1 = [cos(phi(j)) sin(phi(j)); -1*sin(phi(j)) cos(phi(j))];
    Cphi_2 = [cos(pi-phi(j)) sin(pi-phi(j)); -1*sin(pi-phi(j)) cos(pi-phi(j))];
    nx_2d_1 = Cphi_1*marker(j).prin_2d(:,1); %rotate phi deg from prin dirn #1
    nx_2d_2 = Cphi_2*marker(j).prin_2d(:,1); %rotate phi deg from prin dirn #2
    marker(j).nx_2d = [nx_2d_1 nx_2d_2];
    dotnx(j) = dot(marker(j).nx_2d(:,1),marker(j).nx_2d(:,2));

    %directions of no-stretch in 3d space:
     nx3d_1 = marker(j).nx_2d(1,1)*marker(j).e1 + marker(j).nx_2d(2,1)*marker(j).e2;
    nx3d_2 = marker(j).nx_2d(1,2)*marker(j).e1 + marker(j).nx_2d(2,2)*marker(j).e2;
    marker(j).nx_3d  = [nx3d_1' nx3d_2'];

end

if (marker(j).prin_s1 > 0 && marker(j).prin_s2 > 0),
    marker(j).nx_2d = [marker(j).prin_2d(:,1) marker(j).prin_2d(:,1)];
    %only one direction of min strain = direction of lower prin strain
    nx3d_1 = marker(j).nx_2d(1,1)*marker(j).e1 + marker(j).nx_2d(2,1)*marker(j).e2;
    nx3d_2 = marker(j).nx_2d(1,2)*marker(j).e1 + marker(j).nx_2d(2,2)*marker(j).e2;
    marker(j).nx_3d  = [nx3d_1' nx3d_2'];
    count(j) = 1;
end

if (marker(j).prin_s1 < 0 && marker(j).prin_s2 < 0),
    marker(j).nx_2d = [marker(j).prin_2d(:,2) marker(j).prin_2d(:,2)];
    %only one direction of min strain = direction of more positive prin strain
    nx3d_1 = marker(j).nx_2d(1,1)*marker(j).e1 + marker(j).nx_2d(2,1)*marker(j).e2;
    nx3d_2 = marker(j).nx_2d(1,2)*marker(j).e1 + marker(j).nx_2d(2,2)*marker(j).e2;
    marker(j).nx_3d  = [nx3d_1' nx3d_2'];
    count(j) = 1;
end

end

%%%%%%%%%%%%%%%%%%%%%%%%%%%%%%%%%%%%%%%%%%%%%%%%%%%%%%%%%%%%%%%%%%%%%%%%%%%%%%%
%save data to file
%%%%%%%%%%%%%%%%%%%%%%%%%%%%%%%%%%%%%%%%%%%%%%%%%%%%%%%%%%%%%%%%%%%%%%%%%%%%%%%
% put data into vectors
summ = zeros(num_mark,7);
for h = 1:num_mark,
    label(h) = marker(h).label;
    xinit(h) = marker(h).initial(1);
    yinit(h) = marker(h).initial(2);
    zinit(h) = marker(h).initial(3);
    xdef(h) = marker(h).deformed(1);
    ydef(h) = marker(h).deformed(2);
    zdef(h) = marker(h).deformed(3);
    u(h) = marker(h).disp(1);
    v(h) = marker(h).disp(2);
    w(h) = marker(h).disp(3);

    if h > 12 && h < 145,
    epsLL(h,:) = marker(h).epsLL;
    epsTT(h,:) = marker(h).epsTT;
    epsLT(h,:) = marker(h).epsLT;
    meanLL(h) = mean(marker(h).epsLL);
    meanTT(h) = mean(marker(h).epsTT);
    meanLT(h) = mean(marker(h).epsLT);
    prin_s1(h) = marker(h).prin_s1;
    prin_s2(h) = marker(h).prin_s2;
    summ(h,:) = [h marker(h).label meanLL(h)  meanTT(h)  meanLT(h) prin_s1(h)
prin_s2(h)];

    nx1(h,:) = marker(h).nx_2d(:,1)';
    nx2(h,:) = marker(h).nx_2d(:,2)';
end
end
```

```
%write to file
%fid = fopen('computedstrain.txt','w');
%fprintf(fid,'Computed longitudinal and transverse strain for each marker on leg\n\n');
%fprintf(fid,'Label  F11  F12  F21  F22  E11  E12  E21  E22  D11  D22  V11  V21  V12
V22\n\n');
%fprintf(fid,'%6.0f %8.3f %8.3f %8.3f %8.3f %8.3f %8.3f %8.3f %8.3f %8.3f %8.3f %8.3f
%8.3f %8.3f %8.3f \n',summ');
%status = fclose(fid);
```

APPENDIX D: STEP 6 OF STRAIN FIELD ALGORITHM

Quadrant II: The adjacent-grid-point normal strains in the second quadrant are related to the normal and shear strains in the second quadrant's orthogonal measurement basis.

$$\varepsilon_{i,j-1} = \varepsilon_{11}^{II} \cos^2 \theta_{i,j-1}^{II} + \varepsilon_{22}^{II} \sin^2 \theta_{i,j-1}^{II} + 2\varepsilon_{12}^{II} \cos\theta_{i,j-1}^{II} \sin\theta_{i,j-1}^{II} \quad \textbf{(D.1)}$$

$$\varepsilon_{i-1,j-1} = \varepsilon_{11}^{II} \cos^2 \theta_{i-1,j-1}^{II} + \varepsilon_{22}^{II} \sin^2 \theta_{i-1,j-1}^{II} + 2\varepsilon_{12}^{II} \cos\theta_{i-1,j-1}^{II} \sin\theta_{i-1,j-1}^{II} \quad \textbf{(D.2)}$$

$$\varepsilon_{i-1,j} = \varepsilon_{22}^{II} \quad \textbf{(D.3)}$$

The angles $\theta_{i,j-1}^{II}$ and $\theta_{i-1,j-1}^{II}$ are computed by

$$\theta_{i,j-1}^{II} = \arccos\left(\frac{\bar{D}_{i,j-1} \bullet \bar{e}_1^{II}}{\left|\bar{D}_{i,j-1}\right| \left|\bar{e}_1^{II}\right|}\right) \quad \textbf{(D.4)}$$

$$\theta_{i-1,j-1}^{II} = \arccos\left(\frac{\bar{D}_{i-1,j-1} \bullet \bar{e}_1^{II}}{\left|\bar{D}_{i-1,j-1}\right| \left|\bar{e}_1^{II}\right|}\right) \quad \textbf{(D.5)}$$

Equations D.1 through D.3 are solved simultaneously for $\varepsilon_{11}{}^{II}$, $\varepsilon_{22}{}^{II}$, and $\varepsilon_{12}{}^{II}$.

Quadrant III: The adjacent-grid-point normal strains in the third quadrant are related to the normal and shear strains in the third quadrant's orthogonal measurement basis.

$$\varepsilon_{i,j-1} = \varepsilon_{11}^{III} \cos^2 \theta_{i,j-1}^{III} + \varepsilon_{22}^{III} \sin^2 \theta_{i,j-1}^{III} + 2\varepsilon_{12}^{III} \cos\theta_{i,j-1}^{III} \sin\theta_{i,j-1}^{III} \quad \textbf{(D.6)}$$

$$\varepsilon_{i+1,j-1} = \varepsilon_{11}^{III} \cos^2 \theta_{i+1,j-1}^{III} + \varepsilon_{22}^{III} \sin^2 \theta_{i+1,j-1}^{III} + 2\varepsilon_{12}^{III} \cos\theta_{i+1,j-1}^{III} \sin\theta_{i+1,j-1}^{III} \quad \textbf{(D.7)}$$

$$\varepsilon_{i+1,j} = \varepsilon_{22}^{III} \quad \textbf{(D.8)}$$

The angles $\theta_{i,j-1}^{III}$ and $\theta_{i+1,j-1}^{III}$ are computed by

$$\theta_{i,j-1}^{III} = \arccos\left(\frac{\vec{D}_{i,j-1} \bullet \vec{e}_1^{\,III}}{\left|\vec{D}_{i,j-1}\right|\left|\vec{e}_1^{\,III}\right|}\right) \tag{D.9}$$

$$\theta_{i-1,j-1}^{III} = \arccos\left(\frac{\vec{D}_{i+1,j-1} \bullet \vec{e}_1^{\,III}}{\left|\vec{D}_{i+1,j-1}\right|\left|\vec{e}_1^{\,III}\right|}\right) \tag{D.10}$$

Equations D.6 through D.9 are solved simultaneously for $\varepsilon_{11}{}^{III}$, $\varepsilon_{22}{}^{III}$, and $\varepsilon_{12}{}^{III}$.

Quadrant IV: The adjacent-grid-point normal strains in the fourth quadrant are related to the normal and shear strains in the fourth quadrant's orthogonal measurement basis.

$$\varepsilon_{i,j+1} = \varepsilon_{11}^{IV}\cos^2\theta_{i,j+1}^{IV} + \varepsilon_{22}^{IV}\sin^2\theta_{i,j+1}^{IV} + 2\varepsilon_{12}^{IV}\cos\theta_{i,j+1}^{IV}\sin\theta_{i,j+1}^{IV} \tag{D.11}$$

$$\varepsilon_{i+1,j+1} = \varepsilon_{11}^{IV}\cos^2\theta_{i+1,j+1}^{IV} + \varepsilon_{22}^{IV}\sin^2\theta_{i+1,j+1}^{IV} + 2\varepsilon_{12}^{IV}\cos\theta_{i+1,j+1}^{IV}\sin\theta_{i+1,j+1}^{IV} \tag{D.12}$$

$$\varepsilon_{i+1,j} = \varepsilon_{22}^{IV} \tag{D.13}$$

The angles $\theta_{i,j+1}^{IV}$ and $\theta_{i+1,j+1}^{IV}$ are computed by

$$\theta_{i,j+1}^{IV} = \arccos\left(\frac{\vec{D}_{i,j+1} \bullet \vec{e}_1^{\,IV}}{\left|\vec{D}_{i,j+1}\right|\left|\vec{e}_1^{\,IV}\right|}\right) \tag{D.14}$$

$$\theta_{i+1,j+1}^{IV} = \arccos\left(\frac{\vec{D}_{i+1,j+1} \bullet \vec{e}_1^{\,IV}}{\left|\vec{D}_{i+1,j+1}\right|\left|\vec{e}_1^{\,IV}\right|}\right) \tag{D.15}$$

Equations D.11 through D.13 are solved simultaneously for $\varepsilon_{11}{}^{IV}$, $\varepsilon_{22}{}^{IV}$, and $\varepsilon_{12}{}^{IV}$.

APPENDIX E: UNCORRECTED STRAIN TENSOR RESULTS

Because the virtual sensors were raised cones of stiff paint, error was introduced into the circumferential displacement measurement if there was any inconsistency in the location on the cone surface at which the sensor's 3D position was measured. For example, suppose that the base of the cone is selected in the initial configuration of the leg, but the tip of the cone is selected in the deformed configuration of the leg. The result of this inconsistency in location selection is that the circumferential displacement of that sensor is artificially increased. This source of error may explain the anomalies (the very high and very low strains) seen on the inside of the upper thigh and on the tibia. Here the strains were computed to be greater than 150%, which does not make physical sense. In compiling a summary of the results, any results that indicate strains of greater than 100% are ignored (0 of the long strain results, 9 out of the 144 (6%) sensors for circumferential strain, 8 out of 144 for shear strain), because 100% is beyond the failure strain of my most of our skin. Future work is needed to explain exactly why those impossible results occurred and to build robustness into the computational algorithm to avoid them.

Strain tensor component	Percent of results that required correction
Longitudinal	0 %
Circumferential	6.3 %
Shear	5.5 %

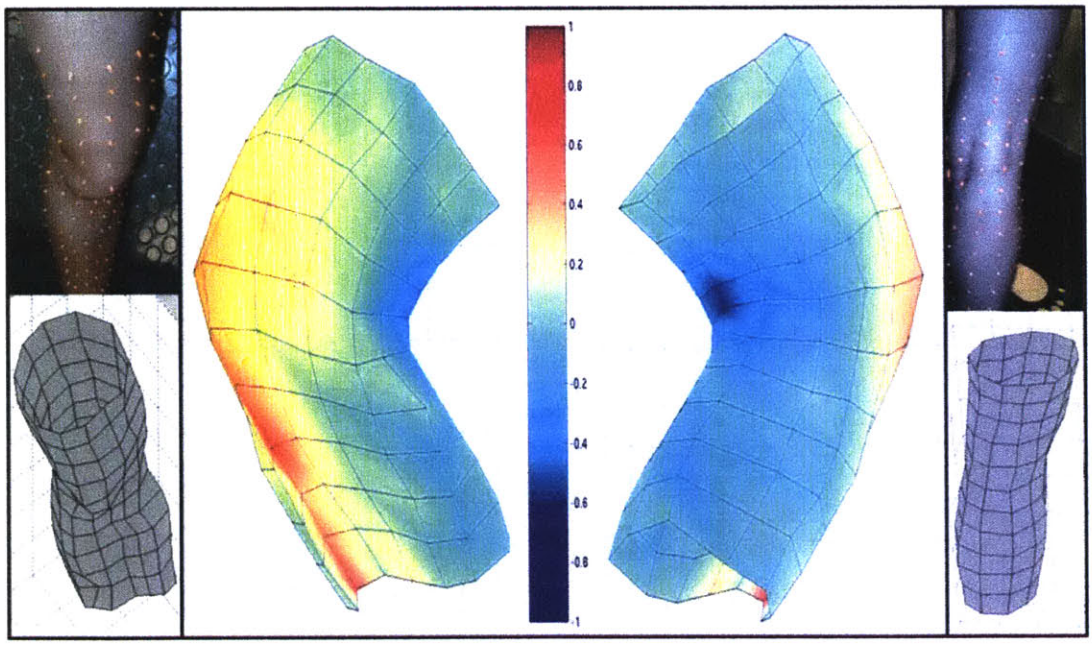

Figure E.1 Uncorrected longitudinal strain

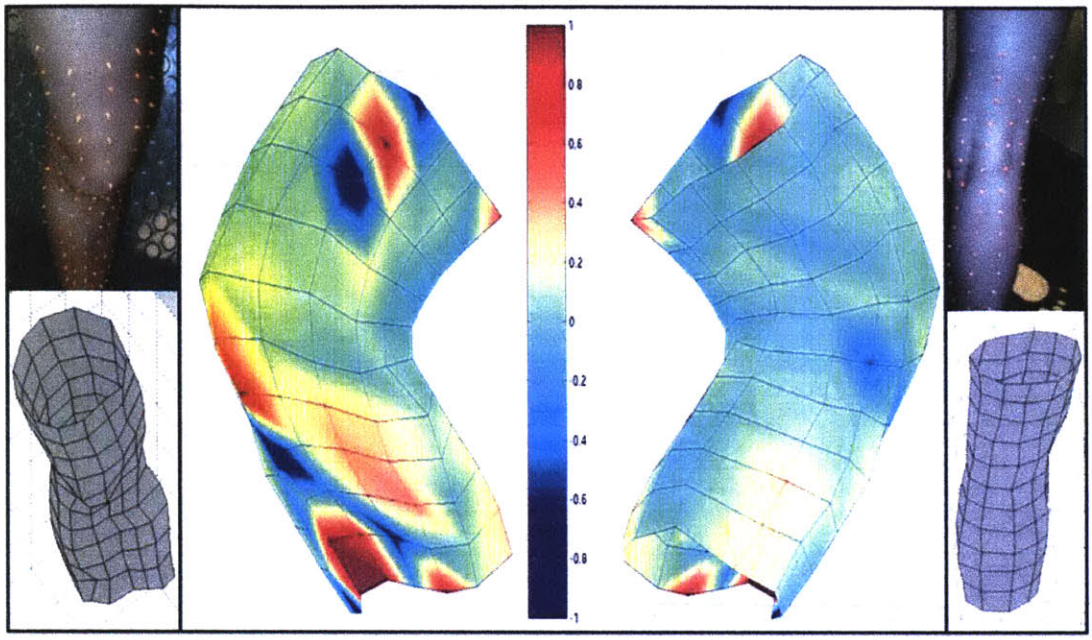

Figure E.2 Uncorrected circumferential strain

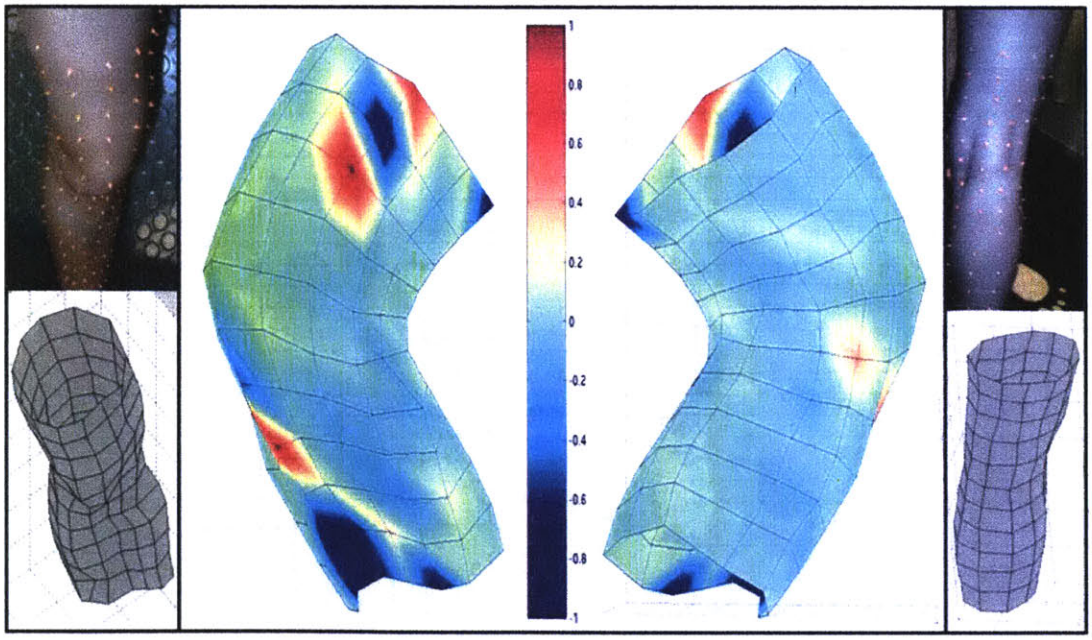

Figure E.3 Uncorrected shear strain

APPENDIX F: CORRECTED SKIN STRAIN RESULTS AND HIGHEST/LOWEST DECILES OF EACH COMPONENT OF SKIN STRAIN TENSOR

Marker Label	Longitudinal Strain	Circumferential Strain	Shear Strain
201	0.04	0.07	0.05
202	0.07	0.10	0.01
203	-0.08	0.10	0.01
204	0.00	-0.04	0.10
205	0.02	-0.06	0.13
206	-0.01	-0.06	0.13
207	0.01	-0.06	-0.06
208	-0.11	-0.09	0.05
209	-0.05	-0.06	0.02
210	-0.05	0.04	0.01
211	0.03	0.04	-0.01
212	0.09	0.04	-0.02
301	0.09	0.13	-0.04
302	0.04	-0.04	0.20
303	0.13	-0.25	0.20
304	-0.05	-0.03	0.23
305	0.05	0.08	-0.09
306	-0.06	-0.17	0.10
307	-0.12	-0.13	0.05
308	-0.15	-0.07	0.05
309	-0.11	0.03	-0.03
310	-0.02	-0.02	0.01
311	0.02	-0.04	0.04
312	0.08	0.04	-0.02
401	0.19	0.07	0.05
402	0.19	0.02	0.07
403	0.13	0.02	0.10
404	0.01	0.13	0.04
405	-0.18	0.03	-0.01
406	-0.33	-0.15	0.02
407	-0.36	0.01	-0.01
408	-0.17	0.06	-0.07
409	-0.12	-0.13	0.13
410	0.00	0.02	0.00
411	0.03	0.08	0.02
412	0.30	0.00	-0.09
501	0.28	0.02	0.05
502	0.31	0.04	0.02
503	0.16	0.09	0.01
504	0.05	0.21	-0.09
505	-0.22	-0.06	0.02
506	-0.46	-0.19	0.06
507	-0.57	-0.05	0.08
508	-0.28	0.04	-0.08
509	-0.22	0.03	-0.03
510	-0.06	-0.09	0.11
511	0.13	0.01	-0.01
512	0.31	0.01	-0.03
601	0.36	0.12	0.01
602	0.24	0.18	-0.01
603	0.27	0.08	-0.07
604	0.05	0.10	-0.06
605	-0.26	-0.05	0.05
606	-0.45	-0.10	0.00
607	-0.59	-0.15	0.15
608	-0.33	-0.03	-0.03
609	-0.25	-0.01	0.05
610	0.02	0.07	-0.02
611	0.27	0.02	-0.09
612	0.40	-0.03	0.03
701	0.33	0.60	-0.32
702	0.17	0.03	0.08
703	0.15	-0.02	0.01
704	0.07	-0.04	0.03
705	0.02	0.06	-0.14
706	-0.34	0.00	0.04

Marker Label	Longitudinal Strain	Circumferential Strain	Shear Strain
707	-0.30	0.00	-0.03
708	-0.31	0.01	0.02
709	-0.12	0.00	0.03
710	0.03	-0.49	0.41
711	0.22	-0.17	0.07
712	0.39	0.10	-0.05
801	0.51	0.99	-0.55
802	0.24	0.19	-0.07
803	-0.01	0.32	-0.13
804	-0.06	0.31	-0.10
805	0.03	0.07	-0.13
806	-0.24	-0.03	0.14
807	-0.09	0.05	-0.10
808	-0.23	0.03	0.05
809	0.01	0.07	-0.06
810	-0.04	0.02	0.06
811	0.14	0.07	-0.06
812	0.18	-0.46	0.54
901	0.70	-0.04	-0.02
902	0.31	0.10	-0.03
903	0.04	0.41	-0.14
904	-0.04	0.34	-0.11
905	-0.17	0.07	0.02
906	-0.14	0.17	-0.06
907	-0.13	-0.02	-0.01
908	-0.11	-0.03	0.02
909	-0.07	0.13	0.01
910	-0.04	0.04	0.04
911	0.12	0.20	-0.07
912	0.17	-0.28	0.02
1001	0.35	-0.06	-0.20
1002	0.22	-0.36	0.17
1003	0.06	0.36	-0.15
1004	0.06	0.49	-0.27
1005	-0.14	-0.09	0.20
1006	-0.03	0.18	-0.01
1007	-0.14	-0.13	0.05
1008	-0.18	-0.06	0.05
1009	-0.11	0.32	-0.06
1010	-0.04	0.15	-0.03
1011	-0.01	0.10	0.03
1012	0.05	-0.44	-0.04
1101	0.47	0.31	-0.50
1102	0.15	0.81	-0.75
1103	0.14	-0.69	0.32
1104	-0.06	-0.15	0.04
1105	-0.14	0.03	0.08
1106	-0.08	0.34	-0.03
1107	-0.10	-0.10	0.00
1108	-0.25	-0.05	0.08
1109	-0.06	0.24	-0.01
1110	-0.01	0.14	-0.02
1111	0.08	-0.06	-0.08
1112	0.00	-0.06	-0.12
1201	0.61	0.06	-0.43
1202	0.07	0.05	-0.71
1203	0.29	-0.21	-0.13
1204	0.03	-0.19	0.07
1205	-0.01	0.06	0.06
1206	-0.08	0.34	0.01
1207	-0.08	0.02	-0.06
1208	-0.03	-0.03	0.04
1209	-0.11	0.26	0.00
1210	-0.10	0.12	0.03
1211	0.04	-0.12	0.06
1212	0.04	0.03	-0.05

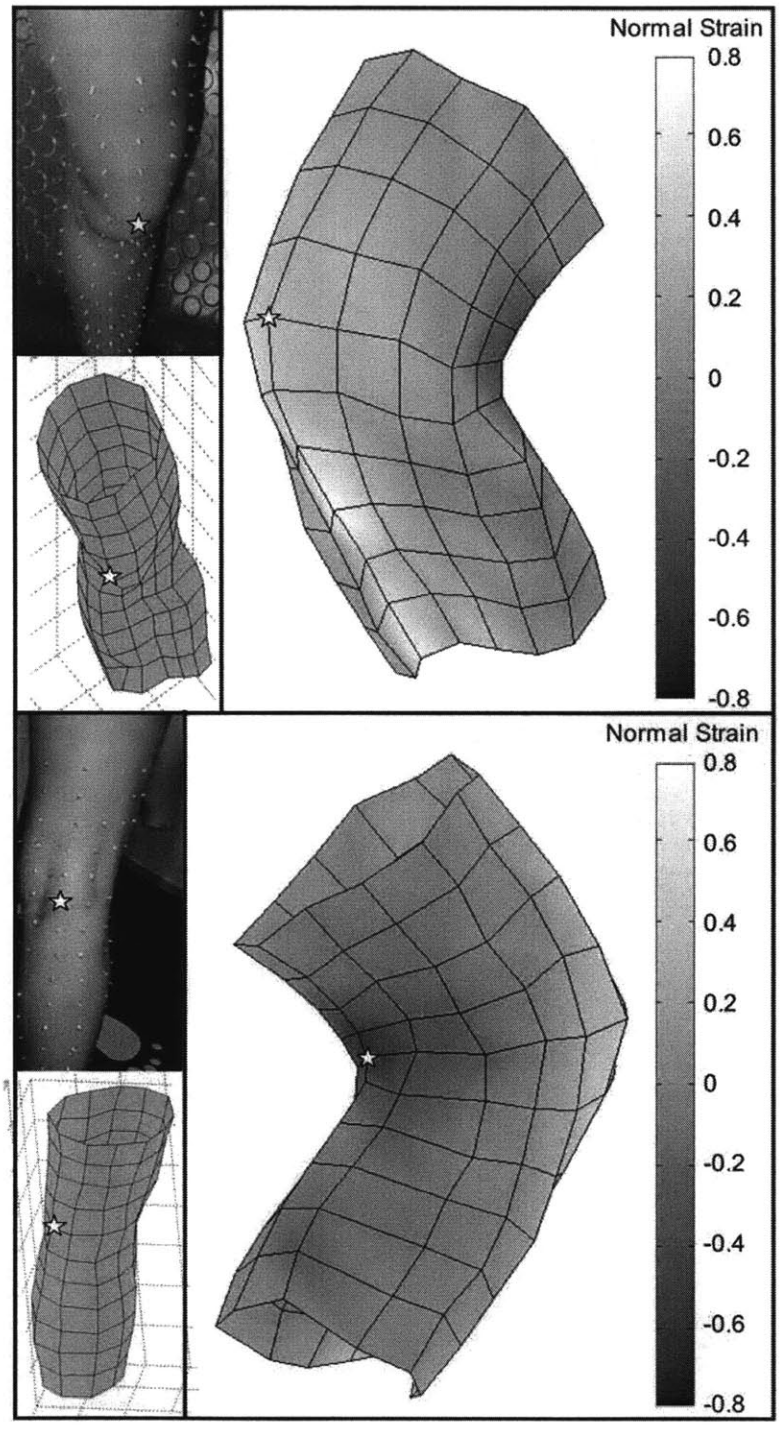

Figure F.1 Longitudinal normal strain of the leg skin during knee flexion, in grayscale. Strain data are displayed on a snapshot of a 3D reconstruction of the deformed position of each tracked point, with the magnitude of the longitudinal strain represented by the grayscale level of the surface surrounding each point. On the sides are photos and 3D reconstructions of the leg in its initial 0-degree non-flexed state. The stars indicate the location of the patella.

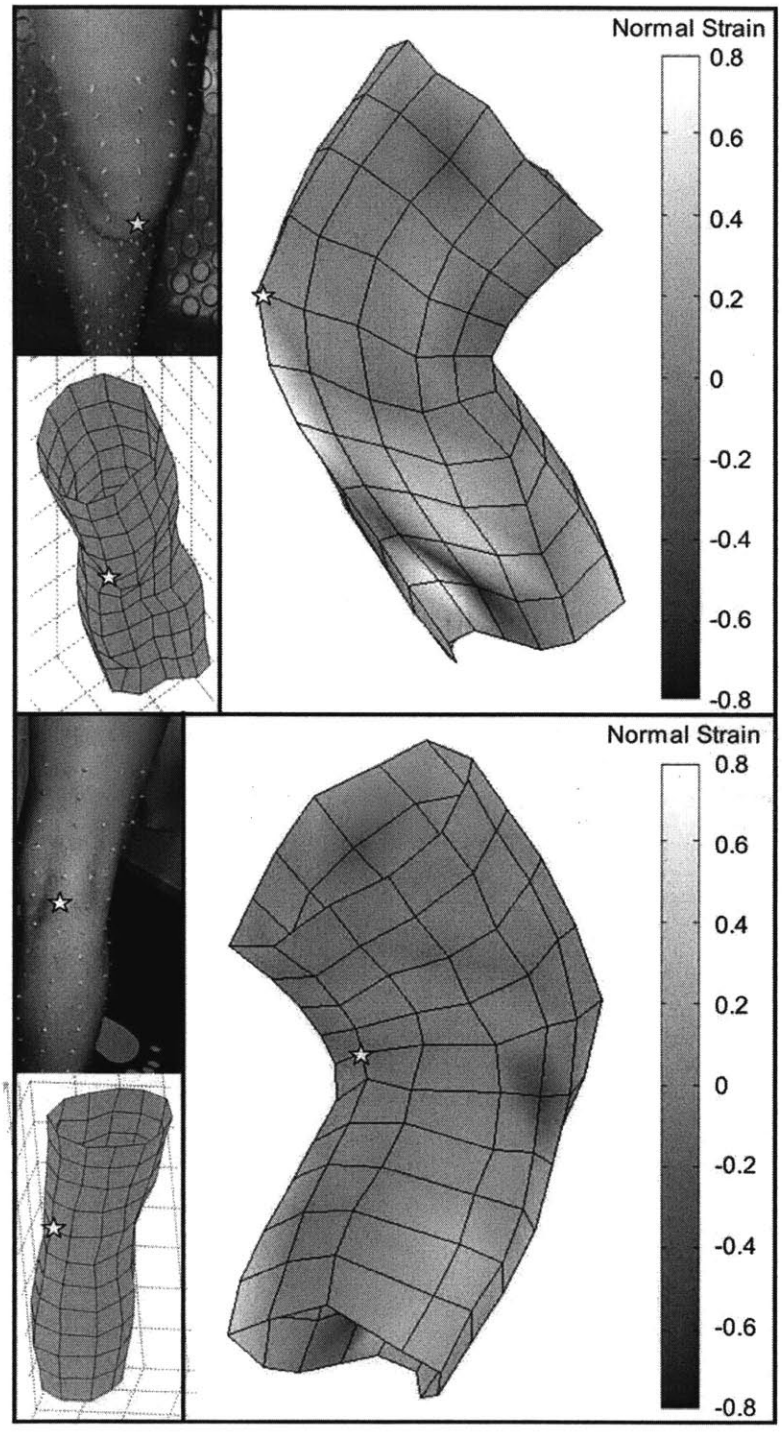

Figure F.2 Circumferential normal strain of the leg skin during knee flexion, in grayscale. Strain data are displayed on a snapshot of a 3D reconstruction of the deformed position of each tracked point, with the magnitude of the longitudinal strain represented by the grayscale level of the surface surrounding each point. On the sides are photos and 3D reconstructions of the leg in its initial 0-degree non-flexed state. The stars indicate the location of the patella.

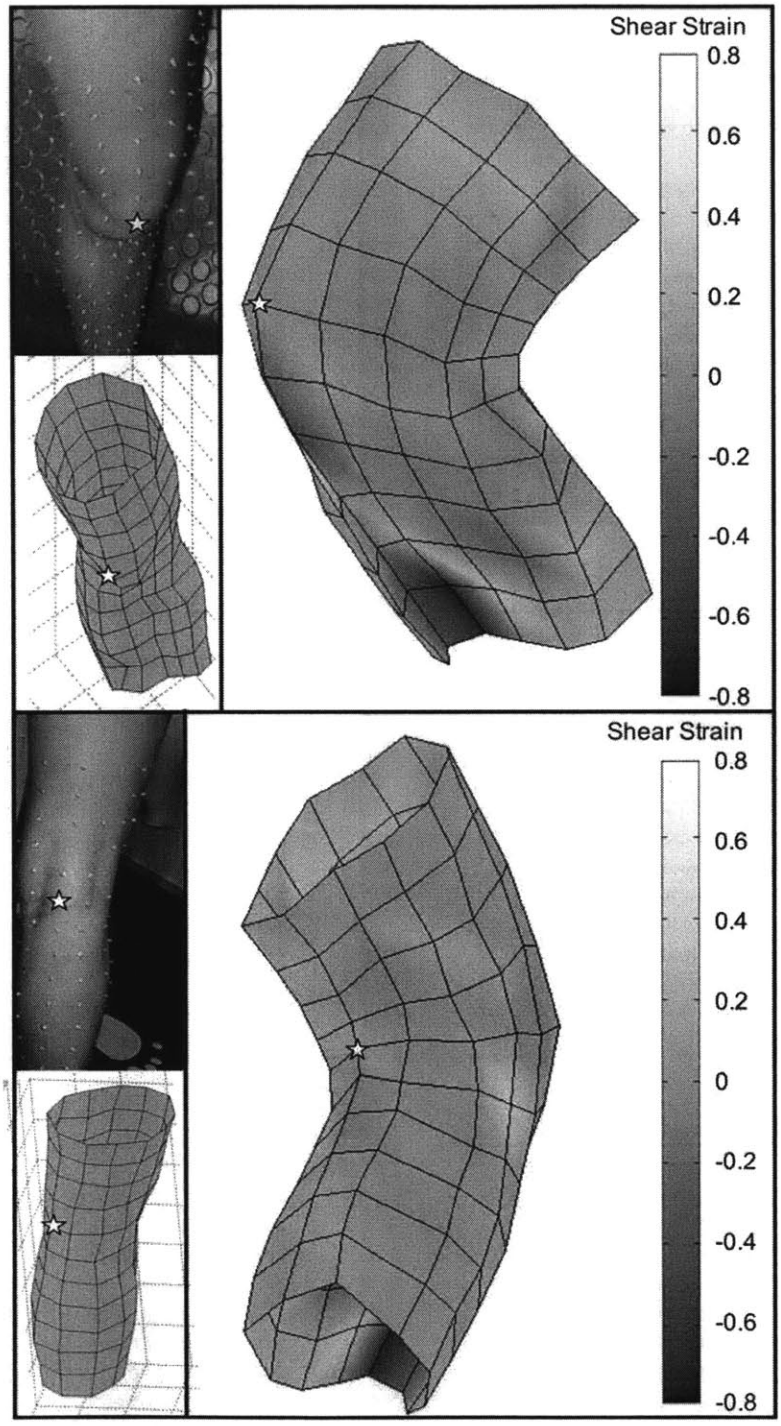

Figure F.3 Engineering shear strain of the leg skin during knee flexion, in grayscale. Strain data are displayed on a snapshot of a 3D reconstruction of the deformed position of each tracked point, with the magnitude of the longitudinal strain represented by the grayscale level of the surface surrounding each point. On the sides are photos and 3D reconstructions of the leg in its initial 0-degree non-flexed state. The stars indicate the location of the patella.

Table F.1 Highest and lowest deciles of each strain tensor component.

Highest Decile of Longitudinal Strains

Location Label	Location Description	Strain Magnitude
901	Anterior Below Knee	0.70
1201	Anterior Below Knee	0.61
801	Anterior Below Knee	0.51
1101	Anterior Below Knee	0.47
612	Anterior At Knee	0.40
712	Anterior At Knee	0.39
601	Anterior At Knee	0.36
1001	Anterior Below Knee	0.35
701	Anterior At Knee	0.33
502	Anterior Above Knee	0.31
902	Anterior Below Knee	0.31
512	Anterior Above Knee	0.31
412	Anterior Above Knee	0.30

Lowest Decile of Longitudinal Strains

Location Label	Location Description	Strain Magnitude
607	Posterior At Knee	-0.59
507	Posterior Above Knee	-0.57
506	Posterior Above Knee	-0.46
606	Posterior At Knee	-0.45
407	Posterior Above Knee	-0.36
706	Posterior At Knee	-0.34
406	Posterior Above Knee	-0.33
608	Posterior At Knee	-0.33
708	Posterior At Knee	-0.31
707	Posterior At Knee	-0.30
508	Posterior Above Knee	-0.28
605	Medial At Knee	-0.26
609	Lateral At Knee	-0.25

Highest Decile of Circumferential Strains

Location Label	Location Description	Strain Magnitude
801	Anterior Below Knee	0.99
1102	Anterior Below Knee	0.81
701	Anterior At Knee	0.60
1004	Medial Below Knee	0.49
903	Medial Below Knee	0.41
1003	Medial Below Knee	0.36
904	Medial Below Knee	0.34
1206	Posterior Below Knee	0.34
1106	Posterior Below Knee	0.34
1009	Lateral Below Knee	0.32
803	Medial Below Knee	0.32
1101	Anterior Below Knee	0.31
804	Medial Below Knee	0.31

Lowest Decile of Circumferential Strains

Location Label	Location Description	Strain Magnitude
1103	Medial Below Knee	-0.69
710	Lateral At Knee	-0.49
812	Anterior Below Knee	-0.46
1012	Anterior Below Knee	-0.44
1002	Anterior Below Knee	-0.36
912	Anterior Below Knee	-0.28
303	Medial Above Knee	-0.25
1203	Medial Below Knee	-0.21
1204	Medial Below Knee	-0.19
506	Posterior Above Knee	-0.19
711	Lateral At Knee	-0.17
306	Posterior Above Knee	-0.17
607	Posterior At Knee	-0.15

Highest Decile of Shear Strains

Location Label	Location Description	Strain Magnitude
812	Anterior Below Knee	0.54
710	Lateral At Knee	0.41
1103	Medial Below Knee	0.32
304	Medial Above Knee	0.23
302	Anterior Above Knee	0.20
303	Anterior Above Knee	0.20
1005	Medial Below Knee	0.20
1002	Anterior Below Knee	0.17
607	Posterior At Knee	0.15
806	Posterior Below Knee	0.14
409	Lateral Above Knee	0.13
205	Medial Above Knee	0.13
206	Posterior Above Knee	0.13

Lowest Decile of Shear Strains

Location Label	Location Description	Strain Magnitude
1102	Anterior Below Knee	-0.75
1202	Anterior Below Knee	-0.71
801	Anterior Below Knee	-0.55
1101	Anterior Below Knee	-0.50
1201	Anterior Below Knee	-0.43
701	Anterior At Knee	-0.32
1004	Medial Below Knee	-0.27
1001	Anterior Below Knee	-0.20
1003	Medial Below Knee	-0.15
903	Medial Below Knee	-0.14
705	Medial At Knee	-0.14
803	Medial Below Knee	-0.13
805	Medial Below Knee	-0.13

APPENDIX G: CONSTRUCTION OF 3D LEG REPLICAS WITH Z CORPORATION 3D PRINTER

Preparation of File

Purchase Magics RP, or download trial version of Magics RP (http://www.materialise.com). You will need to contact company to receive approval to use the trial version.

Use Magics RP to delete everything except the leg portion of the scan model, to add thickness to the leg, and to separate into four or five parts that will each fit into the 3D printer. In the Magics RP application, complete the following steps:

- <Load> the PLY file of the 3D laser scanned body.
- <Edit> → <Rescale> → x 1000
- <Smooth>
- If scan still shows entire body, use <Cut and Punch> to delete everything except the desired leg.
- <FixWizard> to fill holes, delete bad edges, flip normals (keep iterating until part has a good surface).
- <Offset Part> (towards the inside) → <Add Thickness> → 8 mm (leg will be hollow but its shell will be 8 mm thick)
- Measure the total length of the leg, from thigh to ankle. The "Snap Settings" will need to be changed in order to snap a distance marker onto the STL triangles that make up the leg surface.
- Divide the total length (in mm) by 190 to determine the number of segments needed (the maximum height of a 3D printer part is 200 mm, so the laser scan model must be divided into segments of less than 200 mm in height - use 190 mm as a maximum height with a 10 mm margin of error).
- Divide the total length by the number of segments determined in the previous step. Starting from the ankle, measure the required number of segment lengths, and mark them with a distance marker.
- <Cut and Punch> to divide the leg at the locations that have been marked. There should now be four or five longitudinal segments (i.e., upper thigh, lower thigh, knee, upper calf, ankle).
- Save each of the different parts that has been created as a different STL file. To enable <Save Part As>, a green flag must be placed in the "S" column near each part name.

Materials Needed for 3D Printing

The 90-degree leg was printed using starch powder and the Z Corporation 3D printer in the MIT Aero/Astro Gelb Lab.

The 30-degree leg was printed by Chris Krebs, using plaster powder and the Z Corporation at Payload Systems, Inc.

Each part was hardened by infiltration with 450 g of Z Max Epoxy resin plus its associated hardener (the resin and the hardener are mixed together just before application). The epoxy was applied with a 5-cm wide paint brush, and 3 coats of epoxy were applied to each part. All coats were applied within the same 1.5-hour work session.

APPENDIX H: USE AND SHORTCOMINGS OF TEKSCAN PRESSURE SENSORS

The Tekscan pressure measurement system provided body surface pressure data throughout this effort's prototype testing. Manufactured by in South Boston, MA, Tekscan pressure sensors respond to contact loads and transform them into surface pressure measurements. We used type 9801 Tekscan sensors, which are paper thin, flexible, and inextensible, measuring 8 inches long by 3 inches wide with 96 individual load-sensing cells. We placed the sensors on the surface of the leg, underneath the pressure-producing MCP prototype.

The Tekscan system is relatively simple to use but difficult to use with precision and repeatability. The sensors must be prepped and calibrated before each use, and they must be used under a restricted set of loading conditions. Suggestions for the use of Tekscan sensors in other situations can be found in a publication from the Tekscan corporation entitled "Equilibration and Calibration Practical Suggestions, 10/27/03." The most relevant advice from this guide are found below.

Relevant notes from "Equilibration and Calibration Practical Suggestions, 10/27/03" guide for Tekscan use:

- For equilibration and calibration, use compliant material between sensor and bladder
- Possibly use compliant material (urethane foam?) between sensor and leg
- Could calibrate before and after making measurements, to see if drift has occurred for sensor; then edit calibration values of recorded measurements and movies
- Digital output will drift for 30 seconds before leveling off
- Pierce sensors before use in low pressure chamber – otherwise trapped air will cause a "pillow effect"
- Place Teflon paper of silicone spray lubricant over sensor in order to eliminate shear – for our purposes, wear thin nylons on leg, underneath sensor to prevent shear between skin and bottom of sensor
- Regular photocopy paper could be substitute for Teflon paper
- The force-detecting units are called "sensels" and are located at the intersection of the rows and columns of impedance-varying ink
- "Tare" feature on software is not on our older version of software – but we can replicate its function by taking a reading when the sensors are on the curved leg but still unloaded, then subtract that reading's values from the loaded reading
- Recommended sensor adhesives: double-sided tape is fine on non-active region of sensor but its thickness will cause artifacts if placed under active region; spray adhesive can be used on both active and non-active regions (recommended: 3M Adhesive 77)
- Sensor turn-on thresholds:
- Software - default turn-on setting is 3 digital raw counts out of 255 – can change this in noise settings
- Hardware – turn-on is 4 grams per sensel = 0.3 psi if range of sensor is 25 psi; < 0.3 psi if range of sensor is 5 psi (40 mmHg ~= 0.75 psi)
- Clean sensor with damp rag or cloth and alcohol

APPENDIX I: LOW PRESSURE LEG CHAMBER FOR HYPOBARIC TESTING

Construction and Validation of a Low-Pressure Leg Chamber

Cameron Dube, September 2004

In order to assess the performance of a partial-body MCP prototype, a low pressure chamber (LPC) must be constructed around the body part of interest. Small, cylindrical LPC's have been used to conduct tests on forearm and lower leg prototypes [1], [2]. However, our understanding of MCP garments advances it becomes necessary to build a LPC which can test larger prototypes that involve major joints.For this reason a large (approximately 5'x1'x3') LPC was constructed to allow tests on an entire leg, including the knee (Figure I.1). The chamber's sides were constructed from 3/4" clear acrylic sheet. The edges were milled so that the sheets met in two 3/8" joints. Brass machine screws were used to tack the sides together and to apply tension during construction.

Finite elements analysis was performed by Mide Technology Corp. to determined the size of the structural ribs that were required (ribs shown in perspective in Figure I.1). The ribs were constructed of solid 2"x1" T6 6061 aluminum and held together by steel machine screws. The box was made airtight with silicon sealant, and leaks were repaired with flexible quick-dry epoxy. Standard vacuum fixtures were added to provide an emergency quick-release, a manifold, and an atmospheric bypass. A 9" hole was cut in the top surface, and two parts were made to fit it: a 1"-thick aluminum plug for validation, and an adapted polypropylene dry-suit gasket for human testing. Both parts are sealed with an O ring.

To validate the LPC, it was depressurized remotely. The box was determined to be structurally sound; however, at a pressure approximately 20kPa below the operating pressure of (-29 kPa vacuum), the seals begin to leak. This leak mode is actually advantageous -- if the box is ever under-pressurized, the seals will open and will relieve the pressure difference in a non-destructive and safe manner.

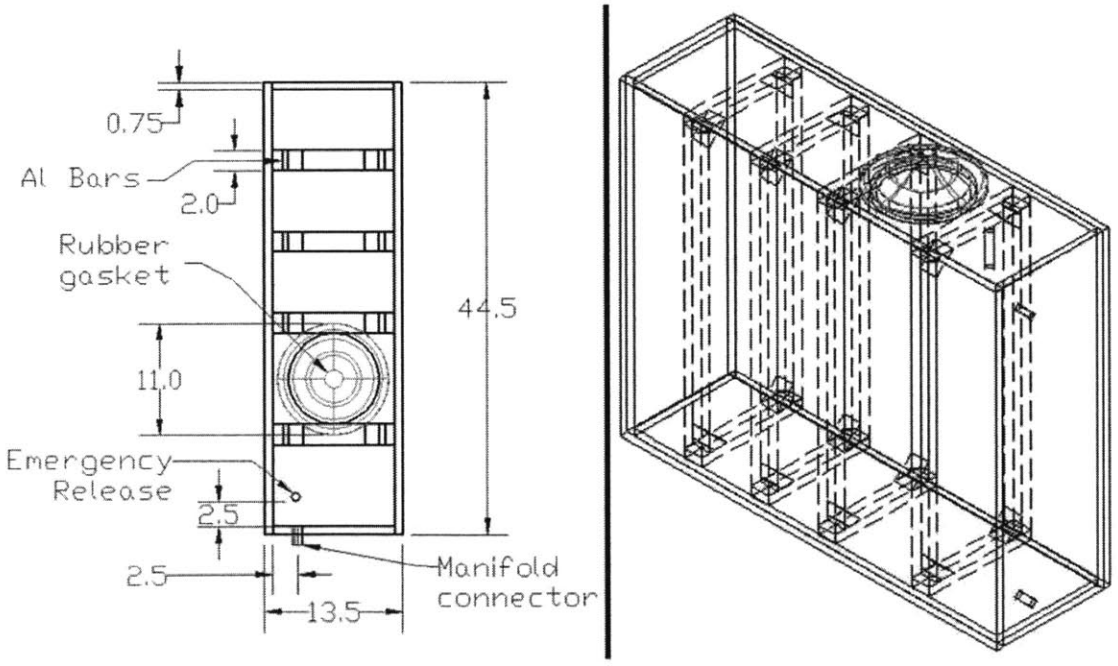

Figure I.1 (Left) Design of the Low Pressure Leg Chamber, with the leg adapter installed/. The manifold and Brass tacking screws are not shown. (Right) Perspective view of the LPLC. Dashed lines show aluminum structural support ribs.

APPENDIX J: DERIVATION OF UNCERTAINTY OF SKIN STRAIN FIELD RESULTS

Position data was collected by manually locating the 156 position trackers (raised dots) on 3D solid models on the computer screen. These dots were small (4-mm diameter at the base) cone-like pointed protrusions from the smooth leg surface. Because they were identified manually, there was inconsistency in the precise location on the cone that was chosen. The experimental procedure called for selecting the sharp tip of the protrusion, but a point closer to the base of the protrusion could have been chosen in error. Such an error in selecting an inconsistent location on the cone surface has the largest effect on the measurement circumferenital strain. Suppose two cones separate from each other during knee flexion, and suppose that in the initial configuration (straight leg), their positions are measured at their tips, according to correct experimental procedure. Now also suppose that in the deformed configuration (bent leg), their positions are measured at the outsides of the bases of the cones. This error causes the final separation to be recorded as larger than it actually is. Consequently, the strain is computed as larger that it actually is. The absolute uncertainty in strain that results from this source of error is 0.14 strain units (14% stretch or contraction). To account for the other sources of error mentioned in Chapter 5 of this thesis, we add 0.6 more strain units of uncertainty. In total, the maximum possible absolute error in strain magnitude is 0.20 strain units. The resultant uncertainty in the angular orientation of the lines of minimum stretch is 30 degrees.

ABSOLUTE ERROR IN STRAIN MAGNITUDE – Figure J.1 and the subsequent equations illustrate the worst case scenario of incorrectly measuring the position of the position tracker cone. The resulting absolute error in the computed strain value is a function of the initial position tracker separation, ℓ_o, and the diameter of the base of the cone, d. The percent error in the computed strain value is a function of ℓ_o, d, and the final separation between the position trackers, ℓ_f (alternatively we can say that the percent error depends on ℓ_o, d, and the strain, ε). In this thesis, the initial separation is fixed at roughly 30 mm, and the average cone diameter is 4 mm. The final separation and the strain are variable over the surface of the leg.

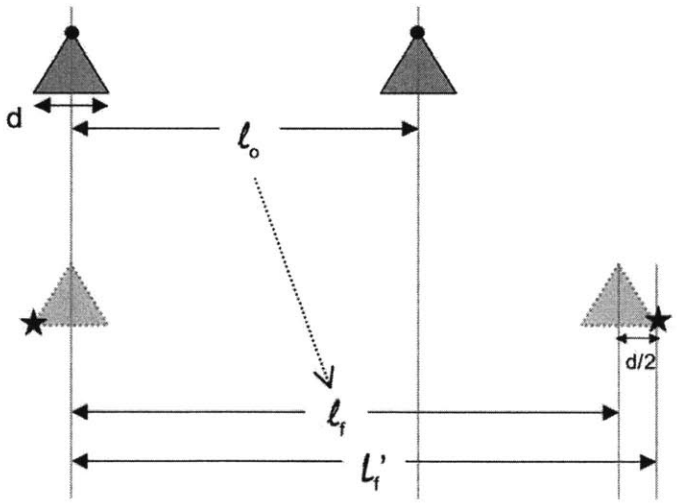

Figure J.1 Schematic of position tracker cones, their initial and final separations, and the possible inconsistency in position measurement. In the initial configuration, the positions of the cones are correctly measured by their tips (black circles). However, in the final configuration, their positions are incorrectly measured at the outside of their bases (black stars).

The true strain, ε, is the change in separation between the cone tips ($\ell_f - \ell_o$),divided by the initial separation between the cone tips (ℓ_o).

$$\varepsilon = \frac{\ell_f - \ell_o}{\ell_o} \tag{J.1}$$

The computed strain, ε ', is incorrect because the final separation has been incorrectly measured as $\ell_f' = \ell_f + d$:

$$\varepsilon' = \frac{\ell_f' - \ell_o}{\ell_o}; \qquad \ell_f' = \ell_f + d \tag{J.2}$$

$$\Rightarrow \quad \varepsilon' = \frac{\ell_f - \ell_o + d}{\ell_o} = \varepsilon + \frac{d}{\ell_o} \tag{J.3}$$

The computed strain is incorrect by an amount equal to d/ℓ_o strain units. Therefore, the absolute uncertainty in strain magnitude due to incorrect position measurement is 0.14 (in units of strain):

$$\varepsilon' - \varepsilon = \varepsilon + \frac{d}{\ell_o} - \varepsilon = \frac{d}{\ell_o} = \frac{4\ mm}{30\ mm} = 0.14 \tag{J.4}$$

Figure J.2 illustrates the effect of decreasing the cone diameter to values less than 4 mm; the plot shows that the uncertainty in strain would be substantially decreased through the use of smaller position trackers.

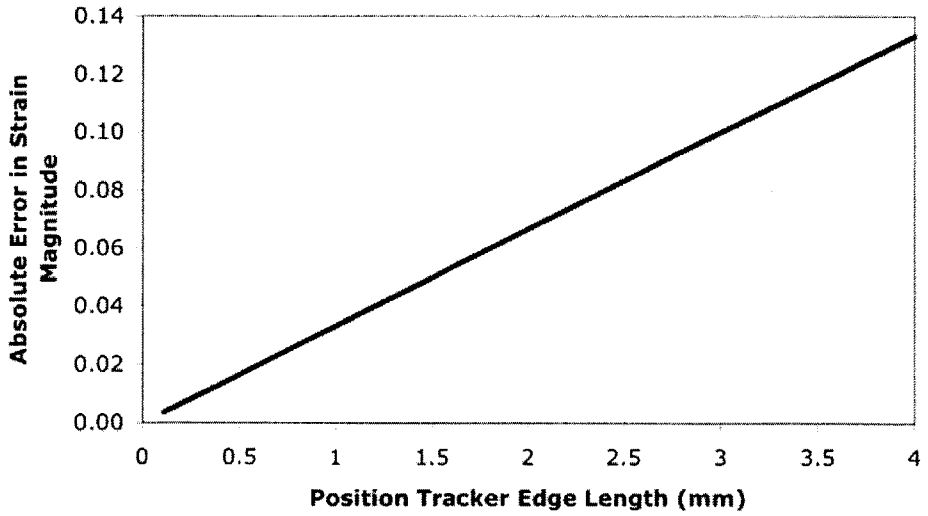

Figure J.2 Maximum possible absolute error in circumferential strain magnitude as a function of the size of the leg surface grid point (in units of strain, where a 10% contraction is represented by 0.1 strain units, and an error of 0.1 indicates that the compute strain value was 0.1 strain units more or less than the true strian value).

RELATIVE ERROR IN STRAIN MAGNITUDE – The relative error in computed strain is equal to the absolute error divided by the true strain. This relative (percent) error in strain magnitude depends on the cone diameter, the initial separation, and the true strain that occurs:

$$\frac{\varepsilon + \frac{d}{\ell_o} - \varepsilon}{\varepsilon} = \frac{d}{\varepsilon \ell_o} \qquad \text{(J.5)}$$

For a cone diameter of 4 mm, an initial separation of 30 mm, and a strain of 0.3 units, the percent error in strain computation is 40% (not 40% stretch or contraction, but 40% of the true strain value). Figure J.3 shows how this percent error in strain can be decreased by using smaller position trackers. The plot also shows that the error affects the truth of small strain (≤ 0.1 strain units) computations much more than large strain computations.

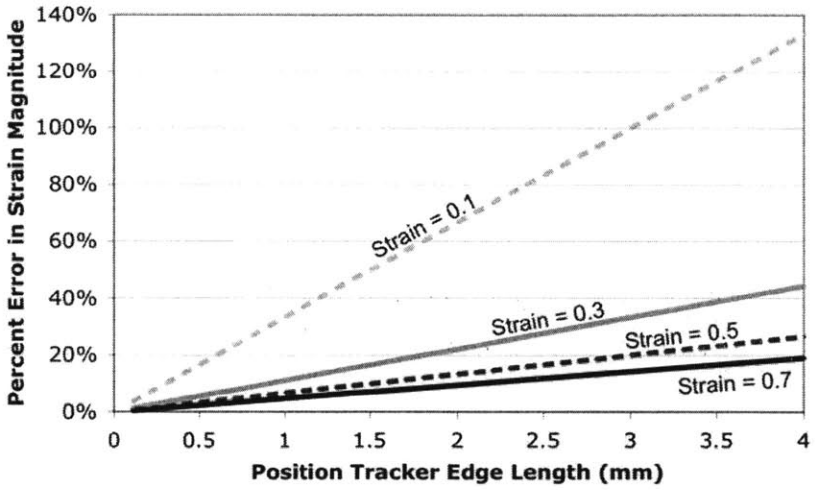

Figure J.3 Maximum possible relative error in circumferential strain magnitude as a function of the size of the leg surface grid point (in units of percentage, where a 10% relative error indicates that the computed strain value was 10% more or less than the true strain value).

ABSOLUTE ERROR IN LINES OF MINIMUM STRETCH ANGLES – Now the question is: how does the 0.2 strain units uncertainty in strain *magnitude* propogate into an uncertainty in strain *direction*? To answer this question, the algorithm for determing the angular orientation of the lines of minimum stretch (described in Section 3.2 of this thesis) was applied to a sample of simulated leg surface points (n = 500). The "true" and "computed" strain tensor components of these leg surface points were known. For the 500 simulated points, the differences between the true and computed strains (the strain magnitude errors) were normally distributed with a mean of zero and a standard deviation of 0.067. This distribution of errors was chosen because it causes almost all (98%) of the computed strain values to fall within ± 0.2 strain units of the true strain values.

The results of this simulation were that most (90%) of the errors in the angular orientation of the lines of minimum stretch were less than 30 degrees.

APPENDIX K: DERIVATION OF MATERIAL REQUIREMENTS FOR SECOND SKIN MECHANICAL COUNTER PRESSURE SUITS

A mechanical counter pressure "second skin" garment may consist of a fine mesh of fibers or narrow fabric tape, all oriented along the lines of non-extension. For this design to be realized, the material property requirements of the fibers or fabric, as well as their orientation, must be determined. An ideal Bio-Suit fiber or narrow fabric has a tensile strength of greater than 60 N (13 lbf) and an elastic modulus that is initially high but that approaches zero as the strain surpasses 30% and the load reaches 30 N. The target operating range for the fiber or fabric is at tensile loads of 30 N +/- 5 N and strains of 50% +/- 20%.

The derivation of these requirements follows: The garment must provide 30 kPa of pressure on the leg surface, and the leg radius can be as large as 10 cm. Garment tension (per longitudinal width) is equal to the product of pressure and radius, so the desired operating tensile load is (30 kPa x 10 cm = 3000 N/m =) 30 N per centimeter of garment. Assume that one fiber or narrow fabric strip bears the load for each longitudinal centimeter, and assume a desired factor of safety of 2. The final tensile strength requirement is (2 x 30 N =) 60 N. The zero-modulus portion of the force-displacement curve allows for the same level of tension to be maintained even when the leg shape changes slightly.

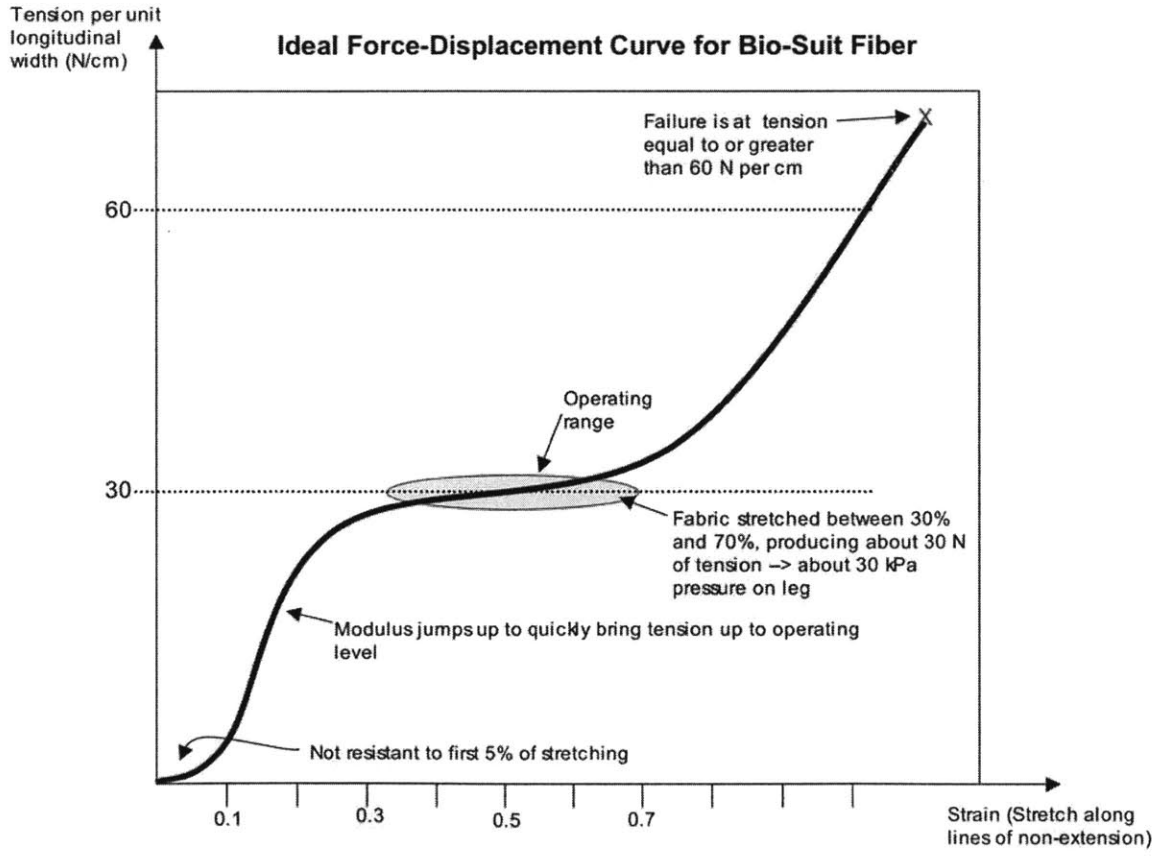

Figure K-1 The ideal material properties for a fiber or narrow fabric for a mechanical counter pressure lines of non-extension garment. Curve indicates tension (per centimeter of longitudinal garment length) as a function of fiber or fabric stretch.

APPENDIX L: MATLAB™ CODE FOR IMPLEMENTATION OF FINITE ELEMENT METHOD TO DETERMINE LEG SKIN STRAIN

```
%c1 and c2 are 2d grid parameters
%x1(t) = f1(c1,c2); x2(t) = f2(c1,c2); x3(t) = f3(c1,c2)
c1 = 0;
c2 = 0;

%N1, N2, N3, N4 are the shape functions that relate c1 and c2 to the 3d
%components of x: x1, x2, x3
dN1dc1 = 0.25*(1+c2);
dN1dc2 = 0.25*(1+c1);
dN2dc1 = 0.25*(-1-c2);
dN2dc2 = 0.25*(1-c1);
dN3dc1 = 0.25*(-1+c2);
dN3dc2 = 0.25*(-1+c1);
dN4dc1 = 0.25*(1-c2);
dN4dc2 = 0.25*(-1-c1);

% for this one example element,
%use markers 0201, 0202, 0101, 0102
%1,2,13,14, respectively

%top right of element = Node 1 = marker 0102
%top left of element = Node 2 = marker 0101
%bottom left of element = Node 3 = marker 0201
%bottom right of element = Node 4 = marker 0202

%X_I_0 = actual 3d coordinates of the nodal point I, in the reference
%configuration
X_1_0 = marker(2).initial;
X_2_0 = marker(1).initial;
X_3_0 = marker(13).initial;
X_4_0 = marker(14).initial;

%X_I_t = actual 3d coordinates of the nodal point I, in the deformed
%configuration
X_1_t = marker(2).deformed;
X_2_t = marker(1).deformed;
X_3_t = marker(13).deformed;
X_4_t = marker(14).deformed;


% now construct the deformation gradient matrix F =>  F = dx/dX
for i = 1:3,
    for j= 1:3,

        F102(i,j) = (dN1dc1*X_1_t(i) + dN2dc1*X_2_t(i) + dN3dc1*X_3_t(i) +
dN4dc1*X_4_t(i))*...
                (dN1dc1*X_1_0(j) + dN2dc1*X_2_0(j) + dN3dc1*X_3_0(j) + dN4dc1*X_4_0(j))^-
1 +...
                (dN1dc2*X_1_t(i) + dN2dc2*X_2_t(i) + dN3dc2*X_3_t(i) +
dN4dc2*X_4_t(i))*...
                (dN1dc2*X_1_0(j) + dN2dc2*X_2_0(j) + dN3dc2*X_3_0(j) + dN4dc2*X_4_0(j))^-
1;
    end
end

%%%%%%%%%%%%%%%%%%%%%%%%%%%%%%%%%%%%%%%%%%%%%%%%%%%%
%Here is what the above loop is doing (it is constructing the deformation gradient
matrix):
% F11 = (dN1dc1*X_1_t(1) + dN2dc1*X_2_t(1) + dN3dc1*X_3_t(1) +
dN4dc2*X_4_t(1))*(dN1dc1*X_1_0(1) + dN2dc1*X_2_0(1) % + dN3dc1*X_3_0(1) +
dN4dc2*X_4_0(1))^-1;

% F12 = (dN1dc1*X_1_t(1) + dN2dc1*X_2_t(1) + dN3dc1*X_3_t(1) +
dN4dc2*X_4_t(1))*(dN1dc1*X_1_0(2) + dN2dc1*X_2_0(2) % + dN3dc1*X_3_0(2) +
dN4dc2*X_4_0(2))^-1;
```

```
% F13 = (dN1dc1*X_1_t(1) + dN2dc1*X_2_t(1) + dN3dc1*X_3_t(1) +
dN4dc2*X_4_t(1))*(dN1dc1*X_1_0(3) + dN2dc1*X_2_0(3) % + dN3dc1*X_3_0(3) +
dN4dc2*X_4_0(3))^-1;


% F21 = (dN1dc1*X_1_t(2) + dN2dc1*X_2_t(2) + dN3dc1*X_3_t(2) +
dN4dc2*X_4_t(2))*(dN1dc1*X_1_0(1) + dN2dc1*X_2_0(1) % + dN3dc1*X_3_0(1) +
dN4dc2*X_4_0(1))^-1;

% F22 = (dN1dc1*X_1_t(2) + dN2dc1*X_2_t(2) + dN3dc1*X_3_t(2) +
dN4dc2*X_4_t(2))*(dN1dc1*X_1_0(2) + dN2dc1*X_2_0(2) % + dN3dc1*X_3_0(2) +
dN4dc2*X_4_0(2))^-1;

% F23 = (dN1dc1*X_1_t(2) + dN2dc1*X_2_t(2) + dN3dc1*X_3_t(2) +
dN4dc2*X_4_t(2))*(dN1dc1*X_1_0(3) + dN2dc1*X_2_0(3) % + dN3dc1*X_3_0(3) +
dN4dc2*X_4_0(3))^-1;


% F31 = (dN1dc1*X_1_t(3) + dN2dc1*X_2_t(3) + dN3dc1*X_3_t(3) +
dN4dc2*X_4_t(3))*(dN1dc1*X_1_0(1) + dN2dc1*X_2_0(1) % + dN3dc1*X_3_0(1) +
dN4dc2*X_4_0(1))^-1;

% F32 = (dN1dc1*X_1_t(3) + dN2dc1*X_2_t(3) + dN3dc1*X_3_t(3) +
dN4dc2*X_4_t(3))*(dN1dc1*X_1_0(2) + dN2dc1*X_2_0(2) % + dN3dc1*X_3_0(2) +
dN4dc2*X_4_0(2))^-1;

% F33 = (dN1dc1*X_1_t(3) + dN2dc1*X_2_t(3) + dN3dc1*X_3_t(3) +
dN4dc2*X_4_t(3))*(dN1dc1*X_1_0(3) + dN2dc1*X_2_0(3) % + dN3dc1*X_3_0(3) +
dN4dc2*X_4_0(3))^-1;

 % F = [F11 F12 F13;F21 F22 F23; F31 F32 F33];
%%%%%%%%%%%%%%%%%%%%%%%%%%%%%%%%%%%%%%%%%%%%%%%%


% for this one example element,
%use markers 0201, 0202, 0101, 0102
%1,2,13,14, respectively

%top right of element = Node 1 = marker 0602
%top left of element = Node 2 = marker 0601
%bottom left of element = Node 3 = marker 0701
%bottom right of element = Node 4 = marker 0702

%X_I_0 = actual 3d coordinates of the nodal point I, in the reference
%configuration
X_1_0 = marker(62).initial;
X_2_0 = marker(61).initial;
X_3_0 = marker(73).initial;
X_4_0 = marker(74).initial;

%X_I_t = actual 3d coordinates of the nodal point I, in the deformed
%configuration
X_1_t = marker(62).deformed;
X_2_t = marker(61).deformed;
X_3_t = marker(73).deformed;
X_4_t = marker(74).deformed;


% now construct the deformation gradient matrix F =>  F = dx/dX
for i = 1:3,
    for j= 1:3,

        F602(i,j) = (dN1dc1*X_1_t(i) + dN2dc1*X_2_t(i) + dN3dc1*X_3_t(i) +
dN4dc1*X_4_t(i))*...
                (dN1dc1*X_1_0(j) + dN2dc1*X_2_0(j) + dN3dc1*X_3_0(j) + dN4dc1*X_4_0(j))^-
1 +...
                (dN1dc2*X_1_t(i) + dN2dc2*X_2_t(i) + dN3dc2*X_3_t(i) +
dN4dc2*X_4_t(i))*...
                (dN1dc2*X_1_0(j) + dN2dc2*X_2_0(j) + dN3dc2*X_3_0(j) + dN4dc2*X_4_0(j))^-
```

```
1;
    end
end


%%%%%%%%%%%%%%%%%%%%%%%%%%%%%%%%%%%%%%%%%%%%%%%%%%%%
%Here is what the above loop is doing (it is constructing the deformation gradient
matrix):
% F11 = (dN1dc1*X_1_t(1) + dN2dc1*X_2_t(1) + dN3dc1*X_3_t(1) +
dN4dc1*X_4_t(1))*(dN1dc1*X_1_0(1) + dN2dc1*X_2_0(1) % + dN3dc1*X_3_0(1) +
dN4dc1*X_4_0(1))^-1;

% F12 = (dN1dc1*X_1_t(1) + dN2dc1*X_2_t(1) + dN3dc1*X_3_t(1) +
dN4dc1*X_4_t(1))*(dN1dc1*X_1_0(2) + dN2dc1*X_2_0(2) % + dN3dc1*X_3_0(2) +
dN4dc1*X_4_0(2))^-1;

% F13 = (dN1dc1*X_1_t(1) + dN2dc1*X_2_t(1) + dN3dc1*X_3_t(1) +
dN4dc1*X_4_t(1))*(dN1dc1*X_1_0(3) + dN2dc1*X_2_0(3) % + dN3dc1*X_3_0(3) +
dN4dc1*X_4_0(3))^-1;

% F21 = (dN1dc1*X_1_t(2) + dN2dc1*X_2_t(2) + dN3dc1*X_3_t(2) +
dN4dc1*X_4_t(2))*(dN1dc1*X_1_0(1) + dN2dc1*X_2_0(1)  %+ dN3dc1*X_3_0(1) +
dN4dc1*X_4_0(1))^-1;

 % F22 = (dN1dc1*X_1_t(2) + dN2dc1*X_2_t(2) + dN3dc1*X_3_t(2) +
dN4dc1*X_4_t(2))*(dN1dc1*X_1_0(2) +
% dN2dc1*X_2_0(2) + dN3dc1*X_3_0(2) + dN4dc1*X_4_0(2))^-1;

% F23 = (dN1dc1*X_1_t(2) + dN2dc1*X_2_t(2) + dN3dc1*X_3_t(2) +
dN4dc1*X_4_t(2))*(dN1dc1*X_1_0(3) + dN2dc1*X_2_0(3) % + dN3dc1*X_3_0(3) +
dN4dc1*X_4_0(3))^-1;


% F31 = (dN1dc1*X_1_t(3) + dN2dc1*X_2_t(3) + dN3dc1*X_3_t(3) +
dN4dc1*X_4_t(3))*(dN1dc1*X_1_0(1) + dN2dc1*X_2_0(1) % + dN3dc1*X_3_0(1) +
dN4dc1*X_4_0(1))^-1;

% F32 = (dN1dc1*X_1_t(3) + dN2dc1*X_2_t(3) + dN3dc1*X_3_t(3) +
dN4dc1*X_4_t(3))*(dN1dc1*X_1_0(2) + dN2dc1*X_2_0(2) % + dN3dc1*X_3_0(2) +
dN4dc1*X_4_0(2))^-1;

% F33 = (dN1dc1*X_1_t(3) + dN2dc1*X_2_t(3) + dN3dc1*X_3_t(3) +
dN4dc1*X_4_t(3))*(dN1dc1*X_1_0(3) + dN2dc1*X_2_0(3) % + dN3dc1*X_3_0(3) +
dN4dc1*X_4_0(3))^-1;

%F = [F11 F12 F13;F21 F22 F23; F31 F32 F33];
%%%%%%%%%%%%%%%%%%%%%%%%%%%%%%%%%%%%%%%%%%%%%%%%%%%%
```

APPENDIX M: SOFTWARE FOR LASER SCAN MANIPULATION, 3D RAPID PROTOTYPING, AND REVERSE ENGINEERING

Introduction: 3D scan models are polygonal meshes, and 3D scans of the whole body are comprised of on the order of 40,000 faces. The greatest challenge to editing and measuring 3D laser scan models is that they are saved as polygonal "meshes" (vertexes + edges) rather than the "solids" that most CAD software applications deal with. It is not a trivial task to convert from a "mesh" to a "solid," especially for meshes that have tens of thousands of faces. Rapidform or MeshWorks for Rhino seem to be the two best options for such conversion. The higher cost Rapidform will performthe conversion much faster than MeshWorks.

Software Title: CyScan

Vendor: Cyberware (www.cyberware.com)
Cost: Unknown, > $1500 (Owned by Natick Soldier Systems Center, Anthropometry Division)
Category: Laser Scan/Polygonal Mesh Viewing and Manipulation
Uses: View laser scan models with various filters (wireframe, shaded, colored, reflective). Edit scans by filling holes, deleting faces, separating into different portions. Measure location of certain points. Do batch processing of many scans to make surface area and volume measurements.
Advantages: Allows user to pick on a certain point, label it, and save its 3D coordinates according to that label.
Disadvantages: Computationally intensive, requires much processor power.

Software Title: Plyview

Vendor: Cyberware (www.cyberware.com)
Cost: Free (download at http://www.cyberware.com/samples/plyview/index.html; User Guide at http://www.cyberware.com/documentation/headus/www/plyview/index.html)
Category: Laser Scan/Polygonal Mesh Viewing
Uses: View .ply laser scan files in 3D, measure location of and distances between points.
Advantages: Free, easy to download and use, low-resource application, fastest way to produce bitmap or jpeg snapshot of a 3D laser scan.
Disadvantages: Viewing only, no file manipulation except for conversion between file types. Available for PCs only.

Software Title: Cyberware File Format Translators

Vendor: Cyberware (www.cyberware.com)
Cost: Free (download at http://www.cyberware.com/support/translators.html)
Category: Polygonal Mesh File Conversion
Uses: Convert from .ply file type to other mesh file types, including .obj, .stl, .iges, .3ds.
Advantages: Free, easy to download and use.
Disadvantages: Object will remain as a "mesh" rather than a "solid" even after conversion to .stl or .obj file type.

Software Title: Rapidform

Vendor: INUS Technology (www.rapidform.com)
Cost: $7500 for educational license (free trial is available)
Category: Reverse Engineering/3D Scan Modeling
Uses: manipulate the mesh objects created by 3D scanning. Partition, deform, resize models. **Measure** surface area, volume, distance, angles, radii, and curvature. Batch processing can be accomplished.
Advantages: Graphical user interface is fairly easy to use; measurement tasks are easy to accomplish and could potentially be automated. Can be used to prepare files for 3D printing –

can import files other than .ply, and can export to different file types. Customer support is high quality and readily available; this is best-selling software.
Disadvantages: Expensive, potentially too many features to be worth the cost. Only for Windows operating system.

Software Title: Magics RP
Vendor: Materialise (http://www.materialise.com/magics-rp/rp_ENG.html)
Cost: Unknown (Free trial available)
Category: Rapid Prototyping/ STL Manipulation
Uses: Prepare for STL, IGES, VDA, STEP, or CAD files for 3D printing (rapid prototyping). Convert mesh STL file (which has been converted from PLY by the Cyberware file format translator) into STL file with thickness. Divide into separate files.
Advantages: Free trial provides all the capabilities necessary to convert a 3D scan model (.ply file) into an .stl file for the 3D printer.
Disadvantages: Only for Windows operating system.

Software Title: Rhinoceros 3.0 + MeshWorks plug-in
Vendor: Robert McNeel & Associates (http://www.rhino3d.com)
Cost: $195 for single educational version of Rhino 3.0; $500 for MeshWorks for Rhino
Category: 3D Modeling of NURBS surfaces; Rapid Prototyping & Reverse Engineering
Uses: Rhino: NURBS solid modeling, drawing of curves, surfaces, and solids; Rhino can manipulate and repair STL files, but any STL meshes must first be converted to solids, so MeshWorks is a necessary add-on for the manipulation 3D scan models with Rhino. MeshWorks is an add-on to Rhino that allows user to manipulate mesh objects by filling holes, deleting faces, edges, and vertices, creating a solid object from a mesh object, offsetting meshes, splitting meshes into different parts.
Advantages: Relatively inexpensive, education version available, widely used in both industry and education.
Disadvantages: Rhino is on Athena Windows machines, but Athena does not allow installation of the additional necessary plug-ins. For Windows operating system only. Trial "evaluation" version only performs the Mesh-To-Solid operation for very small meshes (on the order of 1000 faces).

Software Title: Tecplot
Vendor: MIT/Athena
Cost: Free on MIT Athena
Category: Graphical Data Presentation and Analysis
Uses: Draw figures and graphics from many kinds of data sets, including complicated mesh objects such as whole-body laser scans. Once data set is displayed graphically, points can be clicked on and queried for their location, and other measurements can be taken.
Advantages: 3D data display is good enough to show 4-mm raised dots on body surface in a laser scan mesh object.
Disadvantages:

Software Title: 3DStudio
Category: 3D Animation
Advantages: Available on MIT Athena computers.
Disadvantages: Does not handle laser scan mesh objects – allows for viewing of mesh objects, but does not recognize or allow manipulation of mesh surfaces.

Software Title: Maya
Category: 3D Animation
Advantages: Available on MIT Athena computers.

Disadvantages: Does not handle laser scan mesh objects – allows for viewing of mesh objects, but does not recognize or allow manipulation of mesh surfaces.

APPENDIX N: SOFT TISSUE OF THE HUMAN LEG: CONSIDERATIONS FOR MODELING THE INTERACTIONS BETWEEN A MECHANICAL COUNTER PRESSURE SPACESUIT AND THE HUMAN BODY SURFACE

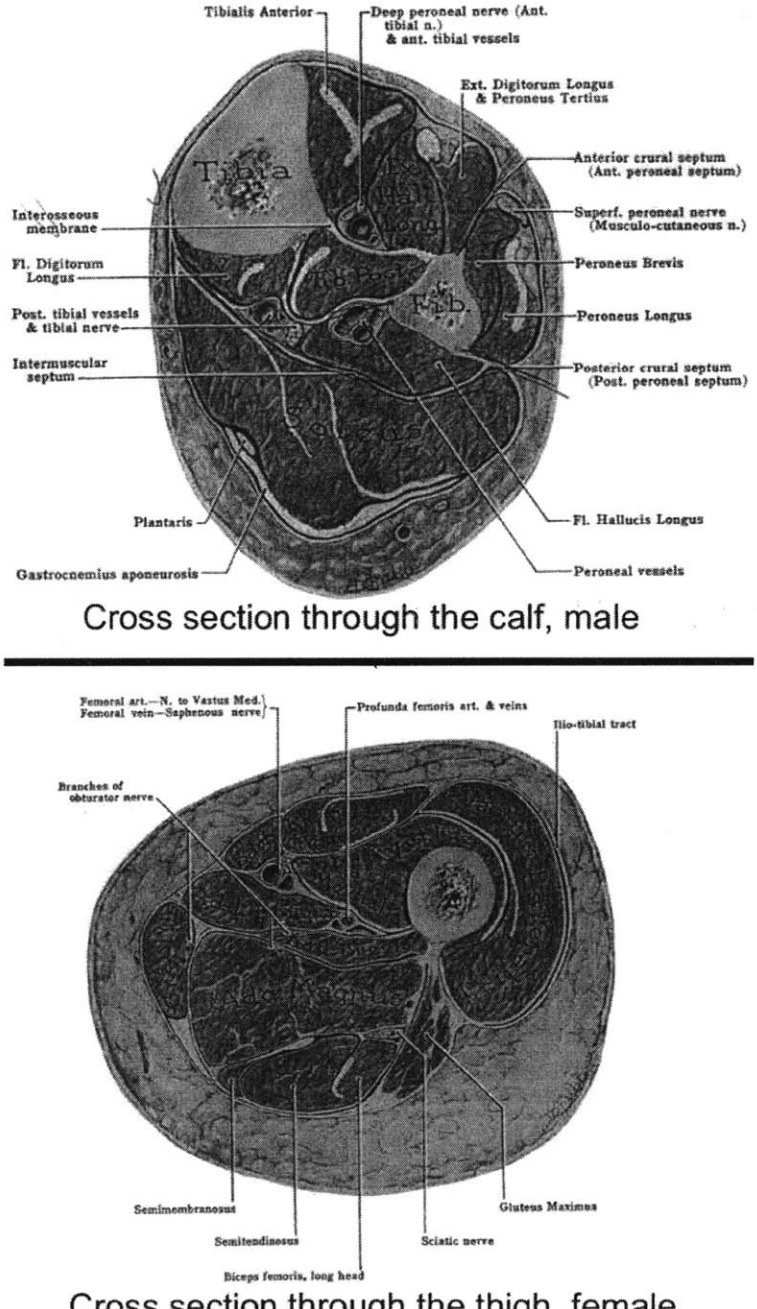

Figure N.1 Cross-sections of the human leg taken at the thigh and the calf [Gray, H. *Gray's Anatomy: The Classic Collector's Edition.* Random House, Inc., New York, 1988]. The elements shown in these drawings must be taken into consideration when predicting either the deformation of the leg during joint flexion or the response of the leg to a mechanical counter pressure garment.